Uterine synchronization analysis during pregnancy and labor using graph theory, classification based on machine learning

Kamil Bader El Dine

Par **Kamil BADER EL DINE**

Uterine synchronization analysis during pregnancy and labor using graph theory, classification based on machine learning

Thèse présentée en cotutelle
pour l'obtention du grade
de Docteur de l'UTC

Soutenue le 9 juin 2022
Spécialité : Bioingénierie et Informatique : Unité de Recherche en Biomécanique et Bioingénierie (UMR-7338)
D2680

CO-DIRECTION THESIS

To obtain the degree of Doctor issued by

Sorbonne University, University of Technology of Compiègne

Doctoral School « Engineering Science »

and

Lebanese University

Doctoral School « Science and Technology »

Spécialité : Bioingénierie et Informatique

Presented and publicly defended by

Bader El Dine Kamil

09-06-2022

Title:

Uterine synchronization analysis during Pregnancy and Labor using graph theory, classification based on machine learning

Jury Members

Noujoud Nader	**Assistant Prof. , Lebanese University**	**Co-Supervisor**
Catherine MARQUE	**Prof., University of Technology of Compiègne**	**Supervisor**
Mohamad KHALIL	**Prof. , Lebanese University**	**Supervisor**
Sandy Rihana	**Prof. , USEK University**	**Reviewer**
Carrault Guy	**Prof. , Rennes University 1**	**Reviewer**
Dan Istrate	**Prof., University of Technology of Compiègne**	**Examiner**
Mohamad Diab	**Prof., Rafik Hariri University**	**Examiner**

To...

Table of Contents

Table of Figures

General Introduction

Chapter 1

Chapter 2

Chapter 3

Chapter 4

Chapter 5

Chapter 6

General Introduction

Some women experience pregnancy difficulties that can lead to premature birth, i.e. delivery before 37 weeks of gestation. According to the World Health Organization (WHO), the perinatal death rate in the most developed parts of the world is around 7 per 1,000 births [1]. Children being born preterm is one of the leading causes of mortality and morbidity. Thus, prematurely born children are at a higher risk of death, as well as health and developmental issues [2].

Furthermore, preterm birth can result in large financial costs and has ramifications for public-sector services including health insurance, education, and other forms of social assistance. For instance, during infancy in 2013, hospital costs were estimated to be $9 billion as a result of birth abnormalities in the United States [3]. However, more days in the uterus can help the fetus mature and ensure the health of both mother and fetus. Thus, one of the most significant keys to preventing preterm labor is its early detection.

Different techniques have been used for the detection of preterm labor. One of the most promising techniques is the electrohysterogram (EHG) [4]. The EHG signal is recorded on the mother's abdomen and represents the electrical activity that induces the mechanical contraction of the myometrium (uterine muscle). It is considered to be a highly accurate sign of the electrical activity of the uterus [5].

Two physiological phenomena are associated to successful labor and delivery: increased excitability of the uterine cells and increased connectivity among myometrial cells, resulting in an increase in the propagation of the action potentials that activate uterine contractions [5].The increase in contraction efficiency is thus linked to two physiological phenomena: cellular excitability and the synchronization of the electrical activity of the whole uterine muscle [5] [6]. Both phenomena may be measured when recording the EHG.

Several studies examined the uterine synchronization using EHG signals analysis. Two main methodologies were used in these studies to examine this synchronization: correlation/connectivity analysis or propagation velocity of the EHGs. The propagation velocity is measured by analyzing either the propagation of complete bursts of EHG [7] or of single spikes detected within a burst [8], [9]. Nonetheless, the spike analysis might be suitable for the analysis of the short distance electrical diffusion process (typically employing small and close electrodes). Giving the long distance synchronization of the whole uterus, EHG burst analysis (with larger and more spaced electrodes) might be more adapted. When using EHG signals for the identification of statistical coupling between uterine contractions recorded throughout labor and/or pregnancy in recent studies, the connectivity study has shown promising results [10]. Then, the graph theory has been applied after the connectivity analysis to improve the classification between pregnancy and labor [11]. However, more work is needed in order to improve the classification between pregnancy and labor, based on EHG processing for the uterine synchronization analysis.

The main objective of this thesis is to propose a new methodology for studying the synchronization of uterine electrical activity by estimating the connectivity between recorded EHG signals. Indeed, for the global analysis (whole burst), in most previous researches, the EHG connectivity matrices were reduced by keeping simply their average [10] or by employing the graph methods [11]. The graph theory approach appears to be a better method to characterize the EHG connectivity matrices than the simple averaging or connectivity values. But the classification methods used in these studies remained very simple.

The machine learning methods is one of the innovative approaches developed in this work in order to enhance the connectivity/graph results. Hence, the information collected from both graph and connectivity methods has been used to fed different machine learning algorithms to classify labor and pregnancy contractions.

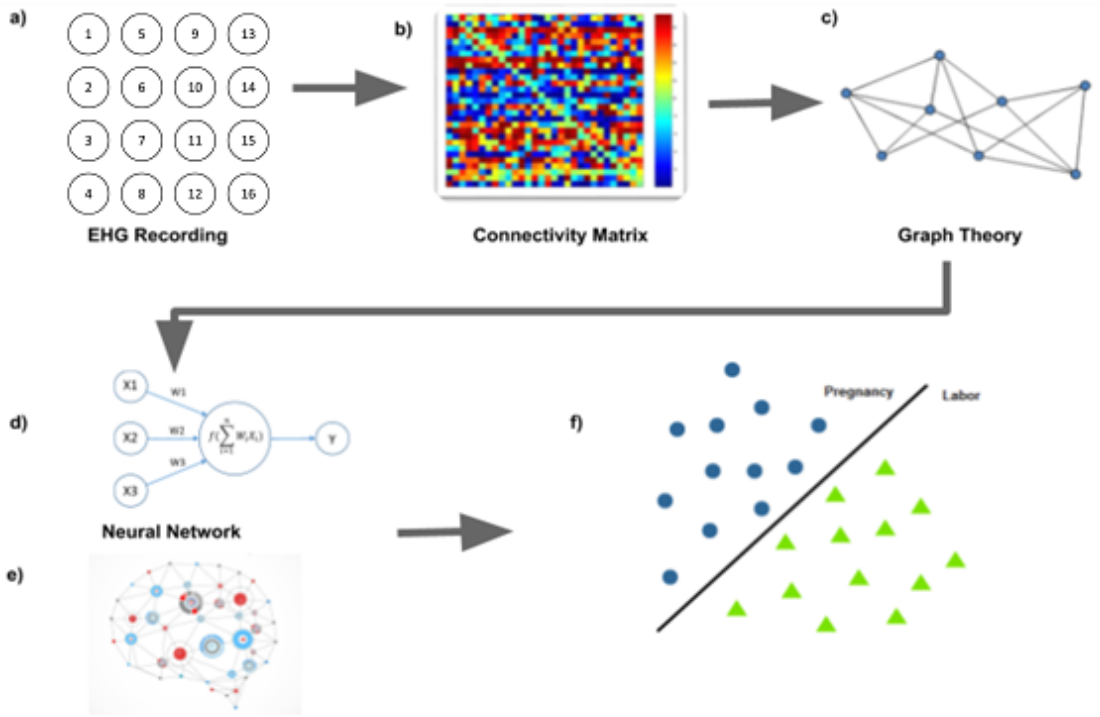

Figure 0.1. Implementing structure. (a) EHG signals. (b) The Connectivity Matrix. (c) Graph Theory. (d)(e) Neural Network and Deep Learning respectively. (f) Classification between Labor and Pregnancy

The whole pipeline of the first part of our work is represented in Figure 0.1. A connectivity matrix is generated from the recorded uterine EHGs, obtained by using a grid of 4x4 electrodes (Figure 0.1a), applying different connectivity methods to the whole EHG bursts (monopolar and denoised) (Figure 0.1b). This computed connectivity matrix is then displayed as a graph from which we extract different metrics (Figure 0.1c). Next, using these metrics as inputs, different neural network (Figure 0.1d) and deep learning (Figure 0.1e) methods are employed to enhance labor and pregnancy classification (Figure 0.1f).

Next, we tested the opportunity to select the best part of the EHG bursts, in order to capture the possible time evolution of the EHG characteristics (windowing approach) as well as the best electrodes to use (best node approach) in order to improve even more this classification results.

Finally, we used a EHG electro-mechanical model developed by our team [12] to simulate EHG signals on the mother's abdomen. We used the simulated EHGs to investigate the impact on the EHG features of the different parameters of the model involved in uterus synchronization.

This manuscript is organized as follows:

Chapter 1 discusses the overall introduction of preterm labor, which is considered to be the main cause for childhood mortality and morbidity. Then, the anatomical and physiological background of the uterus, as well as uterine contractility and its two fundamental factors: cell excitability and uterine synchronization, will be briefly presented. Following that, the chapter will go over the several pregnancy monitoring methods that have been employed to track uterine activity. Afterward, we will present a focus on connectivity/correlation analysis to detect preterm labor. Finally, we will assess the studies that were presented, focusing on the diagnosis of uterine activity and the detection of premature labor risk. Accordingly, the different goals of this work will be precised at the end of this chapter.

Chapter 2 covers the methods and materials developed in this thesis in order to examine the uterine connectivity and to identify labor and pregnancy contractions by applying machine learning methods. First, we will go over the various connectivity/correlation methods that were presented in this work. Note that the graph metrics that we employed will then be explained, along with the suggestion of new graph parameters. Following that, we will go through the machine learning techniques which are used to differentiate between labor and pregnancy contractions. After that, we will describe both types of data used in this work: real and simulated EHGs. Indeed, our team has created a computational EHG model, which we will briefly explain, to generate simulated data. We will furthermore describe the experimental techniques for recording real EHG signals, as well as the data gathering and preparation steps. Finally, we will present the different workflows developed in this work to process real and simulated EHG signals.

Chapter 3 presents work done for the processing of real electrohysterographic signals (EHG) recorded during labor and pregnancy. Using various connectivity methods, we will first evaluate the connectivity between EHG signals. Then, based on the graph theory, we will extract multiple graph metrics from the connectivity matrices obtained from the previous step. Finally, and in order to classify both labor and pregnancy contractions, we will test alternative neural network and machine learning methods on the features extracted from both connectivity alone and connectivity+graph methods. Moreover, we will demonstrate the

power of graph metrics, extracted from connectivity matrices, to enhance the classification results.

Chapter 4 presents the procedures used for the windowing (time analysis) as well as the best node selection approaches to study real EHG signals. To do so, we will divide signals into several windows, which will offer us the opportunity to analyze the ones that generate the best results. This analysis will be done by means of the consensus matrix approach. We will then indicate which window(s) and which nodes are the most efficient for each feature computation.

Chapter 5 shows the results of a simulation module constructed by our team for liking the EHG characteristics [12] to the diverse parameters of the model, involved in uterine synchronization. This will concern first the electrical diffusion (short distance synchronization) and then the mechanotransduction (long distance synchronization) phenomena. To accomplish this, we will conduct various tests to determine which feature(s) and connectivity method(s) would best represent the evolution of these two physiological phenomena: short-distance synchronization via electrical propagation and long-distance synchronization via mechanotransduction. Finally, we will therefore simulate two data sets: first using electrical diffusion (first group, ED), then employing electrical diffusion plus Mechanotransduction (second group, EDM).

Chapter 6 presents the synthesis of all the previous approaches developed in this work. We will compare the results obtained with the best methods selected from chapter 3 (real signals using connectivity, graph, and machine learning methods) to the ones obtained with the best windows and best nodes approaches, from chapter 4, and the to the results obtained when using the best methods selected from chapter 5 (simulated EHG analysis). Finally, the best machine learning method will be applied to the best methods of each part.

A general conclusion and perspectives will finally be presented.

AUTHOR'S PUBLICATION

Journal Paper

K. B. Dine, N. Noujoud, M. Khalil, and C. Marque, "Uterine Synchronization Analysis During Pregnancy and Labor Using Graph Theory, Classification Based on Neural Network and Deep Learning," *IRBM*, Sep. 2021, doi: 10.1016/j.irbm.2021.09.002.

International Conference papers

K. Dine, C. Marque, N. Noujoud, W. El Falou, and M. Khalil, "Pregnancy Labor classification using neural network based analysis," Oct. 2019, pp. 1–4. doi: 10.1109/ICABME47164.2019.8940167.

Chapter 1: Background, Problem, and Preterm Labor Detection

This chapter starts with a general introduction of preterm labor, the main cause of childhood mortality and morbidity. Then, we briefly examine the anatomical and physiological background of the uterus, as well as uterine contractility and its two primary factors: cell excitability and uterine synchronization (short distance by electrical activity propagation, long distance by mechanotransduction process). Afterward, we present the various pregnancy monitoring techniques that has been used to record the uterine activity. Then we focus on the connectivity/correlation analysis used in the preterm labor detection. Finally, we provide an evaluation of the reported studies by focusing on the diagnostic of uterine activity and preterm labor risk detection. This chapter will be terminated by presenting the different goals of this work.

1.1. Introduction

Preterm labor (PTL) is characterized by the birth of infants prior to the completion of 37 weeks of gestation. PTL affects more than 15 million newborns yearly. It is one of the fundamental reasons for under-five years old child mortality. It is held accountable for one million deaths annually. In the United States, preterm newborns reached 11% of all births. The yearly cost of this births outstretched $26 billion [13]. Disability-adjusted life years (DALYs: sum of the years of life lost due to premature mortality and the years lived with a disability) result from preterm birth; they are due to lifelong neurological and developmental sequelae. In the 20th century, the rate of preterm birth increased drastically from less than 7% in the 1960s, to reach a peak of 12.8% in 2006. However, the decrease in indicated late preterm deliveries contributed to lowering the rate to 11.4% in 2013 [14].

Figure 1.1. Estimated numbers of preterm births in 2014 [15]

Out of the 139.95 million live births in 2014 (Figure 1.1), 10.6% of them were preterm, which is estimated to be 14.84 million cases. In North Africa, the preterm birth rate reached 13.4% in 2014, whereas Europe recorded only 8.7% [15].

One biophysical marker recently identified as auspicious of preterm labor is the electrical activity of the uterus. The electrohysterogram (EHG) is the electrical signal related to a uterine contraction, recorded on the mother's abdominal wall. As the electrical activity triggers the mechanical contraction of the myometrium, EHG is thus highly related to the uterine contraction efficiency. The aim of this thesis is to classify between pregnancy and labor contractions by evaluating the EHG signals recorded during these two situations.

1.2. Anatomy and physiology of the uterus

The uterus, or womb, is the heart of the female reproductive system. The uterus is positioned in the abdominal pelvic cavity exactly in the midline. In non-pregnant women, it is a pear-shaped muscular organ located between the rectum and the bladder. During pregnancy, it plays the role of housing and nourishing a fertilized egg until the fetus or offspring is ready for delivery [16].

The uterus is a thick-walled muscular structure; it consists of three layers, the perimetrium (outer layer), myometrium (smooth muscle layer), and the endometrium (inner layer). The thickness of the endometrium and its structure vary based on the hormonal stimulation [17].

The uterus is known as a fibro-muscular organ. It is viewed as a thin-closed membrane where the fetus evolves during pregnancy. It is shaped like a pear, with nearly 4.5 cm broad (side-to-side), 3.0 cm thick, and 7.6 cm long when non-pregnant. The dimensions of the uterus will expand during pregnancy from 8 to 35 cm. The anatomical division of the uterus is two parts (Figure 1.2): the cervix and the body or corpus. The cervix extends into the vagina. At the opposite side, the uterus body is connected to the Fallopian tubes.

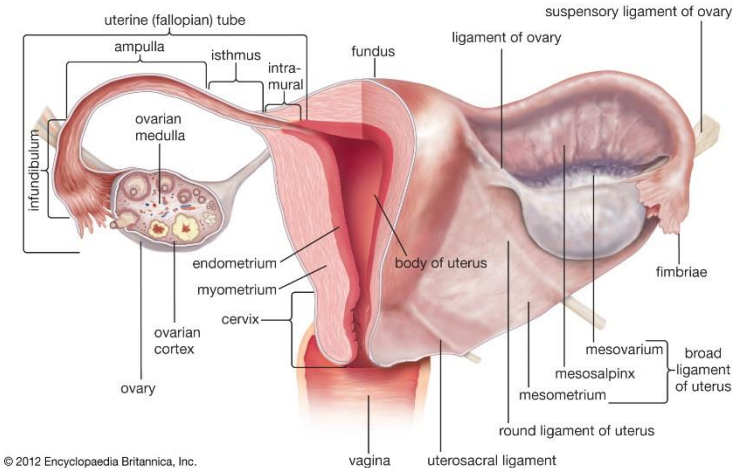

Figure 1.2. Anatomy of the non pregnant human uterus [16].

Prior to pregnancy and throughout the first trimester, the two parts are detached by the uterine “isthmus”, which is represented by a virtual border. When the pregnancy reaches 37 weeks, the lower segment becomes visible [18]. This segment is detected between the cervix and the uterine body. In the final term, this new part of the uterus will reach 10 cm high. Consequently, the uterus will convert from a two-part organ to a three-part organ at the end of the pregnancy. The three parts being the uterine body, the cervix, and the lower segment (Figure 1.3).

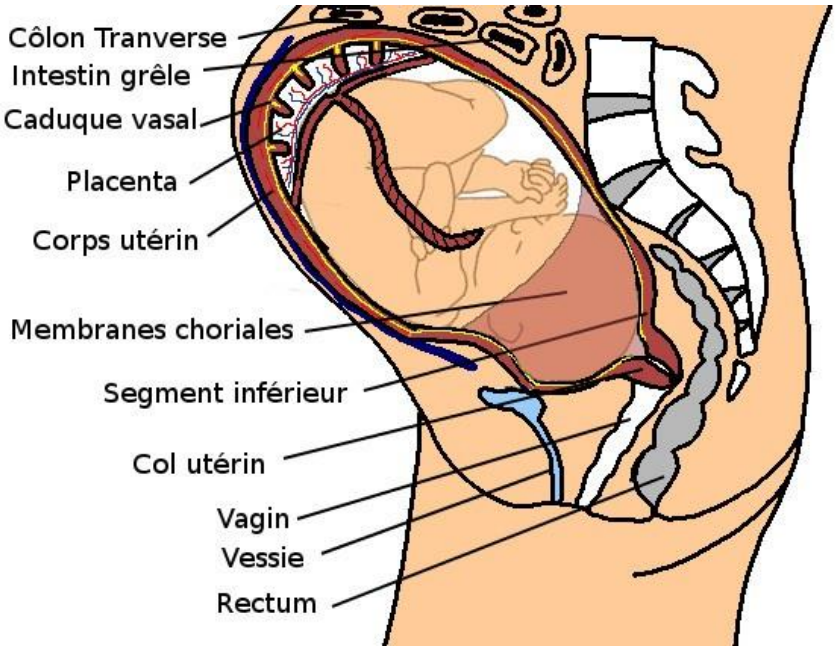

Figure 1.3. Anatomy of the pregnant human uterus with its 3 parts : uterine body (corps utérin), cervix (col utérin) and lower segment (segment inférieur) [7].

1.3. Uterine mechanical activity

With the purpose of solving clinical problems associated with gestation and labor, it is essential to comprehend the physiology of the uterus throughout term and preterm parturition. As mentioned before, the uterus is a smooth muscle organ that goes through particular changes during gestation. It is also recognized for its singular contractility during labor [19].

The pregnant human uterus is divided according to its function into two parts: the uterine corpus, which is its upper part, and the cervix, which is its lower part. The uterine corpus is mostly made up of smooth muscle; it is also divided into upper and lower part. The Fundus (upper part) contracts and thickens during labor, while the isthmus (lower segment) dilates around the fetus and thins. The main role of the isthmus is the junction between the cervix and the fundus [20].

The gravid uterus implicates during most of the pregnancy a phase of relative quiescence accompanied by a period of activity that leads to birth. The Intra Uterine Pressure (IUP) in the activity phase, allows to evidence two types of pregnancy contractions [21]:

- Contractions of low IUP amplitude are also called Low Amplitude High Frequency (LAHF) contractions and are of local influence. They take place within the first trimester of pregnancy with a frequency of about 1/min.
- Contractions of higher IUP amplitude take place at mid-pregnancy with a low frequency of appearance of 1/day at the beginning to reach 1/hour later on. These contractions are named Braxton Hicks contractions. Their influence spreads to a larger portion of the uterus. The Braxton Hicks contractions, during the final weeks of pregnancy, become more frequent and intense.

Following that, the cervix begins to soften and dilate as the pregnancy progresses to its final term, and contractions escalate in amplitude and frequency.

When labor starts, the propagation of electrical activity rises dramatically. The contractions associated with the end of pregnancy fades, and labor contractions take place. These strong and regular contractions spread throughout the uterus in a short time (around 20s to contract the whole uterus), causing the cervix to open and the fetus to be born [5].

1.4. Uterine electrical activity

The electrical activity is the trigger of the mechanical contraction of the muscle fiber. The mechanical effect results from the excitation characteristics of the muscle cells and uterine synchronization (related to the electrical activity spreading). The uterine muscle is made of smooth muscle cells that display negative resting potentials along small and slow spontaneous fluctuations. When the resting potential fluctuations hit a threshold, the induction of an isolated or a burst of action potential occurs [6].

The uterine contractions evolve during pregnancy and throughout labor. During most of pregnancy, the contractions are inefficient and weak; however, during labor, they become efficient and strong. This evolution is associated with the increase in cellular excitability and that of the synchronization of the uterus [22]. Hence, giving birth takes place after the uterine contractions become efficient and regular, that compels the cervix to dilate and pushes the baby out.

To do that, two physiological phenomena can be noticed before labor: an increase in the cell excitability and an increase in the number of simultaneously active myometrial cells. This synchronization results from 2 phenomena: 1) an increase in the propagation of the action potential (electrical diffusion thanks to gap junctions, permitting a local synchronization), 2) the appearance of a mechanotransduction process that permits the long distance synchronization [23].

1.4.1. Cell Excitability

Two types of potential portray the electrical activity of uterine cells. The resting potential, which is the difference between the negative inside and the positive outside of a resting cell. It is unstable and registers slow waves of low amplitude that characterize the electrical baseline. Furthermore, when a given threshold is reached by these slow waves, an action potential (AP) could be generated inducing cell depolarization. When the cell depolarizes, the potential differences throughout the cell membrane reverse. The action potentials are frequently grouped by bursts for uterine cells. Though, during pregnancy, irregular bursts of action potentials mainly compose the physiological electrical activity. Regular bursts of the uterine electrical activity are generated during the end of term and labor contractions. These bursts are made up of regular trains of action potentials [24] spontaneously generated.

1.4.2. Uterine Synchronization

The uterine electrical or magnetic activity might be used to analyze or measure the synchronization of the uterine muscle during uterine contractions. Moreover, it can be used to differentiate between true and false labor [25]. The chemical stimulation at the cellular level results in the depolarization of the uterine muscle cells. As a result, action potentials take place in burst, associated with a magnetic or electrical activity that could be measured. The action potential frequency within a burst, along with the burst duration (both parameters related to cell excitability), as well as the total number of synchronously active cells (related to the uterine synchronization), are related to the frequency, amplitude, and duration of the uterine contractions [26].

Numerous researches were lately committed to investigate the propagation phenomena of the uterine electrical activity throughout pregnancy and labor [27]. Several studies concentrated on pinpointing the pacemaker area of uterine muscle during pregnancy and labor. Uterine pacemakers, on the other hand, have been reported to arise at random throughout the tissue and to shift location during a single or multiple consecutive contractions, also during labor[28] [29].

Furthermore, gap junctions are the way to connect myometrial cells electrically [30]. These junctions are regions where the membranes of two nearby cells come together to form pores that allow electrical connection. So, by making a low-resistance electrical contact between the cells, they create a route for action potentials to flow [31] [30]. Many studies indicated that during most of the pregnancy phases, the cell-to-cell gap junctions are absent or present in very low density [30]. Nevertheless, during labor, a considerable number of gap junctions between myometrial cells are observed[30] [32] ensuring the establishment of synchronized muscle activity (Figure 1.4) as a result of electrical diffusion.

Alejandro et al. [33] lately claimed that enhancing multicellular connection through improved junction function does not necessarily result in bioelectrical normalization of abnormally depolarized multicellular patches.

On the other hand, Jinshan et al. [34], observed that diverse dynamical regimes can be detected throughout a range of gap junction conductance.

During delivery, the smooth muscle cells of the whole uterus are all activated within a short time (about 20 seconds). The cell synchrony is reached by means of two distinct phenomena:

- electrical diffusion: the direct electrical connection permitted thanks to the presence of gap junctions (channels passing through two adacent cell membranes). Thus, the gap junction density controls the rapid electrical synchronisation of close cells (short distance synchronization).

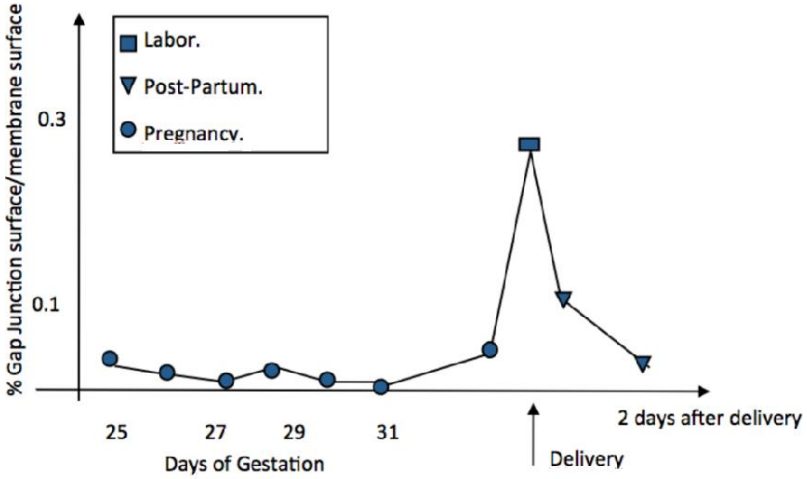

Figure 1.4. He evolution of Gap junction during gestation, delivery, and after delivery [35].

The density of the cell-to-cell contact surfaces starts to increase as pregnancy advances. This increase is considered to be one of the multiple factors that cause labor to instigate [30]. Whereas, in the non-pregnant uterus of rats and humans, the density of the gap junctions becomes absent or slightly present. The density of gap junction abruptly increases just before parturition (figure 1.4) [36]. Consequently, when the time of delivery occurs, the density of the gap junctions reaches approximately 1000/cells in human tissue [36].

- Mechanotransduction process: Even if it is clear that the initiation of action potentials as well as their ability to propagate are crucial during labor, electrical propagation by itself does not permit to explain the fast synchronized contraction of the whole uterus observed during labor [23]. Some observations tend to show that the electrical generation and propagation of the electrical activity is rather a local mechanism, which fails by itself to

induce the whole uterine synchronization [13][14]. Furthermore, Young [23] did not succeed in observing a clear pacemaker area of the uterus. He thus concluded that the electrical generation could be induced by other mechanisms (chemical or mechanical). Therefore, in addition to the action potential generation and propagation across the tissue, he suggested the existence of a mechanotransduction process, as the origin of global uterine muscle synchronization [23]. In this process, a contraction starting from one part of the uterus, induces the contraction of another part, that could be far from the origin of the contraction, by means of the tissue stretching related to the increase in intrauterine pressure (IUP) induced by the contractile part. This theory relies on the presence of electrical stretch-activated channels (SACs) in the membrane of uterine muscle cells [37]. These channels are mechanotransducers that convert tissue stretching (induced by the increase in IUP) into an ionic current, creating thus the depolarization (and then the activity) of previously inactive stretched tissues. This process permits the long distance synchronization of the uterus, faster than with the electrical diffusion alone.

1.5. Pregnancy monitoring and preterm labor detection

1.5.1 Pregnancy monitoring methods

The detection and evaluation of uterine contraction during pregnancy is crucial to prevent the dilation of the cervix, thus avoiding premature birth. Hence, various studies have focused on pregnancy monitoring methods to identify major risks and predict preterm labor.

The most effective method to monitor uterine contractions is the use of Intrauterine Pressure (IUP), since it offers the best information about the uterine contractile condition [38]. However, as it requires the insertion of a catheter into the uterine cavity [39] it is invasive, which makes it impracticable for the monitoring of pregnancy.

Consequently, the external Tocodynamometer is the most commonly used device in monitoring uterine contractions during pregnancy. It is applied in more than 90% of hospital births since it is noninvasive and can be applied to most pregnancies without harming the mother of the fetus. It consists in an external pressure transducer positioned on the mother's abdomen over the uterine fundus [39]. However, this method presents different cons, along with being uncomfortable and inaccurate. Many variables may affect its accuracy, one of the most important being the examiner's subjectivity. This method only permits a reliable counting of the contraction number over a given time interval (generally 10 mm).

Moreover, Light-induced auto fluorescence (LIF) is a noninvasive technique that was suggested for labor monitoring [40]. It measures the changes of cervical tissue through gestation and labor. Although various studies proved its ability to estimate cervical status, along with the useful information it provides, it is not adapted in clinical practice so far for the prediction of preterm labor.

Another noninvasive technique is the Magnetomyography (MMG), which measures the magnetic field related to the action potentials related to the uterine activity. However, as the device is very expensive and requires very special equipment, this method is only used as a research tool [41].

As a new solution, the electrohysterography (uterine electromyography, EHG) is proposed since it is affordable and requires simple equipment to noninvasively record the uterine activity. It provides information on the myometrium from the analysis of electrical activity collected on the mother's abdomen. EHG is made of electrical activity created by active uterine muscle cells, as well as by the noise associated with corrupting electrical and mechanical activities. Thus, the EHG analysis has been proven to be among the most promising methods for monitoring uterine contraction efficiency during pregnancy [21].

1.5.2 Labor detection

To lessen the complications related to premature birth, an early detection approach is crucial. In order to detect labor progress, one should look for uterine contractions firstly, since it is the most important sign in such process. When the uterine contractions activity is monitored, the health of the fetus can be easily assessed and evaluated during pregnancy. Additionally, when the pregnant woman gets into labor, the uterine contractions become stronger, more complex, and gradually become more frequent. Subsequently, uterine contractions are proved to be a decisive indicator for labor detection [42].

Concerning premature birth, and in order to guarantee the survival of both the fetus, monitoring the uterine contractions become necessary since it would permit to differentiate between premature labor and normal pregnancy contractions [43]. On top of that, monitoring uterine contractions can also play a major role in detecting the fetal risk of health distress alongside complications that can occur in pregnancy, like tachysystole, uterine rupture, and the abruption of the placenta that can cause premature birth.

In order to detect an early premature labor, using the external tocographic signal during pregnancy, and counting only the number of uterine contractions has been demonstrated to be not predictive of delivery. To efficiently detect preterm labor risk, one has to search for signs of robust and frequent contractions, different from the ones normally recorded during pregnancy. At last, and of major importance, a noninvasive method has to be used to monitor the uterine contractions signals of a pregnant woman. That is why most of the work done nowadays to detect preterm labor is based on the processing the EHG recorded from the abdomen of the pregnant woman [42]. More precise diagnosis and true labor prediction are expected from the use of EHG in clinical practice. This will help in the process of avoiding any needless hospitalizations and lowering the cost of healthcare [44]. This is extremely important for patients that are threatened with preterm birth, as it has become one of the primary

causes of neonatal morbidity in advanced nations, and it frequently necessitates costly procedures.

1.5.3. Uterine Electrohysterography

Since its inception in the 1960s, Electrohysterography (EHG), also known as uterine electromyography, has become a non-invasive monitoring technique for measuring uterine dynamics and predicting the initiation of labor [26] [27].

Indeed, the uterine muscle electrical activity is captured by the EHG. The EHG signals are recorded noninvasively by using electrodes, which are placed on the surface of the pregnant women's abdomen. Thousands of myometrial smooth muscle cells depolarize and repolarize, resulting in uterine electrical activity triggering the mechanical contraction [22]. Uterine contractility is a direct result of all the myometrial cells exhibiting electrical activity. As the mechanical contraction trigger, EHG is a better candidate for uterine contractions detection than external tocography. Additionally, EHG has been widely studied for its ability to detect uterine contractions and predict premature birth. Many studies have suggested different signal processing techniques to extract linear, nonlinear, and propagation characteristics of EHG to differentiate uterine contractions from term and preterm delivery [37][38]. Nevertheless, there have been no consistent results [47]. The use of multiple EHG recording protocols as well as the different populations (normal pregnancies, risk pregnancies, laboring women) used in these previous studies may be one of the causes for this inconsistency, in addition to varied features extracted from the EHG signals and different diagnostic tools used. The majority of EHG signals were captured using general physiological signal acquisition devices, which were not suited for pregnant women. EHG, TOCO, and/or maternal perception (which reflect electrical activity, mechanical effect, and mother's feelings), were not recorded by the same device at the same time, causing the time comparison between these signals to be biased.

Based on EHG signals processing, many studies used different concepts in order to classify contractions between labor and pregnancy, or for preterm labor detection. They used different features that could represent the two phenomena involved in uterine efficiency: either the cell excitability (when only one EHG lead is processed at a time, which is called the monovariate approach [48]), or uterine synchronization (when processing more than one EHG signal at a time, usually two, called the bivariate approach [10]). Some agreement has been obtained concerning the features able to represent the cell excitability (monovariate approach) [27]. Concerning, the uterine synchronization, the process is more complex. The features extracted from the EHG should be able to represent the two different physiological systems involved in uterine synchronization: the electrical diffusion (short distance synchronization), as well as the mechanotransduction process (long distance synchronization). For this purpose, the Correlation/Connectivity analysis is thus one important aspect to investigate.

1.6. Connectivity/Correlation analysis

The study of correlation between signals recorded on multiple channels is not a new approach. It has been widely used in EEG signals analysis [50]. As far as EHG signal is concerned, this procedure has been used in a number of researches involving human or animal EHG recordings by studying the connection at the electrode and at the uterine level (after source localization) in order to reveal critical details concerning uterine activity synchronization.

Hence, multiple studies have shown that analyzing the propagation of uterine electrical activity is an effective method for identifying and distinguishing pregnancy and labor contractions [51] [8]. When employing invasive recordings, this propagation phenomenon may be explored at a micro level on animal uteri, but it can also be studied at the skin level with abdominal electrodes. However, throughout pregnancy and labor, some of these studies were attentive to the propagation pattern or velocity of uterine activity in the uterus [7] [8]. Other authors examined statistical couplings and delays (also known as correlation/connectivity) between the different electrodes to investigate the propagation phenomenon [11].

1.6.1 Propagation of the electrical activity: directionality and velocity

The propagation of uterine electrical activity, related to the electrical conduction, has been explored in a variety of species and with different approaches, with the assumption of a linear propagation in most of the cases. These studies tried to evidence either the directionality or the velocity of the propagation.

- **Propagation directionality:**

Some researches on the propagation of uterine electrical activity in labor (in both animals and women) indicated a predominant downward propagation where the base of the burst originates in the upper/ovarian part of the uterus, in women and guinea-pigs [52] [53]. While in different studies applied to women, upward and multidirectional propagation patterns have been reported [54] [55]. However, women who delivered successfully vaginally, had a significant downward direction of uterine activity [56] [57].

Furthermore, many studies based the analyzes on single spikes manually identified and segmented from EHG bursts, rather than on the entire EHG burst. The propagation of single spikes has been shown to be more significant to the prediction of labor than the examination of the entire burst [31] [58] [59] [60].

Lammers et al. [60] studied the propagation in an isolated preterm rat myometrium along with an in a complete guinea-pig uterus at term using a two-dimensional high-density grid [52]. According to the authors of these investigations, the propagation of single spikes is

unpredictable and can propagate spontaneously in a circular manner. When recorded in the placental insertion area of a pregnant guinea pig uterus, sparse and fractionated spike propagation was observed [52]. Miller et al. [31] found increasing recruitment in the axial direction preterm but not at term in rat uterine strips. On the other hand, when Parkington et al.[29] used an array of six extracellular glass-pore surface electrodes on rat uterine strips, progressive recruitment was observed only in the axial direction preterm and not at term (3 mm apart). While other studies [31] [61] were conducted on the intact uterus of pregnant ewes using pairs of stainless-steel wires stitched into the myometrium. According to their findings, individual spikes do not propagate among electrodes when their inter-distance is greater than 3 cm over the longitudinal and circumferential layers of the myometrium [29].

Additional studies focused their analysis on the activity of the uterus on the placental area. Weaker potentials, slower propagations, and a shorter length constant were revealed in microelectrode recordings in the placental region, specifically in rat myometrium [61]. Extracellular recordings on a pregnant cat revealed that the placental area was less excitable and displayed little or no spontaneous activity [62].

- **Propagation velocity:**

A growing number of animal and human studies have evidenced that the propagation of single electrical spikes in the myometrium is linear. This assumption permits to estimate the propagation velocity [7] [63] [60] [52] [59]. The propagation velocity of electrical spikes in the uterus was measured for the first time [64] for the guinea-pig, the rabbit, and the cat. After some time, countless studies have fixated on the propagation velocity by using diverse recording methods on different species like guinea-pig [64], cat [64] [62], rat [61] [31], and ewe [29]. They reported propagation velocity values for guinea-pig ranging from 0.1 to 0.3 cm/s [64], and for the cat ranging from 6 cm/s in [64], 9-10 cm/s in vivo and 8-12 in vitro [62]. For the rat, Kanda and Kuriyama [61] obtained values of 6.6 ± 2.2 cm/s (at 7 days gestational age (GA)), 12.3 ± 3.2 cm/s (at 15 days GA), 33.4 ± 4.1 cm/s (at 22 days GA) in non-placental regions; and 1.3 ± 0.4 cm/s (at 15 days GA), 2 ± 0.9 cm/s (at 22 days GA) in placental regions. In [31] the values were 9.2 ± 0.6 cm/s (in the longitudinal layers), 2.3 ± 0.7 cm/s (in the circumferential directions) in pregnancy, while the values in labor were 10.5 ± 1.3 cm/s (in the longitudinal layers) and 4 ± 0.8 cm/s (in the circumferential directions).

Additionally, Parkington et al. [29] evidenced that the propagation velocity in the longitudinal direction rose dramatically from pregnancy (7.2 ± 0.3 cm/s) to labor (13.3 ± 0.7 cm/s) in the intact uterus of pregnant ewes [29].

Wikland and Lindblom [65] observed a velocity ranging from 1 to 2 cm/s using the biopsies technique of the myometrium.

On women, the MMG was also utilized to calculate the propagation velocity of uterine contractions [66]. The propagation was multidirectional, with speeds ranging from 1.9 to 3.9 cm/s, according to the results. Using the intrauterine pressure, Wolfs & van Leeuwen [67] predicted on women a somewhat increased propagation velocity during labor (2.5-5 cm/s).

Other authors assessed the propagation velocity (PV) by evaluating the propagation of complete bursts of EHG [7] [54], or single spikes found within bursts using a two-dimensional flexible grid with 64 electrodes [7] [9] [46]. These studies found a PV of 5.30 ± 1.47 cm/s during pregnancy and of 8.65 ±1.90 cm/s during labor.

Later on, the combination of PV and peak frequency (PF) has yielded the highest classification rate (96%) for distinguishing labor from non-labor contractions [7]. Hence, PV levels have been reported in a significantly larger population of pregnant women than in the aforementioned studies [7]. In the following studies, only two pairs of typical bipolar surface electrodes were employed.

Mikkelsen et al. [54] calculated the inter channel delay using three electrodes positioned on the median vertical axis of the abdomen and the center of mass of the EHG burst enveloped as a reference. When the upper and the lower uterine segments are analyzed separately, authors recorded average values equal to 2.15 cm/s (ranging between 0.66 and 13.8 cm/s) and 1.53 cm/s (ranging between 0.58 and 6.7 cm/s) for the upper and lower uterine segments respectively [54]. Lately, Lange et al. used 16-channel two-dimensional electrode grids for their EHG recordings. For 35 contractions, the calculated average propagation velocity was 2.18 (±0.68) cm/s [55].

- **Correlation/connectivity:**

So far, none of the above-mentioned studies have reached the clinical practice. More recent research has employed the correlation/connectivity between EHG signals as a new feature to investigate the propagation phenomena by investigating the statistical coupling between recorded signals.

The correlation between EHG envelopes observed at multiple places in the uterus of birthing macaques was initially studied by Duchene et al [68]. Mansour el al.[6] employed the inter-correlation function to investigate the transmission of internal uterine EMG using four internal electrodes on pregnant monkeys [6]. The signals were initially filtered into the frequency bands: Fast Wave Low (FWL) and Fast Wave High (FWH). Their results show that the correlation for FWL is higher throughout labor than for FWH.

Additionally, Marque et al. used the linear correlation coefficient (R2) on women and found that low frequencies have a stronger correlation than high frequencies [69]. Duchêne et al. [5] studied uterine EMG propagation by applying autocorrelation, cepstrum, and

deconvolution [70]. The obtained results suggest that none of the developed methods can demonstrate linear propagation of the whole EHG bursts.

The linear inter-correlation was employed for EHG propagation analysis by Karlsson et al [21]. To do so, they used 16 electrodes for the recording of EHGs. They also exhibited an animation of the electric potential development as well as a temporal correlation presentation, where they found complicated activation patterns.

More recently, Diab et al [71] found that while nearing labor, the correlation of uterine electrical activity extends throughout the matrix and in all directions, but remains more concentrated down, towards the cervix [72].

The nonlinear correlation coefficient H2 was used by Hassan et al.[10] in order to evaluate the non-linear correlation between 16 EHG signals captured by a matrix of 4x4 electrodes placed on the mother's abdomen [73]. Authors discovered a relevant variation between pregnancy and labor contractions in addition to an increase in the correlation of EHGs when labor advances [74].

A comparative study of numerous correlation measures applied to EHG signals was recently conducted [75]. The nonlinear correlation coefficient (H2), General synchronization (H), and the Granger causality (GC) were the methods compared in this study. They tested these methods according to their sensitivity to several characteristics of the signal (nonstationary, frequency content) or to the recording protocol (bipolar or monopolar), in order to improve the classification of EHG bursts recorded during pregnancy and labor when using coupling detection methods. A grid of 16 electrodes (4x4) was used to record EHG signals from 48 women during pregnancy (174 contractions) and labor (115 contractions). As a result, there was no evidence of a monotonic increase in the H2 coefficient from pregnancy through labor.

Nader et al. [11] recently proposed to use the Imaginary part of coherence method (ICOH) as a potential approach for measuring functional connectivity of EHG signals [76]. Usually, the linear relationship between two EHG-channels at a specific frequency is measured by estimating the coherence between them [77]. The main problem of Coherence method is that it is highly influenced by the volume conduction. However, new methods for solving this issue have been recently proposed. The Imaginary Part Of Coherency (ICOH), suggested by Nolte in 2004, is one of these new methods [76]. The Icoh method is known to be not influenced by volume conduction problems.

Additionally, Nader et al [11] proposed a completely new approach based on the graph theory analysis combined with the connectivity methods to investigate the characterization of the correlation among uterine electrical activities. Indeed, in all the previously cited method, the mean of the feature (connectivity method) was computed over the multiple electrodes,

loosing thus some topographic information that could be of interest. By considering the resultant correlation matrix as a graph, consisting of nodes sets (electrodes) connected by edges (connectivity/correlation values between electrodes), they extracted useful characteristics to represent the evolution of the graph dynamic.

In their studies, they used different graph theory-based metrics, which were extracted from the connectivity matrices to analyze the uterine activity connectivity. They used this new approach to investigate the power of graph parameters to first characterize the uterine connectivity evolution from pregnancy to labor, and second, discriminate the contractions between pregnancy and labor. The best graph metric was evidenced as being the graph Strength that gave an 80% classification rate between labor and pregnancy contractions.

This approach is promising as the graph analysis is able to better characterize the connectivity obtained from multiple electrode pairs. In the previous studies, when different connectivity values were obtained from different electrode pairs, for one given contraction, the authors usually used the mean of these values to characterize the contraction. With the graph analysis, the dynamic of the graph could be studied by extracting the different topographic evolution of the connectivity values. We expect that this analysis will be able to better represent the synchronization due to the mechanotransduction, which is more complex than the one related to the electrical diffusion.

1.7. Windowing approach

The sliding window approach has been widely applied to process different bio signals as a simple and easy-to-use technique to catch the non-stationary characteristics of the signals.

Concerning the EHG and the connectivity approach, and in order to enhance the method performance, Diab et al. presented a filtered time-varying strategy [78]. They retained solely the EHG low-frequency band (FWL, which is thought to be more connected to EHG propagation, and less sensitive to the abdominal tissues filtering effect) by filtering the signal in this lower band, and then used a windowing approach in order to catch the possible time varying evolution of the non-linear correlation. The obtained Filtered Windowed-h2 (FW_h2) showed promising performance as it results in an increase from pregnancy to labor. Despite these promising results, FW_h2 takes more execution time than the classical correlation analysis.

Whilst effective, this approach carries some critical limitations related to the selection of window specifications (length, overlap). Though a too short window may decrease the specificity through noisy fluctuations, a too large window may decrease the sensitivity in detecting fast temporal changes of interest.

1.8. Uterine contraction model

To test different processing tools, it is often proposed to use a model of the process under investigation, in order to evaluate the performance of the different tools when varying the parameters controlling the process. Different studies have worked on simulating a phenomenon that creates uterine contractions. In our work, we chose to simulate EHG signals by means of an electromechanical model developed in our team.

This model is based on an electrical approach developed by Rihana et al [79] by using a classical Hodgkin-Huxley-type approach adapted to the specificity of uterine cell, then further simplified by Laforêt et al [12] to reduce its computing time. This model simulates the generation and the propagation of uterine electrical activity taking into consideration the flow of ions specific to uterine myocytes. More recently, Yochum et al [77] improved the model by introducing chemical and mechanical phenomena, in order to simulate the force generated by the cells, the intra uterine pressure and the stretching of the uterine tissue. This mechanical behavior permitted them to model the mechanotransduction process that allows the coordination of uterine contractions, by estimating tissue stretching and considering stretch-sensitive channels (SSC). As a result, this model considers the electrical, chemical, and mechanical phenomena that simulate the synchronized contraction of the whole uterus while keeping in mind the electrical activity propagation limit distance. They used MRI images to obtain a realistic mesh of a uterus divided into electrically isolated sections. This model may be used to simulate the EHG signal measured on the mother's abdomen by linking it to a volume conduction, which was adapted by Rabotti et al [63].

Yochum et al [77] established this first multi-physical and multi-scale model, with a simplified mechanical approach, by combining many sub-models previously developed by his team, and others. For example, they used the Burszyn et al [78] model to simulate the force generated by the active cells, based on the excitation/contraction model of a uterine cell, developed by Hai and Murphy [79]. Recently, Verwaerde et al [80] improved the mechanical part of this model by creating a more realistic mechanical behavior of the uterine muscle, based on a finite element (FE) analysis. This model considers a realistic 3D geometry of the uterus and of the mother's abdomen and also includes behavioral rules for the uterine tissue and the intra amniotic fluid. It thus permits a better simulation of the intra uterine pressure and of the tissue stretching. But, as this model is currently under development and is consuming much more time than the Yochum's one [77], for testing our tools, we will use in this work the simplified Yochum's model to generate simulated EHGs with different situations of electrical diffusion and mechanotransduction process [49].

1.9. Proposed Approach

Premature birth is still known as a major issue in obstetrics and it is still attracting many researchers to conduct more studies. Based on the above overview, it is known that the uterus is a complicated organ and it is necessary to understand its function. For that, it is

crucial to detect the beginning of labor and predicting preterm labor. The most promising method for recording uterine contractility is based on the abdominal EHG, as many studies have suggested that using this signal to detect labor might be quite effective.

From all the approached used to process the EHG, the connectivity analysis between EHG signals, used for the classification of labor and pregnancy contractions, yielded encouraging results.

Nevertheless, the authors assessed the correlation between numerous EHG signals using different connectivity methods, in particular, all previous studies about the synchronization of uterine electrical activity listed above [72]. Recently, A new technique based on graph theory analysis has been proposed [11]. The correlation matrices were defined using various connectivity approaches applied to the EHGs. Then, each correlation matrix was modeled as a graph with a group of nodes (electrodes) connected by edges (values of connectivity between electrodes). The graph parameters extracted from these connectivity matrices, were used as input features of a classifier.

In this thesis, we propose that the results of the connectivity matrix and graph methods, as well as the classification tool (machine learning and neural network methods), should be analyzed, in order to improve the classification of pregnancy and labor contractions, based on the connectivity of EHG signals.

The work presented in this document will thus be parted in 3 main sections:

- Improve the classification tools and the graph analysis: based on the previously defined approach, we first proposed other graph parameters (as features) and then we tested the classification tools (based on different approach) that permit the best classification between pregnancy and labor contractions using real EHG signals.
- Use time varying analysis of the EHG connectivity: The previous proposed approaches considered the whole burst duration for the connectivity analysis of one given contraction. As this connectivity may evolve along the burst duration, especially in the presence of mechanotransduction, we tested whether a windowed approach improves or not the classification results obtained from real EHG signals.
- Test the connectivity features on simulated signals: in order to select the features that are most sensitive to electrical diffusion and to mechanotransduction process, we simulated signals using different values of the model parameters involved in both synchronization aspects of the uterine activity. This analysis permitted us to identify the features that could be of interest to characterize the uterine synchronization, and therefore the contraction efficiency.

The last part of this document presents a synthesis of these 3 different analyses, the results of which are applied to real EHG signals, and this part proposes directions to further improve the detection of preterm labor.

CHAPTER 2: Materials and Methods

In this chapter, we will present the methods and materials used in this thesis to study uterine connectivity and to classify labor and pregnancy contractions based on machine learning methods. First, we will see the different connectivity/correlation methods used in this study. Then we will explain the graph metrics that we applied, including the proposition of new graph parameters. Next, we will explain the machine learning algorithms applied for the classification of contractions between labor and pregnancy ones. Afterwards, we will describe both kinds of data used in this work: the real and the simulated EHGs. We will shortly present the simulated data that were generated by means of a computational EHG model developed in our team. We will also describe the experimental protocol used to record real EHG signals, the data acquisition, and the different preprocessing steps. Finally, we will illustrate the workflow process concerning real and simulated EHG signals.

2.1. Introduction

Various studies have been conducted on the propagation of uterine electrical activity based on various methods and distinct species. We will describe the main methods that we used in this work in order to classify between pregnancy and labor contractions.

Numerous measures have been retrieved using electrohysterogram (EHG) and graph approaches in various studies [11], dramatically expanding the available features. Therefore, analyzing this massive number of parameters became occasionally difficult. Hence, feature selection was used to reduce the number of parameters and select the ones that were mostly related to the target.

2.2. Correlation Analysis

The term "connectivity" refers to the correlation that represents the statistical connections between two-time series. This connectivity could be structural (for example as for some brain networks [83]), functional, or effective. As there is no evidence of any anatomical network on the uterine muscle, we will not focus on structural connectivity. Functional connectivity (statistical interaction) is specified as a temporal correlation between several signals recorded from separate channels with no additional information regarding the direction of the correlation. Whereas effective connectivity (causal relationship) [84], which considers the direction of information flow between two signals [85], specifies the influence of one signal on the other one. We have used in this study four functional and effective connectivity measures, previously used for EHG analysis, including the classical linear (R2) and nonlinear (H2) correlation coefficients [73], the modified version of H2 (FW_h2), and the imaginary part of the coherence (ICOH) that have been evidenced as promising in previous studies [11].

2.2.1. The Cross-correlation Coefficient (R2)

In the time domain, the cross-correlation method measures the linear correlation between two variables X and Y [86]. The following equation can be used to estimate this coefficient for the two-time series X(t) and Y(t):

$$\mathrm{R2} = max_t \frac{cov^2(X(t),Y(t+\tau))}{var(X(t))var(Y(t+\tau))} \qquad (1)$$

where *cov* and *var* are the covariance and variance between the two-time series X(t) and Y(t), respectively. The time shift is represented by τ. The R2 value ranges from 0 (independence of X and Y) to 1 (X and Y are fully correlated).

2.2.2. The Nonlinear Correlation (H2)

The nonlinear correlation coefficient (H2) measures the nonlinear relationship between two variables. It is derived from the two signals X(t) and Y(t) of length N, by evaluating the value of X as a function of the value of Y [73]. Given X, a nonlinear regression curve can be used to estimate the value of Y. By subtracting the explained variance from the original, the unexplained variance is calculated.H2, which is the nonlinear correlation value, indicates the reduction in the variance of Y that may be gained by forecasting the Y values from those of X, as $\mathrm{H2}$ = (total variance - unexplained variance)/total variance, according to the regression curve.

$$H2_{X/Y} = \frac{\sum_{k-1}^{N} Y(k)^2 - \sum_{k-1}^{N}(Y(K) - f(X_i))^2}{\sum_{k-1}^{N} Y(k)^2} \qquad (2)$$

where the nonlinear regression curve (linear piecewise approximation) is denoted by $f(X_i)$. The estimator $\mathrm{H2}_{Y/X}$ ranges from 0 to 1. When H2 = 0, Y is completely independent of X, while when H2 = 1, Y is fully determined by X. The nonlinear correlation coefficient is asymmetrical, thus $H2_{Y/X} \neq H2_{X/Y}$, providing details on the direction of the information [86]. This asymmetry feature will not be examined in our study, since we are only concerned with the presence or absence of a nonlinear relationship between two signals. We will not study the directionality of connectivity.

2.2.3. Filtered Windowed H2 (FW_h2)

$\mathrm{FW\_h2}$ Is a modified version of the nonlinear correlation coefficient $\mathrm{H2}$ [72] . This method consists of filtering the EHG signal in a low-frequency band and then windowing it. It is mostly based on the hypothesis that EHG propagation is more closely associated with its low frequency bands (FWL: 0.1-0.3 HZ) [68]. Diab et al [72] evidenced that when these two preprocessing stages were combined, the resulting Filtered-Windowed- $\mathrm{H2}$ (FW_h2)

produced the best results in the classification of contractions between labor and pregnancy, with an obvious increase in FW_h2 from pregnancy to labor.

2.2.4. Imaginary Part of Coherence (ICOH)

Coherence is a measure that has been extensively used to evidence, in the frequency domain, the relationships between time series, in case when the volume conduction effects directly the true coherence value. Volume conduction results when the electrical activity is recorded and processed at a distance from its source, which is the case while recording abdominal EHGs. Due to this reason, new strategies have been presented to tackle this issue by focusing only on the imaginary part of the coherence [76]. The underlying hypothesis is that the interaction displaying zero-lag of the real parts of the coherence between signals, indicates a fake interaction, whereas the imaginary part of the coherence function may reflect realistic interactions, reflecting the true correlation between signals [76].

The linear correlation among two signals X and Y, as a function of frequency, is provided by the coherence (C) function. It is defined as their separate auto-spectral density functions C_{XX} and C_{YY} normalized by their cross spectral density function C_{XY}. The imaginary part of coherence (ICOH) is thus defined as follows:

$$ICOH = \frac{|\mathrm{Im}C_{XY}(f)|}{\sqrt{|C_{XX}(f)||C_{YY}(f)|}} \quad (3)$$

where the linear correlation between two signals X and X or Y as a function of frequency is represented by the C functions.

2.3. Graph Theory

In most of the previous studies, the connectivity matrices generated between EHGs, whatever the connectivity measure used, were converted into a single value for each contraction by averaging the connectivity values over the matrix [73]. This averaging permitted a simple computation bust lose the topographic information contained in the connectivity matrix. To overcome this problem and describe more precisely the whole connectivity matrix, a graph theory approach was proposed by Nader et al. [11] to evaluate the connectivity estimated using these various methods throughout the full connectivity matrix. They examine the ability of graph parameters to extract useful information concerning the evolution of uterine connectivity from pregnancy to labor and to classify their contractions. We have used in our work different metrics derived from the graph theory methods used in [11], such as Strength (Str), Clustering Coefficient (CC), and Efficiency (Eff). Furthermore, in this work, we proposed to test two new graph parameters, PageRank (PR) and Betweenness Centrality (BC), and compare their results with the previous methods in order to improve the classification results.

2.3.1. Overview

Historically, the study of networks has been primarily the core of graph theory, a branch of discrete mathematics. Since its founding in 1736, when a Swiss mathematician, Leonhard Euler, authored the solution to the Königsberg bridge (Figure 2.1) problem [87] (which entails finding a round trip that passes only once through each of the bridges in the Prussian city of Königsberg), the Graph Theory has embraced many interesting developments. It provided answers to a variety of practical questions, including: what is the highest flow per unit time from a source to a sink in a network of pipes? How to color sections of a map with the fewest colors possible so that adjoining regions receive different colors? Or how to fill n jobs with the highest reported utility by n people?

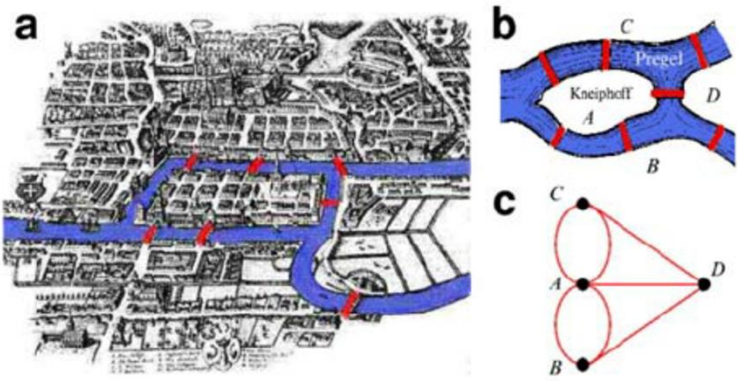

Figure 2.1. The Königsberg bridge puzzle[87].

Network analysis has a variety of applications in biology and medicine, including drug target revelation, identifying protein or gene function, developing effective treatment methods for diverse diseases, and enabling early detection of disorders [88]. The emphasized network categories in systems biology include protein-protein interaction networks [89], biochemical networks, transcriptional regulation networks, signal transduction, or metabolic networks [90], which typically share features and properties. In the domain of neuroscience, graph theory has lately been implemented for brain connectivity analysis and is currently regarded as a potential research frontier topic [91].

2.3.2. Definition

A set of nodes and edges defines a graph. The edges are the lines that link two/multiple nodes in a graph, and the vertices/vertex are the nodes. G can be used to mathematically represent a graph. In social networks (SN), for example, a user's graph is G(U, V), where U is the list of individuals and V is the set of edges indicating the link between the users or items [92].

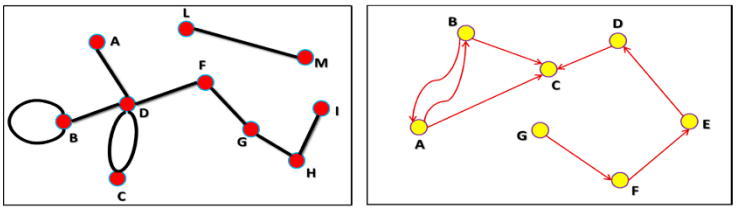

(a) Example of an undirected graph. (b) Example of the directed graph.

Figure 2.2. Pictorial overview of the directed and undirected graphs[92].

Two types of graphs exist: directed and undirected, as shown figure 2.2.

The edges of undirected graphs have no direction (figure 2.2a). For example, there is a relationship between L and M in figure 2.2a, which is the same as saying that there is a link between M and L. Because there is no difference in the interpretation/understanding, we can refer to the line between M and L as (L→M) or (L←M). People and friendship in a social network, or scientists and co-authored articles in a collaboration network, are possible examples of the undirected graph.

The edges of directed graphs, on the other hand, have a specified direction (i.e., the ingoing and the outgoing can be viewed). In certain circumstances, the graphs are drawn with arrowheads on the edges. Digraphs are the most popular name for directed graphs [91]. Figure 2.2b shows an example of a directed graph. Web page and hyperlink connections, Twitter follower graphs, interactions between users as well as the impact of one user on another in social networks are all possible applications of the directed graph.

In our case, the connectivity matrix can be presented as a graph, where the nodes are the electrodes and the weights of edges are the connectivity value between the corresponding electrodes (nodes). As we are interested in this study only on functional connectivity, an undirected graph could be used. A directed graph would be needed to represent effective connectivity.

2.3.3. Graph Parameters

Different metrics can be used to characterize the graph connectivity. The parameters that have been tested in the previous study on EHG connectivity [1] are the following:

2.3.3.1. Strength

The strength (Str) of a node shows its significance and connectivity in relation to other nodes in the network; the strength of a node is the total of the weights (connectivity value in our case) of the edges connecting to it and may be described as:

$$S_i = \sum_{j \epsilon N} w_{ij} \qquad (4)$$

where the i_{th} and j_{th} nodes are indicated by i and j, respectively. N is the total number of nodes in the graph, and w_{ij} is the connectivity value for the relation between the two nodes i and j [93].

2.3.3.2. Clustering Coefficient

Watts and Strogatz [94] developed the clustering coefficient (CC) as a graph measure. CC reflects the degree to which nodes tend to associate together or connect to other nodes, and it captures the degree to which a given node neighbors link to one another.

$$C_i = \frac{2t_i}{k_i(k_i - 1)} \qquad (5)$$

Where *i* is the node, t_i is the node triangular connections number, and $k_i(k_i\text{-}1)$ is the number of graph maximum potential edges [11].

A clustering coefficient is a number that ranges from 0 (none of the node i neighbors are linked to each other) to 1 (all the node i neighbors are linked to each other where they form a complete graph). C_i is the probability in which two node neighbors will attach to each other. As a result, C = 0.5 denotes that there is a 50% chance that two of node neighbors are connected.

2.3.3.3. Efficiency

Local efficiency (EFF) illustrates the surrogate measure of graph clustering properties [87]. It is the inverse of the shortest path between node pairs.

$$E = \frac{1}{N(N-1)} \sum_{i,j \in N, i \neq j} \frac{1}{d_{ij}} \qquad (6)$$

where the i_{th} and j_{th} nodes are represented sequentially by i and j. The value between two nodes i and j, which represents the shortest path, is expressed as d_{ij}. The overall number of nodes in the graph is denoted by N.

2.4. Proposed graph parameters

In order to test a new graph parameter that could be abler to evidence the appearance of the mechanotransduction process, we proposed to use and compare to the previously used graph parameters, 2 new parameters are defined below:

2.4.1. PageRank

PageRank (PR) is not a brand-new concept. Citation research, which dates back to the 1940s, has a lengthy history of analyzing the quality of publication based on citations. Prior to the electronic network, academic scholars relied on printed journals, magazines, and conference proceedings as their primary source of information. Citations analyses, particularly co-citation analysis, create an inventive method for analyzing and ranking documents, authors, and journals [95].

The number of citations is a bibliometric index that is used to assess the impact of scientific publications. However, there are several flaws in this measurement, as it does not consider the value of the cited papers: A citation from an unclear study has the same value as a citation from a widely cited, ground-breaking work [96]. This obstacle is alleviated by the PageRank algorithm, which assigns higher weights to highly cited publications (i.e., publications with more inlinks) and articles cited by less highly cited papers (e.g., publications are linked by a less important papers). As a result, PageRank was chosen as a complementary method to citation analysis, which permits to highlight publications recommended by highly cited articles [97]. PageRank value may be a better indicator of importance because it considers both the number of citations and the prestige of the citing publications [98], incorporating the paper visibility and authority at the same time.

One such method of ranking by importance is the PageRank algorithm, which is primarily used by the search engine Google for link analysis. The notion, which was first applied to web pages, suggests that a web page's relevance increases when it is linked to other high-important pages. As a result, for a closed system of overall online web pages, a merit system can be built by assigning a relative weighting (as a percentage of the entire database) to each web page [99].

The worth of a page is determined by the number of links referring to it. Therefore, as long as a page is found on the network, it is more likely to contain more web page links. Old web pages have a greater PR value than fresh web pages, according to the algorithm.

$$PR(u) = (1 - d) + d \sum_{U \in Bu} \frac{PR(u)}{N_u} \quad (7)$$

where u is the node (electrode), Nu denotes the number of connections from u, and d denotes the damping factor, which can range from 0 to 1.

The page rank value is the mean of the PR(u) equations retrieved from each node.

2.4.2. Betweenness Centrality

Bavelas first proposed the idea of betweenness centrality (BC) in 1948 [100]. The significance of the concept of vertex centrality lies in a vertex's ability to govern information flow in a network. Positions are seen as fundamentally central due to the considerable distance between them and can thus facilitate, obstruct, or bias message transmission [101].

The focus of betweenness centrality is on identifying nodes that are commonly found on the shortest path between two other nodes [102]. As a result, betweenness centrality generates a relational value depending on the local role of the node concerning the nodes in between [103]. Nodes discovered on a path between two other nodes regulate the flow of information between them, ranging from full control (when only one path exists between the two other nodes) to restricted control (when many paths exist between nodes) [102].

The betweenness centrality of a graph computes the probability of a single vertex to be more central than most of the other vertices in the graph [101]. It is based on the differences in centrality between the most central vertex and the others. According to Freeman [102], the average variation between the measures of the centrality of the most central vertex and all the other vertices is the betweenness centrality of a graph.

It counts the number of times a node is placed on the network shortest path between other nodes. It assesses the degree to which the investigated node can act as a communication control point [103].

The BC of a vertex v can be estimated as follows:

$$BC(v) = \sum_{s \neq v \neq t} \frac{\sigma st(v)}{\sigma_{st}} \qquad (8)$$

where $\sigma_{st}(v)$ represents the number of the shortest path passing through vertex v and trail from s to t, while σ_{st} is the number of shortest paths from s to t [104].

The betweenness centrality value is the mean of the vertexes (v) that is retrieved from the BC equations.

For all these graph parameters, that are computed at the node level, the values associated to one burst of EHG are the mean of their values extracted from the 16 nodes.

2.5. Feature Selection Methods

In our study, we plan to compare the power of the classical connectivity methods (one EHG burst is represented by the mean, over the 4x4 matrix, of all the connectivity values), for the 4 tested connectivity methods (R2, H2, FW_h2, ICOH), and of the 5 graph parameters extracted from each matrix (Str, CC, EFF, PR, BC), to classify pregnancy and labor contractions. This will give us 24 features (4 + 5x4) to represent one burst of EHG associated with one contraction.

A high number of input parameters in classification generates pattern recognition problems. The Feature Selection is among the most essential and widely used strategies in data preparation to reduce the number of parameters and choose the most relevant ones.

In machine learning and data mining challenge, a proper representation of data from all features is a significant issue. With feature selection [105], the cost of computing is reduced, and classification performance can be improved.

The search strategy, defined in feature selection, identifies a relevant subset of *n* features F_{Best} from the initial subset of *m* features F, with *n*<*m*, as shown in figure 2.3. It is based on a criterion function whose value is greater when using the subsets of size *n* than when using the *m* original features. The objective function and system criterion are always used to determine the significance of a selected group of features. A classification function is a tool for allocating patterns or assessing the efficiency of each subset in predicting the class output or pattern [106]. For the feature selection process, first, the objective function assesses candidate subsets and provides a measure indicating how good they are. The search technique then uses this information to choose new candidates, attempting to find the optimal subset without affecting the classification accuracy.

Hence, Feature selection provides several benefits, including lowering the number of features and eliminating irrelevant, redundant, or noisy features [107]. Furthermore, it has the potential to dramatically improve the mining performance of learning algorithms, including learning speed and predictive accuracy.

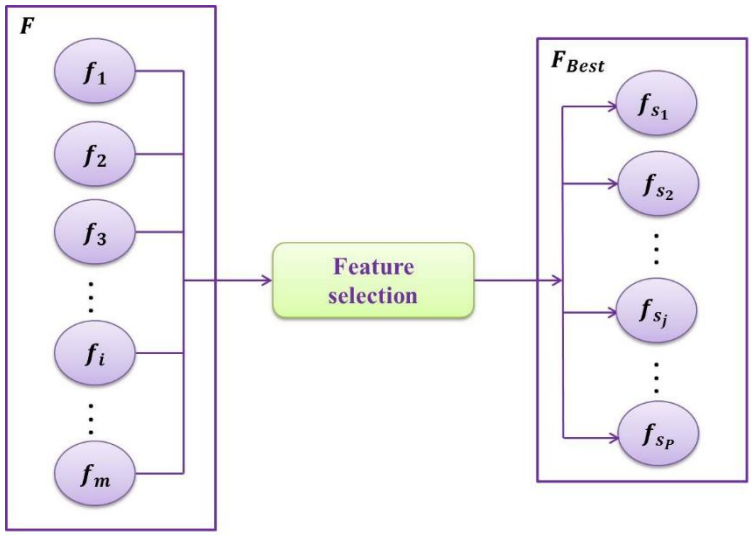

Figure 2.3. Feature Selection technique [108].

Suppose that $F = \{f1 , f2 , \dots , fi , \dots , fm \}$ is a set of features of size m, where m is the total number of original features and $i = 1 \dots m$. J is a function that evaluates a subset of features [72]. We anticipate that the best subset of features will yield the highest value of J.

The goal of the selection is to discover a subset of size n ($n < m$), of F_{Best} = { 1 , $fs2$, … , fsj , … , fsn }, $sj \in \{1 \dots m\}$, and $F_{Best} \subseteq F$ such as:

$$J(F_{Best}) = Max\ J(SC) \qquad (9)$$

where SC is a candidate subset of features, $SC \subseteq F$ and the size of SC is a number n < m.

In our study, we will use, as evaluation function, the F1 score (Fscore) value, defined in the following formula:

$$F1 = 2\ x\ \frac{precision\ x\ recall}{precision + recall} \qquad (10)$$

where *precision* measures the proportion of truly positive results (often known as the positive predictive value), recall is the capacity of a test to correctly identify positive results (also known as sensitivity).

2.6. Artificial Intelligence and classification

2.6.1. Introduction

Artificial Intelligence (AI) is one of the most challenging areas of computer science. AI is pointed to machines that are trained to think like humans, duplicate their actions, and replicate human intelligence. Artificial intelligence strongest feature is its ability to streamline and take actions that have the best possibility of achieving a certain goal [109].

The purpose of this section is to summarize the history of artificial intelligence and to highlight its most promising methods and solutions for our application.

2.6.2. Definition

Computerized approaches that apply knowledge, reasoning, self-learning, and decision-making to make machines smarter are referred to as artificial intelligence (AI). AI is a computer science field that focuses on the construction and development of intelligent agents in the form of computer programs, thus allowing them to comprehend the artifact behavior [109].

AI techniques were developed for data association using expert systems and neural networks. Expert systems are computer systems created to mimic the capacity of human brain decision-making. They are often based on knowledge and produce specialized knowledge and expertise. The information gained during the development of an expert system will be used to base the decision on the efficiency of the expert system which, on the other hand, is determined by the amount of knowledge preprogrammed in it. Permanence, increased

reliability, consistency, reduced costs, and rapid response are direct benefits of expert systems [110]. One of these expert systems is the neural network (NN) family.

Software-simulated processing units, neurons (or nodes), in artificial neural networks (ANN) are trained to tackle issues. The development of NNs is based on historical data and associated outcomes. The NN compares its response to the test input data to a pre-determined result. The weight of each node can be modified according to a specified algorithm using this method.

2.6.3. Historical summary

In 1956, and during his first meeting on the subject, John McCarthy was the first to develop the name “artificial intelligence”. Nevertheless, the quest to understand the ability of machines to actually think began far earlier. Vannevar Bush developed a system that magnifies information and understanding in his seminal work "We May Think.". Alan Turing published a paper five years later on the idea that a machine could simulate human intelligence and perform tasks such as chess [111].

In the late 1960s, artificial intelligence researchers and theorists' initial promises appeared to be hollow. However, artificial intelligence research has been decomposed into a variety of sub-fields after two decades, and development has been slower than some had predicted. Then, AI began to take off between 1957 and 1974. Computers have gotten quicker, cheaper, and more accessible by accumulating more information, allowing them to store more data. Machine learning algorithms have also advanced, and individuals now have a better idea of which algorithm to use for a particular problem.

Marvin Minsky, in 1970, told Life Magazine, "From three to eight years of age we will have a machine with the general intelligence of an average human being” [112].

AI was reinvigorated in the 1980s by two factors: an expansion of the algorithmic toolbox, and an increase in funding. When John Hopfield and David Rumelhart popularized the principles of "deep learning," [113] computers were able to learn from experience.

Many of the artificial intelligence historic goals were achieved throughout the 1990s and 2000s. Gary Kasparov, the reigning world chess champion and grandmaster, was defeated by Deep Blue, a computer chess program, in 1997, marking the first time a reigning world chess champion has been conquered by a computer as well as a significant step toward the program of artificially intelligent decision-making.

2.6.4 Machine Learning

The machine learning (ML) domain is concerned with creating an algorithm that generates a result based on prior knowledge and data [114]. Generally, it is exercised to characterize the computer systems that typically need human intelligence like visual perception, speech recognition, translation, decision-making, and prediction. ML approaches require the

acquisition of both training and testing data in order to create and assess classification results [115].

Hence, in machine learning, several learning rules have been employed. In our study, we used two methods (supervised and unsupervised). The purpose of supervised learning is to forecast/classify a given outcome of interest, and it is a role method used as a prediction tasks describer [116]. This method can analyze immense datasets, such as clinical, demographic, and social predictors [117]. On the other hand, unsupervised learning is extremely effective in describing tasks, since its purpose is to try to uncover correlations in a data structure without establishing a measured outcome [118]. It is used for data preprocessing like feature extraction, feature selection, and resampling [119].

Accordingly, various activation functions have been proposed throughout the history of machine learning; though, establishing an appropriate activation function for a specific model has become among the most significant issues for automated machine learning [120]. In this study, we employed the classical sigmoid function generated by Richards [121] in all methods.

We will present below the different machine learning methods that are used in this study.

2.6.4.1 Neural network

Artificial neural network (ANN) is a versatile and powerful supervised machine learning approach that mimics the functions of the human brain. The human brain consists of neurons, and it contains roughly 85 billions of them [117]. The application of ANNs has the advantage of making models, from complex natural systems with large inputs, easier to use and more precise.

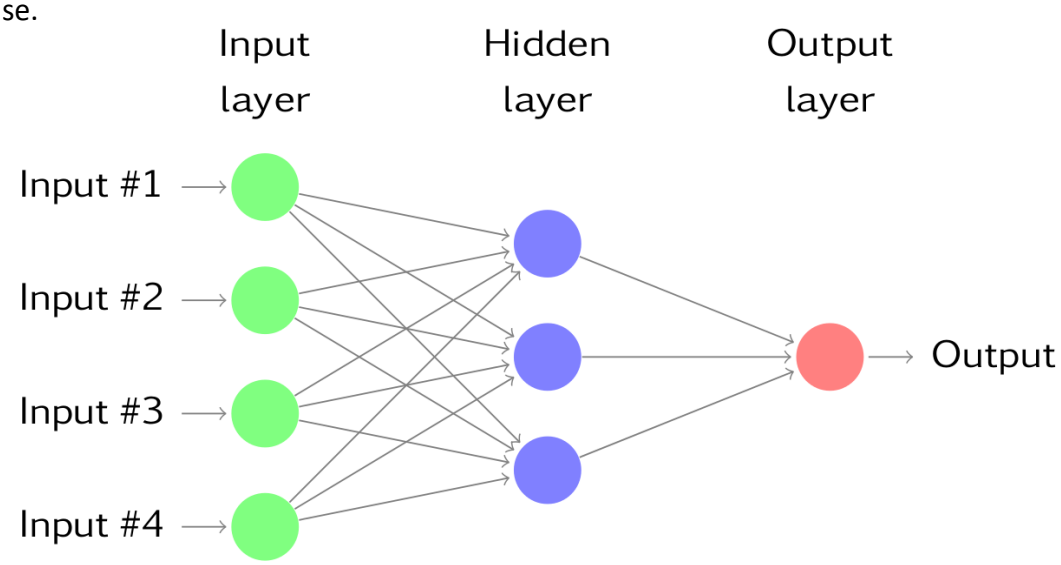

Figure 2.4. Neural Network Structure[118].

In the term 'artificial neural network', the word network refers to the interconnections between the neurons in each of the multiple system levels. Figure 2.4 presents an example system made of three layers. The first layer is made up of input neurons that convey data to

the second layer of neurons via synapses and then to the third layer of output neurons via further synapses. More complex systems will have more layers of neurons. The synapses keep track of "weights," which are used to alter data in calculations [122].

2.6.4.2 Multilayer Perceptrons

The Multilayer Perceptrons (MLP) model seems to be the most often used type of artificial neural network (ANN) for data modeling. MLP network design is composed of neurons arranged in layers (Input Layer, Hidden Layer(s), Output Layer) [123] as shown in figure 2.5. The MLP model belongs to a type of ANN known as a feedforward neural network. A feedforward neural network is an elementary sort of neural network that may simulate continuous functions, MLP is a supervised classification method.

All of the input nodes form the first layer in the MLP model, while the hidden part is divided into one (or more) hidden layers. Assume MLP has N layers: the first layer is the input, the N_{th} layer is the output, and layers 2 to N-1 are hidden layers.

A neuron K can be mathematically characterized by the following two equations:

$$y_k = f(u_k + b_k) \qquad (11)$$

$$u_k = \sum_{i=1}^{n} w_{ki}\, x_i \qquad (12)$$

where x_1, x_2, x_3, …, x_n indicates the input signals, w_{k1}, w_{k2}, w_{k3}, …, w_{kn} are the connection weights of the neurons, u_k is the linear output of the linear combination among weighted inputs, b_k is the bias term, f is the activation function, and y_k is the output signal of the neuron[124].

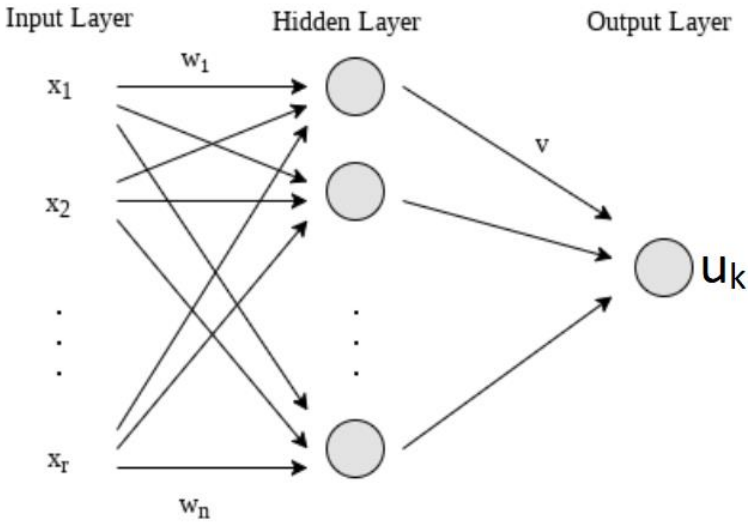

Figure 2.5. MLP Structure [125].

2.6.4.3. Support Vector Machine

Support Vector Machine, commonly known as (SVM), is identified for its ability to deal with linear and non-linear data respectively. For organization and regression tasks, the method uses statistical learning theory to establish decision boundaries between data points from multiple classes and divide them with the highest margin [126]. SVM is a supervised classification method.

SVM basic motivation is to separate many classes in the training set with a surface that optimizes the margin among them (Figure 2.6). In other terms, SVM permits to increase the model capacity of generalization.

Consider N separable training data [127] to understand how the SVM works.

$$(x_1, y_1), \ldots, (x_n, y_n), x_i \in R^d \text{ and } y_i \in (-1, +1) \quad (13)$$

where x_i is a feature input vector and y_i the class label (negative or positive) of a training compound *i*.

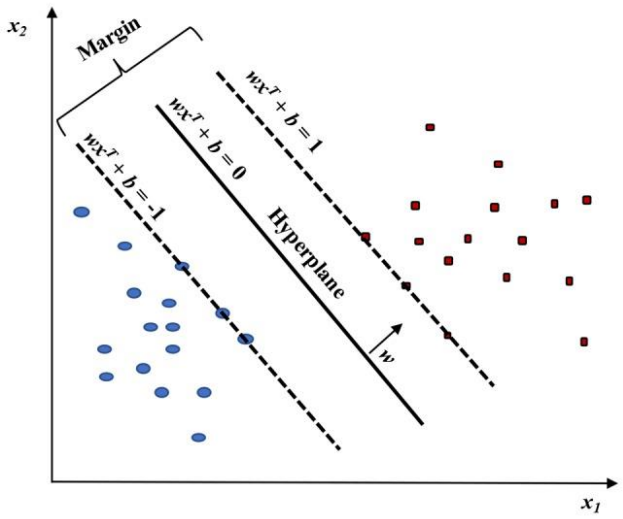

Figure 2.6. SVM Structure [127].

As a result, the ideal hyperplane can be defined as: $wx^T + b=0$

where *w* denotes weight vector, *x* denotes input feature vector, and *b* denotes bias.

For all elements of the training set, the *w* and *b* would meet the following inequalities:

$$wx_i^T + b \geq +1 \; if \; y_i = 1 \quad (14)$$

$$wx_i^T + b \leq -1 \; if \; y_i = -1 \quad (15)$$

The goal of SVM model training is to identify *w* and *b* such that the hyperplane divides the data and maximizes the margin $1 / ||w||^2$.

2.6.4.4. Logistic Regression

Pierre François Verhulst, a French mathematician, invented the logistic regression function in the 19th century to describe the expansion of human populations and the conduct of autocatalytic chemical reactions [128].

LR, a supervised approach, can be used when the research method is focused on determining whether or not an event occurred rather than when it occurred (time course information is not used). It is especially useful for models with illness states (diseased or healthy) and decision-making (yes or no) and commonly utilized in health sciences research [129].

The logistic regression model is based on a logistic function [130] that estimates and describes the relationship among a dependent variable Y as shown in figure 2.7. The output Y takes just two possible values, arising from the occurrence or absence of an event, and independent variables influencing that phenomenon.

$$P = \frac{e^{(b0+b1*x)}}{1 + e^{(b0+b1*x)}} \qquad (16)$$

where *b0* and *b1* are denoted by weights or coefficient values. *b0* represents the bias or intercept, and *b1* is the coefficient.

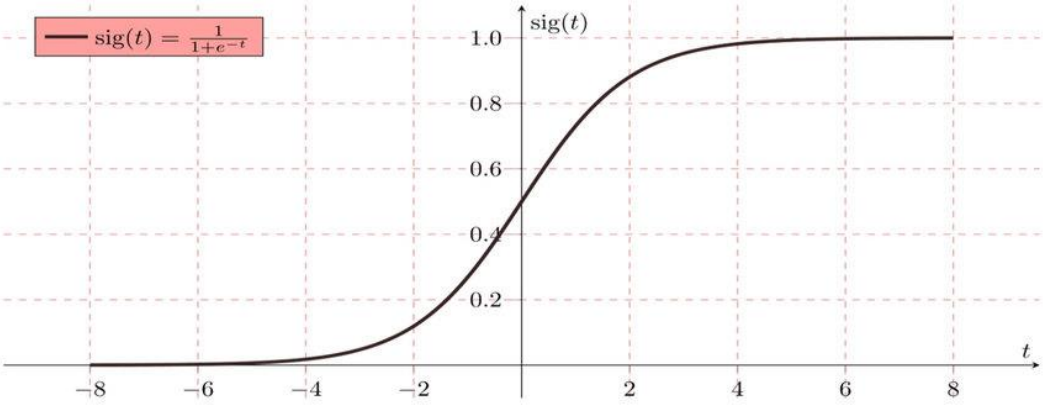

Figure 2.7. Logistic Regression Structure [131].

If the probability of success is determined (presuming Y is a dichotomous variable with values of 1 – for the existence of the event, we are concerned with (success) and 0, for the opposite case (failure).

2.4.4.5. Naive Bayes

The Naive Bayesian classification algorithm is simple in that it assumes that the classification attributes are independent of one another and that they do not interact.

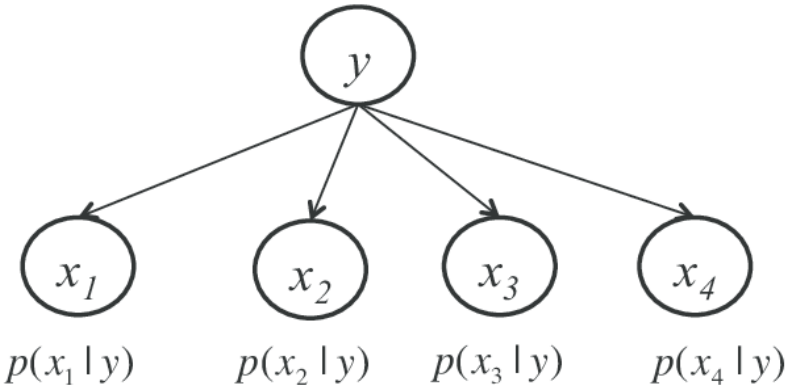

Figure 2.8. Example of naive bayes model for integrating data sources [132].

The Bayes' theorem can be used to create predictions based on available evidence and previous knowledge. It is a supervised approach. With accumulated evidence, the prediction changes. In technical terms, the prediction is the investigators' focus on the posterior probability. Prior probability is a concept that describes the most likely guess on the outcome without any extra evidence. The existing evidence is expressed in terms of likelihood, which reflects the likeliness of a predictor given a specific outcome. The likelihood is calculated using the training dataset. The following equation [133] expresses Bayes' theorem mathematically.

$$P(A|B) = \frac{P(B|A) * P(A)}{P(B)} \quad (17)$$

P(A) and *P(B)* are the likelihoods of events A and B without considering each other. *P(A|B)* is A conditional probability on B, and *P(B|A)* is B conditional probability on A. A is a series of categorical result occurrences, and B is a series of predictors in naive Bayes classification.

Using Bayesian probability terminology, the above equation can be written as:

$$Posterior = \frac{prior*likelihood}{evidence} \quad (18)$$

The term "naive" denotes that the predictors are independent of one another when the outcome value is the same.

2.6.4.6. Random Forest

Random Forest (RF) is a regression and classification ensemble learning method. Breiman [134] developed a method that combines sampling and random feature selection to create a collection of decision trees with controlled modification. RF is a supervised machine learning algorithm that is based on a decision tree algorithm. In the ensemble, every decision taken is built using a sample that has a replacement that is derived from the training data.

Random Forest is made up of a set of un-pruned regression trees that are built using bootstrap sampling from the primary training data. The bootstrap resampling of the data used to train each tree increases the tree diversity. Root nodes, branch nodes, and leaf nodes make up each tree. Increasing the number of trees increases the precision of the outcome. The ideal node splitting feature is chosen for each node of a tree from a set of m features chosen randomly from a feature space of size M [135].

$$RF = \frac{1}{N}\sum_{i=1}^{N}(f_i - y_i)^2 \qquad (19)$$

where N is the number of data points, f_i is the value returned by the model, and y_i is the actual value for data point i.

2.6.4.7. Gradient Boosting Machines

The gradient boosting machine (GBM) algorithm is categorized as a supervised ensemble approach in machine learning. The gradient boosting model, commonly known as AdaBoost, was first proposed by Freund and Schapire for classification difficulties [136]. It is a machine-learning technique that may be used in both regression and classification conflicts.

As an ensemble method, gradient boosting can be characterized as follow:

$$y = \mu + \sum_{m=1}^{M} v h_m(y; X) + e \qquad (20)$$

where y denotes the vector of the nodes, μ denotes the mean of the iterations, v denotes the shrinkage factor, h_m is the predictor model, whereas X is the matrix of corresponding data, and e denotes the residual vector.

2.6.4.8. Deep Learning

Deep learning is a branch of machine learning based on a set of algorithms that attempt to model high-level abstractions in data by combining multiple processing layers with complex structures, or by combining various non-linear transformations. Deep learning techniques have created a lot of enthusiasm in the research community, especially in tackling many challenging tasks by learning from raw sensor data. Deep learning is embodied in an expansive family of machine learning methods focused on examining representations of data.

The phrase deep learning was initially used in the 2000s, when Convolutional Neural Networks (CNNs), a computational original model from the 1980s but that trained effectively

in the 1990s, could deliver remarkable results in visual object recognition tasks as computer vision algorithm [137].

Deep learning algorithms extract complex representation automatically from a massive amount of unsupervised data. Artificial intelligence, which has the broad objective of imitating the human brain ability to recognize, evaluate, learn, and make judgments, especially for exceedingly hard issues, is driven by these algorithms. Deep Learning algorithms that attempt to imitate the hierarchical learning address of the human brain [138], have benefited greatly from work relating to these complex challenges.

There are several deep learning methods available; however, in this study, we chose two of the most used methods, RNN and LSTM, to assess the performance of deep learning for the classification of pregnancy and labor contractions.

2.6.4.8.1 Recurrent Neural Networks

Recurrent neural networks, which is known as (RNN), is a type of managed machine learning model made up of artificial neurons with one or several additional feedback loops. RNN is an administered form that requires a training dataset of input-target pairings, and the feedback loops are recurrent cycles across time or sequence (semi-supervised approach). This allows RNNs, in principle, to map from the entire history of the inputs to an output vector.

By adjusting the network weights, the goal is to reduce the variance between target pairs and the output [139].

The cyclic connections in RNN allow it to learn the temporal dynamics of subsequent data. Multiple nodes make a hidden layer in an RNN [140]. Figure 2.9 represents a schematic diagram of an RNN node. Each node has a function that uses its current input x_t and the previously hidden state h_{t-1} to produce the currently hidden state h_t and output y_t according to the equations:

$$h_t = \theta_h(W_h x_t + U_h h_{t-1} + b_h) \qquad (21)$$

$$y_t = \theta_y(W_y h_t + b_y) \qquad (22)$$

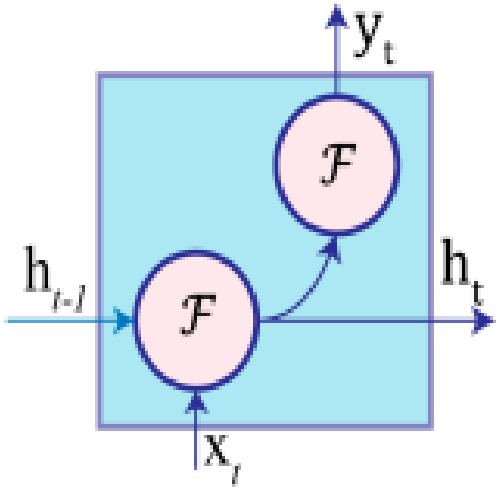

Figure 2.9. Schematic diagram of an RNN node where ℎt-1 is the previous hidden state, xt is the current input sample, ℎt is the current hidden state, yt is the current output, and ℱ is the activation function [141].

where W_h, U_h, and W_y are the weights for the hidden-to-hidden recurrent connection, input-to hidden connection, and hidden-to-output connection, respectively. b_h and b_y are bias terms for the hidden and output states, respectively. Furthermore, there is an activation function $\mathcal{F}$ linked with each node denoted by θ_h and θ_y. This is an element-wise non-linearity function, frequently chosen from several existing functions, such as the sigmoid, hyperbolic tangent, or rectified linear unit. We used a sigmoid function to test the power of this method for the classification between pregnancy and labor.

2.6.4.8.2. Long Short Term Memory

In practice, RNNs can suffer from the 'vanishing gradient' problem, where gradient information disappears or explodes as it is propagated back through time, which can limit the RNN memory. One solution to this problem is the 'long short-term memory' (LSTM) architecture, which uses a 'memory cell' with a gated input, gated output, and gated feedback loop.

LSTM is a supervised classification method, LSTM has been developed by Hochreiter and Schmidhuber as an evolution of RNN in order to address conflicts of the aforementioned RNN deficiencies by adding more interactions per module (or cell). Consequently, LSTMs are capable of learning long-term dependencies and remembering information for a lengthy period of time [142].

The state of the memory cells is the key to the LSTM model, which is made up of a rare group of memory cells that replace the RNN hidden layer neurons. To preserve and update the state of memory cells, the LSTM model filters information via the gate structure. It has input,

forgotten, and output gates in its door structure. There are three sigmoid layers within every memory cell. Figure 2.10 represents the structure of LSTM network.

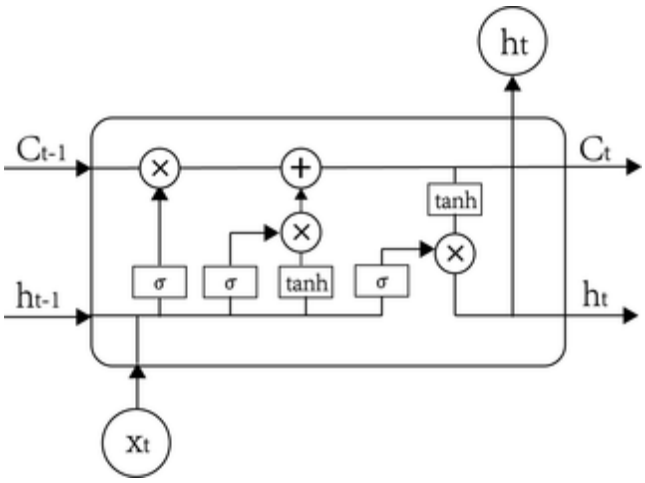

Figure 2.10. Structure of long short term memory(LSTM)[143].

The memory cell accepts the previous moment of the output h_{t-1} and the current moment of the external information x_t as inputs and merges them into a long vector [h_{t-1}, x_t] through σ transformation to become as follows:

$$f(k) = g(W_f \left(h(k-1), x(k)\right) + b_f \,) \qquad (23)$$

where W_f and b_f are the weight matrix and bias of the forgotten gate, respectively, and g is the sigmoid function. The major purpose of the forgotten gate is to keep track of how much of the prior time cell state C_{t-1} is reserved for the present time cell state C_t. Based on h_{t-1} and x_t, the gate will output a value between 0 and 1. The value of 1 indicates full reserve while 0 indicates total discernment [143].

The input gate, in order to prevent unnecessary data from accessing the memory cells, controls the current time network input x_t confined in the cell state C_t. It serves two functions: one is to determine the state of the cell that has to be updated; the sigmoid layer selects the value to be updated, as presented in Eq (24). The other option is to update the information in the cell state. To control how much new information is introduced, a new candidate vector is initiated through the *tanh* layer, as indicated in Eq (25). Lastly, Eq (26) is used to renew the cell state of the memory cells:

$$i_t = \sigma(W_t \,(h_{t-1}, x_t) + b_i \,) \qquad (24)$$

$$\check{C}_t = tanh(W_c\ (h_{t-1}, x_t) + b_c\ ) \qquad (25)$$

$$C_t = f_t * C_{t-1} + i_t \check{C}_t \qquad (26)$$

The output gate controls the amount of current cell state that is discarded. A sigmoid layer determines the output information initially, and then the cell state is analyzed by *tanh* and multiplied by the sigmoid layer output to generate the final output portion:

$$O_t = \sigma(W_\sigma\ (h_{t-1}, x_t) + b_0\ ) \qquad (27)$$

The cell final output value is then defined as:

$$h_t = O_t * \tanh(C_t) \qquad (28)$$

2.6.5. Classifier performance

In order to compare the performances of the different classification methods tested in this work, we used classical metrics:

2.6.5.1 Receiver Operating Characteristic (ROC):

We applied Receiver Operating Characteristic (ROC) [144] to display the performance of the different methods tested. Early in the 1950s, ROC analysis was created with the detection theory of the electronic signal [145]. One of the early applications was in radar, where it was used to split observer variability from the signal delectability. In the early 1950s, psychologists used the ROC approach to study the relationship between the properties of physical stimuli and the associations of psychological experience.

For a binary classifier system, the ROC curve is the plot of the true positive rate (TPR) against the false positive rate (FPR) for various threshold settings. The area beneath the ROC curve (AUC) is a global measure of a test ability to discriminate or not between two groups (in our case, pregnancy and labor) if a provided condition occurs. An AUC of 0.5 indicates that there is no discrimination ability in the test (is no better than chance), whereas an AUC of 1.0 indicates that the test has perfect discrimination [146].

In our case, if we want to determine whether a contraction is an efficient contraction (it has been recorded during labor), the definitions of specificity and sensitivity will be as follows [11]:

When a contraction has been recorded during pregnancy, specificity refers to the likelihood that a test result will be negative (true negative rate, expressed as a percentage).

$$\text{Specificity} = \frac{TN}{FP+TN} \qquad (29)$$

When a contraction has been recorded during labor, sensitivity refers to the likelihood that a test result will be positive (true positive rate, expressed as a percentage).

$$\text{Sensitivity} = \frac{TP}{TP+FN} \qquad (30)$$

where TP, TN, FP and FN stand respectively for True Positive, True Negative, False Positive and False Negative values (figure 2.11).

2.6.5.2 Confusion matrix:

The confusion matrix is a summary of prediction results on a classification problem. The number of correct and incorrect predictions are summarized with count values and broken down by each class. We have used this method to determine the best nodes in the matrix [147]. Figure 2.11 shows an example of a confusion matrix presentation. TP, TN, FP, FN are represented respectively.

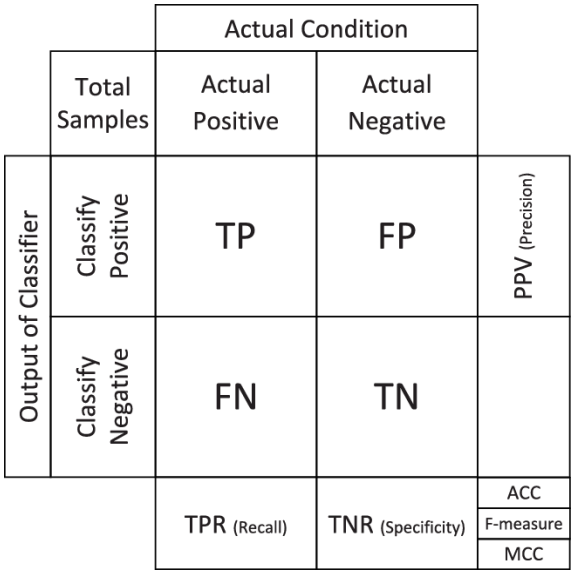

Figure 2.11. The confusion matrix and relevant evaluation index [148].

2.6.5.3 Student Test:

To select the features the most sensitive to either electrical diffusion or mechanotransduction process, we have used the student test, a method suited for small samples [149].

$$t = \frac{m - \mu}{s/\sqrt{n}} \quad (31)$$

Where t is the Student t-test, m is the mean, μ is the theoretical value, s is the standard deviation and n is variable set size.

2.7. Data

We tested our new approach on real EHG signals recorded on the mother's abdomen. These signals were collected from women during pregnancy or labor[150], preprocessed, and used to evaluate the clinical power of this new uterine contractility quantification for detecting premature labor. The EHG signals from a woman's abdomen are described below.

We have also used EHG signals simulated by using a uterine model developed in our team [82] in order to compare the performance of the different used features (connectivity methods, connectivity + graph parameters) to represent the evolution of either the electrical diffusion or the mechanotransduction process.

We present in this section both kinds of data used in this work: real and simulated EHGs.

2.7.1. Real EHGs signals

To record the electrical activity of the uterine muscle, we followed a standard protocol established in prior work. After careful preparation of the skin, in order to reduce the interelectrode impedance, the woman's abdominal skin is covered with a grid of 16 monopolar electrodes (4x4 matrix), with two extra electrodes on each of her hips. The hip electrodes are used as reference electrodes. They used Ag/AgCl electrodes (8mm diameter, 17.5 mm between centers of two adjacent electrodes), an alignment frame, a double-sided hypoallergenic sticky sheet, and a silicone backing, that are all parts of the standardized system in order to standardize and ease the electrode positioning [150].

The grid on the abdomen is located as follows: the third column of the electrode grid is located on the uterus median vertical axis; the 10^{th}–11^{th} pair of electrodes must be located halfway between the uterine fundus and pubic symphysis (Figure 2.12a). They avoid the navel by sliding the matrix up and down while remaining as near to the desired position as feasible. During the recordings, a tocodynamometer sensor was also placed on the abdomen for the simultaneous recording of EHG and TOCO signals. A 16-channel (up to 32) multi-purpose physiological signal recorder was used to make the measurements (Porti 32, TMSi). Figure 2.12b shows a typical example of electrode and tocodynamometer sensor arrangement. Figure 2.12c illustrates the electrode numbering distribution as viewed while looking at the woman's abdomen.

During pregnancy recordings, the woman was asked to sit in a reclining chair, with support, for instance, a tiny pillow, placed behind the right side of the body to prevent the syndrome of aortocaval compression. For the labor recordings, the woman was laying in her maternity room bed. The woman was requested to sign an informed consent form, and the Helsinki declaration was followed in every way. A pregnancy recording lasted approximately one hour, while a labor recording lasted at least half an hour (considering the delivery conditions).

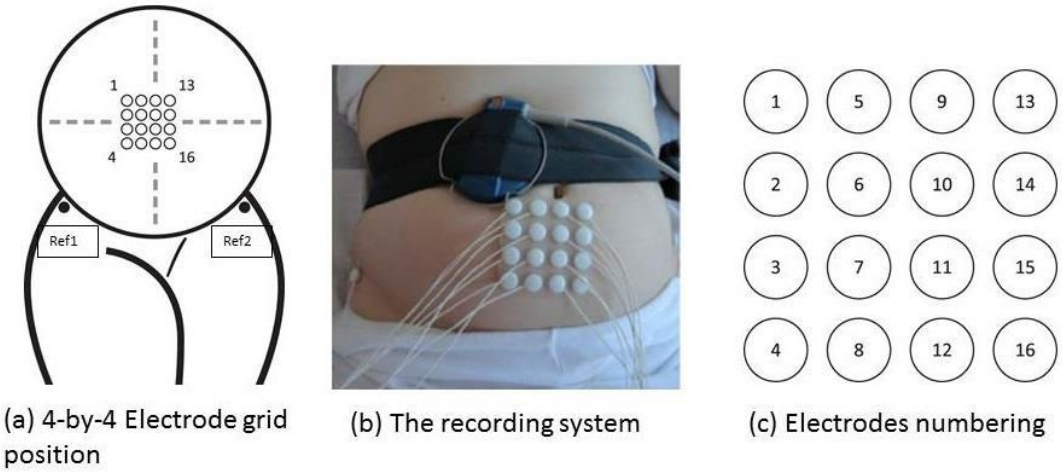

*Figure 2.12. The grid of 4*4 electrodes system used for the uterine EHG measurement. (a) The grid position on the woman abdomen. (b) The recording system composed of the grid of electrodes, two references electrodes and the TOCO sensor. (b) The electrodes*

They followed up with the pregnant women after the recording to classify their signals whether pregnancy or labor. The EHGs were designated "labor" only if they were measured a maximum of 24 hours before delivery. The signals were marked "pregnant" if the delivery took place later. After applying an antialiasing filter, the sampling frequency was set to 200 Hz. The data were collected at the Landspitali university hospital in Reykjavik, Iceland, following an ethical committee-approved protocol by Iceland (VSN02-0006-V2), and also at the Center of Obstetrics and Gynecology in Amiens, France, following an ethical committee-approved protocol by the French committee (VSN02-0006-V2) (ID-RCB 2011-A00500-41).

Data Pre-processing

Based on the tocodynamometer trace recorded simultaneously, the bursts of EHG associated with uterine contractions (muscle activity) were manually segmented. The tocodynamometer paper trace (which reflects the mechanical activity of the abdomen) was digitalized to make uterine contraction segmentation easier (figure 2.13a).

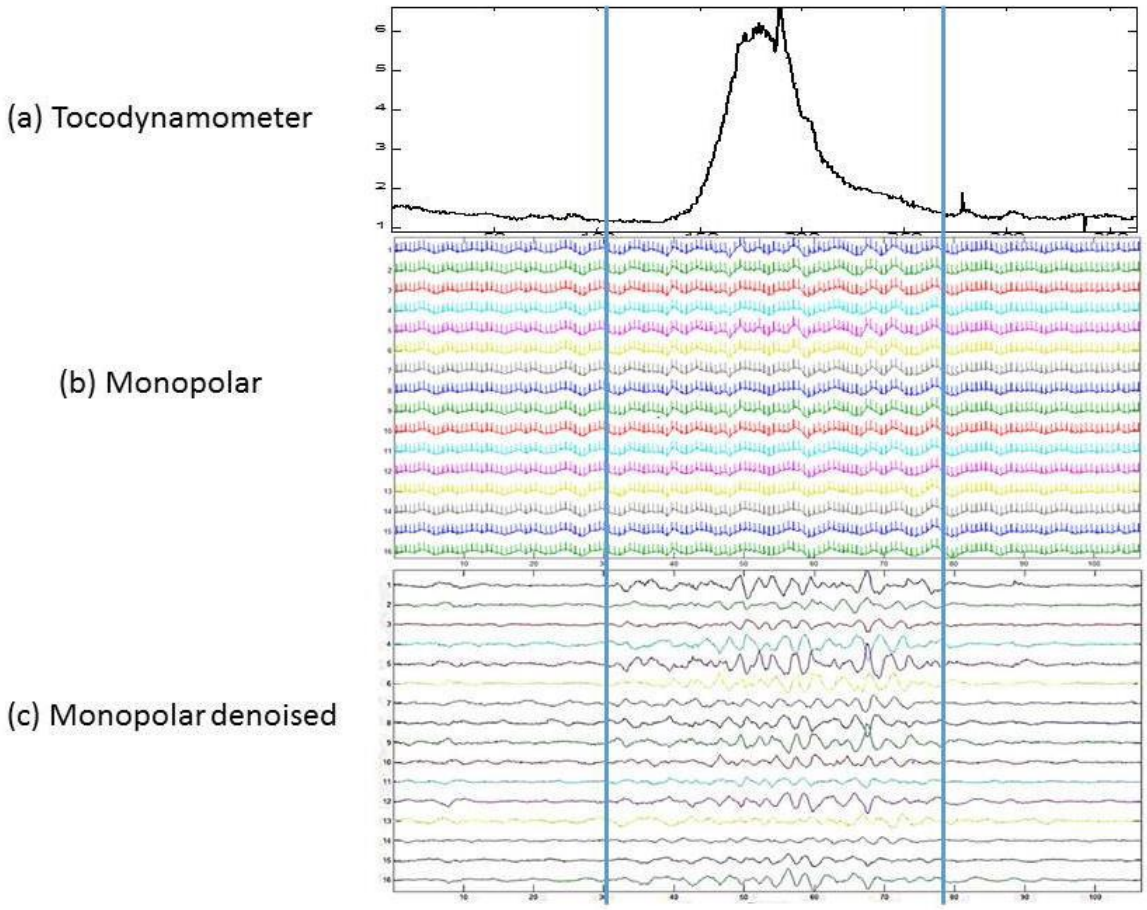

Figure 2.13. Segmentation and Denoising of the recorded EHG signals. (a) TOCO signal used for segmentation. (b) Monopolar raw EHGs. (c) Monopolar EHGs after denoising[151].

EHG signals are affected by different artifacts, such as the mother's cardiac activity, electronic noises, drip pump noise, etc. Using a CCA-EMD approach previously developed by our team, the segmented bursts (contractions) were then denoised [10]. This algorithm, which combines blind source identification with canonical correlation analysis (BSS CCA) and empirical mode decomposition (EMD), allows monopolar EHGs to be denoised effectively. Figure 2.13 shows an example of the signals that were acquired. The digitized TOCO trace (Figure 2.13a), monopolar recorded signals (Figure 2.13b), and monopolar signals after denoising (Figure 2.13c). We obtained 183 labor and 247 pregnancy bursts after segmentation and denoising. These contractions were collected from 35 healthy women.

2.7.2. Simulated EHGs Signals

In order to compare the performance of the different features used at the input of classification algorithm (connectivity methods alone, connectivity + graph parameters) and in order to represent the evolution of the electrical diffusion or the mechanotransduction

process, we used simulated EHGs signals created by using a uterine model developed in our team [82].

This model can be divided into numerous sub-models that have been developed to simulate the phenomenon of mechanotransduction, which was proposed by Young as a new hypothesis for understanding uterine activity synchronization during labor [23]. The first sub-model generates the action potentials (APs) obtained thanks to ion exchanges across the cell membrane (Hodgkin-Huxley approach). It also gives the calcium concentration of every cell, by modeling this ionic activity at the cellular level. The next sub-model, the mechanical contraction model, uses this concentration as an input variable to determine the force created by each cell, related to its electrical activity. Thanks to the 2 following sub-models, these forces are then used to determine the displacement of each node. The model geometry is updated based on these displacements, and the stretches of each cell are calculated. These stretches then influence the opening of ion channels sensitive to stretching, which are subsequently introduced back to the cellular electrical sub-model. As a result, the electrical activity of the stretched cells changes, resulting in new calcium concentrations in these cells, new forces, and a new step of the simulation process linking the different sub-models goes on [82].

The simulated EHGs are obtained by integrating the APs generated by each active cell, thanks to 2 other sub-models: one representing the abdominal conducting volume (muscle, fat, and skin), the other one representing the electrodes.

Figure 2.14 shows the diagram of the electro-mechanical part of this model, figure 2.15 the representation of the conducting volume and the electrodes models, and Figure 2.16 an example of the simulated signal.

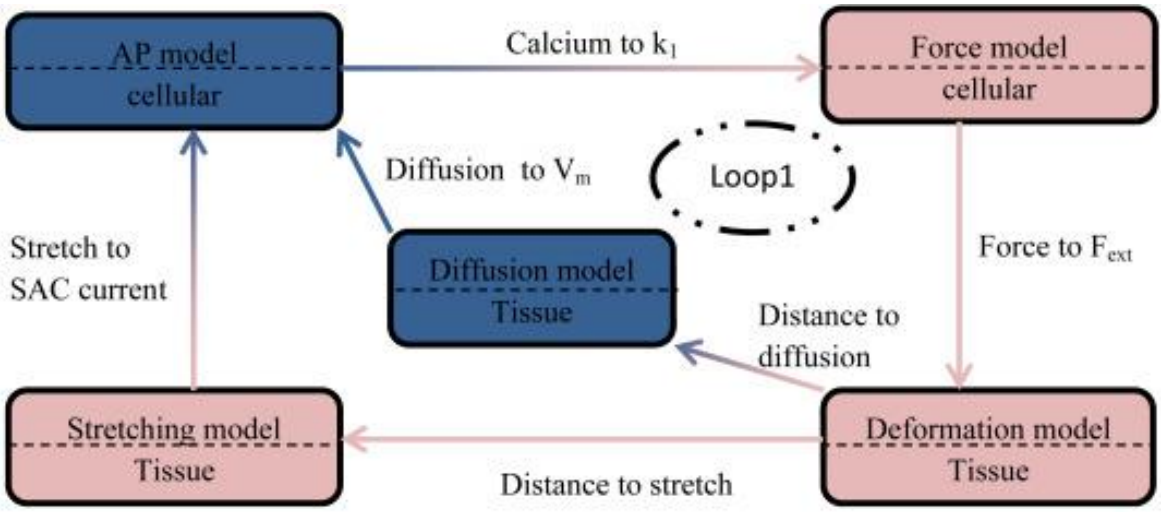

Figure 2.14. Diagram of the uterine muscle model. The blue boxes represent the electrical models and the red boxes the mechanical ones. Notice that the arrow respects the color change when going from the electrical to the mechanical model (and vice-versa)

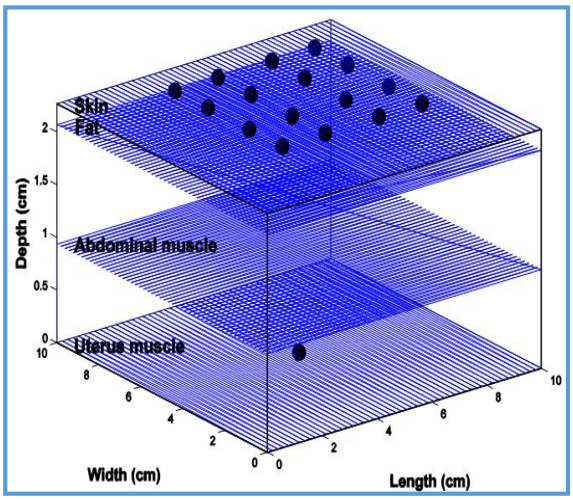

Figure 2.15. Schematic representation of the conducting volume and of the electrodes

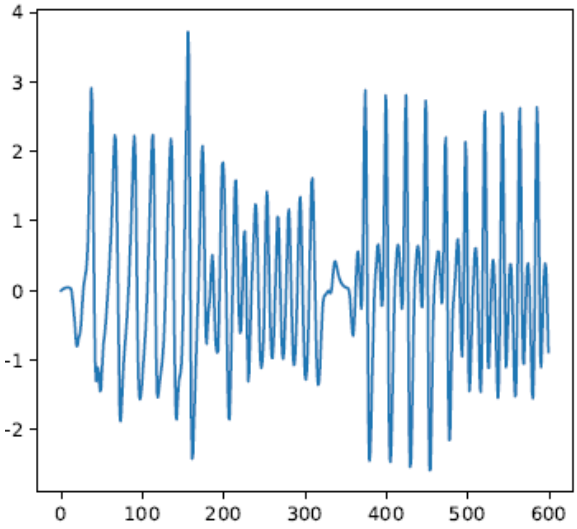

Figure 2.16. Example of a simulated EHG

2.8. Work Content

The work done during this thesis is parted in 3 main studies:

- **Machine learning applied to real signals**

Figure 2.17 illustrates the entire pipeline of our work. From the recorded uterine EHGs, obtained by using a grid of 4x4 electrodes (Figure 2.17a), a connectivity matrix is calculated using different connectivity methods from the whole signals (monopolar and denoised) (Figure 2.17b).

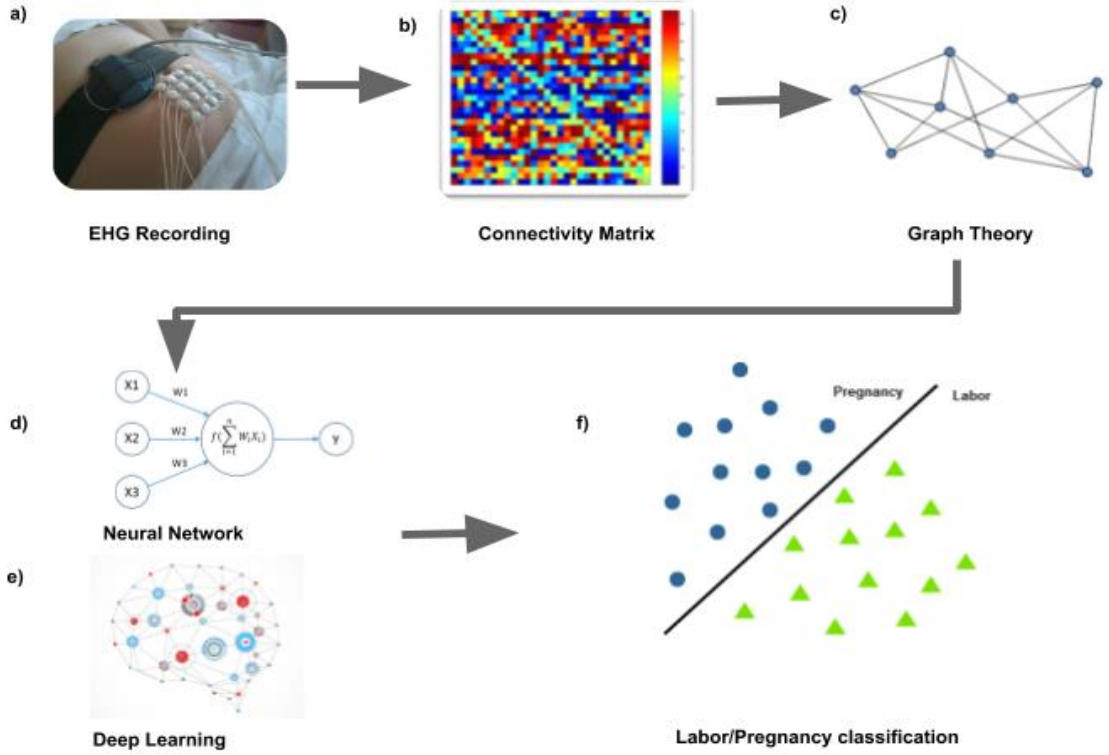

*Figure 2.17. Implementing structure. (a) EHG signals recorded by 4*4 electrodes grid. (b) The Connectivity Matrix. (c) Graph Theory presentation (d)(e) Neural Network and Deep Learning respectively. (f) Classification between Labor and Pregnancy*

Graph parameters are then extracted from these connectivity matrices for every approach (Figure 2.17c). Then, we used these metrics as inputs to, for example, alternative neural network (Figure 2.17d) and deep learning (Figure 2.17e) methods, in order to classify the signals between labor and pregnancy contractions (Figure 2.17f).

We will test in this part of our study different classification methods in order to select, after feature selection, the one that gives the best results. The results of this analysis will be presented in Chapter 3.

- **Windowing Approach for real signals**

As the EHGs are known to be non-stationary signals, and as we also expect the connectivity to evolve during a contraction (thanks to the electrical diffusion and to the mechanotransduction process), we have applied to real signals a windowing approach in order to select the best windows that contain the most significant information. The signals are thus first divided into N windows. Then, we applied the connectivity methods on each

window. The results of the connectivity matrix are then represented as a graph for each window. Afterward, to classify between pregnancy and labor, numerous neural network and machine learning methods are applied to each window, for the different input parameters (connectivity method alone, connectivity method + graph parameters). At the end, for each tested method, we get a confusion matrix for all the windows. Finally, we estimate the average of these matrices to get a consensus matrix for all the methods. The complete pipeline is presented in figure 2.17.

We aim from this part is to find if there is a best window to represent the connectivity during a contraction. The complete pipeline is presented in figure 2.18.

We also tested if there exists a best electrode location that gives better results than when using the whole contraction and all the electrodes information.

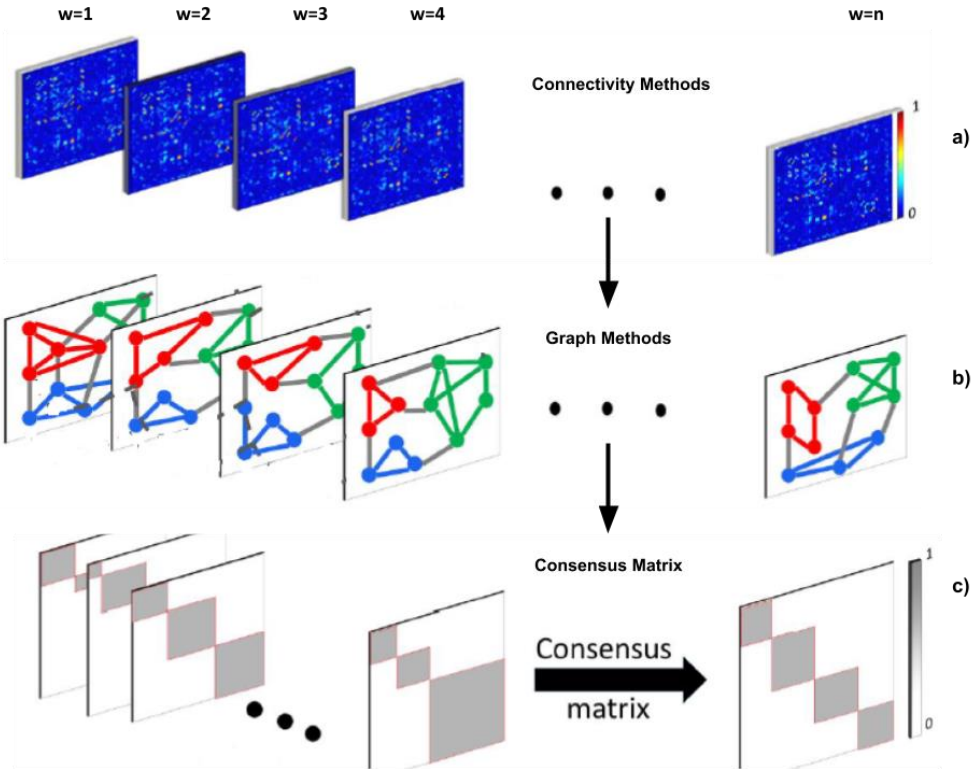

Figure 2.18. Implementing windowing structure. Dividing the signals to n windows. (a) estimating the connectivity matrix for each window. (b) Extract Graph parameters for each window. (c) Apply the consensus matrix on each window

The results of this analysis will be presented in Chapter 4.

- **Selection of features based on simulated signals**

We have used the model developed in our team [12] to simulate EHG signals in two situations:

- Signals with only electrical diffusion (ED) by varying the resistance of the tissues.

- Signals with ED plus Mechanotransduction (EDM), by changing the five parameters that control this phenomenon.

For these two situations, the parameters were varied in a range (plus and minus the default value). These parameters are:

Res: is the resistance of the tissue that controls the electrical diffusion. Its range is [24, 80] Ohms.

Lambda_sig (λ): λ is the slope of the sigmoid that controls the opening of the SSC (stress sensitive channels), its range is [3, 27].

Beta_sig(σ): σ is the SSC sigmoid shift, its range is [1, 10].

SACCH_nbmax(nbCES) : nbCES is the number of SSC per cell, its range is between [20, 200].

Current_Na_etirement(ICES_Na) : ICES_Na is the ion current for the sodium SSC, its range is [0.005, 0.13] uA/cm2.

SACCH_current(ICES_Ca): ICES_Ca is the ion current for the calcium SSC, its range is [0.0007, 0.017] uA/cm2.

In the first situation (ED, short distance synchronization), we will test the effect of changing the resistance (uterine synchronization by electrical diffusion) on the signal connectivity characteristics. Theoretically, when the resistance of the tissue decreases, the synchronization is supposed to increase (easier diffusion).

In the second situation (EDM, constant short and varying long distance synchronization), we will change the value of five parameters to check the effect of these variables on the signal connectivity characteristics. For each of the five parameters, when the parameter value increases, the long-distance synchronization is supposed to increase.

The results of this analysis will be presented in Chapter 5.

We have used the Python 3.8 [152] for the development of machine learning methods and graph methods. We have also used matlab [153] for the connectivity/correlation estimation.

CHAPTER 3: Uterine Synchronization Analysis during Pregnancy and Labor

In the following chapter, we will present the framework developed for the processing of electrohysterographic signals (EHG) recorded during labor and pregnancy. We will first present the measurement the connectivity between EHG real signals using different connectivity methods. Then, by using the graph theory, we will show the extraction of different graph parameters from the obtained connectivity matrices. Finally, we will present the different neural network and machine learning methods on the features obtained from both graph and connectivity methods in order to classify between labor and pregnancy contractions. Moreover, we will also indicate the power of graph parameters extracted from the connectivity matrices to improve the classification results.

3.1. Introduction

In this study, we use real electrohysterographic signals (EHGs) records by using a multichannel system. In our study, we recorded 16 monopolar EHG signals per contraction, recorded with a 4x4 electrode matrix placed on the woman's abdomen.

To analyze the uterine synchronization during pregnancy and Labor, we used various connectivity measures, graph methods, and machine learning methods to distinguish between pregnancy and labor contractions recorded at various terms.

As explained in the preceding chapter, the EHG signals used in this study were recorded from 35 women. In total, 247 pregnancy and 183 labor contractions were identified from these recordings. In order to analyze the EHG connectivity, we used four connectivity methods: The cross-correlation coefficient (R2), the nonlinear correlation (H2), the Filtered Windowed H2 (FW_h2), and the Imaginary part of coherence (ICOH).

The resulting connectivity matrices are then viewed as graphs. By definition, a graph is a mathematical abstract structure made up of vertices (V) or nodes, which correspond to the electrodes in our study, and edges (E) that connect pairs of those vertices, and correspond in our study to the computed connectivity. Then, five graph parameters have been extracted for each correlation/connectivity matrix: Strength (Str), Clustering Coefficient (CC), and Efficiency (Eff), previously used in a recent study, as well as PageRank (PR) and Betweenness Centrality (BC), which were proposed for the first time in this study.

As mentioned before, and to classify between pregnancy and labor, various classification methods have been tested based on either the results of connectivity methods (connectivity alone) or the extracted graph parameters (connectivity + graph parameters), as inputs. For this, we used classical as well as deep learning approaches. By comparing these techniques, we can select the most accurate approach for distinguishing between labor and pregnancy

contractions. In this work, we tested the following methods: Logistic Regression (LR), Naive Bayes (NB), Support Vector Machine (SVM), Multilayer Perceptrons (MLP), Random Forest (RF), Gradient Boosting Machines (GBM), Recurrent Neural Networks (RNN) and Long Short-Term Memory (LSTM).

As a final point, we compared the results obtained by each method with those obtained by the previously employed approach, in the context of EHG correlation analysis, to assess the added value of machine learning and that of graph metrics.

3.2. PREGNANCY VS. LABOR CLASSIFICATION

3.2.1 Graph Measures

In this section, we will evaluate the performance of the two new added graph parameters (Page Rank -PR- and Betweeness Centrality -BC-) on the results of the connectivity methods. We will also present the ROC curves results for each parameter combined with the different connectivity methods used in our study.

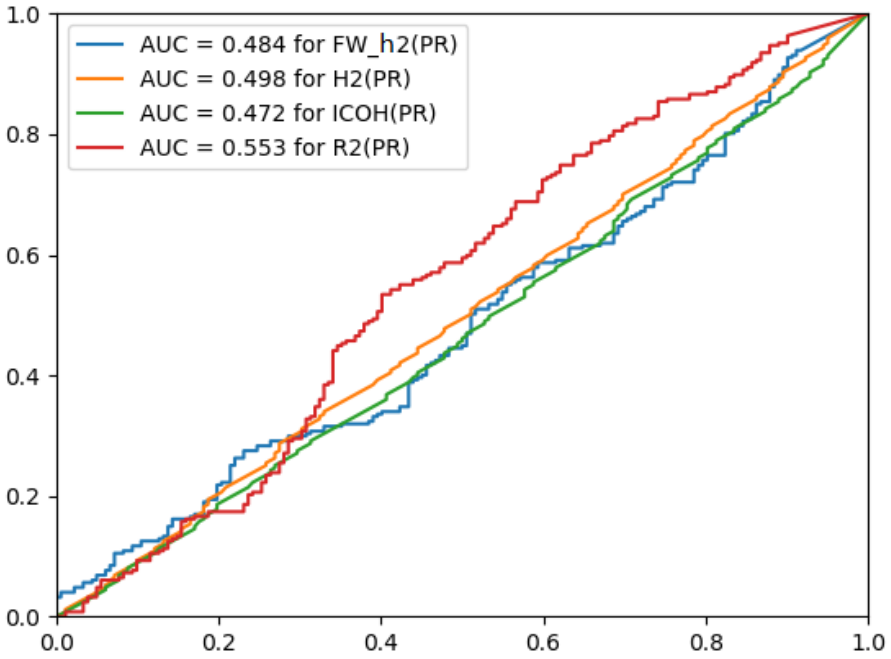

Figure 3.1. ROC Curves for Page Rank (PR) parameter combined with all the connectivity methods. FW_h2(PR), H2(PR), ICOH(PR), R2(PR) represents respectively the results obtained with FW_h2, H2, ICOH and R2 connectivity methods combined with PR parameter.

Figure 3.1, presents the ROC curves obtained for the Page Rank (PR) extracted from the different connectivity matrices. The best result was obtained with R2(PR), which area under the curve (AUC) is 0.553, then for H2(PR) which is 0.498. The AUC value when using FW_h2(PR) indicated 0.484. Lastly, the AUC value when using ICOH(PR) obtained the lowest AUC with 0.472. The AUC remains small for all the PR values, whatever the connectivity method used.

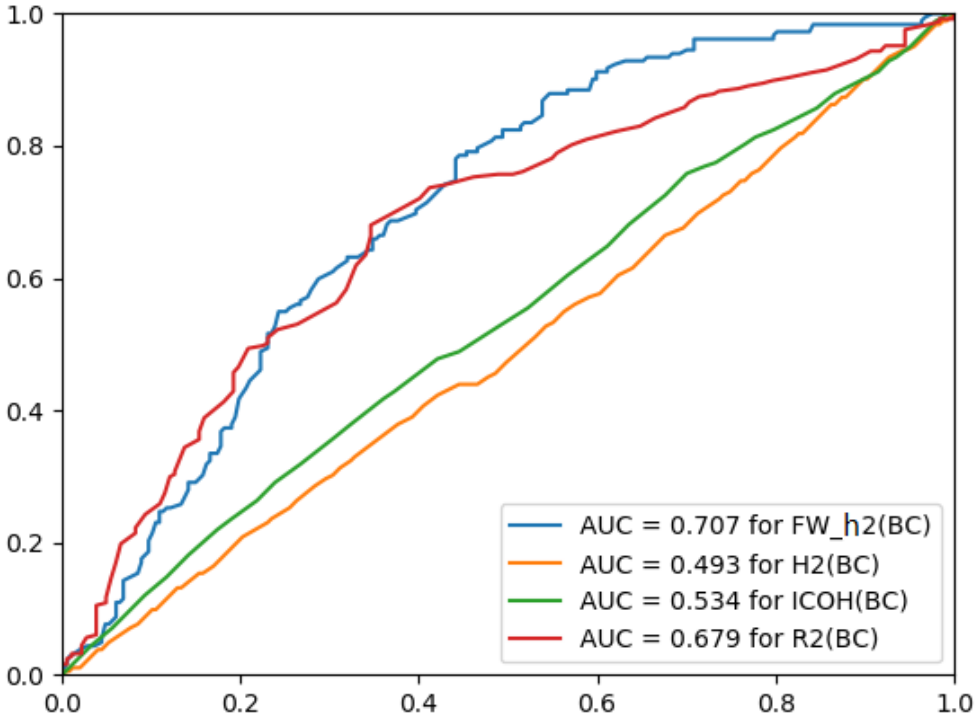

Figure 3.2. ROC Curves for Betweenness Centrality(BC) parameter combined all the connectivity methods. FW_h2(BC), H2(BC), ICOH(BC), R2(BC) represents respectively the results obtained with FW_h2, H2, ICOH and R2 connectivity methods combined with BC para

Figure 3.2 presents the ROC curves obtained when using Betweenness Centrality as a graph parameter applied to the different connectivity matrices.

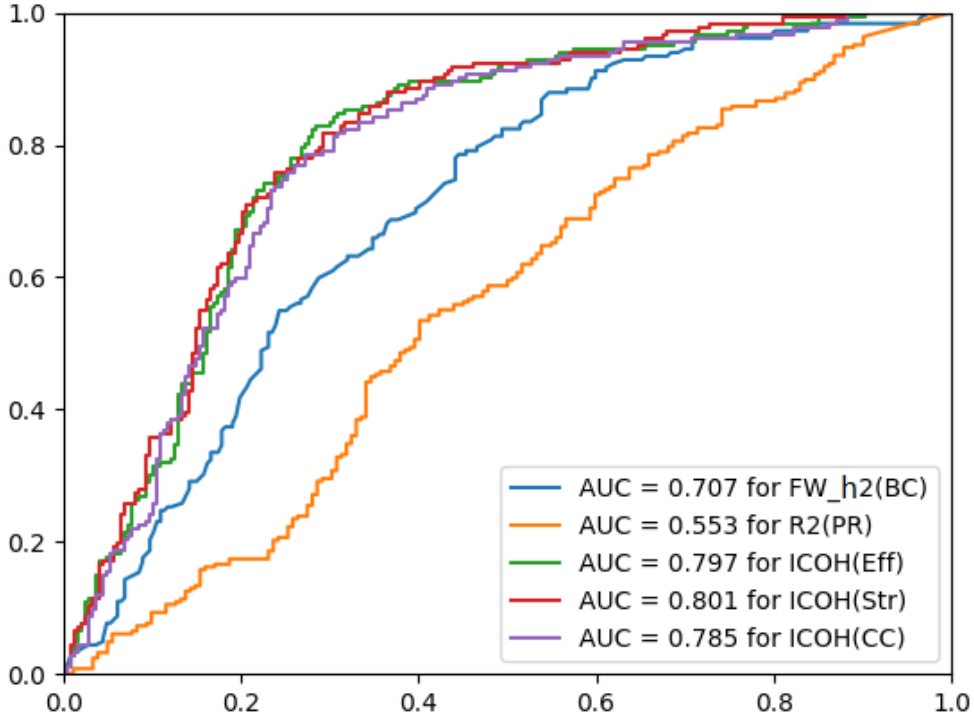

Figure 3.3. ROC Curves for each best result from each graph methods used, FW_h2(BC), R2(PR), ICOH(Eff), ICOH(Str) and ICOH(CC) represents respectively the best results for BC, PR, Eff, Str and CC.

The best result was obtained when using FW_h2(BC) which AUC equals 0.707. Then, the AUC value when using R2(BC) is 0.679, with ICOH(BC) 0.534, and, when using H2(BC), the AUC is 0.493 which is the lowest value.

In order to evaluate the importance of the newly added graph parameters (BC and PR), we have compared the best results obtained in this study with the recent best one [151]. In figure 3.3 we compare FW_h2(BC) and R2(PR) (that represent respectively the best results for BC and PR) with ICOH(Eff), ICOH(Str), and ICOH(CC) (that represent the previously obtained best results for respectively Eff, Str, and CC). The best result obtained with these new proposed graph parameters, obtained by combining the FW_h2 with Betweenness Centrality FW_h2(BC), presents an AUC of 0.707, which is lower than the previously obtained AUC. Nevertheless, as these new graph parameters, BC and PR, behave better with two connectivity measures (R2 and FW_h2) different from the one, ICOH, that performed better with the graph parameters previously studied (Eff, Str, and CC), we decided to keep them in the following step of this study. Indeed, they may bring complementary information concerning the connectivity of the uterine EHG.

We will thus include all the possible combinations of connectivity values, with or without graph parameters as inputs of the machine learning methods to test if some of them permit to improve the classification between pregnancy and labor contractions.

3.2.2 Machine Learning Measures

Concerning the classification between labor and pregnancy, we used four connectivity methods: R2, H2, ICOH, FW_h2. Thus, we have obtained four different connectivity matrices. In this study, we extracted five graph metrics to assess the benefits of graph theory, (Str, CC, Eff, PR, BC) from each matrix. As a result, for each contraction (associated to 16 EHGs), we get 24 parameters that can be used as potential inputs of the classifier: 4 means of the connectivity values over the 16 EHGs- when using the connectivity measures alone + 4x5=20 when using the 5 graph parameters extracted from each of the 4 connectivity matrices.

Feature selection:

For classification purposes, the first step is to evaluate the most important parameters in terms of pregnancy/labor classification. As explained in the preceding chapter, we will use the Fscore method as a feature selection tool.

Figure 3.4 shows the Fscore value of all the 24 possible parameters.

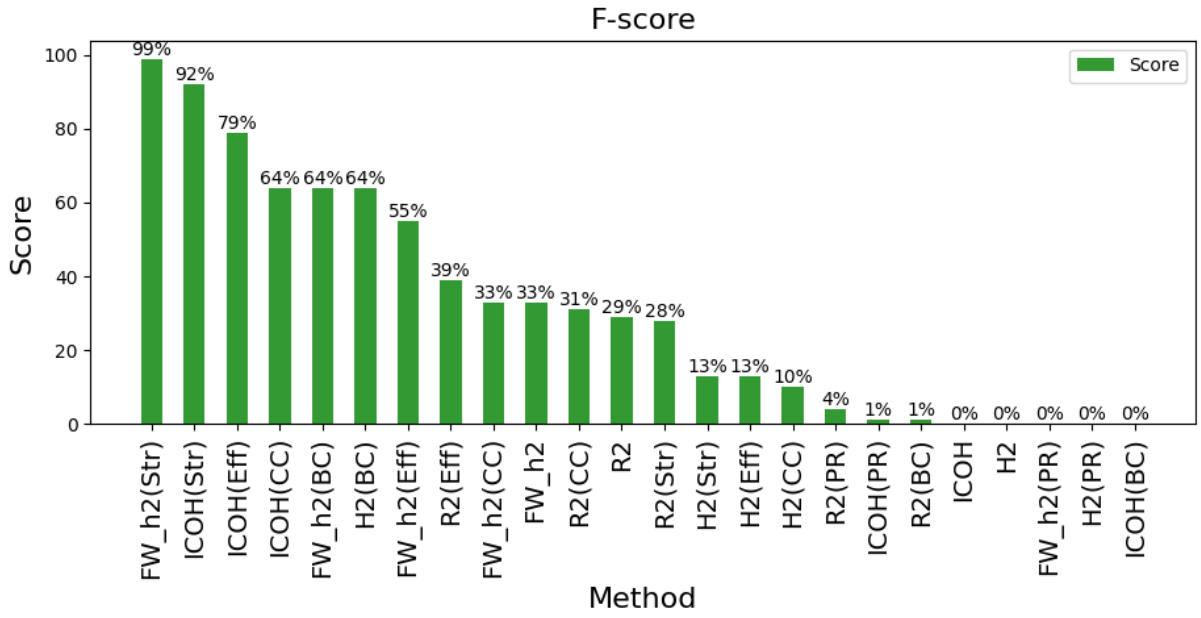

Figure 3.4. Fscore results for each parameter.

Following the use of machine learning methods, we attempted to identify the best number of parameters based on Fscore results. We thus changed the number of parameters used as input of a classifier, starting by 3 parameters (the 3 first best obtained from Fscore), and then adding the following parameters, thanks to the Fscore order (Figure 3.4).

Table 3.1, presents each set of n tested parameters with their corresponding AUC value when using logistic regression for the classification between pregnancy and labor. The best result was obtained when we used the best 9 parameters with AUC value equal to 0.946. We will thus further use in this study only the best 9 parameters ranked by Fscore. These parameters are: FW_h2(Str), ICOH(Str), ICOH(Eff), ICOH(CC), FW_h2(BC), H2(BC), FW_h2(Eff), R2(Eff) and FW_h2(CC). We can evidence with this result that BC seems of importance and that all the

connectivity methods are selected as bringing pertinent information for classification purposes.

Table 3.1: AUC values for Selected n parameters from Fscore

Selected n parameters from Fscore	***AUC Value***
First best 3 parameters	*0.808*
First best 6 parameters	*0.931*
First best 9 parameters	***0.946***
First best 12 parameters	*0.937*
First best 16 parameters	*0.941*
First best 20 parameters	*0.940*
All parameters	*0.933*

Best training/testing sets

In the following step, we tried to choose the best training/testing sets. As to find the optimal data sets for both training and testing phases, we have tested different percentages for partitioning the data in each set. We then estimated the AUC for the logistic regression classification between pregnancy and labor. The specific problem in our study is that, most of the time, an EHG recording is associated with multiple contractions. For the partition between training and testing sets, all the contractions of a given recording are automatically attributed to the same set (either training or testing) to prevent any possible bias in the classification results.

Table 3.2 shows the results obtained with different training/testing data percentages. The best results were obtained when we used 70% for training and 30% for testing, with an AUC equal to 0.94. We thus chose to select this percentage for the following step of the study.

Table 3.2: AUC for different training/Test data sets distribution.

Training data parentage	***Test data parentage***	***AUC Value***
20%	*80%*	*0.80*
30%	*70%*	*0.80*
40%	*60%*	*0.82*
50%	*50%*	*0.86*
60%	*40%*	*0.91*
70%	***30%***	***0.94***
80%	*20%*	*0.70*

Classifier selection :

To compare the performance of machine learning algorithms, we applied several classification methods with the 9 best parameters obtained in this previous step as input and with a 70%/30% partition of the data between training and testing sets. We have chosen to test SVM, Naïve bayes, MLP, Random Forest, GBM, RNN, LSTM and Logistic Regression.

Table 3.3, presents the results of the different neural network and machine learning methods tested. The Logistic regression gives the highest AUC value, equal to 0.946, while Naïve Bayes gives the worst results, with an AUC equal to 0.791. SVM and MLP give similar results (AUC equal to 0.941 and 0.937 respectively) close to the best performance. Random Forest, GBM, and RNN give similar intermediary results.

Table 3.3: Machine learning Classification Results

Classification Method	***AUC Value***	***Specificity***	***Sensitivity***	***Accuracy***
SVM	*0.941*	*0.92*	*0.85*	*0.88*
Naïve Bayes	*0.791*	*0.71*	*0.75*	*0.73*
MLP	*0.937*	*0.94*	*0.81*	*0.86*
Random Forest	*0.894*	*0.84*	*0.78*	*0.80*
GBM	*0.897*	*0.87*	*0.81*	*0.83*
RNN	*0.893*	*0.88*	*0.83*	*0.84*
LSTM	*0.920*	*0.93*	*0.87*	*0.89*
Logistic Regression	***0.946***	***0.95***	***0.87***	***0.90***

Figure 3.5 presents the ROC curves associated to these results.

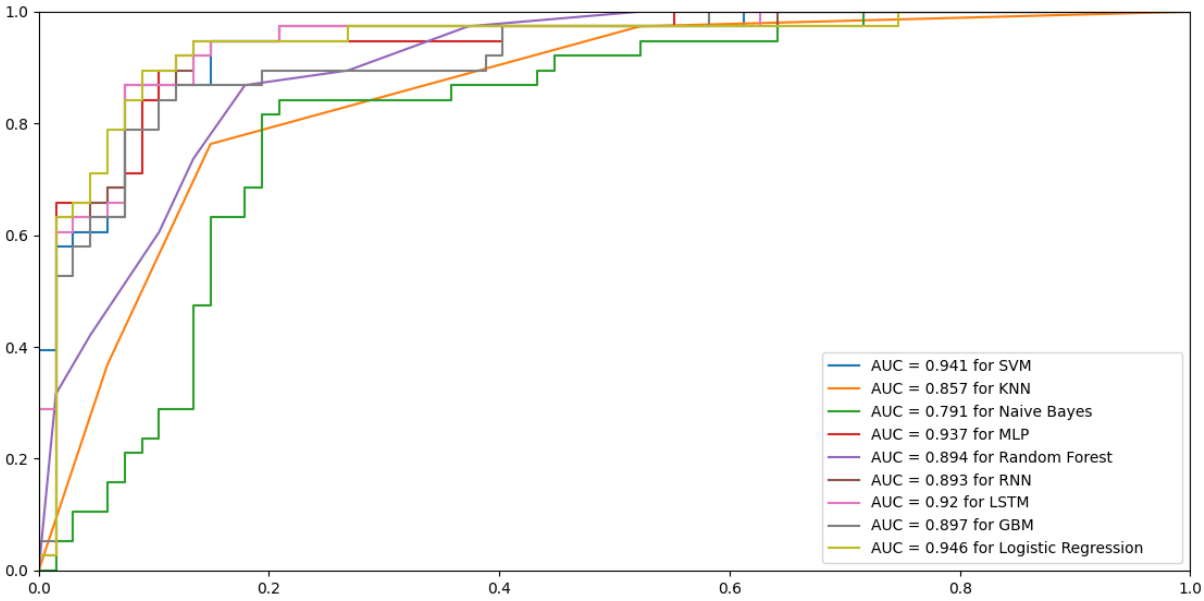

Figure 3.5. Roc Curve of classification methods

The confusion matrix that represents the performance of the logistic regression approach is presented in Figure 3.6. If we are interested in detecting a risk of preterm labor, from a clinical point of view, the positive value is associated with a labor contraction (efficient contraction, that could be associated with a risk of preterm labor if recorded during pregnancy) and the negative value with a normal pregnancy contraction (inefficient contraction). In our results, the true positive value, TP (a Labor contraction is classified as Labor) is 0.87, the true negative value, TN (a Pregnancy contraction is classified as Pregnancy) is 0.95. The false positive value, FP (a Pregnancy contraction is classified as Labor) is only 0.05, and the false negative value, FN (a Labor contraction is classified as Pregnancy) is only 0.13, the assessed specificity is 0.95, whereas the sensitivity is 0.87, and the accuracy is 0.90.

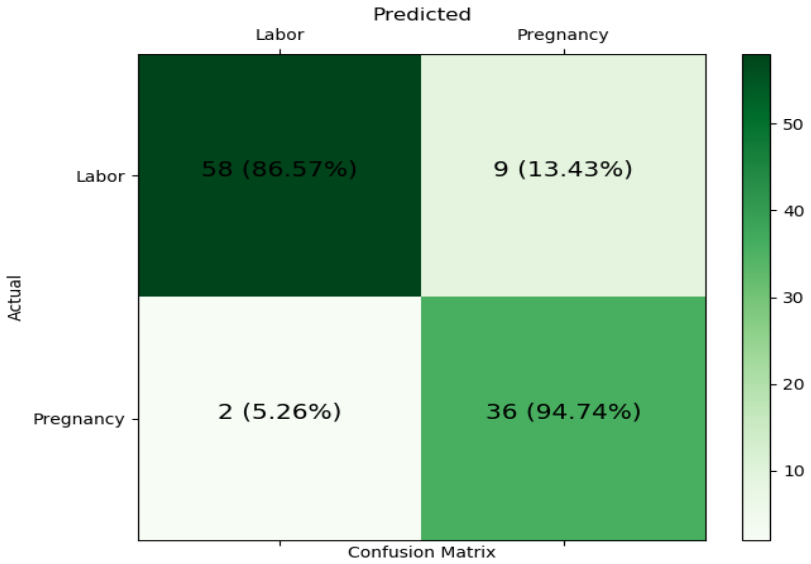

Figure 3.6. Logistic regression confusion matrix

Table 3.4: COMPARISON OF AUC OBTAINED FOR LABOR: PREGNANCY CLASSIFICATION FOR DIFFERENT PARAMETERSALONE AND WHEN USING CLASSIFICATION TOOLS

Method	AUC	*Method*	AUC
ICOH	0.504	*FW_h2 (PR)*	0.484
ICOH (Eff)	0.797	*FW_h2 (BC)*	0.707
ICOH (CC)	0.785	*R2*	0.667
ICOH (Str)	0.801	*R2 (Eff)*	0.676
ICOH (PR)	0.472	*R2 (CC)*	0.665
ICOH (BC)	0.534	*R2 (Str)*	0.665
H2	0.639	*R2 (PR)*	0.553
H2 (Eff)	0.667	*R2 (BC)*	0.679
H2 (CC)	0.651	*SVM*	0.941
H2 (Str)	0.587	*Naïve Bayes*	0.791
H2 (PR)	0.708	*MLP*	0.937
H2 (BC)	0.697	*Random Forest*	0.894
FW_h2	0.658	*GBM*	0.897
FW_h2 (Eff)	0.693	*RNN*	0.893
FW_h2 (CC)	0.661	*LSTM*	0.920
FW_h2 (Str)	0.762	***Logistic Regression***	**0.946**

Table 3.4, summarize all the results obtained when using:

- The mean over the 16 electrodes of the connectivity values alone, for the 4 methods: ICOH, FW_h2, R2, and H2.

- The results obtained with the 5 graph parameters extracted from each connectivity matrix: Eff, CC, Str, PR, BC

- When using the 8 machine learning tools with the 9 best parameters as input: SVM, Naïve Bayes, MLP, Random Forest, GBM, RNN, LSTM, Logistic Regression.

The first thing to notice is that, except for PR, using a graph parameter improves the results of the classification obtained when using the connectivity values alone, whatever the connectivity method used. This enhances the interest in using a graph analysis rather than the mean of the connectivity values to characterize the evolution of uterine synchronization between pregnancy and Labor.

The second point of interest is that machine learning methods showed the best overall performances in classification between labor and pregnancy from the results obtained. The AUC values were always higher, when using machine learning algorithms (including neural network and deep learning), than when using a single connectivity (or connectivity + graph parameter) value. Thus, this observation confirms the interest in this new analysis approach based on machine learning combined with graph parameters extracted from the connectivity matrix. The best result obtained when using logistic regression is AUC=0.946, which is higher than the latest results obtained in [151], where the best AUC value recorded was 0.801 when they used the imaginary part of coherence combined with Strength graph parameter (ICOH(Str)). Nevertheless, ICOH associated with Strength remains the best parameter when used alone in our analysis.

The third point of interest is that the best 9 parameters when we used the AUC value of each parameter are: Icoh(Str), Icoh(Eff), Icoh(CC), FW_h2(Str),H2(PR), FW_h2(BC), H2(BC), FW_h2(Eff) and R2(BC), we noticed that 7 of these 9 parameters are common with the best 9 parameters from Fscore, we can evidence with this result that Fscore seems of importance as a feature selection tool.

3.3 DISCUSSION AND CONCLUSION

In this chapter, we have displayed the results of a new approach aiming at identifying the evolution of the connectivity of uterine electrical activity between pregnancy and labor, at the electrode (surface abdomen) level.

In previous studies, the EHG connectivity matrices were commonly converted to a single value per contraction by generally averaging the connectivity values over the whole electrode set [73]. As a result, valuable information was undoubtedly lost. To try to improve the process and avoid such problems while quantifying the whole connectivity matrix, a recent approach [11] applied for the first time an analysis based on the graph theory to uterine EHG. This study examined the capability of the graph parameters to evidence the evolution of uterine connectivity from pregnancy to labor, and also to distinguish between the contractions recorded during pregnancy and labor. Although the results provided by this recent study were promising, unfortunately, it only used one classification tool [11], which was by all means insufficient.

In this chapter, various machine learning methods were tested for the purpose of classifying between labor and pregnancy contractions. We studied the performance of diverse classification methods based on machine learning algorithms, some are classical (neural network, SVM, Random forest…), while others are based on a deep learning approach (RNN, LSTM). In addition to that, we proposed to use new graph parameters (PR, BC).

In a first step, Fscore permitted the selection of the 9 most effective features for classification. We can notice that all of them are features extracted by means of the graph analysis. These

first results provide a confirmation that the graph theory approach demonstrates its better ability to illustrate the synchronized development of the uterine muscle between pregnancy and labor. Therefore, this approach proved to be better than the only connectivity approach when used alone. We can conclude that when the Fscore is used as a feature selection tool, using the 9 best selected parameters, rather than 24 original ones, gives better results for the classification.

Then, we were able to evidence that the new proposed approach improves the classification performance when compared to the previous studies [11]. So, the results showed when the Logistic regression method was applied (AUC=0.95) were significantly higher than the results previously obtained (AUC=0.801) [154]. These results prove that using a combination of different parameters (9 in our case) is better than using only one parameter [11].

Moreover, regarding the classification tools tested here, the AUC obtained for logistic regression (LR AUC=0.946) was higher than the ones obtained when using deep learning methods (RNN AUC=0,893, LSTM AUC = 0,920). This could be explained by the fact that LR showed better performance on a small amount of data (in this work 430 contractions were studied), whereas deep learning is known to be more efficient and to show better performance on a big amount of data [155].

We have verified in this study the effectiveness of the new proposed approach (connectivity + graph parameter + machine learning) for the purpose of distinguishing between labor and pregnancy contractions. Hence, we hope that this novel technique will have a significant clinical impact in detecting preterm birth that is triggered by preterm labor.

Undeniably, preterm labor is caused by effective contractions that occur too early in the pregnancy (before 37 weeks of gestation). As a result, any processing or classification tool that permits the characterization of the contraction efficiency by processing EHG signals could be a valuable tool in the early detection of the preterm labor risk, and thus reduce hazardous consequences for the baby.

Despite this, a classification rate of 0.95 for specificity and 0.87 for sensitivity between labor and nonlabor groups is still regarded as clinically unsatisfactory. Some improvement can be done in the processing of surface EHG: selection of the best electrode(s) to represent the connectivity, windowing approach to consider the non-stationarity of the signals as well as the temporal evolution of the connectivity, due to the possible appearance of the mechano-transduction process. Therefore, chapter 4 will present the results of the studies done in both directions: electrode selection, windowing approach.

A better comprehension of the mechanotransduction process and of its influence on EHG characteristics should also permit an improvement of these results. Chapter 5 will present the results obtained by using, for the first time, a multi-physic multi-scale model of the uterine activity, to select the features that would permit to evidence at best the electrical diffusion and the mechanotransduction process.

CHAPTER 4: Windowing Approach and Electrode Selection

Throughout this chapter, we will examine on the real EHG signals the potential of using a windowing approach to better extract the EHG characteristics concerning uterine synchronization. We expect this approach to better consider the non-stationarity of the signals as well as the temporal evolution of the connectivity related to the possible appearance of the mechano-transduction process. In order to do that, we will part each EHG burst into windows and study the ones that produce the best results. We will also test, by using the consensus matrix, which one(s) among the 16 electrodes permit to obtain the best results for this classification.

4.1. Introduction

In order to analyze the synchronization of the uterine throughout pregnancy and labor, we applied the windowing approach by dividing each EHG burst (representing a contraction) into n windows (Figure 4.1a). Then, on each window, we estimated the connectivity methods. The results obtained from the connectivity matrix were then represented as graphs, where the nodes are the electrodes, and the connectivity values the edges (Figure 4.1b). So, these graphs are associated to different times along the duration of each EHG burst. Then, the graph theory method is applied to the respective windows for each time to extract from these graphs the features defined previously. At last, several neural network and machine learning methods are used to categorize pregnancy and labor. To do so, the machine learning algorithms are fed with all the features extracted from the connectivity matrix with or without the graph analysis.

The final output of this process is the consensus matrix. A Consensus matrix, which is also referred to as 'co-classification matrix' [156], is a technique for detecting communities in vast networks. It contains values that indicate each node ratio by determining how much more tightly connected they are with the other nodes within a real network (in our case a EHG burst), when compared with how connected they might be in a random network. After that, the process combines communities repeatedly into a single node and performs modularity clustering on the condensed graphs by using the Louvain algorithm [157].We thus obtained the nodes that are most important in the network. Finally, we generated a final consensus matrix (using the same approach as before) by calculating the ratio of each node to the other nodes in the same module across all time frames.

In this study, we used only three connectivity methods: linear correlation coefficient (R2), nonlinear correlation (H2), and Imaginary part of coherence (ICOH). Indeed, as stated in its name, Filtered-windowed_h2, FW_h2 is not applicable with the proposed windowing approach as this method already uses a windowing approach. So, it is worthless to apply the

windowing twice. On the matrices obtained with these 3 connectivity methods, we extracted the different graph parameters: Strength (Str), Clustering Coefficient (CC), Efficiency (Eff), PageRank (PR), and Betweenness Centrality (BC). To select the best approach for classifying labor and pregnancy, we used only the best classification methods selected in the previous chapter: Logistic Regression and Multilayer Perceptrons (MLP) respectively.

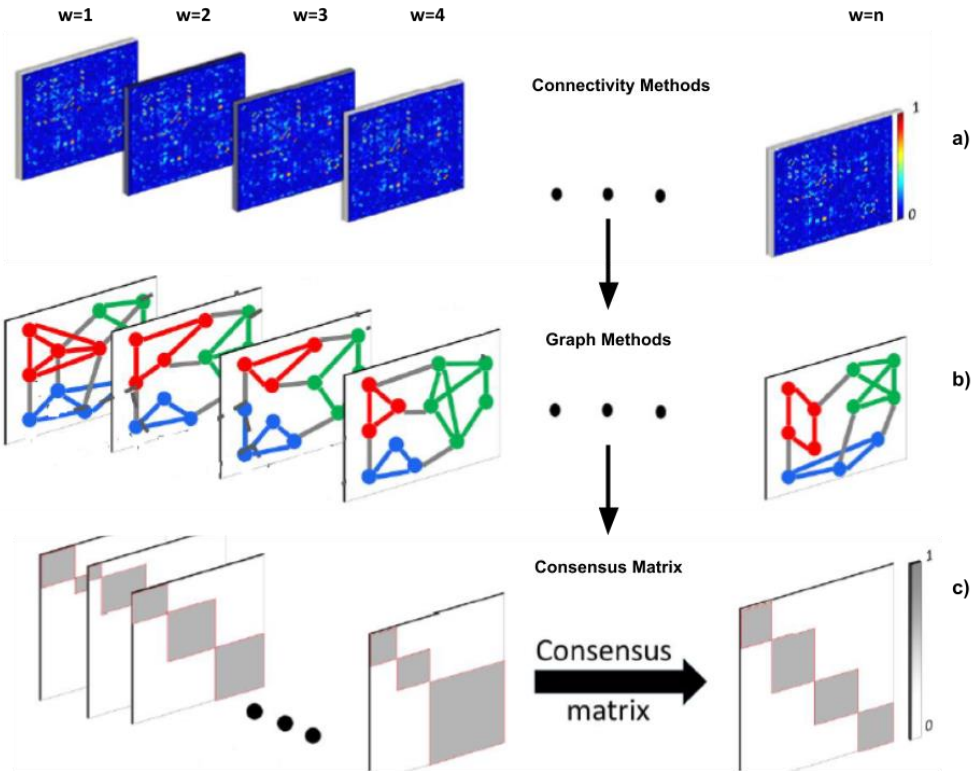

Figure 4.1. Implemented approach: Division of the signals into n windows, (a) estimation of the connectivity matrix for each window. (b) Extraction of the Graph parameters for each window. (c) Computation of the consensus matrix on each window

4.2. Pregnancy vs. Labor classification using a windowing approach

4.2.1 Signals length

The used EHG signals, collected by using monopolar electrodes in a 4x4 matrix (which is placed on the abdomen of the mother), record bursts of activity related to contractions during pregnancy and labor. The first problem we had to tackle is the fact that, due to the various situations encountered during the recordings, the duration of the EHG bursts can be very different from one contraction to another (range: 60s - 578s).

When using a windowing approach, we have to determine the window duration and the number of windows used to represent each EHG burst. If we want to compare the results obtained for all the contractions, we have to find a common way to study them: same length

and same number of windows. Therefore, in our study, all signals should have the same fixed length.

To determine a fixed length of analysis for all the signals, we tested different signal lengths and chose a duration of 60 seconds (12000 points), to represent each burst related to one contraction. To select the position of this 60 seconds length along each burst, we used the power method [158]. To do so, we identified the maximum of each EHG power to locate the interesting part of the signal. We then took 30 seconds before and 30 seconds after this maximum power to select the 60 seconds of interest used for the windowing approach.

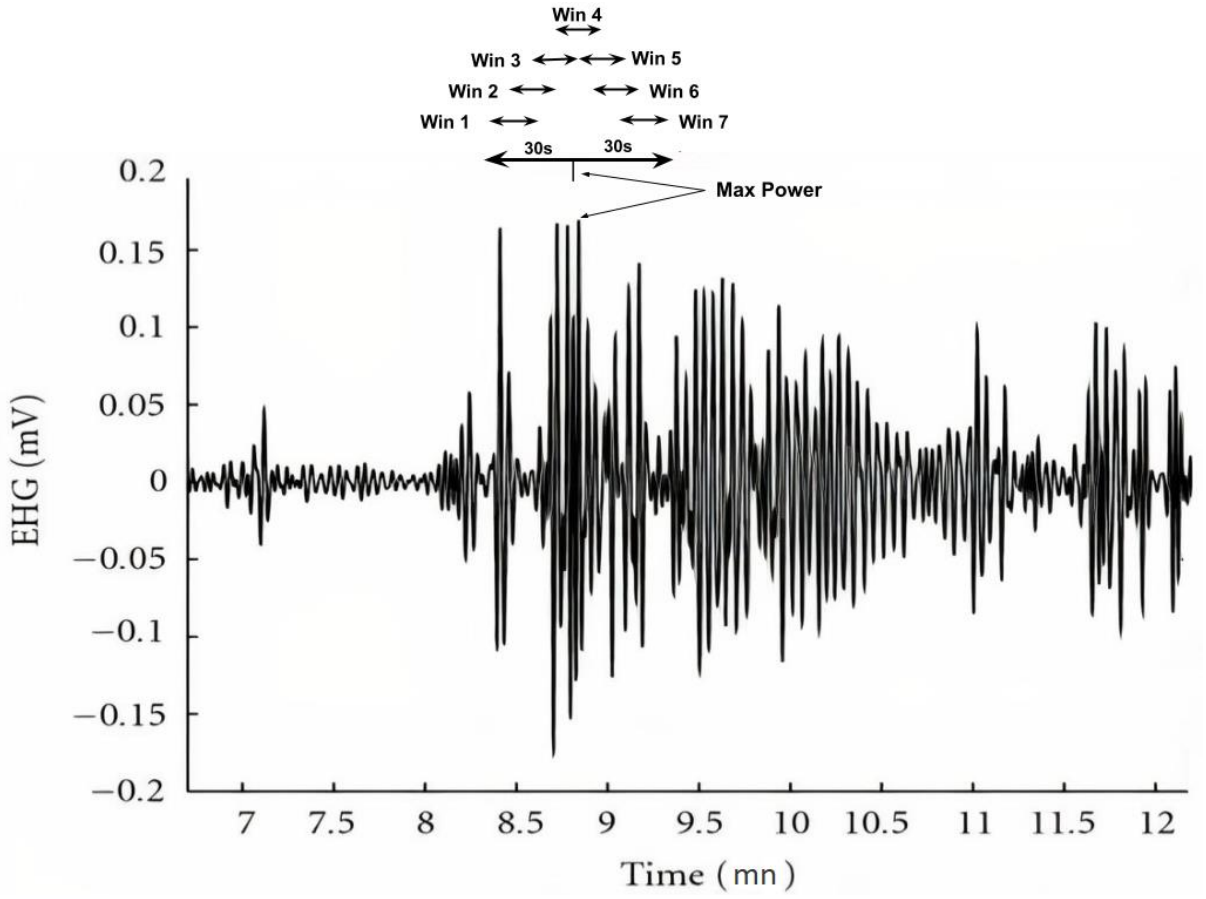

Figure 4.2. Example of the EHG signal with the place of the max power energy and the place of each window [159].

In figure 4.2, we can see the location of the signal maximum power. Then, we took 6000 points (30 sec) before and after the max power of the signal. The resultant signal length is then 12000 points (60 seconds).

Hence, this pre-processing permitted us to get all signals of the same length in order to split them with the same number of windows all of the same length.

4.2.2 Sliding windows

For the window length, we chose a duration of 3000 points (15 seconds) recommended by [160], which was recently used to estimate instantaneous phase difference of instantaneous

amplitude correlation, and we also chose 50% overlapping windows. Thus, as each signal contains 12000 points, we obtain 7 windows for each EHG signal (figure 4.2).

4.2.3 Windowing results

Step 1: Connectivity analysis

As explained before, all the processed EHG signals have the same length and are divided into 7 windows. So, the connectivity methods, graph methods, and consensus matrix are estimated for each window. Finally, each method windows will give a consensus matrix.

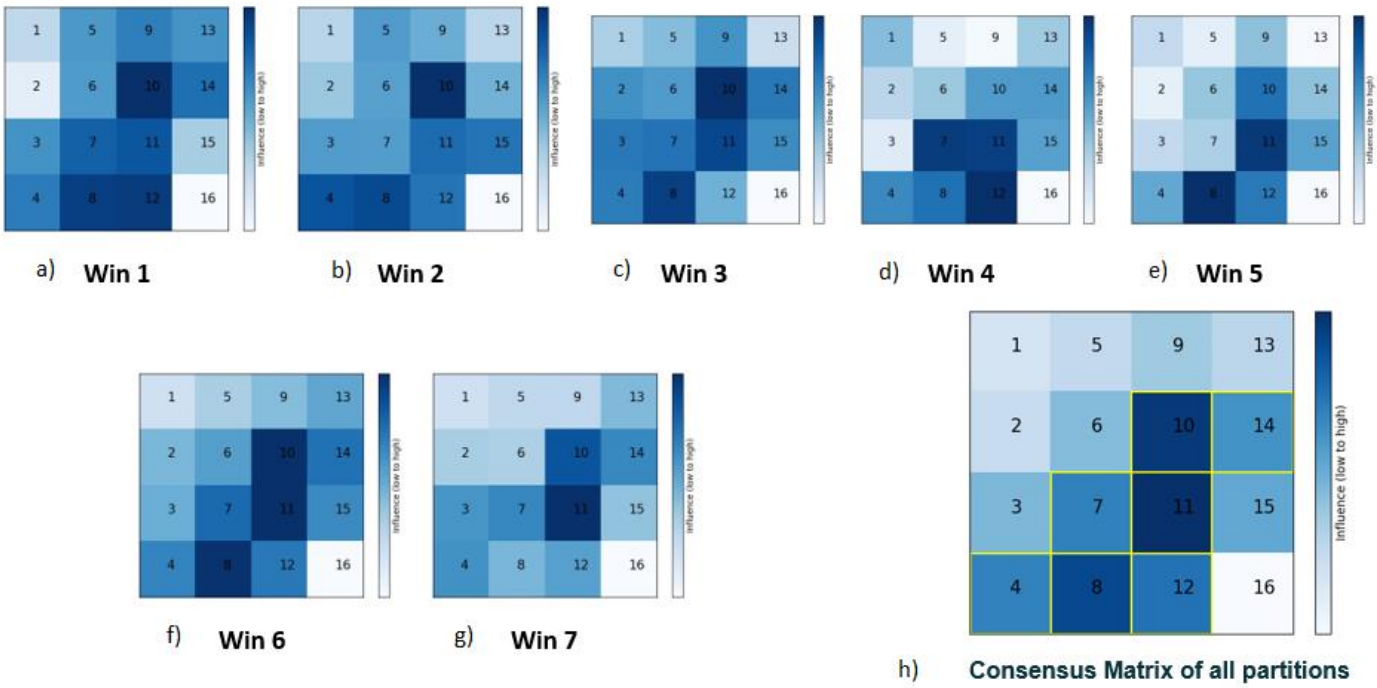

Figure 4.3. Consensus matrices of each window using R2(BC): from a) to g) results of each window respectively from window 1 to window 7, h) mean consensus matrix over all windows

Figure 4.3 presents an example of the results, by using R2(BC), of the consensus matrices for the 7 windows (Figure 4.3(a)-4.3(g) respectively) and of the mean consensus matrix over all the windows (Figure 4.3(h)). In this final consensus matrix, we drew a yellow box around the most significant nodes that are: 4, 7, 8, 10, 11, 12, and 14. The results of the consensus matrices for all the methods and parameters are presented in [Annex A].

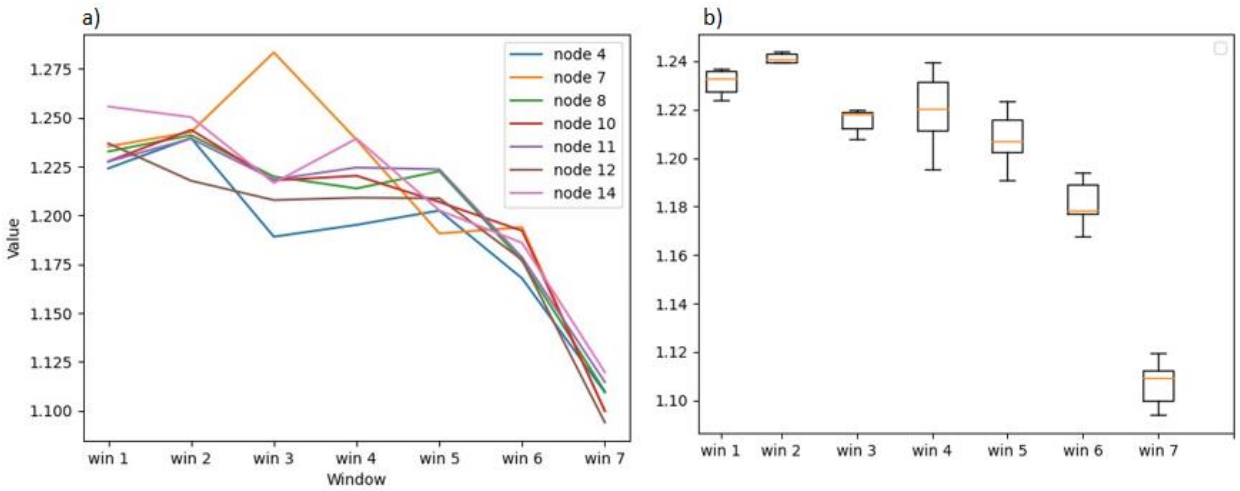

Figure 4.4. Analyses of each window for the methods R2(BC), a) values of the most important nodes (4,7,8,10,11,12, 14) in each window, b) boxplot for the most important nodes in each window

Following this step, we have estimated the R2(BC) values for the most significant nodes. Figure 4.4(a) represents the values of the most important nodes for each window. We can notice that the highest R2(BC) values for most of these nodes are located in window 2, except for node 7 which has the highest value in window 3. Figure 4.4(b) represents the boxplot of the most significant nodes for each window. We can observe that window 2 gives the best results.

The results for the best window(s) for all methods and parameters are presented in table 4.1. All the results will be presented in [Annex A].

Table 4.1: Best window(s) for each method

Method	***Best Window(s)***	***Method***	***Best Window(s)***
R2	*Window 6*	*H2(PR)*	*Window 4*
R2(Str)	*Window 4 and Window 5*	*H2(BC)*	*Window 7*
R2(Eff)	*No noticeable best window*	*H2(CC)*	*Window 2 and Window 5*
R2(PR)	*Window 4 and Window 5*	*ICOH*	*Window 7*
R2(BC)	*Window 3 and Window 4*	*ICOH(Eff)*	*Window 4*
R2(CC)	*Window 2 and window 7*	*ICOH(Str)*	*Window 5 and Window 7*
H2	*Window 5*	*ICOH(PR)*	*Window 2 and Window 6*
H2(Str)	*Window 7*	*ICOH(BC)*	*Window 2 and Window 5*
H2(Eff)	*Window 4*	*ICOH(CC)*	*Window 2 and Window 4*

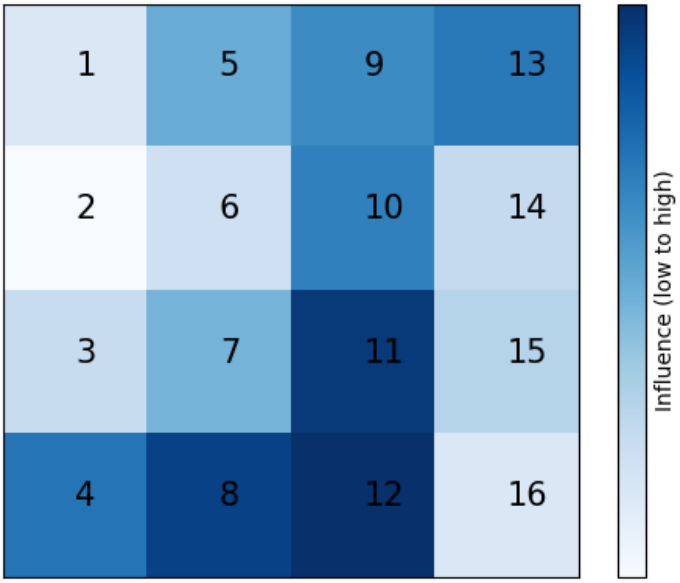

Figure 4.5: Average consensus matrix of all windows and all methods

Finally, we have estimated the average consensus matrix of all methods in an attempt to evidence the best nodes, windows, and parameters from all the methods in the classification between labor and pregnancy (results presented in [Annex A]). The best nodes, as shown in figure 4.5, are 8, 9, 10, 11, and 12. The nodes 9-12 correspond to the median vertical axis of the mother's abdomen and have already been evidenced as the best electrode location to record EHG [161]. The best results were located in window 4 (selected 7 times), which each located right in the middle of the studied window (justifying thus the choice of the maximum of power to select the signal to process), followed by window 5 (selected 6 times) and 2 (selected 5 times) as shown in table 4.1.

Furthermore, we will use for the classification, only the available parameters (without FW_h2 parameters) from the best 9 parameters ranked by Fscore (see Chapter 3). These 5 available parameters are: ICOH(Str), ICOH(Eff), ICOH(CC), H2(BC), and R2(Eff).

Step 2: Pregnancy/labor classification

For this classification step, we applied the artificial intelligence methods to the best results obtained in the previous steps. Thus, we used here the best windows (2, 4, and 5), the best nodes (8, 9, 10, 11, and 12), and the best parameters (ICOH(Str), ICOH(Eff), ICOH(CC), H2(BC), R2(Eff)) previously selected. We also used Logistic regression and MLP as classification methods, as they presented the best results in chapter 3. Then, we compared the results obtained by using the windowing to those obtained when using all the 7 windows together and then the whole signal, for each EHG burst. We also compared the results obtained when using the best nodes to the results obtained when using all nodes. The results are presented in table 4.2.

Table 4.2: Results of different methods, windows and nodes

Method	***Window***	***Nodes***	***AUC Value***
Logistic Regression	*Window* 2	*Best nodes*	*0.*825
MLP	*Window* 2	*Best nodes*	*0.*797
Logistic Regression	*Window* 2	*All nodes*	*0.*836
MLP	*Window* 2	*All nodes*	*0.*841
Logistic Regression	*Window* 4	*Best nodes*	*0.*865
MLP	*Window* 4	*Best nodes*	*0.*797
Logistic Regression	*Window* 4	*All nodes*	*0.*838
MLP	*Window* 4	*All nodes*	*0.*841
Logistic Regression	*Window 5*	*Best nodes*	*0.*821
MLP	*Window 5*	*Best nodes*	*0.771*
Logistic Regression	*Window 5*	*All nodes*	*0.*792
MLP	*Window 5*	*All nodes*	*0.821*
Logistic Regression	*All Windows*	*Best nodes*	*0.*911
MLP	*All Windows*	*Best nodes*	*0.896*
Logistic Regression	*All Windows*	*All nodes*	*0.*902
MLP	*All Windows*	*All nodes*	*0.*883
Logistic Regression	***Whole signal***	***Best nodes***	***0.918***
MLP	*Whole signal*	*Best nodes*	*0.903*
Logistic Regression	*Whole signal*	*All nodes*	*0.914*
MLP	*Whole signal*	*All nodes*	*0.897*

As shown in table 4.2, the best results were obtained when using the whole signals and the best nodes. Then, the next best result is obtained when we used all windows combined together, which gave better result that when using only one window. Thus, when we used only one window, window 4 recorded better result than window 2 and window 5. As presented in figure 4.6, the best result obtained when taking the features from the whole signals and the best nodes gave an AUC= 0.918. These results are close but smaller than the previously obtained results in Chapter 3, which gave an AUC= 0.946 while applying also the FW_h2 parameters.

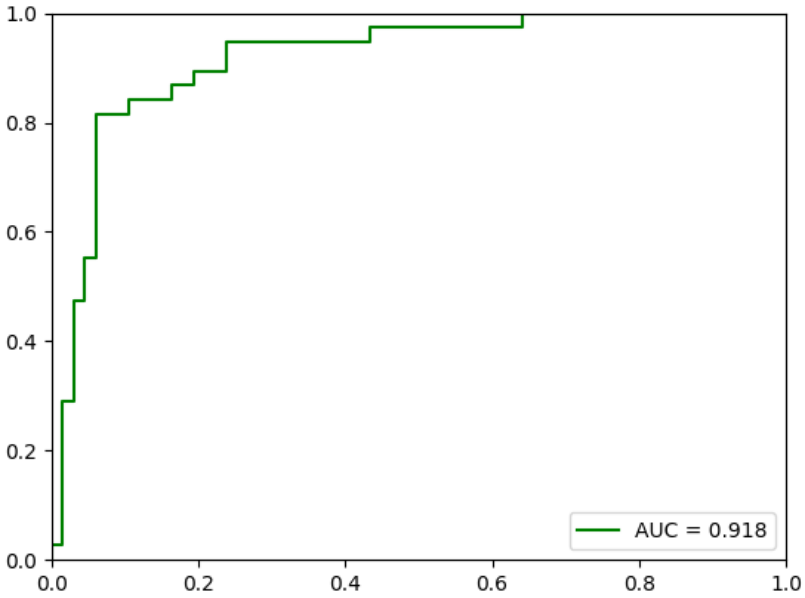

Figure 4.6. Whole signals - best nodes - Logistic Regression (AUC: 0.918)

Therefore, we can conclude that the results are better when we chose the best nodes instead of choosing all the nodes together. However, the windowing approach did not improve the classification between labor and pregnancy.

Concerning the window size, the AUC seems to increase when we increase the signal duration. This is confirmed by the results presented Table 4.3, were we computed, from the best nodes, the features either from their specific best window(s) (line 1) or from the concatenation of the windows of interest for most of the features (W2, W4 and W5 concatenated (line 2). The minimum value of AUC obtained (AUC=0.865), when using Logistic regression, is equal or higher than when using only one window (AUC=0.821-0.865). The maximum value (AUC=0.881) is smaller than when using all the windows (W1 to W7, AUC=0.902) or the whole signal (AUC=0.918).

Table 4.2: Results of different windows size, with best nodes and Logistic regression

Condition	Window choice	AUC Value
Specific window(s)	ICOH(Str): window 5 and window 7 concatenated ICOH (Eff): window 4 ICOH(CC): window 2 and window 4 concatenated H2(BC): window 7	0.865
Best windows concatenated	Window 2, window 4 and window 5 concatenated	0.881

4.3 DISCUSSION AND CONCLUSION

In this chapter, we defined a new approach in order to identify the connectivity from the EHG signals, considering the non-stationarity of the signals as well as the possible temporal evolution of the connectivity.

First, the EHG signals were resized to 12000 points (60 seconds), centered on the most powerful part of the EHG burst, in order to process all the signals with the same length. After that, the selected parts of the signals were divided into 7 windows to examine the windowing effect on the classification, and also to see which window provides the best results.

For the classification between pregnancy and labor, based on features extracted from the connectivity methods (ICOH, R2, and H2) with or without graph parameters (Str, CC, Eff, PR, and BC), we used the two best methods chosen from the preceding chapter (Logistic regression and MLP).

We noticed that whatever the windows used, selecting only the best nodes provides better results than using all the nodes.

At the opposite, concerning the windowing part, the recorded AUC of the logistic regression on the whole signals and the best nodes (AUC=0.918) was slightly higher than the all windows together and higher than the selection of only one window, (best result with all windows and best nodes is AUC=0.911, while the best result with only one window and best nodes, which is window 4, is AUC=0. 865).

We can conclude from the acquired results that the AUC values increase when we select the best nodes rather than all 16 nodes, and also increase when the signal size increases too. For that reason, the results are better when we use the whole contraction bursts (using all the signal length for each EHG burst rather than the selected 60 s).

Nevertheless, when we compare the different execution times between the two scenarios, the execution time decreased when the number of nodes and the signal length decreased. Therefore, the main question is whether we can lose information (about 0.3%) but win in execution time.

Finally, and to conclude this study, the windowing approach can successfully be used to minimize the time of execution to classify between pregnancy and labor, while also losing some precision in the classification. This approach could further be of great help in detecting preterm labor early on by enabling us a fast characterization of the uterine contraction and risk detection all along pregnancy.

CHAPTER 5: Simulated EHG Signals Analyses

In this chapter, we deliver a new framework using simulated signals for determining the features sensitive to the uterine connectivity. We have simulated EHG signals in different groups in order to identify which connectivity method(s) and graph parameter(s) will permit us to better represent the evolution of the two physiological phenomena driving the uterine synchronization: short-distance propagation (by means of electrical diffusion) and long-distance synchronization (by means of mechanotransduction). For the EHGs simulation, we have used the uterine model developed by our team [12] and by focusing first on the electrical diffusion alone, then by studying electrical diffusion plus Mechanotransduction process.

5.1. Introduction

The simulation module developed by our team [1] can simulate EHG signals measured on the mother's abdomen. We used the simulated EHGs to investigate the impact of the different parameters of the model involved in uterus synchronization on the EHG features.

As the model simulates the EHG signals measured on the abdomen of the pregnant woman, in our case, we will model a matrix of 16 (4x4) surface electrodes, similar to the one used to record real data, to generate our simulated EHGs.

For real signals analysis, two experimental measurement techniques are often used: the monopolar approach [162] and the bipolar approach [72]. For the monopolar approach, the EHG signal from each single electrode is considered, whereas, in the bipolar approach, the difference between the signals acquired by two nearby electrodes is considered. This latter approach improves the signal-to-noise ratio by removing the common-mode noise, but it can generate a bias in signal correlation studies. However, since our signals are simulated, they are far less noisy than real experimental signals. Therefore, the bipolar approach is not essential. Thus, to study the features, we only evaluated the monopolar signals [82]. As a result, we got 16 EHG signals for each simulation (length of several tens of seconds).

In order to analyze the effect of electrical and mechanotransduction model parameters on the synchronization of the uterus, we simulated the signals in two classes. First, signals simulated with the electrical diffusion alone (ED, group 1) by adjusting the tissue resistance; then, signals simulated with ED and Mechanotransduction (EDM, group 2) by keeping the tissue resistance constant and varying the different model parameters that influence the mechanotransduction. We could not study the mechanotransduction alone, as a certain level of electrical diffusion is needed to induce the uterine tissue stretching, and thus the mechanotransduction process. We plan by this study, to identify the best features (connectivity alone, connectivity + graph analysis) that will permit to follow the changes in the EHG characteristics induced when changing the model parameters [82].

Figure 5.1 presents an example of the signals from group 1 (electrical diffusion alone, ED), while Figures 5.2, 5.3, 5.4, 5.5, and 5.6 present signal samples from group 2 (EDM) with values for Beta_sig, Current_Na_etirement, Lambda_sig, SACCH_nbmax, and SACCH_current parameters respectively, different from the standard values.

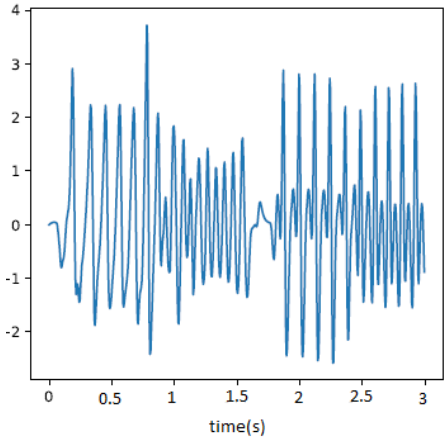

Figure 5.1. Sample signal of group 1 when changing the resistance parameter

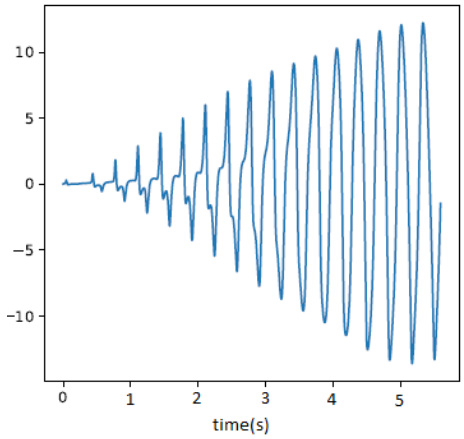

Figure 5.2. Sample signal of group 2 when changing the Beta_sig parameter

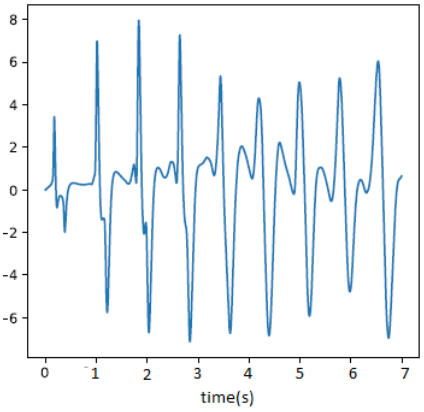

Figure 5.4. Sample signal of group 2 when changing the Current_Na_etirement parameter

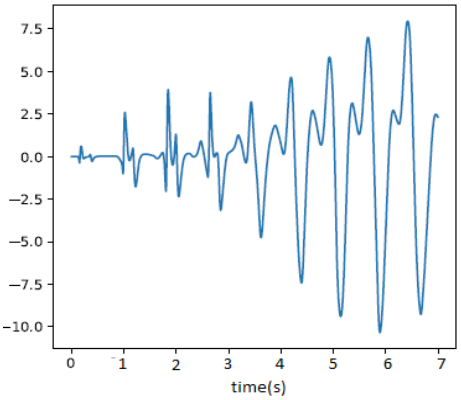

Figure 5.3. Sample signal of group 2 when changing the Lambda_sig parameter

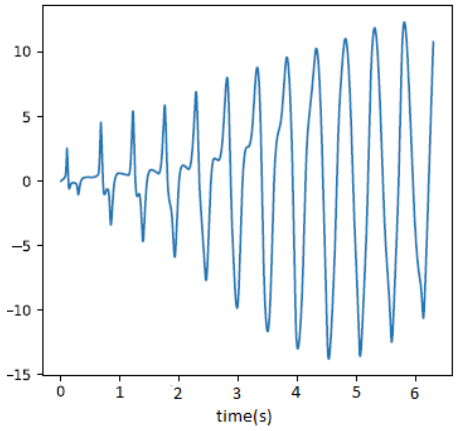

Figure 5.5. Sample signal of group 2 when changing the SACCH_nbmax parameter

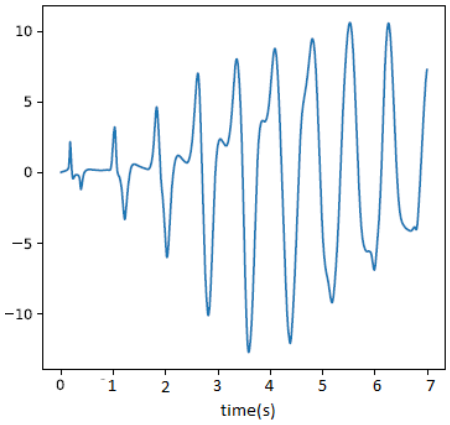

Figure 5.6. Samp le signal of group 2 when changing the SACCH_current parameter

5.2. ED and EDM study

As mentioned before, the simulated signals were divided into two groups: ED and EDM. For each class, we studied the effect of the different model parameters on the EHG features used for the connectivity analysis. Thus, we first had to define the model parameters and the range of values tested. Then, we had to adapt to the simulated EHGs characteristics, the features defined on the real EHGs.

5.2.1. Model parameters

For the first group (ED), there is only one model parameter that controls the uterine synchronization via electrical diffusion, which is the resistance of the tissues. Theoretically, when the tissue resistance decreases, the synchronization should increase (thanks to an easier diffusion) [82]. Hence, as the model default resistance value is 40 Ω, we used a range of values around this default value to test the effect of varying this parameter. The tested values are: 24 Ω, 28 Ω, 32 Ω, 36 Ω, 40 Ω, 44 Ω, 48 Ω, 52 Ω, 56 Ω, 60 Ω, 64 Ω, 68 Ω, 72 Ω, 76 Ω, and 80 Ω.

For the second group (EDM, i.e. with long distance synchronization), five parameters control the mechanotransduction process, as defined in Chapter 2. Table 5.1 presents the values used to test their effect on the EHG characteristics, for each one of these parameters.

Table 5.1: EDM Parameters

	Definition	Selected values
Lambda_sig (λ)	λ is the sigmoid slope that governs the SSC's opening (stress sensitive channels)	3, 6, 9, 12, 15, 18, 21, 24, and 27
Beta_sig(σ)	σ is the SSC sigmoid shift	1, 2, 3, 4, 5, 6, 7, 8, 9, and 10
SACCH_nbmax(nbCES)	nbCES is the number of SSC per cell	20, 40, 60, 80, 100, 120, 140, 160, 180, and 200
Current_Na_etirement(ICES_Na)	ICES_Na is the ionic current for the sodium SSC (μA/cm2)	0.005, 0.007, 0.009, 0.01, 0.03, 0.05, 0.07, 0.09, 0.11, and 0.13
SACCH_current(ICES_Ca)	ICES_Ca is the ionic current for the calcium SSC (μA/cm2)	0.0007, 0.0009, 0.002, 0.004, 0.006, 0.008, 0.01, 0.013, 0.015, and 0.017

For all of the parameters controlling the mechanotransduction process, we expect the synchronization to increase when the parameter value increases [82].

We run 50 simulations for each selected situation (choice of model parameters). We also tested if the differences between the feature values obtained with different model parameter values are significant or not, by means of the Student test.

5.2.2. Frequency filter of FW_h2 method analyses

The features that were used to characterize the connectivity of simulated EHG signals are the same as the ones used on the real EHG signals: H2, R2, FW_h2, and ICOH.

For H2, R2, and ICOH, we computed the connectivity methods for the simulated EHGs as described in Chapter 2.

For FW_h2, we had to adapt the used filter to the spectral content of the simulated signals, which is not exactly the same as the real EHG one.

The real EHG is composed of two frequency components, known as FWL (Fast Wave Low, 0.1 to 0.3 Hz) and FWH (Fast Wave High, 0.3 to 2 Hz). The propagation of uterus electrical activity is thought to be more linked to FWL, while the uterus excitability is thought to be more linked to FWH [48]. Thus, Terrien et al. [48] studied the effect of filtering EHG signals into their different frequency components (low FWL and high FWH components). Diab et al.[78] proposed a new feature, based on the nonlinear correlation method, FW_h2, and evidenced that filtering the signals in the FWL band (0.1 to 0.3 Hz) improves the pregnancy/labor

classification rate. This result supports the hypothesis that FWL is linked to uterine activity propagation and that it may reflect the uterus increased coordination during labor.

Thus, the filter used in FW_h2 should be adapted to the FWL frequency band. To study the filter adapted to the simulated EHGs, we computed the power spectral density (PSD) of these simulated signals, for the different parameter values. The PSDs were computed by means of the Welch periodogram algorithm.

Figures 5.7 to 5.12 present the PSD obtained when varying: beta_sig parameter, current_Na_etirement, lambda_sig, tissue resistance, SACCH_current, and SACCH_nbmax, respectively.

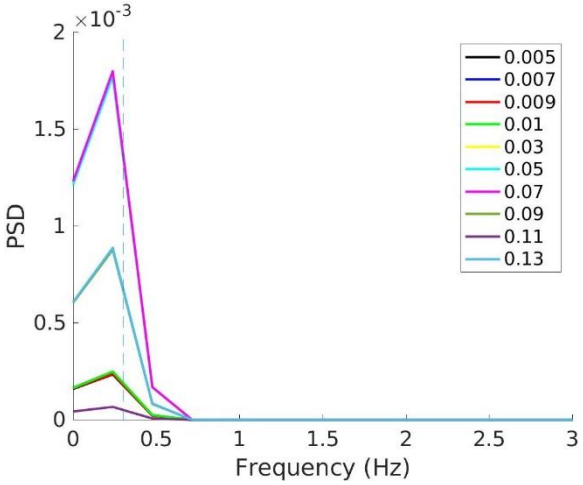

Figure 5.7. PSD for different beta_sig values

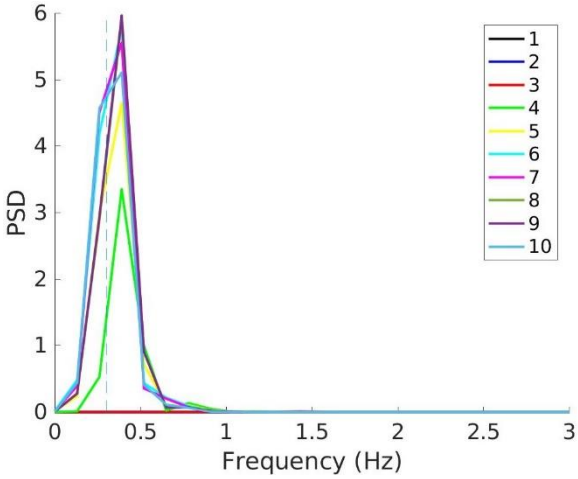

Figure 5.8. PSD for different current_Na_etirement values

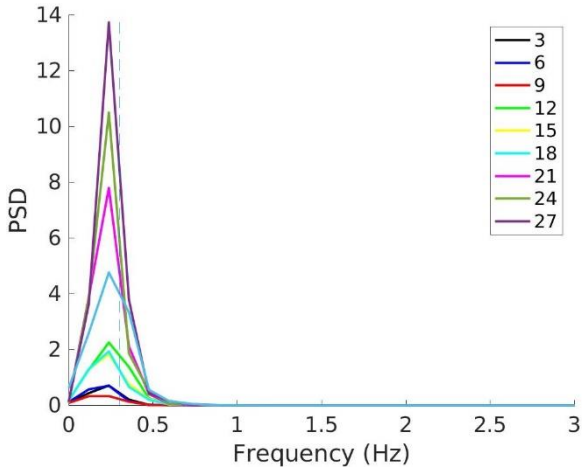

Figure 5.9. PSD for different lambda_sig values

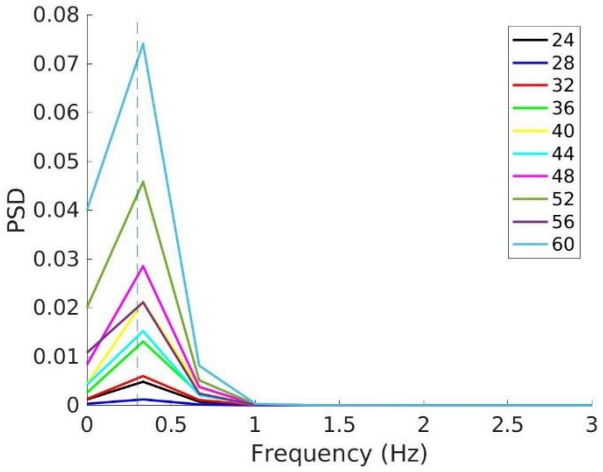

Figure 5.10. PSD for different resistance values

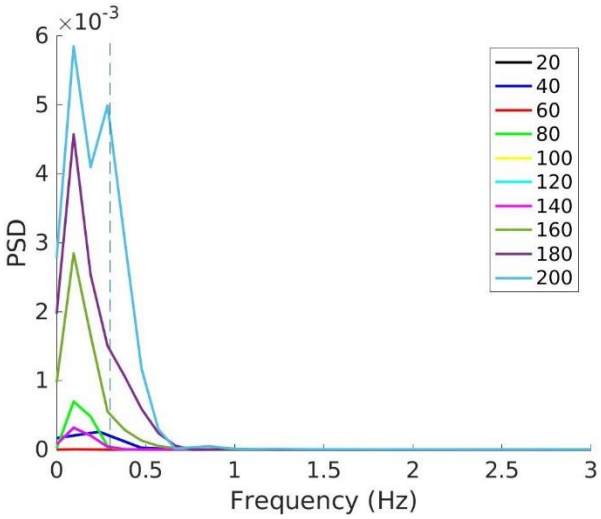

Figure 5.11. PSD for different SACCH_nbmax values

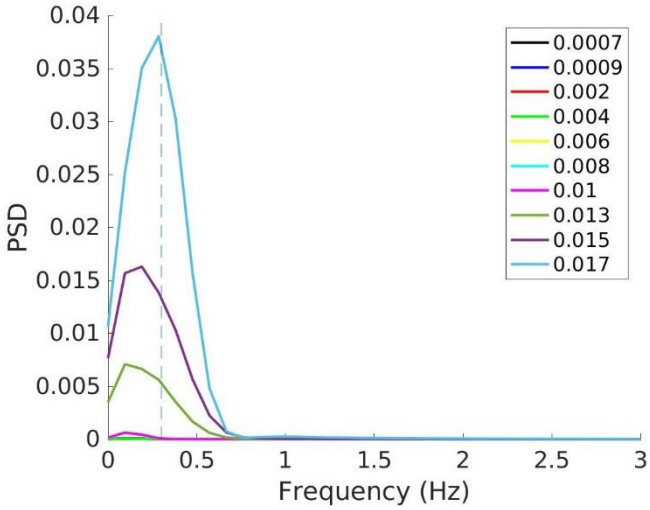

Figure 5.12. PSD for different SACCH_current values

The results presented above show that the PSDs of simulated EHGs contain mainly FWL, which ranges between 0.1 Hz and 0.7 Hz. In order to test the effect of the model parameters on the FW_h2 method, we will use a 0.1-0.7 Hz filter for FW_h2 applied to simulated EHGs.

5.2.3. Results

To examine the effects of varying the different parameters on synchronization, we have compared the results with a reference value. The reference value was considered as the first feature value defined for the first parameter value in each model parameter range. The comparison process was done by dividing every feature result by the reference. Therefore, for all parameters, the value derived for the smallest value is regarded to be 1, and we get a normalized effect for the variation. In this context, we can determine if the feature is increasing or decreasing as a function of the model parameter. When the value is smaller than 1, then it is decreasing; however, when the value is higher than 1, it is increasing. To compare numerically our results, we computed a linear regression on the obtained feature values. Consequently, if the slope is positive, then the feature increases with the model parameter, while if the slope is negative, the feature decreases with the parameter.

As an illustration, Figure 5.13 presents the results obtained for H2 when varying the tissue resistance. All the results are presented in [Annex B].

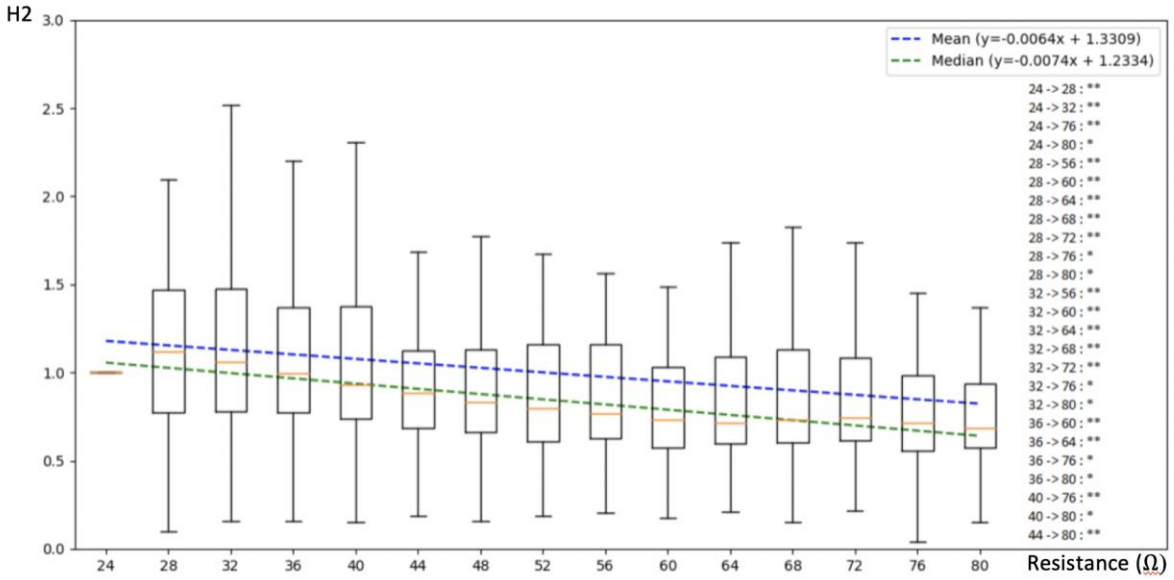

Figure 5.13. Evolution of H2 function of the tissue resistance. Top right corner: equations of the linear regression computed from the mean and the variance of the feature values. Right column: results of the significative differences obtained for differ

In Tables 5.2, 5.3, 5.4, and 5.5, we can see the slope obtained for every connectivity method R2, H2, ICOH, and FW_h2, respectively, with and without the use of the graph analysis (Eff, BC, Str, CC, and PR).

As stated previously, for the resistance parameter (ED group), we anticipated a decrease in the feature values (negative slope). For the five parameters related to mechanotransduction (EDM group), we expected the connectivity methods to increase as the parameter values increased (positive slope). For each parameter, the expected results are indicated in black and the unexpected results are indicated in red.

Table 5.2: R2 results for all the parameters

	lambda_sig		SACCH_nbmax		beta_sig		current_Na_etirement		SACCH_current		Resistance	
Method	Mean	Median	Mean	Median	Mean	Median	Mean	Median	Mean	Median	Mean	Median
R2	-0.0102	-0.0016	-0.0123	-0.0071	0.0353	0.0353	-0.0002	-0.0009	-0.0073	0.0013	-0.0009	-0.0009
R2(Eff)	0.0033	0.0011	0.0001	0.001	-0.0078	-0.0039	-0.0021	-0.0003	0.0004	0.0004	-0.0003	-0.0004
R2(BC)	-0.007	-0.0041	-0.0062	-0.001	0.0143	0.0075	0.0009	0.0013	-0.0047	-0.0014	-0.0008	-0.0008
R2(Str)	-0.0063	-0.0036	-0.0086	-0.0012	0.0064	0.0063	-0.0019	0.001	-0.0071	-0.0019	-0.0014	-0.0007
R2(CC)	-0.0078	-0.0047	-0.0082	-0.0043	0.0202	0.0124	-0.001	0.0002	-0.0035	0.0013	-0.0013	-0.0015
R2(PR)	-0.0092	-0.002	0.0006	-0.0035	0.0073	0.0063	0.003	-0.0002	0.0043	-0.0001	-0.0014	-0.0019

Table 5.3:H2 results for all the parameters

	lambda_sig		SACCH_nbmax		beta_sig		current_Na_etirement		SACCH_current		Resistance	
Method	Mean	Median	Mean	Median	Mean	Median	Mean	Median	Mean	Median	Mean	Median
H2	-0.0034	-0.0034	0.0051	0.0049	-0.0062	-0.0084	0.0044	0.0039	-0.0016	-0.0038	-0.0064	-0.0074
H2(Eff)	-0.0024	-0.0021	0.0003	0.0038	-0.0104	-0.0064	0.0004	0.0026	-0.0049	-0.0028	-0.0046	-0.0042
H2(BC)	-0.0038	-0.0023	-0.001	0.0001	-0.0003	-0.0005	0.0014	0.0011	-0.0044	-0.0048	-0.0028	-0.0028
H2(Str)	0.0255	0.0477	0.0189	0.0266	0.0038	0.001	0.0074	-0.0145	0.0188	0.0228	0.0018	0.0001
H2(CC)	-0.0019	-0.0024	-0.0015	-0.0001	-0.0036	0.0013	-0.0014	0.0003	-0.0011	0.0012	-0.0004	-0.0003
H2(PR)	-0.0049	-0.0039	0.0016	0.0013	-0.0041	-0.0035	0.0032	0.0036	-0.0019	-0.0019	-0.0043	-0.0044

Table 5.4: FW_h2(filter: 0.1-0.7 Hz) results for all the parameters

	lambda_sig		SACCH_nbmax		beta_sig		current_Na_etirement		SACCH_current		Resistance	
Method	Mean	Median	Mean	Median	Mean	Median	Mean	Median	Mean	Median	Mean	Median
FW_ h2	0.0017	0.0022	0.0018	0.0019	-0.0003	0.0002	0.0008	0.0008	0.0009	0.0011	0.0006	0.0008
FW_ h2(Eff)	0.0005	0.0006	-0.007	-0.0049	-0.0031	0.0021	0.0001	0.002	-0.0017	0.0011	-0.0005	-0.0004
FW_ h2(BC)	0.0021	0.0027	-0.0005	0.001	-0.0006	0.0035	0.0002	0.0014	-0.0017	0.0009	-0.0017	-0.0014
FW_ h2(Str)	0.0015	0.0016	-0.002	0.001	-0.0032	0.0057	-0.0024	-0.0005	-0.0027	-0.0012	-0.0001	-0.0006
FW_ h2(CC)	0.0007	0.0007	0.0006	0.0006	0.0018	0.0023	0.0006	0.0003	0.0004	0.0003	-0.0037	-0.0031
FW_ h2(PR)	0.0089	0.0276	0.0121	0.0029	0.0221	0.0015	0.0014	0.0001	-0.0016	-0.0004	-0.0003	0.0001

Table 5.5: ICOH results for all the parameters

	lambda_sig		SACCH_nbmax		beta_sig		current_Na_etirement		SACCH_current		Resistance	
Method	Mean	Median	Mean	Median	Mean	Median	Mean	Median	Mean	Median	Mean	Median
ICOH	-0.0003	0.0019	0.0032	0.0054	-0.0053	0.0005	-0.0008	-0.0014	0.031	0.0017	0.0001	0.0008
ICOH (Eff)	0.0002	-0.0004	-0.0021	0.0006	-0.0063	-0.0013	-0.0031	-0.0012	-0.0023	0.0001	-0.0007	-0.0009
ICOH (BC)	-0.0001	-0.0005	-0.0019	0.0013	-0.0075	-0.0081	-0.0016	0.0004	-0.0025	0.0003	-0.0004	-0.0002
ICOH (Str)	-0.0029	-0.0129	0.0168	0.0067	-0.0053	-0.0005	0.0147	0.032	0.0029	0.0064	0.002	-0.0004
ICOH (CC)	-0.0001	-0.0005	0.0007	0.0013	-0.0008	-0.0008	0.0007	0.0005	0.0	0.0005	0.0003	0.0002
ICOH (PR)	-0.0036	-0.0039	0.0063	0.0003	0.0063	0.0008	0.0044	0.0011	0.0017	0.0024	0.0007	0.0001

Regarding the electrical diffusion alone, the best result is clearly obtained with H2, which exhibits higher slopes, that is a higher sensitivity to the resistance variation, for most of the graph parameters used.

Concerning the mechanotransduction process, the 9 most sensitive features are presented in table 5.6 when computing the mean slope (first column) and the median slope (second column). The analysis developed to obtain these rankings is presented in [Annex C].

As a reminder, table 5.6 also presents the 9 best parameters previously selected by using Fscore and AUC on real signals.

The features extracted by means of FW_h2, alone or plus graph parameters, are selected 7 times among the 18 best parameters selected from real EHGs and 9 times among the 18 best parameters selected from simulated EHGs. Thus, it appears that FW_h2 (with or without graph parameters) is of importance to characterize the mechanotransduction process and the uterine synchronization. On the opposite, R2 is the worst method, being selected only 3 times, twice from real EHGs and once with simulated EHG, and always associated with a graph parameter.

Table 5.6: Best 9 features selected by the different methods used on real (Fscore and AUC) and simulated EHGs (Mean and median slopes). The features indicated in blue are the ones selected by Fscore

Simulated EHGs		***Real EHGs***	
Simu_Mean	Simu_Med	*Real_Fscore*	*Real_AUC*
H2(Str)	FW_h2(BC)	*FW_h2 (Str)*	*ICOH (Str)*
FW_h2(PR)	H2(Str)	*ICOH (Str)*	*ICOH (Eff)*
FW_h2(CC)	ICOH(Str)	*ICOH (Eff)*	*ICOH (CC)*
R2(PR)	FW_h2(CC)	*ICOH (CC)*	*FW_h2 (Str)*
H2	FW_h2	*FW_h2 (BC)*	*H2 (PR)*
ICOH(PR)	FW_h2(Eff)	*H2 (BC)*	*FW_h2 (BC)*
FW_h2	H2(Eff)	*FW_h2 (Eff)*	*H2 (BC)*
FW_h2(BC)	FW_h2(PR)	*R2 (Eff)*	*FW_h2 (Eff)*
ICOH(Str)	H2	*FW_h2 (CC)*	*R2 (BC)*

H2 (with or without graph parameters) is selected more often from simulated EHGs, than from real EHGs. Furthermore, the features extracted from H2 appear of importance mainly with the electrical diffusion alone, which is in agreement with the idea that H2 reflects the linear and non-linear correlation that should be altered linearly by tissue resistance changes.

Concerning the graph parameters, they appear of importance, mainly on real EHGs, as only two connectivity methods alone (H2 and FW_h2) are selected and only 4 times among the 18 best parameters selected from simulated EHGs, and never from the real EHGs (Table 5.7). The best graph parameter appears to be Str (as also evidenced in a previous study done on real EHGs [7]), followed by Eff and BC, justifying the proposition of this new graph parameter.

Table 5.7: Occurrence of each graph parameter among the best parameters selected from real and simulated EHGs.

	None	**Str**	**CC**	**Eff**	**PR**	**BC**
Simulated EHGs	4	4	2	2	4	2
Real EHGs	0	4	3	5	1	5
Sum	*4*	*8*	*5*	*7*	*5*	*7*

5.3 DISCUSSION AND CONCLUSION

In this present chapter, we examined the impact of the model parameters that control the uterine synchronization (electrical diffusion and mechanotransduction process), on the features extracted from simulated EHG signals to characterize the uterine connectivity. We used a model developed by our team [12] to generate EHG signals in two groups: signals with electrical diffusion only (ED) by changing the tissue resistance, and signals with ED and Mechanotransduction (EDM) by changing the different parameters that influence this phenomenon. For the ED group, we expected a decrease in connectivity measure with the increasing resistance. While for the EMD group, we expected an increase in connectivity when increasing the values for each parameter.

The best features when using mean function are H2(Str), FW_h2 alone and with PR, BC, and CC, H2 alone or with Str, R2(PR), and ICOH(Str) are the best features to evidence a change in the mechanotransduction process. H2 alone and with Eff, PR, and BC are the best features to evidence a change in the electrical diffusion.

FW_h2 method (with and without graph parameters) appeared to be good the best connectivity method to use to characterize uterine connectivity, since they consistently produce better results on real and simulated signals. Nevertheless, FW_h2 takes a longer execution time.

Finally, and to conclude with this first try, we demonstrated that the electromechanical model, even imperfect, can be successfully used to select features suited for the monitoring of uterine synchronization by using simulated EHG signals. The differences noticed between the selection done either by Fscore on real signals or from simulated signals could be explained by the simplifications included in the model. The fact that we tested also the effect of one parameter at a time differs from what happens with real EHGs, when all the parameters might evolve simultaneously.

Another fact that can impact the results is that the small size of the recording matrix of electrodes (less than 10cm x 10cm) does not permit to investigate properly the mechanotransduction process which is associated with long-distance diffusion. The mechanotransduction process is thus poorly represented on the EHG signals collected or simulated in this study. A wider distance between electrodes should permit to record more precisely this long-distance synchronization.

CHAPTER 6: Synthesis of best Connectivity, Graph and Machine Learning methods on Real EHG Signals

This chapter presents a synthesis of all the steps that we tested to improve the classification of EHGs between pregnancy and labor based on connectivity analysis. In this study, we compare the results obtained for the classification of real EHGs when using each set of best 9 features selected from Fscore and AUC values (from real signals) and mean and median slopes (from simulated signals). These best 9 feature sets will be tested for the classification of real EHGs (pregnancy vs. labor) by using the best classification method, the whole burst duration, and the 16 nodes. Then, the feature set giving the best result will be used to test the effect of best windows and best nodes selection.

6.1. Methodology

Previously in this study, we used a multichannel system in order to obtain real electrohysterographic signals (EHGs). Accordingly, with a 4x4 electrode matrix positioned on the woman's abdomen, we were able to record contractions by means of 16 monopolar EHG signals during pregnancy and labor [73].

So far, we have used several connectivity measures, graph theory metrics, and machine learning methods to differentiate between pregnancy and labor contractions, in order to evaluate uterine synchronization during pregnancy and labor.

To analyze the EHG connectivity, we have tested four connectivity methods: cross-correlation coefficient (R2) [86], nonlinear correlation (H2) [73], Filtered Windowed H2 (FW_h2) [72], and imaginary part of coherence (ICOH) [76].

Then, we have used five metrics extracted from the graph analysis of the 4 obtained connectivity matrices: Strength (Str) [93], Clustering Coefficient (CC) [94], Efficiency (Eff) [87], PageRank (PR) [95], and Betweenness Centrality (BC)[100].

The features obtained from these connectivity methods and graph metrics were fed into different machine learning methods: Logistic Regression (LR) [128], naïve Bayes (NB) [132], Support Vector Machine (SVM) [126], Multilayer Perceptrons (MLP) [123], Random Forest (RF) [134], Gradient Boosting Machines (GBM) [136], Recurrent neural networks (RNN) [139], and Long Short-Term Memory (LSTM) [142].

We also tested in our study a windowing approach [160], which involves decomposing real signals into windows. This process will give us the opportunity to find the best windows and the best nodes (electrodes) that give the most reliable information for the classification. In

this step, we applied the same previous process on each window except that, for this windowing approach, we have used three different types of connectivity methods: linear correlation coefficient (R2), nonlinear correlation (H2), and imaginary part of coherence (ICOH). Moreover, Strength (Str), Clustering Coefficient (CC), Efficiency (Eff), PageRank (PR), and Betweenness Centrality (BC) were also employed as graph metrics. Then, as for the machine learning methods, we chose the best method previously obtained: Logistic Regression (LR).

Simulated EHG signals, which are generated by using simulation modules developed by our team [12], permitted us to test the different feature sensitivity to the model parameters related to uterine synchronization. Signals are then generated by controlling either the electrical diffusion or the mechanotransduction process. We then computed the previous features on the EHG signals produced by each simulated surface electrode. This analysis permitted us to select feature sets that evidenced the greatest sensitivity to the model parameter controlling the uterine synchronization.

This last study aims to put together these different steps in order to retain the best ones that will allow us to improve the classification of real EHGs between pregnancy and labor contractions: best feature set, best windows, and best nodes.

6.2. Results

6.2.1. Best feature set

The best 9 feature sets, which were previously selected, are presented in Table 6.1. We obtained 4 sets, 2 selected from real EHGs (Fscore, AUC), and 2 selected from simulated EHGs (Mean slope, Median slope).

The AUC values presented in the last column of Table 6.1 are the classification results obtained when using each feature set as input of the Logistic regression, on the whole burst duration and with the 16 monopolar signals for each contraction (classical approach). We used for this step a 4-fold approach [163].

We can notice that the feature set that gives the best result (AUC=0.929) is the one selected by Fscore, from real EHGs (Chapter 3): FW_h2 (Str), ICOH (Str), ICOH (Eff), ICOH (CC), FW_h2 (BC), H2 (BC), FW_h2 (Eff), R2 (Eff), and FW_h2 (CC).

Furthermore, the classification power of each feature of this set, separately, is presented in Table 6.2. The best result is obtained with H2(BC) (AUC=0.742), which is smaller than the AUC obtained with any of the 4 feature sets. These results confirm the fact that using different features (connectivity method + graph metrics) at the same time as inputs to a machine learning method improves the classification of EHGs when compare to the use of one feature at a time, regardless of the feature set.

Table 6.1: Results classification with each best feature set and using 4-fold approach, each feature with the best selected window and using the best nodes.

Feature selection (EHG origin)	**feauture set**	**AUC Mean ±SD**
Fscore (real)	**FW_h2(Str), ICOH(Str), ICOH(Eff), ICOH(CC), FW_h2(BC), H2(BC), FW_h2(Eff), R2(Eff), FW_h2(CC)**	**0.929 ±0.025**
AUC (real)	ICOH (Str), ICOH (Eff), ICOH (CC), FW_h2 (Str), H2 (PR), FW_h2 (BC), H2 (BC), FW_h2 (Eff), R2 (BC)	0.903 ±0.023
Mean slope (simulated)	H2(Str), FW_h2(PR), FW_h2(CC), R2(PR), H2, ICOH(PR), FW_h2, FW_h2(BC), ICOH(Str)	0.842 ±0.036
Median slope (simulated)	FW_h2(BC), H2(Str), ICOH(Str), FW_h2(CC), FW_h2, FW_h2(Eff), H2(Eff), FW_h2(PR), H2	0.884 ±0,019

Table 6.2: AUC values for the best features from Fscore, each feature with the best selected window and using the best nodes.

	H2 (BC)	FW_h2 (Str)	FW_h2 (Eff)	R2 (Eff)	FW_h2 (CC)	FW_h2 (BC)	ICOH (Eff)	ICOH (CC)	ICOH (Str)
AUC	**0.742**	0.601	0.598	0.547	0.484	0.483	0.477	0.473	0.471

For the following step, we will thus use the 9 features selected by Fscore.

6.2.2. Best windows and best nodes

From the previous study done in Chapter 4, the best windows are windows 2, 4, and 5. Regarding the best nodes, the results are nodes 8, 9, 10, 11, and 12.

Thus, we tested in this study, by using Logistic Regression, the 9 features of the Fscore test (best feature set), with the features computed from the 5 best nodes. Concerning the windows, as evidenced in Chapter 4, each feature is associated with a specific best window and windows sizes. The best windows for each feature were:

- All windows concatenated (60s duration) for FW_h2(Str), FW_h2(BC), FW_h2(Eff), R2(Eff), and FW_h2(CC)
- W2 for ICOH(CC)
- W4 for ICOH(Eff)
- W5 for ICOH(Str)
- W7 for H2(BC)

We thus proposed to compare different options for the window choice, from which the 9 features are computed:
- *Option 1:* Each feature is computed from its best window (as extracted from Chapter 4) and the best nodes.
- *Option 2:* All the features are computed from the concatenation of the windows of interest for most of the features (W2, W4, and W5 concatenated), and the best nodes. This option will present simplified processing when compared to option 1.
- *Option 3:* All the features are computed from the whole signals and the best nodes.

Table 6.3: Results classification with different set of features and windows

Option	**Window choice**	**AUC Value**
Option 1	FW_h2(Str), FW_h2(BC), FW_h2(Eff), R2(Eff) and FW_h2(CC): All Windows ICOH(CC): window 2 ICOH(Eff): window 4 ICOH(Str): window 5 H2(BC): window 7	0.904
Option 2	All windows for the 9 features	0.928
Option 3	**Whole signals for all features**	**0.955**

Table 6.3 presents the results obtained when using Logistic Regression with the best set of features (9 features selected from Fscore), the best nodes (8, 9, 10, 11, and 12), and different windows (3 options).

The best result (AUC=0.955) is obtained when using the whole signal. This result confirms the one obtained in Chapter 4 with a reduced number of features. The associated ROC curve is presented in figure 6.1 and the confusion matrix in figure 6.2.

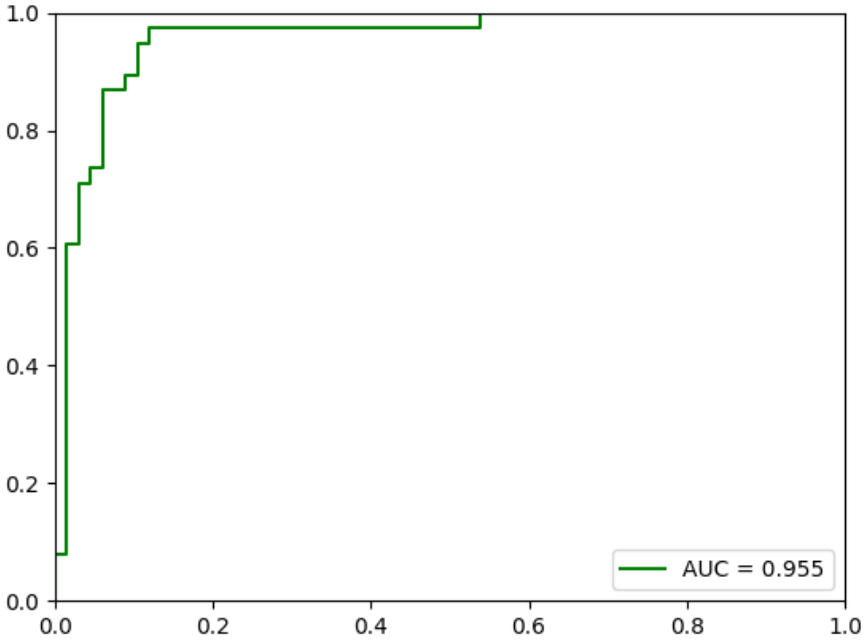

Figure 6.1. ROC Curve for logistic regression, Fscore feature set, best nodes, whole signal.

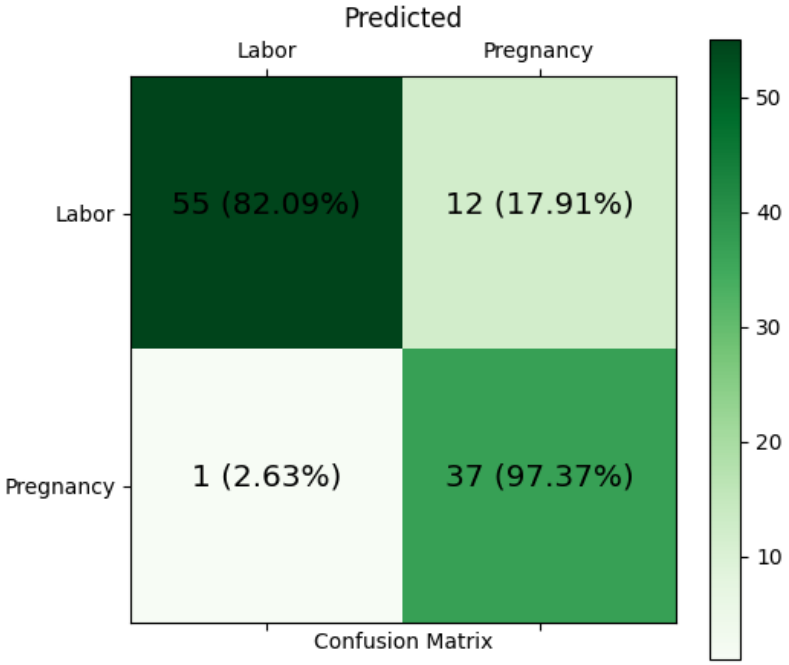

Figure 6.2: Logistic regression confusion matrix

In terms of clinical interpretation, Table 6.4 compare the results obtained with Logistic Regression when using the classical approach (whole signal, the 16 nodes), or the best results obtained here (whole signal, best nodes).

Table 6.4: Previous (16 nodes, whole signal) and new approaches (9 best nodes, whole signal) with Logistic Regression

Nodes	AUC Value	Specificity	Sensitivity	PPV	NPV
All nodes	0.946	0.95	**0.87**	0.97	**0.80**
Best nodes	**0.955**	**0.97**	0.82	**0.98**	0.76

The problematic being to detect preterm labor, the new proposed approach (using the 5 best nodes rather than the 16 nodes) gives a better AUC, a better Specificity, and a better Positive Predictive Value (PPV). When using all the nodes, we obtain a better Sensitivity and a better Negative Predictive Value (NPV).

6.3 Discussion and Conclusion

In this chapter, we have applied the best sets of features obtained previously for connectivity methods and graph metrics (Fscore and AUC from real EHGs, Mean and Median slopes from simulated EHGs), and best machine learning methods (Logistic regression) on real EHGs. These methods were applied to the best windows (W2, W4, W5, and W7) and best nodes (8, 9, 10, 11, and 12) obtained when applying the windowing approach.

First, the best set of features selected, thanks to a 4-fold approach, is the one extracted by Fscore when using the 16 nodes (all the nodes) and the whole signals, with an average of AUC values 0.929 (±0.025). When we compared the performance of each one of the best features used alone, without applying machine learning, the results indicated that H2(BC) gave the best result with AUC=0.742. This confirms the power of machine learning to improve the classification of contraction in pregnancy or labor, based on EHG connectivity analysis.

Then we tested different combinations of the best windows, the best features of the Fscore set, and the best nodes. We obtained the best result when we used the whole signals with the best 9 features from Fscore and the best nodes; the AUC value obtained is 0.955.

Therefore, the results indicated that when the best nodes and features were applied on the whole signals (AUC=0.955), they were higher than the results previously attained (AUC=0.946) when we used the 16 nodes instead (Chapter 3).

These studies also proved that when we use the FW_h2 features, the results are better than when we use only the other features (as in Chapter 4).

Finally, the studies proved that the results are better when we used only 5 best nodes instead of 16 nodes. But the windowing approach did not improve the results. Indeed, the longer the window of analysis is, the better are the classification results.

If we consider the difference in execution time between the two situations (all windows concatenated vs. the whole burst duration) an important question remains whether it is better to lose 2.5% of AUC but gain in execution time?

Another question of importance is the clinical application of this test for the detection of preterm labor. From a clinical point of view, is it more important to increase the positive predictive value, thus reducing the number of false positive cases? In that case, the use of only 5 nodes, with their higher specificity and higher PPV, would be the best choice. Or, is it better to increase the number of good detections of normal pregnancy, and thus avoid the false negative cases? In that case, the choice of the 16 nodes, with their higher NPV and higher Sensitivity would be the best choice.

These questions have to be answered by the clinicians. The choice is theirs.

To conclude, we proved that combining the best features and methods, and the selection of the best nodes could be used to effectively shorten the time it takes to classify between pregnancy and labor. In conclusion, the following approach could be useful to detect preterm labor early by enabling a proper monitoring of the uterine contractions throughout pregnancy.

General Conclusion, Discussion and Perspectives

In this thesis, we have proposed an innovative approach for determining the functional connectivity of uterine electrical activity for the sake of clinical use. Our approach is based on the use of machine learning methodologies to examine the synchronization of uterine electrical activity. This approach was applied on real and simulated EHG signals.

Many studies [4], [53], [56] have previously employed the electrohysterography (EHG) processing to characterize contraction efficiency and detect preterm labor. EHG is a noninvasive signal that measures the uterine electrical activity [5]. Furthermore, two physiological phenomena are known to regulate the efficiency of uterine contractions that precede labor and delivery: i) increased cell excitability and ii) increased synchronization of the uterus. Two phenomena control this synchronization: first, increased connectivity between myometrial cells, thanks to the apparition of Gap Junctions, that further results in an increase in local diffusion of action potentials [5]; second, increased mechanotransduction sensitivity at the cell level, allowing for a longer distance activation of the uterine muscle linked to the uterine tissue stretching [23].

As for the global analysis of the uterine synchronization (whole burst), in most earlier research, the EHG correlation matrices were limited to the use of their mean and variances (or standard deviation) [78]. Hence, a recent study proposed to use a graph theory-based analysis [11], which appeared to be a more efficient technique to characterize the EHG connectivity matrices than the use of a simple averaging. However, the results obtained in pregnancy-labor classification from this study were based on very simple classification tools. For this reason, we proposed to use in this work a machine learning approach. Machine learning approach was applied to classify labor and pregnancy contractions using information derived from both graph and connectivity methods.

First, we have demonstrated in this work that, when compared to earlier studies based on graph-based analysis, that the machine learning approach is more effective in classifying between pregnancy and labor [11]. Machine learning methods were fed by either connectivity features or by connectivity+graph features. As a first step, Fscore enabled the selection of the 9 most effective features for classification, which were all parameters extracted from the graph analysis. Nevertheless, these results confirmed that the graph theory approach is able to better follow the synchronized development of uterine muscle between pregnancy and labor.

Then, when compared to earlier studies [11], we were able to show that the machine learning approach enhances classification performance. The results achieved while using the Logistic regression method were much higher than the values attained formerly [4].

Nevertheless, several limitations and improvements can be mentioned:

Signals at the abdominal surface level

We applied the logistic regression method on the whole EHG bursts [12]; we were able to get a classification rate of 95%. These results indicate that the combination of many parameters (9 in our case) gives better results than using a single parameter [11].

However, we could even improve these results by applying the following steps:

- In order to validate the clinical impact of the suggested approach, it should be applied to a wider database, including signals recorded on women in premature labor, which are currently absent from our database. In this case, a distinction between normal and premature labor will be useful in evaluating the clinical effectiveness of the proposed approach as well as a better understanding of the mechanism of premature labor, still insufficiently understood.
- Depending on the uterine synchronization analysis, a combination of multiple graph parameters increased the classification rate. While increasing the number of features improves classification, it also increases the execution time. So, to tradeoff between time and high classification, selecting only the best number of features is critical.
- In this thesis, we focused the work on functional connectivity methods without taking into consideration the connectivity directionality. Another type of connectivity, known as effective connectivity that delves at the causality of relationships, might be able to reveal additional information regarding the synchronization potential directionality.
- The number of windows is critical. In this thesis, we have used 7 windows. We noticed that reducing the number of windows can enhance categorization by increasing the number of points in each window.
- We employed overlapping between consecutive windows; however, some points are exchanged between them. Thus, non-overlapping could be a new way to determine which window is indeed the best.

Simulated signals

We have studied the impact of different uterine model parameters related to short and long-distance synchronization, on the simulated EHG characteristics. We used a uterine model developed by our team [12] to simulate EHG signals. These signals were grouped in two data sets: i) signals based only on electrical diffusion (ED) alone, by varying the tissue resistance parameter, and ii) signals based on ED plus Mechanotransduction (EDM) by varying the five parameters affecting this phenomenon. We expect that the contractions induced by mechanotransduction would be more similar to those recorded during labor.

We concluded that H2, alone and with Eff, PR, and BC as graph metrics, are the best features to evidence a change in the electrical diffusion. H2(Str), FW_h2 (alone and with PR, BC, and CC), H2 (alone and with Str), R2(PR), and ICOH(Str) are the best features to evidence a change in the mechanotransduction process. FW_h2 method (with and without graph parameters) appeared to be the best connectivity method to use to characterize uterine connectivity, since it consistently produces better results on real and simulated signals.

However, some possible approach modifications could help enhance these results as mentioned below:

- There are only 11 meshes for uterus model in the database. However, increasing the number of meshes would likely improve the reliability of the results.
- Changing the filter in the method FW_h2 improved the results; perhaps finding the ideal filter can improve the results even more.
- We only examined one parameter in the first class (ED) and 5 in the second one (EDM) from a "standard" configuration of the model parameters [8]; nonetheless, other model parameters may affect the simulations; thus, experimenting with other parameters values may be a way to improve these results.
- A sensitivity analysis of the whole electro-mechanical model should permit to point out the complexity of determining the parameter variation intervals, and their possible interactions. But we were limited by the number of trajectories required for this analysis, from a temporal perspective.

Synthesis of the best methods

We have used the best sets of features obtained formerly for connectivity methods and graph metrics (Fscore and AUC from real EHGs, Mean and Median slopes from simulated EHGs), as well as the best machine learning method (Logistic regression) to classify pregnancy and labor real EHGs. These methods were applied to the best windows (W2, W4, W5, and W7) and best nodes (8, 9, 10, 11, and 12) selected when applying the windowing approach.

The set of features extracted by Fscore when employing all 16 nodes (all nodes) and all signals, with an average of AUC values of 0.929 (±0.025), is proved to be the best set of features.

Then we tested different combinations of the best windows, the best features of the Fscore set, and the best nodes. We obtained the best result when we applied the whole signals with the best 9 features from Fscore and the best nodes. We obtained an AUC value of 0.955.

Some possible approach adjustments could assist in improving these outcomes:

- We only used 4-fold sets; increasing the number of k-fold sets would likely increase the result reliability.

- Since the windows now have a fixed length, taking them as a percentage of the signal length by taking it directly part from the whole signal would probably increase the reliability of the result.

Final conclusion

To draw a conclusion, we have provided a new approach based on machine learning that uses connectivity and graph methods as input. Our results demonstrate that when implemented at the abdomen level, this machine learning based approach has a high potential for quantifying uterine synchronization in order to have an improved classification between pregnancy and labor. Ultimately, we anticipate that this method will be utilized to differentiate between labor and nonlabor situations during pregnancy, which will aid in the early detection of premature labor.

References

[1] T. Lander, “Neonatal and perinatal mortality: country, regional and global estimates.,” Neonatal and perinatal mortality: country, regional and global estimates., 2006

[2] R. L. Goldenberg, J. F. Culhane, J. D. Iams, and R. Romero, “Epidemiology and causes of preterm birth,” *The Lancet*, vol. 371, no. 9606, pp. 75–84, Jan. 2008, doi: 10.1016/S0140-6736(08)60074-4.

[3] S. D. Grosse, N. J. Waitzman, N. Yang, K. Abe, and W. D. Barfield, “Employer-Sponsored Plan Expenditures for Infants Born Preterm,” *Pediatrics*, vol. 140, no. 4, p. e20171078, Oct. 2017, doi: 10.1542/peds.2017-1078.

[4] C. Marque, J. M. Duchene, S. Leclercq, G. S. Panczer, and J. Chaumont, “Uterine EHG processing for obstetrical monitoring,” *IEEE Trans Biomed Eng*, vol. 33, no. 12, pp. 1182–1187, Dec. 1986, doi: 10.1109/TBME.1986.325698.

[5] D. Devedeux, C. Marque, S. Mansour, G. Germain, and J. Duchêne, “Uterine electromyography: a critical review,” *Am. J. Obstet. Gynecol.*, vol. 169, no. 6, pp. 1636–1653, Dec. 1993, doi: 10.1016/0002-9378(93)90456-s.

[6] S. Mansour, D. Devedeux, G. Germain, C. Marque, and J. Duchêne, “Uterine EMG spectral analysis and relationship to mechanical activity in pregnant monkeys,” *Med Biol Eng Comput*, vol. 34, no. 2, pp. 115–121, Mar. 1996, doi: 10.1007/BF02520015.

[7] M. Lucovnik *et al.*, “Noninvasive uterine electromyography for prediction of preterm delivery,” *Am J Obstet Gynecol*, vol. 204, no. 3, p. 228.e1–10, Mar. 2011, doi: 10.1016/j.ajog.2010.09.024.

[8] C. Rabotti, M. Mischi, J. O. E. H. van Laar, G. S. Oei, and J. W. M. Bergmans, “Inter-electrode delay estimators for electrohysterographic propagation analysis,” *Physiol Meas*, vol. 30, no. 8, pp. 745–761, Aug. 2009, doi: 10.1088/0967-3334/30/8/002.

[9] H. de Lau, C. Rabotti, R. Bijloo, M. J. Rooijakkers, M. Mischi, and S. G. Oei, “Automated conduction velocity analysis in the electrohysterogram for prediction of imminent delivery: a preliminary study,” *Comput Math Methods Med*, vol. 2013, p. 627976, 2013, doi: 10.1155/2013/627976.

[10] M. Hassan, S. Boudaoud, J. Terrien, B. Karlsson, and C. Marque, “Combination of canonical correlation analysis and empirical mode decomposition applied to denoising the labor electrohysterogram,” *IEEE Trans Biomed Eng*, vol. 58, no. 9, pp. 2441–2447, Sep. 2011, doi: 10.1109/TBME.2011.2151861.

[11] N. Nader *et al.*, “Pregnancy monitoring using graph theory based analysis,” in *2015 International Conference on Advances in Biomedical Engineering (ICABME)*, Sep. 2015, pp. 73–76. doi: 10.1109/ICABME.2015.7323254.

[12] M. Yochum, J. Laforet, and C. Marque, “An electro-mechanical multiscale model of uterine pregnancy contraction,” *Computers in Biology and Medicine*, vol. 77, Aug. 2016, doi: 10.1016/j.compbiomed.2016.08.001.

[13] M. B. Wallenstein, S. L. Carmichael, and D. K. Stevenson, “8 - Prematurity and Stillbirth,” in *Avery’s Diseases of the Newborn (Tenth Edition)*, C. A. Gleason and S. E. Juul, Eds. Philadelphia: Elsevier, 2018, pp. 78-81.e3. doi: 10.1016/B978-0-323-40139-5.00008-5.

[14] H. A. Frey and M. A. Klebanoff, “The epidemiology, etiology, and costs of preterm birth,” *Semin Fetal Neonatal Med*, vol. 21, no. 2, pp. 68–73, Apr. 2016, doi: 10.1016/j.siny.2015.12.011.

[15] S. Chawanpaiboon *et al.*, “Global, regional, and national estimates of levels of preterm birth in 2014: a systematic review and modelling analysis,” *The Lancet Global Health*, vol. 7, no. 1, pp. e37–e46, Jan. 2019, doi: 10.1016/S2214-109X(18)30451-0.

[16] M. A. Ameer, S. E. Fagan, J. N. Sosa-Stanley, and D. C. Peterson, “Anatomy, Abdomen and Pelvis, Uterus,” in *StatPearls*, Treasure Island (FL): StatPearls Publishing, 2022. Available: http://www.ncbi.nlm.nih.gov/books/NBK470297/

[17] A. Gasner and A. P A, “Physiology, Uterus,” in *StatPearls*, Treasure Island (FL): StatPearls Publishing, 2020. Available: http://www.ncbi.nlm.nih.gov/books/NBK557575/
[18] F. Zara and O. Dupuis, “Chapter 15 - Uterus,” in *Biomechanics of Living Organs*, vol. 1, Y. Payan and J. Ohayon, Eds. Oxford: Academic Press, 2017, pp. 325–346. doi: 10.1016/B978-0-12-804009-6.00015-8.
[19] “An Uterine Electromyographic Activity as a Measure of Labor Progression | IntechOpen.” https://www.intechopen.com/chapters/25830
[20] H. Schwalm and V. Dubrauszky, “The structure of the musculature of the human uterus—muscles and connective tissue,” *American Journal of Obstetrics and Gynecology*, vol. 94, no. 3, pp. 391–404, Feb. 1966, doi: 10.1016/0002-9378(66)90661-2.
[21] B. Karlsson, J. Terrien, V. Gudmundsson, T. Steingrimsdottir, and C. Marque, “Abdominal EHG on a 4 by 4 grid: mapping and presenting the propagation of uterine contractions,” in *11th Mediterranean Conference on Medical and Biomedical Engineering and Computing 2007*, Berlin, Heidelberg, 2007, pp. 139–143. doi: 10.1007/978-3-540-73044-6_35.
[22] R. E. Garfield and W. L. Maner, “Physiology and Electrical Activity of Uterine Contractions,” *Semin Cell Dev Biol*, vol. 18, no. 3, pp. 289–295, Jun. 2007, doi: 10.1016/j.semcdb.2007.05.004.
[23] R. C. Young, “Mechanotransduction mechanisms for coordinating uterine contractions in human labor,” *Reproduction*, vol. 152, no. 2, pp. R51-61, 2016, doi: 10.1530/REP-16-0156.
[24] B. M. Sanborn, “Ion channels and the control of myometrial electrical activity,” *Semin Perinatol*, vol. 19, no. 1, pp. 31–40, Feb. 1995, doi: 10.1016/s0146-0005(95)80045-x.
[25] C. Ramon, H. Preissl, P. Murphy, J. D. Wilson, C. Lowery, and H. Eswaran, “Synchronization analysis of the uterine magnetic activity during contractions,” *Biomed Eng Online*, vol. 4, p. 55, Oct. 2005, doi: 10.1186/1475-925X-4-55.
[26] H. Eswaran, H. Preissl, J. D. Wilson, P. Murphy, S. E. Robinson, and C. L. Lowery, “First magnetomyographic recordings of uterine activity with spatial-temporal information with a 151-channel sensor array,” *Am J Obstet Gynecol*, vol. 187, no. 1, pp. 145–151, Jul. 2002, doi: 10.1067/mob.2002.123031.
[27] C. Rabotti and M. Mischi, “Propagation of electrical activity in uterine muscle during pregnancy: a review,” *Acta Physiol (Oxf)*, vol. 213, no. 2, pp. 406–416, Feb. 2015, doi: 10.1111/apha.12424.
[28] J. M. Marshall, “Effects of estrogen and progesterone on single uterine muscle fibers in the rat,” *Am J Physiol*, vol. 197, pp. 935–942, Oct. 1959, doi: 10.1152/ajplegacy.1959.197.4.935.
[29] H. C. Parkington, R. Harding, and J. N. Sigger, “Co-ordination of electrical activity in the myometrium of pregnant ewes,” *J Reprod Fertil*, vol. 82, no. 2, pp. 697–705, Mar. 1988, doi: 10.1530/jrf.0.0820697.
[30] R. E. Garfield, S. Sims, and E. E. Daniel, “Gap junctions: their presence and necessity in myometrium during parturition,” *Science*, vol. 198, no. 4320, pp. 958–960, Dec. 1977, doi: 10.1126/science.929182
[31] S. M. Miller, R. E. Garfield, and E. E. Daniel, “Improved propagation in myometrium associated with gap junctions during parturition,” *Am J Physiol*, vol. 256, no. 1 Pt 1, pp. C130-141, Jan. 1989, doi: 10.1152/ajpcell.1989.256.1.C130.
[32] R. E. Garfield and R. H. Hayashi, “Appearance of gap junctions in the myometrium of women during labor,” *American Journal of Obstetrics and Gynecology*, vol. 140, no. 3, pp. 254–260, Jun. 1981, doi: 10.1016/0002-9378(81)90270-2.
[33] A. Riol, J. Cervera, M. Levin, and S. Mafe, “Cell Systems Bioelectricity: How Different Intercellular Gap Junctions Could Regionalize a Multicellular Aggregate,” *Cancers*, vol. 13, no. 21, Art. no. 21, Jan. 2021, doi: 10.3390/cancers13215300.
[34] J. Xu, S. N. Menon, R. Singh, N. B. Garnier, S. Sinha, and A. Pumir, “The Role of Cellular Coupling in the Spontaneous Generation of Electrical Activity in Uterine Tissue,” *PLOS ONE*, vol. 10, no. 3, p. e0118443, Mar. 2015, doi: 10.1371/journal.pone.0118443.

[35] R. E. Garfield, S. Sims, and E. E. Daniel, “Gap junctions: their presence and necessity in myometrium during parturition,” *Science*, vol. 198, no. 4320, pp. 958–960, Dec. 1977, doi: 10.1126/science.929182.
[36] R. E. Sheldon *et al.*, “Alterations in gap junction connexin43/connexin45 ratio mediate a transition from quiescence to excitation in a mathematical model of the myometrium,” *J R Soc Interface*, vol. 11, no. 101, Dec. 2014, doi: 10.1098/rsif.2014.0726.
[37] F. Sachs, “Stretch-Activated Ion Channels: What Are They?,” *Physiology (Bethesda)*, vol. 25, no. 1, pp. 50–56, Feb. 2010, doi: 10.1152/physiol.00042.2009.
[38] R. E. Garfield *et al.*, “Methods and devices for the management of term and preterm labor,” *Ann N Y Acad Sci*, vol. 943, pp. 203–224, Sep. 2001, doi: 10.1111/j.1749-6632.2001.tb03803.x.
[39] R. E. Garfield, K. Chwalisz, L. Shi, G. Olson, and G. R. Saade, “Instrumentation for the diagnosis of term and preterm labour,” *J Perinat Med*, vol. 26, no. 6, pp. 413–436, 1998, doi: 10.1515/jpme.1998.26.6.413.
[40] R. E. Garfield *et al.*, “Control and assessment of the uterus and cervix during pregnancy and labour,” *Hum Reprod Update*, vol. 4, no. 5, pp. 673–695, Oct. 1998, doi: 10.1093/humupd/4.5.673.
[41] D. Escalona-Vargas, M. Zhang, and H. Eswaran, “Connectivity Measures of Uterine Activity using Magnetomyography,” Jul. 2018, vol. 2018. doi: 10.1109/EMBC.2018.8513498.
[42] H. Allahem and S. Sampalli, “Automated uterine contractions pattern detection framework to monitor pregnant women with a high risk of premature labour,” *Informatics in Medicine Unlocked*, vol. 20, p. 100404, Jan. 2020, doi: 10.1016/j.imu.2020.100404.
[43] L. F. Bastos, W. van Meurs, and D. Ayres-de-Campos, “A model for educational simulation of the evolution of uterine contractions during labor,” *Computer Methods and Programs in Biomedicine*, vol. 107, no. 2, pp. 242–247, Aug. 2012, doi: 10.1016/j.cmpb.2011.09.016.
[44] S. Beck *et al.*, “The worldwide incidence of preterm birth: a systematic review of maternal mortality and morbidity,” *Bull World Health Organ*, vol. 88, no. 1, pp. 31–38, Jan. 2010, doi: 10.2471/BLT.08.062554.
[45] J. Mas-Cabo, Y. Ye-Lin, J. Garcia-Casado, J. Alberola-Rubio, A. Perales, and G. Prats-Boluda, “Uterine contractile efficiency indexes for labor prediction: A bivariate approach from multichannel electrohysterographic records,” *Biomedical Signal Processing and Control*, vol. 46, pp. 238–248, Sep. 2018, doi: 10.1016/j.bspc.2018.07.018.
[46] H. de Lau, C. Rabotti, H. P. Oosterbaan, M. Mischi, and G. S. Oei, “Study protocol: PoPE-Prediction of Preterm delivery by Electrohysterography,” *BMC Pregnancy Childbirth*, vol. 14, p. 192, Jun. 2014, doi: 10.1186/1471-2393-14-192.
[47] D. Alamedine, M. Khalil, and C. Marque, “Comparison of Different EHG Feature Selection Methods for the Detection of Preterm Labor,” *Computational and Mathematical Methods in Medicine*, Dec. 23, 2013. https://www.hindawi.com/journals/cmmm/2013/485684/.
[48] J. Terrien, T. Steingrimsdottir, C. Marque, and B. Karlsson, “Synchronization between EMG at Different Uterine Locations Investigated Using Time-Frequency Ridge Reconstruction: Comparison of Pregnancy and Labor Contractions,” *EURASIP J. Adv. Signal Process.*, vol. 2010, no. 1, Art. no. 1, Dec. 2010, doi: 10.1155/2010/242493.
[49] D. Alamedine, M. Khalil, and C. Marque, “Parameters extraction and monitoring in uterine EMG signals. Detection of preterm deliveries,” *IRBM*, vol. 34, no. 4, pp. 322–325, Nov. 2013, doi: 10.1016/j.irbm.2013.08.003.
[50] Z. Huang and M. Wang, “A review of electroencephalogram signal processing methods for brain-controlled robots,” *Cognitive Robotics*, vol. 1, pp. 111–124, Jan. 2021, doi: 10.1016/j.cogr.2021.07.001.
[51] W. J. E. P. Lammers, “The electrical activities of the uterus during pregnancy,” *Reprod Sci*, vol. 20, no. 2, pp. 182–189, Feb. 2013, doi: 10.1177/1933719112446082.

[52] W. J. E. P. Lammers *et al.*, “Patterns of electrical propagation in the intact pregnant guinea pig uterus,” *Am J Physiol Regul Integr Comp Physiol*, vol. 294, no. 3, pp. R919-928, Mar. 2008, doi: 10.1152/ajpregu.00704.2007.

[53] J. G. Planes, J. P. Morucci, H. Grandjean, and R. Favretto, “External recording and processing of fast electrical activity of the uterus in human parturition,” *Med Biol Eng Comput*, vol. 22, no. 6, pp. 585–591, Nov. 1984, doi: 10.1007/BF02443874.

[54] E. Mikkelsen, P. Johansen, A. Fuglsang-Frederiksen, and N. Uldbjerg, “Electrohysterography of labor contractions: propagation velocity and direction,” *Acta Obstet Gynecol Scand*, vol. 92, no. 9, pp. 1070–1078, Sep. 2013, doi: 10.1111/aogs.12190.

[55] L. Lange, A. Vaeggemose, P. Kidmose, E. Mikkelsen, N. Uldbjerg, and P. Johansen, “Velocity and Directionality of the Electrohysterographic Signal Propagation,” *PLOS ONE*, vol. 9, no. 1, p. e86775, Jan. 2014, doi: 10.1371/journal.pone.0086775.

[56] T. Y. Euliano, D. Marossero, M. T. Nguyen, N. R. Euliano, J. Principe, and R. K. Edwards, “Spatiotemporal electrohysterography patterns in normal and arrested labor,” *Am J Obstet Gynecol*, vol. 200, no. 1, p. 54.e1–7, Jan. 2009, doi: 10.1016/j.ajog.2008.09.008.

[57] C. S. Buhimschi, “Spatiotemporal electromyography during human labor to monitor propagation of the uterine contraction wave and diagnose dystocia,” *Am J Obstet Gynecol*, vol. 200, no. 1, pp. 1–3, Jan. 2009, doi: 10.1016/j.ajog.2008.09.007.

[58] C. E. Melton and J. T. Saldivar, “IMPULSE VELOCITY AND CONDUCTION PATHWAYS IN RAT MYOMETRIUM,” *Am J Physiol*, vol. 207, pp. 279–285, Aug. 1964, doi: 10.1152/ajplegacy.1964.207.2.279.

[59] W. J. Lammers, “Circulating excitations and re-entry in the pregnant uterus,” *Pflugers Arch*, vol. 433, no. 3, pp. 287–293, Jan. 1997, doi: 10.1007/s004240050279.

[60] W. J. Lammers, K. Arafat, A. el-Kays, and T. Y. el-Sharkawy, “Spatial and temporal variations in local spike propagation in the myometrium of the 17-day pregnant rat,” *Am J Physiol*, vol. 267, no. 5 Pt 1, pp. C1210-1223, Nov. 1994, doi: 10.1152/ajpcell.1994.267.5.C1210.

[61] S. Kanda and H. Kuriyama, “Specific features of smooth muscle cells recorded from the placental region of the myometrium of pregnant rats,” *J Physiol*, vol. 299, pp. 127–144, Feb. 1980, doi: 10.1113/jphysiol.1980.sp013115.

[62] E. E. Daniel and S. A. Renner, “Effect of the placenta on the electrical activity of the cat uterus in vivo and in vitro,” *Am J Obstet Gynecol*, vol. 80, pp. 229–244, Aug. 1960, doi: 10.1016/0002-9378(60)90118-6.

[63] C. Rabotti, M. Mischi, L. Beulen, G. Oei, and J. W. M. Bergmans, “Modeling and identification of the electrohysterographic volume conductor by high-density electrodes,” *IEEE Trans Biomed Eng*, vol. 57, no. 3, pp. 519–527, Mar. 2010, doi: 10.1109/TBME.2009.2035440.

[64] E. Bozler, “Action potentials of visceral smooth muscles and their relation to mechanical activity,” *Nihon Heikatsukin Gakkai Zasshi*, vol. 6, no. 2, pp. 63–65, Jun. 1970.

[65] M. Wikland and B. Lindblom, “Relationship between electrical and mechanical activity of the isolated term-pregnant human myometrium,” *Eur J Obstet Gynecol Reprod Biol*, vol. 20, no. 6, pp. 337–346, Dec. 1985, doi: 10.1016/0028-2243(85)90057-7.

[66] D. Escalona-Vargas, R. B. Govindan, A. Furdea, P. Murphy, C. L. Lowery, and H. Eswaran, “Characterizing the Propagation of Uterine Electrophysiological Signals Recorded with a Multi-Sensor Abdominal Array in Term Pregnancies,” *PLoS One*, vol. 10, no. 10, p. e0140894, 2015, doi: 10.1371/journal.pone.0140894.

[67] G. M. Wolfs and M. van Leeuwen, “Electromyographic observations on the human uterus during labour,” *Acta Obstet Gynecol Scand Suppl*, vol. 90, pp. 1–61, 1979, doi: 10.3109/00016347909156375.

[68] J. Gondry, C. Marque, J. Duchene, and D. Cabrol, “Electrohysterography during pregnancy: preliminary report,” *Biomed Instrum Technol*, vol. 27, no. 4, pp. 318–324, Aug. 1993.

[69] C. Marque, “Analyse de la dynamique des contractions utérines par électromyographie abdominale,”, 1987. /paper/Analyse-de-la-dynamique-des-contractions-ut39rines-Marque/a9355b5bc5cc6f58673065fca316102ff2202049.
[70] J. Duchene, C. Marque, and S. Planque, “Uterine EMG Signal : Propagation Analysis,” in [1990] Proceedings of the Twelfth Annual International Conference of the IEEE Engineering in Medicine and Biology Society, Nov. 1990, pp. 831–832. doi: 10.1109/IEMBS.1990.691421.
[71] M. O. Diab, “Classification des signaux EMG Utérins Afin de Détecter Les Accouchements Prématurés,” 2007. Available: https://www.semanticscholar.org/paper/Classification-des-signaux-EMG-Ut%C3%A9rins-Afin-de-Les-Diab/8d5e8850d1958a6ffbe68f94b126b651ea2b404b
[72] A. Dima, A. Diab, C. Muszynski, B. Karlsson, M. Khalil, and C. Marque, “Selection algorithm for parameters to characterize uterine EHG signals for the detection of preterm labor,” *Signal Image and Video Processing*, vol. 8, Jul. 2014, doi: 10.1007/s11760-014-0655-2.
[73] M. Hassan, J. Terrien, C. Muszynski, A. Alexandersson, C. Marque, and B. Karlsson, “Better pregnancy monitoring using nonlinear correlation analysis of external uterine electromyography,” *IEEE Trans Biomed Eng*, vol. 60, no. 4, pp. 1160–1166, Apr. 2013, doi: 10.1109/TBME.2012.2229279.
[74] C. Muszynski *et al.*, “[Evolution of electrohysterogram signals synchronization according to term of pregnancy: interest for preterm labor diagnosis].,” *Gynécologie, obstétrique & fertilité*, vol. 40, pp. 344–9, Apr. 2012.
[75] A. Diab, J. Laforet, B. Karlsson, and C. Marque, “Estimation of coupling and directionality between signals evidenced on physiological uterine EMG model and on real uterine EMG signals,” Sep. 2013, vol. 41. doi: 10.1007/978-3-319-00846-2_178.
[76] G. Nolte, O. Bai, L. Wheaton, Z. Mari, S. Vorbach, and M. Hallett, “Identifying true brain interaction from EEG data using the imaginary part of coherency,” *Clin Neurophysiol*, vol. 115, no. 10, pp. 2292–2307, Oct. 2004, doi: 10.1016/j.clinph.2004.04.029.
[77] P. Nunez *et al.*, “EEG coherency. I: Statistics, reference electrode, volume conduction, Laplacians, cortical imaging, and interpretation at multiple scales,” *Electroencephalography and Clinical Neurophysiology*, vol. 103, pp. 499–515, Dec. 1997.
[78] A. Diab, O. Falou, B. Karlsson, and C. Marque, “Effect of filtering on the classification rate of nonlinear analysis methods applied to uterine EMG signals,” Aug. 2015, vol. 2015, pp. 4182–4185. doi: 10.1109/EMBC.2015.7319316.
[79] S. Rihana, J. Santos, S. Mondie, and C. Marque, “Dynamical analysis of uterine cell electrical activity model,” *Conf Proc IEEE Eng Med Biol Soc*, vol. 2006, pp. 4179–4182, 2006, doi: 10.1109/IEMBS.2006.260288.
[80] L. Bursztyn, O. Eytan, A. J. Jaffa, and D. Elad, “Mathematical model of excitation-contraction in a uterine smooth muscle cell,” *Am J Physiol Cell Physiol*, vol. 292, no. 5, pp. C1816-1829, May 2007, doi: 10.1152/ajpcell.00478.2006.
[81] C. M. Hai and R. A. Murphy, “Cross-bridge phosphorylation and regulation of latch state in smooth muscle,” *Am J Physiol*, vol. 254, no. 1 Pt 1, pp. C99-106, Jan. 1988, doi: 10.1152/ajpcell.1988.254.1.C99.
[82] J. Verwaerde, J. Laforet, C. Marque, and A. Rassineux, “Statistical shape analysis of gravid uteri throughout pregnancy by a ray description technique,” *Med Biol Eng Comput*, vol. 59, no. 10, pp. 2165–2183, Oct. 2021, doi: 10.1007/s11517-021-02402-1.
[83] O. Sporns, G. Tononi, and R. Kötter, “The Human Connectome: A Structural Description of the Human Brain,” *PLoS Comput Biol*, vol. 1, no. 4, p. e42, Sep. 2005, doi: 10.1371/journal.pcbi.0010042.
[84] K. J. Friston, “Functional and effective connectivity in neuroimaging: A synthesis,” *Human Brain Mapping*, vol. 2, no. 1–2, pp. 56–78, 1994, doi: https://doi.org/10.1002/hbm.460020107.

[85] K. Lehnertz, “Assessing directed interactions from neurophysiological signals--an overview,” *Physiol Meas*, vol. 32, no. 11, pp. 1715–1724, Nov. 2011, doi: 10.1088/0967-3334/32/11/R01.
[86] K. Ansari-Asl, F. Wendling, J. J. Bellanger, and L. Senhadji, “Comparison of two estimators of time-frequency interdependencies between nonstationary signals: application to epileptic EEG,” *Conf Proc IEEE Eng Med Biol Soc*, vol. 2006, pp. 263–266, 2004, doi: 10.1109/IEMBS.2004.1403142.
[87] S. Boccaletti, V. Latora, Y. Moreno, M. Chavez, and D.-U. Hwang, “Complex networks: Structure and dynamics,” *Physics Reports*, vol. 424, no. 4, pp. 175–308, Feb. 2006, doi: 10.1016/j.physrep.2005.10.009.
[88] G. A. Pavlopoulos *et al.*, “Using graph theory to analyze biological networks,” *BioData Min*, vol. 4, p. 10, Apr. 2011, doi: 10.1186/1756-0381-4-10.
[89] M. Pellegrini, D. Haynor, and J. M. Johnson, “Protein interaction networks,” *Expert Rev Proteomics*, vol. 1, no. 2, pp. 239–249, Aug. 2004, doi: 10.1586/14789450.1.2.239.
[90] H. Jeong, B. Tombor, R. Albert, Z. N. Oltvai, and A. L. Barabási, “The large-scale organization of metabolic networks,” *Nature*, vol. 407, no. 6804, pp. 651–654, Oct. 2000, doi: 10.1038/35036627.
[91] E. Bullmore and O. Sporns, “Complex brain networks: graph theoretical analysis of structural and functional systems,” *Nat Rev Neurosci*, vol. 10, no. 3, pp. 186–198, Mar. 2009, doi: 10.1038/nrn2575.
[92] A. Majeed and I. Rauf, “Graph Theory: A Comprehensive Survey about Graph Theory Applications in Computer Science and Social Networks,” 2020. doi: 10.3390/inventions5010010.
[93] M. Rubinov and O. Sporns, “Complex network measures of brain connectivity: Uses and interpretations,” *NeuroImage*, vol. 52, no. 3, pp. 1059–1069, Sep. 2010, doi: 10.1016/j.neuroimage.2009.10.003.
[94] D. J. Watts and S. H. Strogatz, “Collective dynamics of ‘small-world’ networks,” *Nature*, vol. 393, no. 6684, Art. no. 6684, Jun. 1998, doi: 10.1038/30918.
[95] H. Small, “Co-citation in the scientific literature: A new measure of the relationship between two documents,” *Journal of the American Society for Information Science*, vol. 24, no. 4, pp. 265–269, 1973, doi: https://doi.org/10.1002/asi.4630240406.
[96] S. Maslov and S. Redner, “Promise and Pitfalls of Extending Google’s PageRank Algorithm to Citation Networks,” *J. Neurosci.*, vol. 28, no. 44, pp. 11103–11105, Oct. 2008, doi: 10.1523/JNEUROSCI.0002-08.2008.
[97] Y. Ding, E. Yan, A. Frazho, and J. Caverlee, “PageRank for ranking authors in co-citation networks,” *Journal of the American Society for Information Science and Technology*, vol. 60, no. 11, pp. 2229–2243, 2009, doi: https://doi.org/10.1002/asi.21171.
[98] N. Ma, J. Guan, and Y. Zhao, “Bringing PageRank to the citation analysis,” *Information Processing & Management*, vol. 44, no. 2, pp. 800–810, Mar. 2008, doi: 10.1016/j.ipm.2007.06.006.
[99] E. J. Yates and L. C. Dixon, “PageRank as a method to rank biomedical literature by importance,” *Source Code for Biology and Medicine*, vol. 10, no. 1, p. 16, Dec. 2015, doi: 10.1186/s13029-015-0046-2.
[100] A. Bavelas, “A Mathematical Model for Group Structures,” *Human Organization*, vol. 7, no. 3, pp. 16–30, Mar. 2009, doi: 10.17730/humo.7.3.f4033344851gl053.
[101] S. K. Raghavan Unnithan, B. Kannan, and M. Jathavedan, “Betweenness Centrality in Some Classes of Graphs,” *International Journal of Combinatorics*, Dec. 25, 2014. https://www.hindawi.com/journals/ijcom/2014/241723/.
[102] L. C. Freeman, “A Set of Measures of Centrality Based on Betweenness,” *Sociometry*, vol. 40, no. 1, pp. 35–41, 1977, doi: 10.2307/3033543.

[103] L. Leydesdorff, "'Betweenness Centrality' as an Indicator of the 'Interdisciplinarity' of Scientific Journals," *Journal of the American Society for Information Science and Technology*, vol. 58, Jul. 2007, doi: 10.1002/asi.20614.
[104] A. Plutov and M. Segal, "The delta-betweenness centrality," in *2013 IEEE 24th Annual International Symposium on Personal, Indoor, and Mobile Radio Communications (PIMRC)*, Sep. 2013, pp. 3376–3380. doi: 10.1109/PIMRC.2013.6666731.
[105] M. Deriche, "Feature Selection using Ant Colony Optimization," in *2009 6th International Multi-Conference on Systems, Signals and Devices*, Mar. 2009, pp. 1–4. doi: 10.1109/SSD.2009.4956825.
[106] S. Ding, "Feature Selection Based F-Score and ACO Algorithm in Support Vector Machine," in *2009 Second International Symposium on Knowledge Acquisition and Modeling*, Nov. 2009, vol. 1, pp. 19–23. doi: 10.1109/KAM.2009.137.
[107] Huan Liu and Lei Yu, "Toward integrating feature selection algorithms for classification and clustering," *IEEE Transactions on Knowledge and Data Engineering*, vol. 17, no. 4, pp. 491–502, Apr. 2005, doi: 10.1109/TKDE.2005.66.
[108] D. Alamedine, "Selection of EHG parameter characteristics for the classification of uterine contractions,", 2015. /paper/Selection-of-EHG-parameter-characteristics-for-the-Alamedine/894db018888443d4e1dc14ebbbc772c47ec8e466.
[109] K. Wang, "Computational Intelligence in Agile Manufacturing Engineering," in *Agile Manufacturing: The 21st Century Competitive Strategy*, A. Gunasekaran, Ed. Oxford: Elsevier Science Ltd, 2001, pp. 297–315. doi: 10.1016/B978-008043567-1/50016-4.
[110] X. E. Gros, "2 - Data Fusion – A Review," in *NDT Data Fusion*, X. E. Gros, Ed. Oxford: Butterworth-Heinemann, 1997, pp. 5–42. doi: 10.1016/B978-034067648-6/50004-9.
[111] A. M. Turing, "I.—COMPUTING MACHINERY AND INTELLIGENCE," *Mind*, vol. LIX, no. 236, pp. 433–460, Oct. 1950, doi: 10.1093/mind/LIX.236.433.
[112] M. Haenlein and A. Kaplan, "A Brief History of Artificial Intelligence: On the Past, Present, and Future of Artificial Intelligence," California Management Review, vol. 61, p. 000812561986492, Jul. 2019, doi: 10.1177/0008125619864925
[113] B. Rao, "The Role of Artificial Intelligence (AI) in Condition Monitoring and Diagnostic Engineering Management (COMADEM): A Literature Survey," *American Journal of Artificial Intelligence*, vol. 5, p. 17, Jan. 2021, doi: 10.11648/j.ajai.20210501.12.
[114] A. K. Raz, J. Llinas, R. Mittu, and W. F. Lawless, "Chapter 12 - Engineering for emergence in information fusion systems: A review of some challenges☆," in *Human-Machine Shared Contexts*, W. F. Lawless, R. Mittu, and D. A. Sofge, Eds. Academic Press, 2020, pp. 241–255. doi: 10.1016/B978-0-12-820543-3.00012-2.
[115] K. Pawluszek-Filipiak and A. Borkowski, "On the Importance of Train–Test Split Ratio of Datasets in Automatic Landslide Detection by Supervised Classification," *Remote Sensing*, vol. 12, no. 18, Art. no. 18, Jan. 2020, doi: 10.3390/rs12183054.
[116] R. Jafari-Marandi, "Supervised or unsupervised learning? Investigating the role of pattern recognition assumptions in the success of binary predictive prescriptions," *Neurocomputing*, vol. 434, pp. 165–193, Apr. 2021, doi: 10.1016/j.neucom.2020.12.063.
[117] Z. Zhang, "A gentle introduction to artificial neural networks," Annals of Translational Medicine, vol. 4, no. 19, Art. no. 19, Oct. 2016, doi: 10.21037/atm.2016.06.20.
[118] E. K. Karuiru, G. O. Orwa, and J. M. Kihoro, "Sarima Versus Time Lagged Feedforward Neural Networks in Forecasting Precipitation," *American Journal of Theoretical and Applied Statistics*, vol. 5, no. 6, Art. no. 6, Nov. 2016, doi: 10.11648/j.ajtas.20160506.15.
[119] F. Liu, P. Du, F. Weng, and J. Qu, "Use clustering to improve neural network in financial time series prediction," Sep. 2007, pp. 89–93. doi: 10.1109/ICNC.2007.796.
[120] B. Yuen, M. T. Hoang, X. Dong, and T. Lu, "Universal activation function for machine learning," *Sci Rep*, vol. 11, no. 1, p. 18757, Sep. 2021, doi: 10.1038/s41598-021-96723-8.

[121] F. J. RICHARDS, “A Flexible Growth Function for Empirical Use,” *Journal of Experimental Botany*, vol. 10, no. 29, pp. 290–300, 1959.
[122] M. M. Fischer, “Neural Networks for Spatial Data Analysis,” in *The SAGE Handbook of Spatial Analysis*, 1 Oliver’s Yard, 55 City Road, London England EC1Y 1SP United Kingdom: SAGE Publications, Ltd, 2009, pp. 375–396. doi: 10.4135/9780857020130.n20.
[123] Z. Ali *et al.*, “Forecasting Drought Using Multilayer Perceptron Artificial Neural Network Model,” *Advances in Meteorology*, May 02, 2017. https://www.hindawi.com/journals/amete/2017/5681308/.
[124] A. Hashemi Fath, F. Madanifar, and M. Abbasi, “Implementation of multilayer perceptron (MLP) and radial basis function (RBF) neural networks to predict solution gas-oil ratio of crude oil systems,” *Petroleum*, vol. 6, no. 1, pp. 80–91, Mar. 2020, doi: 10.1016/j.petlm.2018.12.002.
[125] T. Silva, P. Siqueira, C. Beneti, M. Buzzi, and L. Calvetti, “Identification of Severe Weather Event with 3D meteorological radar and MLP,” Jan. 2017. doi: 10.20906/CPS/CILAMCE2017-0368.
[126] H. Bisgin *et al.*, “Comparing SVM and ANN based Machine Learning Methods for Species Identification of Food Contaminating Beetles,” *Scientific Reports*, vol. 8, no. 1, Art. no. 1, Apr. 2018, doi: 10.1038/s41598-018-24926-7.
[127] S. HUANG, N. CAI, P. P. PACHECO, S. NARANDES, Y. WANG, and W. XU, “Applications of Support Vector Machine (SVM) Learning in Cancer Genomics,” *Cancer Genomics Proteomics*, vol. 15, no. 1, pp. 41–51, Dec. 2017, doi: 10.21873/cgp.20063.
[128] N. Bacaër, “Verhulst and the logistic equation (1838),” Jan. 2011, doi: 10.1007/978-0-85729-115-8_6.
[129] E. Y. Boateng and D. Abaye, “A Review of the Logistic Regression Model with Emphasis on Medical Research,” *Journal of Data Analysis and Information Processing*, vol. 07, pp. 190–207, Jan. 2019, doi: 10.4236/jdaip.2019.74012.
[130] A. Borucka, “Logistic regression in modeling and assessment of transport services,” *Open Engineering*, vol. 10, no. 1, pp. 26–34, Jan. 2020, doi: 10.1515/eng-2020-0029.
[131] G. Battineni, G. G. Sagaro, C. Nalini, F. Amenta, and S. K. Tayebati, “Comparative Machine-Learning Approach: A Follow-Up Study on Type 2 Diabetes Predictions by Cross-Validation Methods,” Machines, vol. 7, no. 4, Art. no. 4, Dec. 2019, doi: 10.3390/machines7040074.
[132] J. Thomas and L. Sael, “Overview of integrative analysis methods for heterogeneous data,” *2015 International Conference on Big Data and Smart Computing, BIGCOMP 2015*, pp. 266–270, Mar. 2015, doi: 10.1109/35021BIGCOMP.2015.7072811.
[133] A. P. Wibawa *et al.*, “Naïve Bayes Classifier for Journal Quartile Classification,” *International Journal of Recent Contributions from Engineering, Science & IT (iJES)*, vol. 7, no. 2, Art. no. 2, Jun. 2019.
[134] L. Breiman, “Random Forests,” *Machine Learning*, vol. 45, no. 1, pp. 5–32, Oct. 2001, doi: 10.1023/A:1010933404324.
[135] R. Rahman, S. R. Dhruba, S. Ghosh, and R. Pal, “Functional random forest with applications in dose-response predictions,” *Scientific Reports*, vol. 9, no. 1, Art. no. 1, Feb. 2019, doi: 10.1038/s41598-018-38231-w.
[136] O. González-Recio, J. A. Jiménez-Montero, and R. Alenda, “The gradient boosting algorithm and random boosting for genome-assisted evaluation in large data sets,” *Journal of Dairy Science*, vol. 96, no. 1, pp. 614–624, Jan. 2013, doi: 10.3168/jds.2012-5630.
[137] A. Carrio, C. Sampedro, A. Rodriguez-Ramos, and P. Campoy, “A Review of Deep Learning Methods and Applications for Unmanned Aerial Vehicles,” *Journal of Sensors*, Aug. 14, 2017. https://www.hindawi.com/journals/js/2017/3296874/.
[138] M. M. Najafabadi, F. Villanustre, T. M. Khoshgoftaar, N. Seliya, R. Wald, and E. Muharemagic, “Deep learning applications and challenges in big data analytics,” *Journal of Big Data*, vol. 2, no. 1, p. 1, Feb. 2015, doi: 10.1186/s40537-014-0007-7.

[139] H. Salehinejad, S. Sankar, J. Barfett, E. Colak, and S. Valaee, “Recent Advances in Recurrent Neural Networks,” Dec. 2017.
[140] A. Murad and J.-Y. Pyun, “Deep Recurrent Neural Networks for Human Activity Recognition,” *Sensors*, vol. 17, p. 2556, Nov. 2017, doi: 10.3390/s17112556.
[141] C. McDaniel and S. Quinn, “Developing a Start-to-Finish Pipeline for Accelerometer-Based Activity Recognition Using Long Short-Term Memory Recurrent Neural Networks,” Jan. 2018, pp. 31–40. doi: 10.25080/Majora-4af1f417-005.
[142] X.-H. Le, H. V. Ho, G. Lee, and S. Jung, “Application of Long Short-Term Memory (LSTM) Neural Network for Flood Forecasting,” *Water*, vol. 11, no. 7, Art. no. 7, Jul. 2019, doi: 10.3390/w11071387.
[143] J. Qiu, B. Wang, and C. Zhou, “Forecasting stock prices with long-short term memory neural network based on attention mechanism,” *PLOS ONE*, vol. 15, no. 1, p. e0227222, Jan. 2020, doi: 10.1371/journal.pone.0227222.
[144] M. H. Zweig and G. Campbell, “Receiver-operating characteristic (ROC) plots: a fundamental evaluation tool in clinical medicine,” *Clin Chem*, vol. 39, no. 4, pp. 561–577, Apr. 1993.
[145] J. A. Swets, “Indices of discrimination or diagnostic accuracy: their ROCs and implied models,” *Psychol Bull*, vol. 99, no. 1, pp. 100–117, Jan. 1986.
[146] N. A. Obuchowski, “ROC Analysis,” *American Journal of Roentgenology*, vol. 184, no. 2, pp. 364–372, Feb. 2005, doi: 10.2214/ajr.184.2.01840364.
[147] S. Visa, B. Ramsay, A. Ralescu, and E. Knaap, “Confusion Matrix-based Feature Selection.,” Jan. 2011, vol. 710, pp. 120–127.
[148] B. Xia, H. Zhang, Q. Li, and T. Li, “PETs: A Stable and Accurate redictor of Protein-Protein Interacting Sites Based on xtremely-Randomized ree,” *IEEE Transactions on NanoBioscience*, vol. 14, pp. 1–1, Nov. 2015, doi: 10.1109/TNB.2015.2491303.
[149] Y. Skaik, “The bread and butter of statistical analysis ‘t-test’: Uses and misuses,” *Pak J Med Sci*, vol. 31, no. 6, pp. 1558–1559, 2015, doi: 10.12669/pjms.316.8984.
[150] A. Alexandersson, T. Steingrimsdottir, jérémy Terrien, C. Marque, and B. Karlsson, “The Icelandic 16-electrode electrohysterogram database,” *Scientific Data*, vol. 2, p. 150017, Apr. 2015, doi: 10.1038/sdata.2015.17.
[151] N. Nader *et al.*, “Graph analysis of uterine networks using EHG source connectivity,” in *2017 Fourth International Conference on Advances in Biomedical Engineering (ICABME)*, Oct. 2017, pp. 1–4. doi: 10.1109/ICABME.2017.8167554.
[152] A. Bogdanchikov, M. Zhaparov, and R. Suliyev, “Python to learn programming,” *Journal of Physics Conference Series*, vol. 423, p. 2027, Apr. 2013, doi: 10.1088/1742-6596/423/1/012027.
[153] D. Ibrahim, “Engineering simulation with MATLAB: improving teaching and learning effectiveness,” *Procedia Computer Science*, vol. 3, pp. 853–858, Jan. 2011, doi: 10.1016/j.procs.2010.12.140.
[154] K. B. el Dine, C. Marque, N. Nader, W. Falou, and M. Khalil, “Pregnancy Labor classification using neural network based analysis,” in *2019 Fifth International Conference on Advances in Biomedical Engineering (ICABME)*, Oct. 2019, pp. 1–4. doi: 10.1109/ICABME47164.2019.8940167.
[155] P. Sharma and A. Singh, “Era of deep neural networks: A review,” in *2017 8th International Conference on Computing, Communication and Networking Technologies (ICCCNT)*, Jul. 2017, pp. 1–5. doi: 10.1109/ICCCNT.2017.8203938.
[156] D. S. Bassett, M. A. Porter, N. F. Wymbs, S. T. Grafton, J. M. Carlson, and P. J. Mucha, “Robust detection of dynamic community structure in networks,” *Chaos*, vol. 23, no. 1, p. 013142, Mar. 2013, doi: 10.1063/1.4790830.
[157] V. D. Blondel, J.-L. Guillaume, R. Lambiotte, and E. Lefebvre, “Fast unfolding of communities in large networks,” *J. Stat. Mech.*, vol. 2008, no. 10, p. P10008, Oct. 2008, doi: 10.1088/1742-5468/2008/10/P10008.

[158] H. Trussell, “Maximum power signal restoration,” *IEEE Transactions on Acoustics, Speech, and Signal Processing*, vol. 29, no. 5, pp. 1059–1061, Oct. 1981, doi: 10.1109/TASSP.1981.1163682.
[159] M. P. G. C. Vinken, C. Rabotti, M. Mischi, J. O. E. H. van Laar, and S. G. Oei, “Nifedipine-Induced Changes in the Electrohysterogram of Preterm Contractions: Feasibility in Clinical Practice,” *Obstetrics and Gynecology International*, vol. 2010, p. e325635, Jun. 2010, doi: 10.1155/2010/325635.
[160] P. Tewarie *et al.*, “Tracking dynamic brain networks using high temporal resolution MEG measures of functional connectivity,” *NeuroImage*, vol. 200, pp. 38–50, Oct. 2019, doi: 10.1016/j.neuroimage.2019.06.006.
[161] D. Alamedine, C. Marque, and M. Khalil, “Channel selection for monovariate analysis on EHG,” in *2015 International Conference on Advances in Biomedical Engineering (ICABME)*, Sep. 2015, pp. 85–88. doi: 10.1109/ICABME.2015.7323257.
[162] P. Gao *et al.*, “Comparison of electrohysterogram signal measured by surface electrodes with different designs: A computational study with dipole band and abdomen models,” *Sci Rep*, vol. 7, p. 17282, Dec. 2017, doi: 10.1038/s41598-017-17109-3.
[163] F. Ahmed, Y. Ali, and S. Shamsuddin, “Using K-Fold Cross Validation Proposed Models for Spikeprop Learning Enhancements,” *International Journal of Engineering and Technology(UAE)*, vol. 7, pp. 145–151, Oct. 2018, doi: 10.14419/ijet.v7i4.11.20790.

Annex A: Consensus matrices

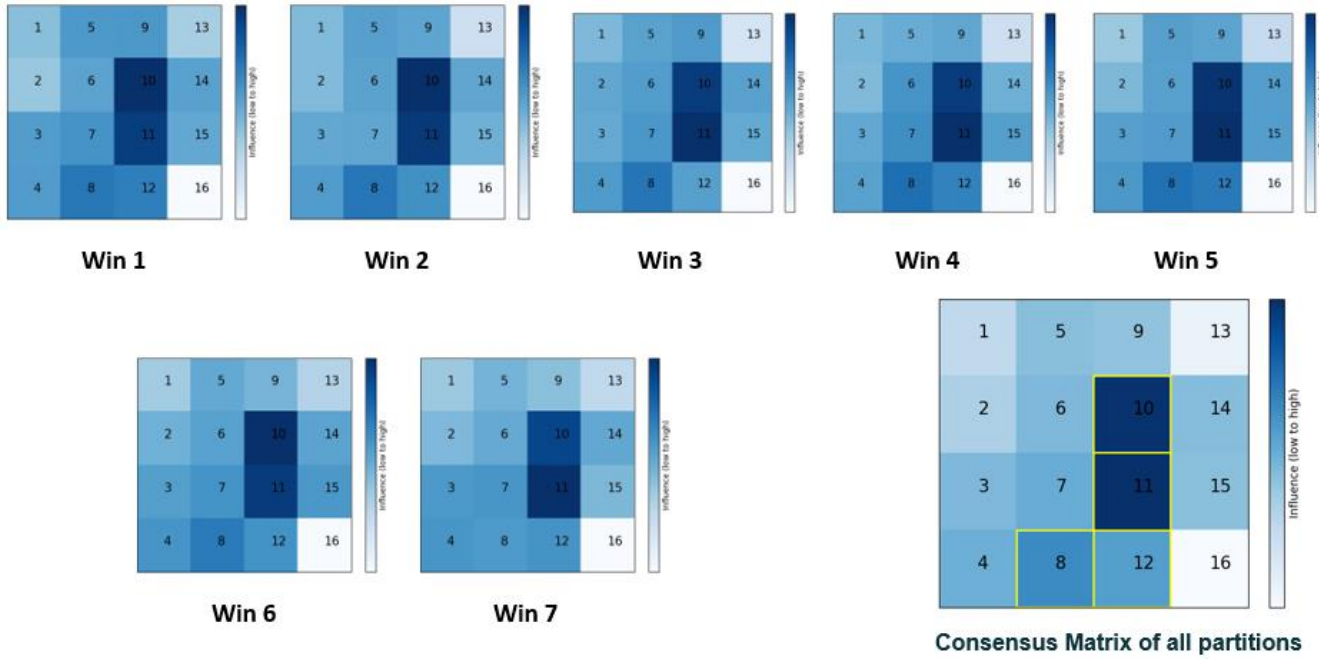

Figure A.1 Consensus matrices of each window using R2

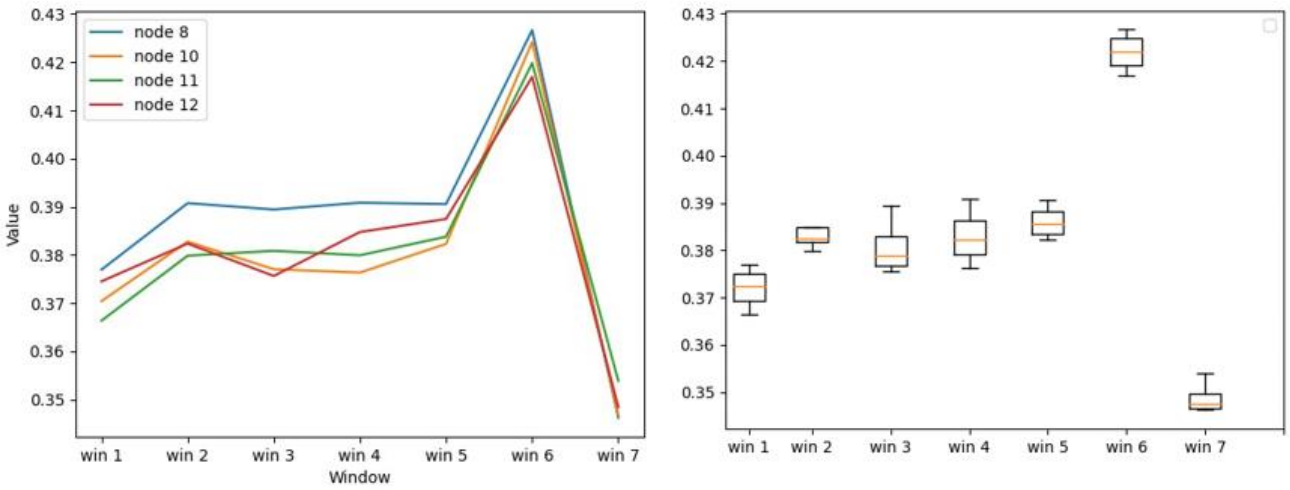

Figure A.2 Analyses of each window for the methods R2

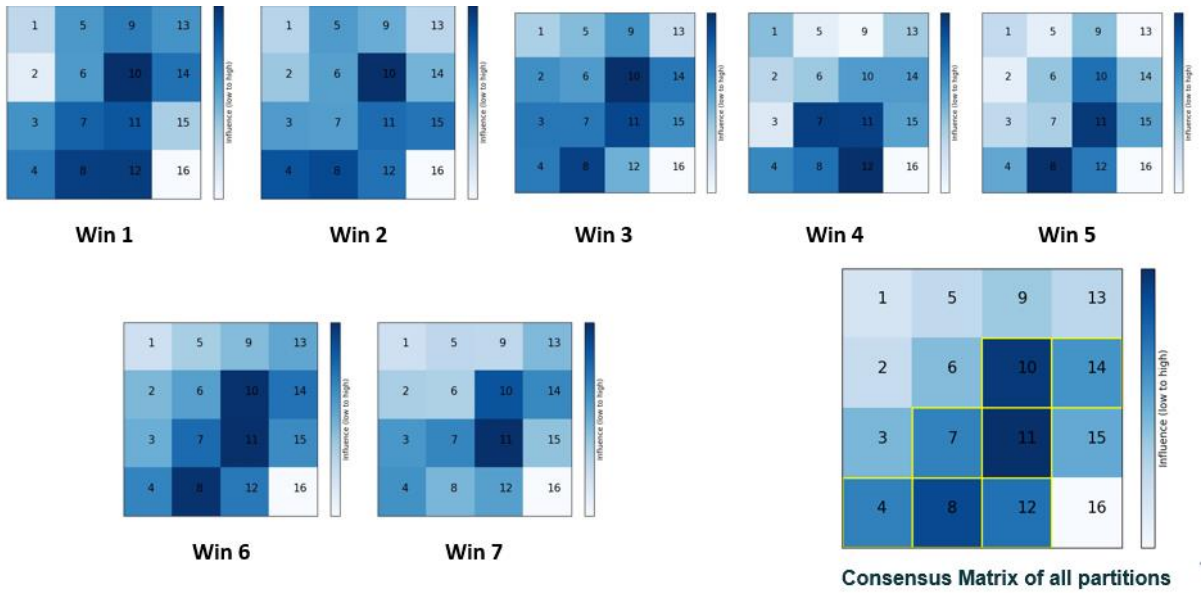

Figure A.3 Consensus matrices of each window using R2(Str)

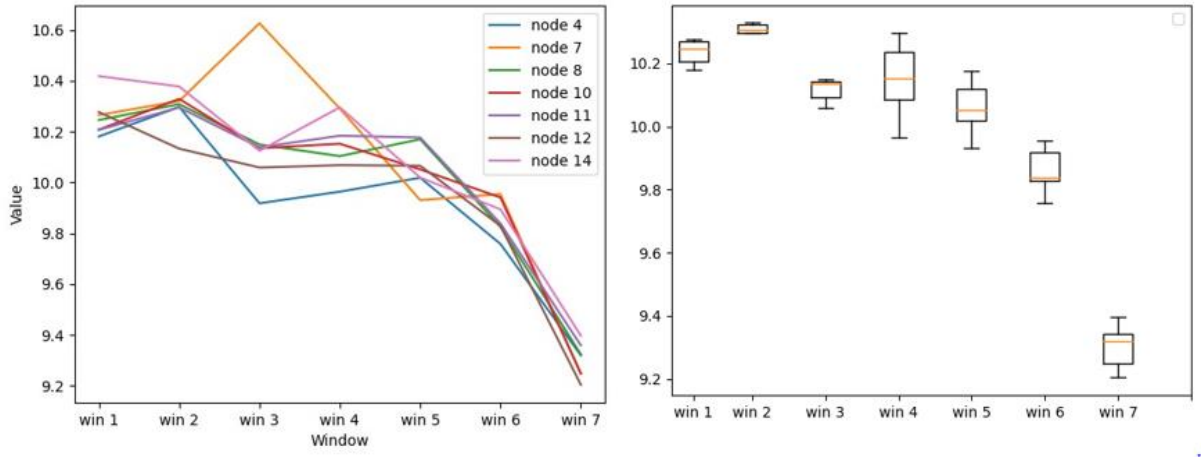

Figure A.4 Analyses of each window for the methods R2(Str)

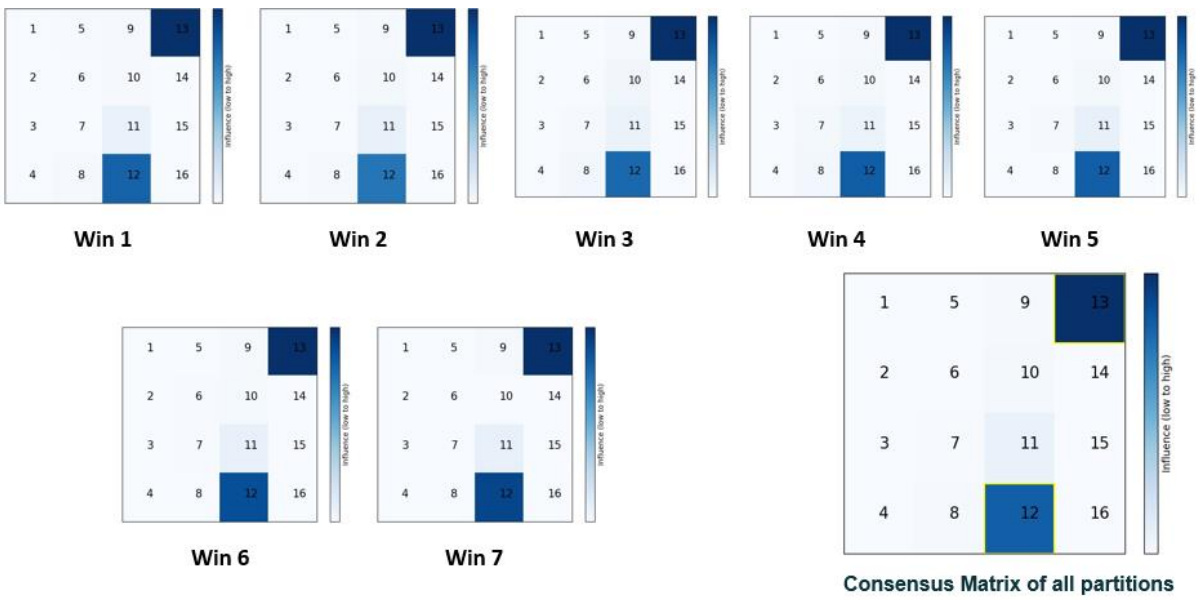

Figure A.5 Consensus matrices of each window using R2(Eff

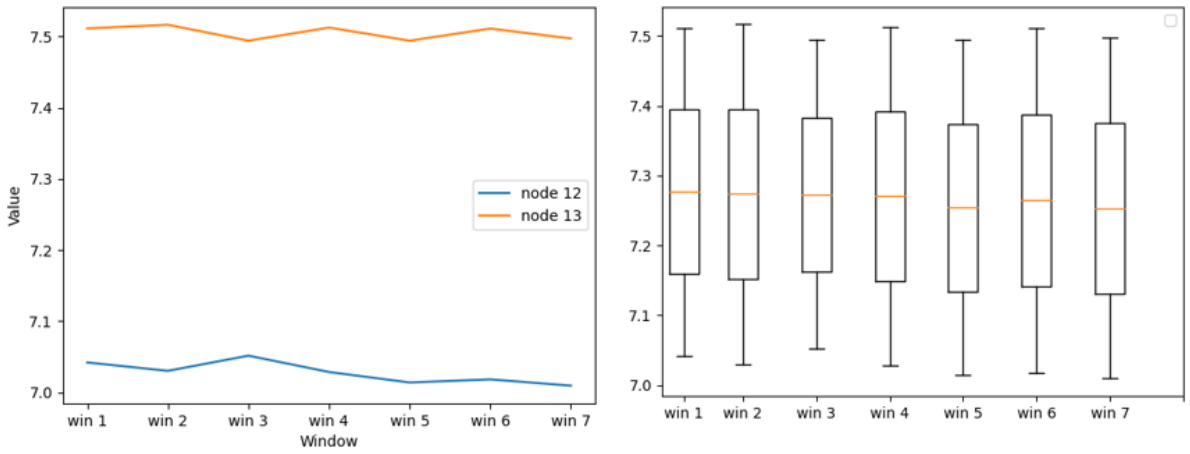

Figure A.6 Analyses of each window for the methods R2(Eff

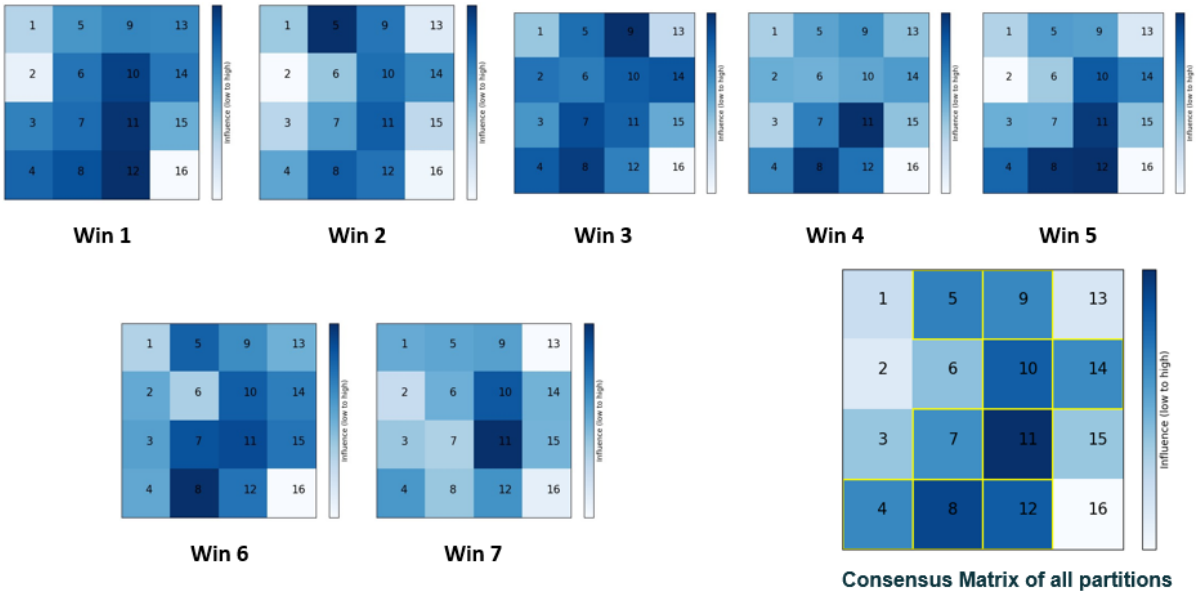

Figure A.7 Consensus matrices of each window using R2(PR)

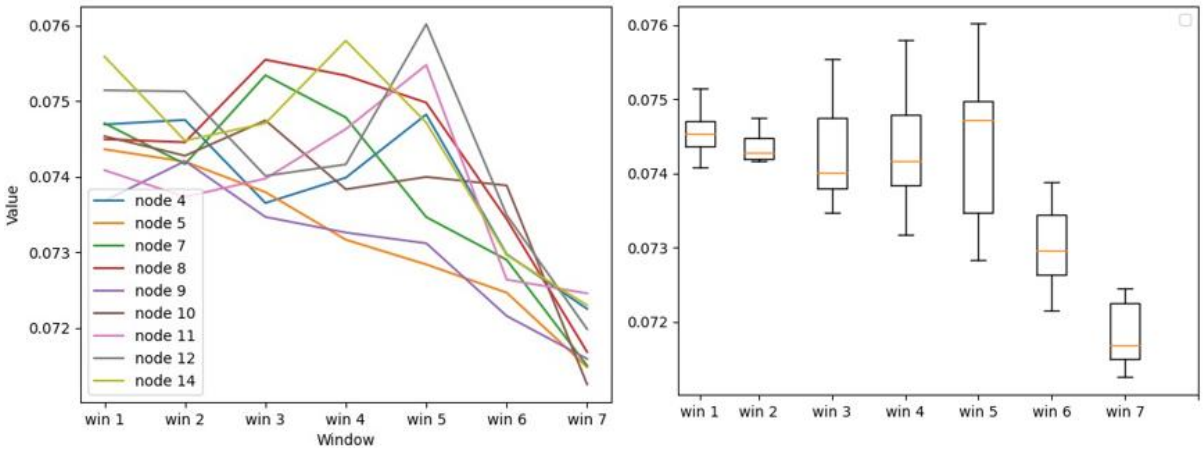

Figure A.8 Analyses of each window for the methods R2(PR)

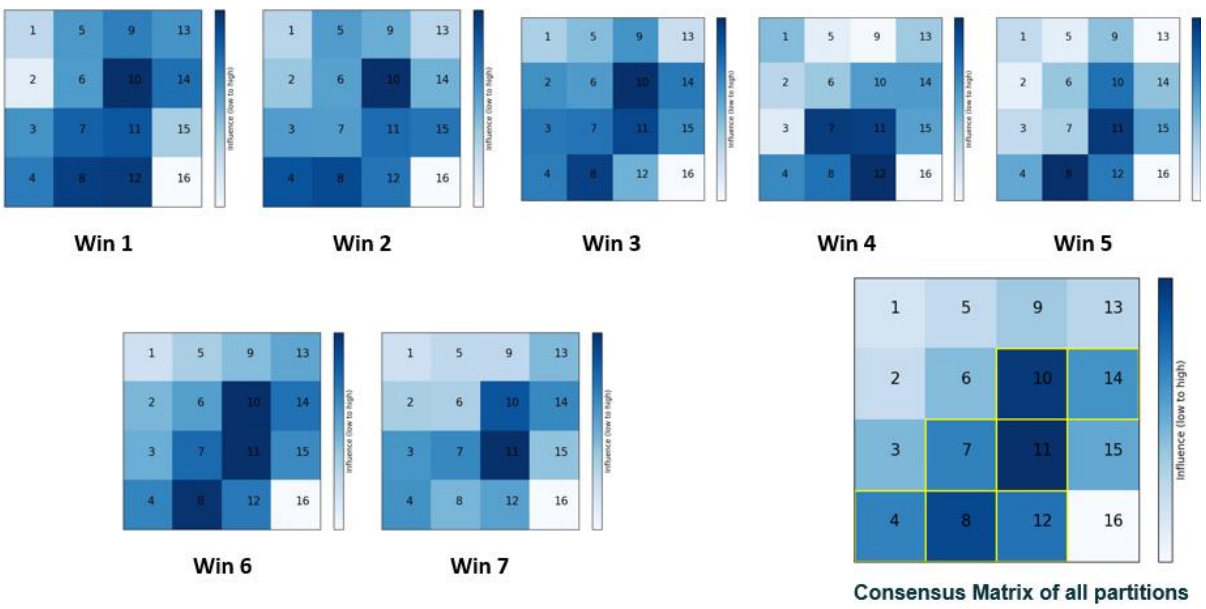

Figure A.9 Consensus matrices of each window using R2(BC)

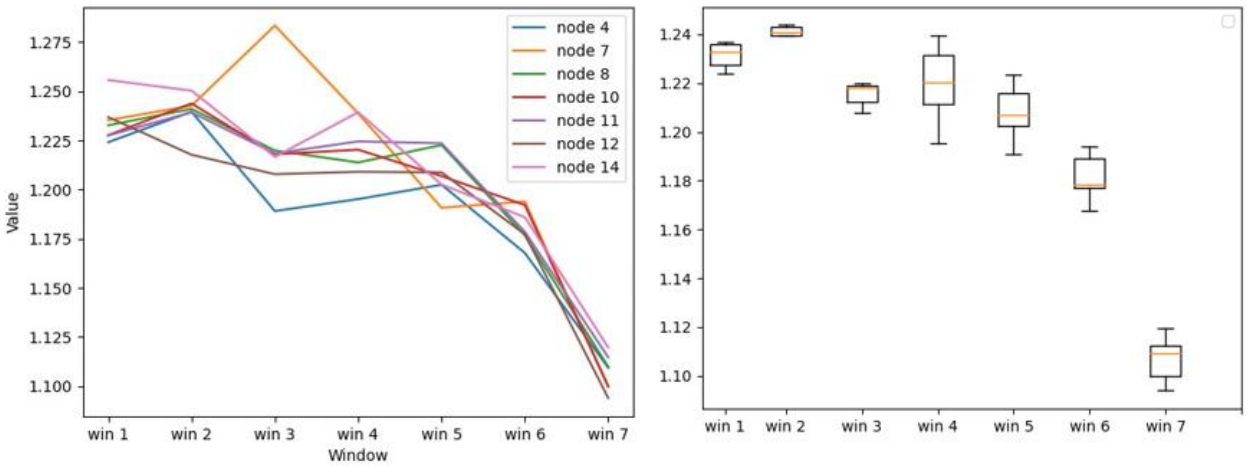

Figure A.10 Analyses of each window for the methods R2(BC)

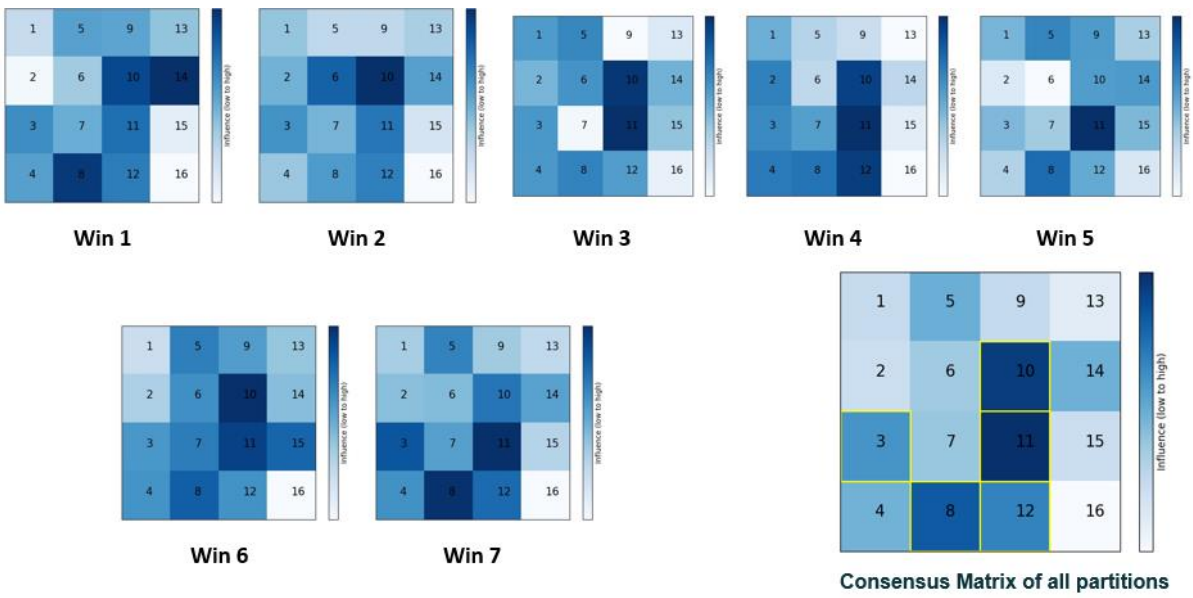

Figure A.11 Consensus matrices of each window using R2(CC)

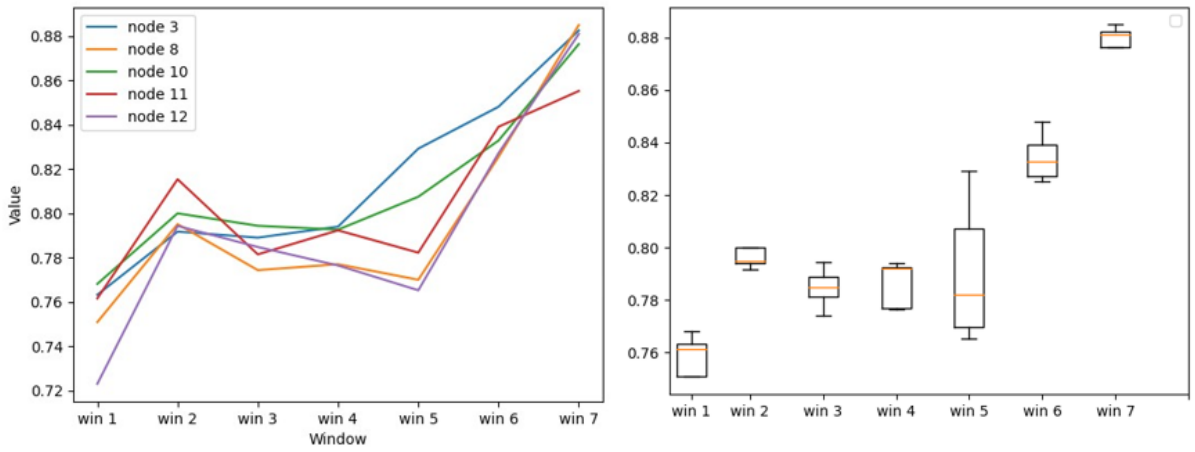

Figure A.12 Analyses of each window for the methods R2(CC)

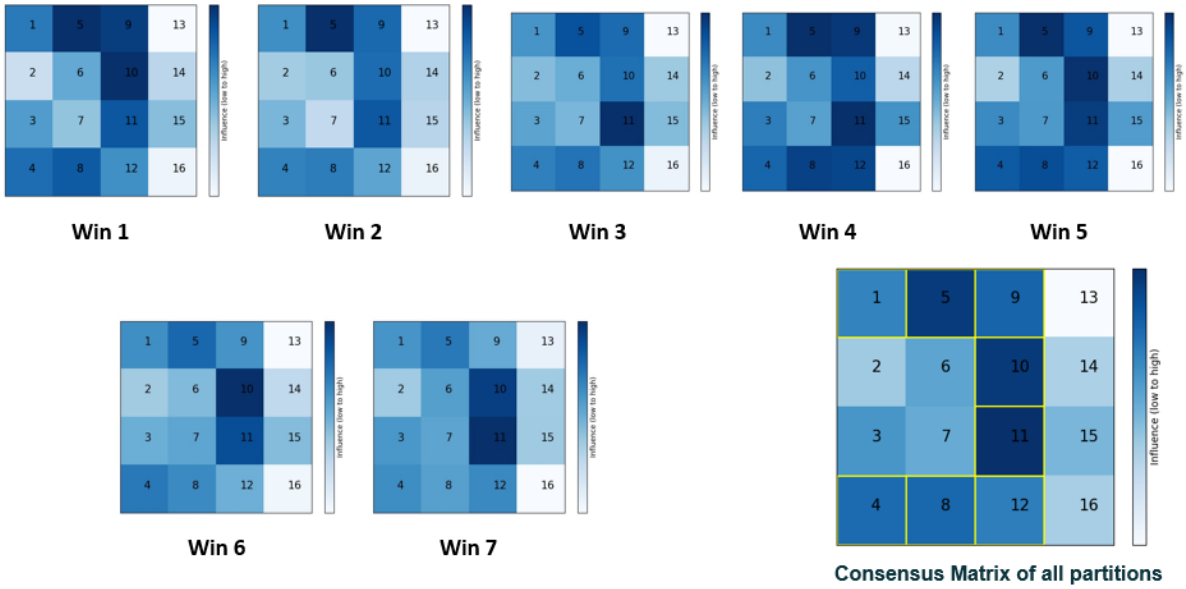

Figure A.13 Consensus matrices of each window using H2

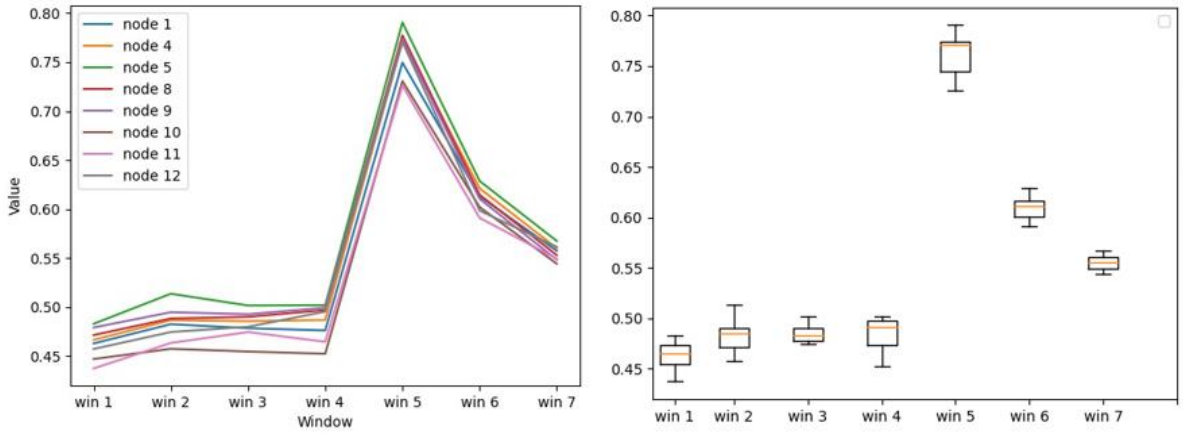

Figure A.14 Analyses of each window for the methods H2

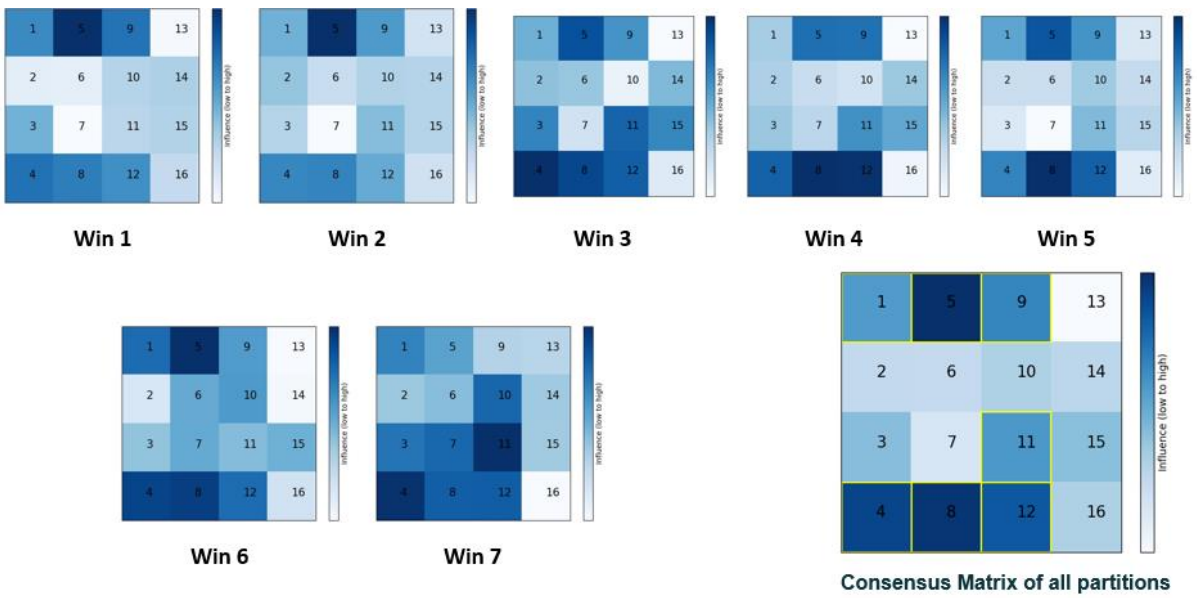

Figure A.15 Consensus matrices of each window using H2(Str)

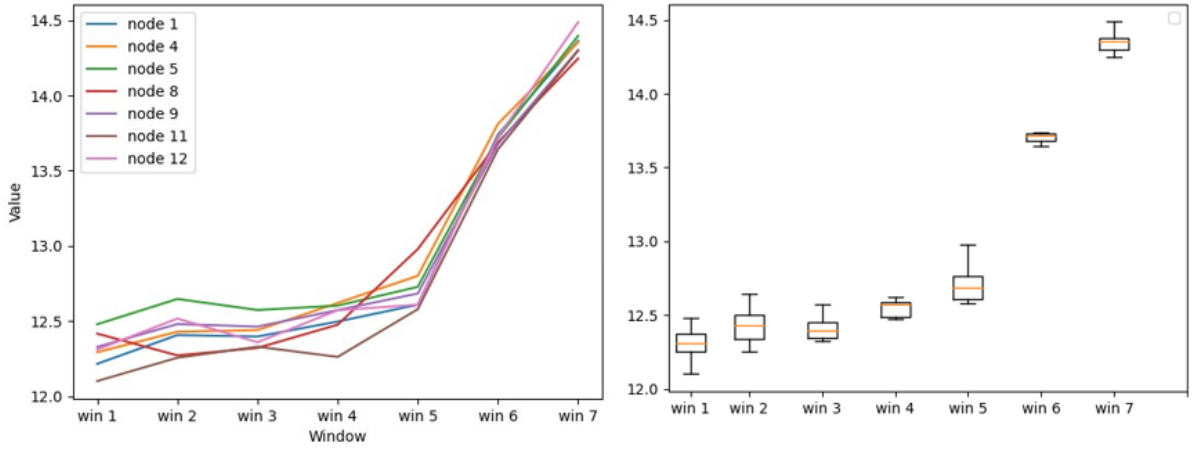

Figure A.16 Analyses of each window for the methods H2(Str)

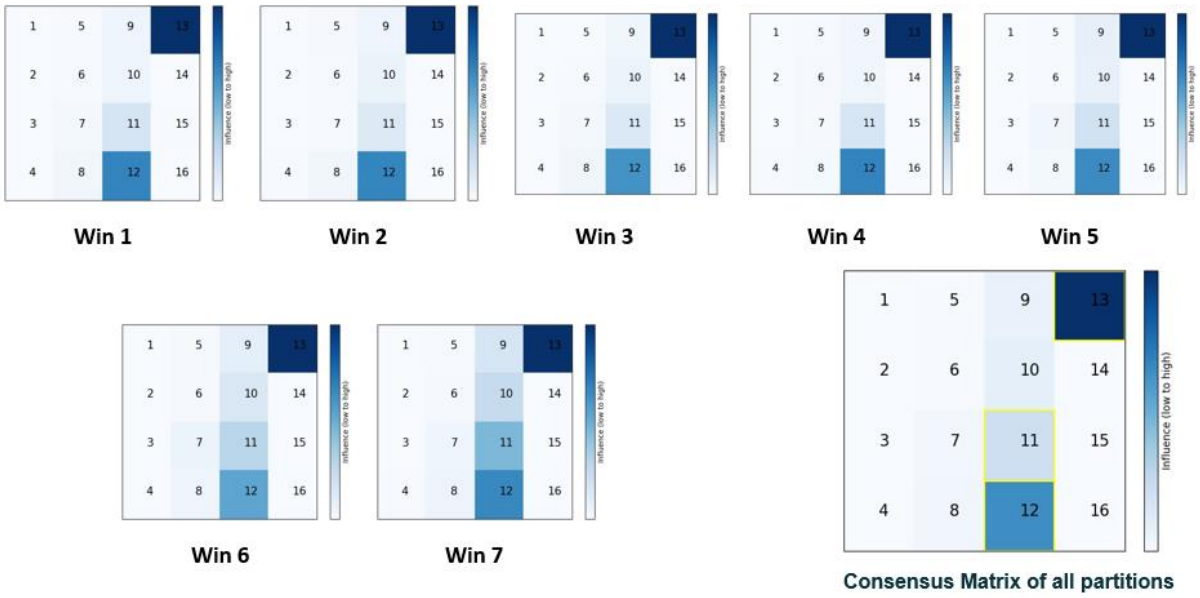

Figure A.17 Consensus matrices of each window using H2(Eff

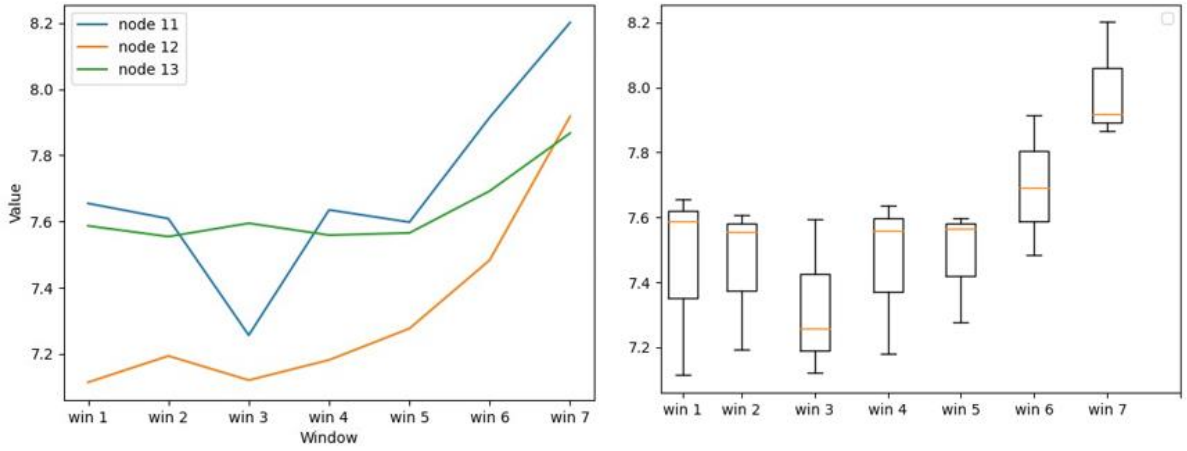

Figure A.18 Analyses of each window for the methods H2(Eff

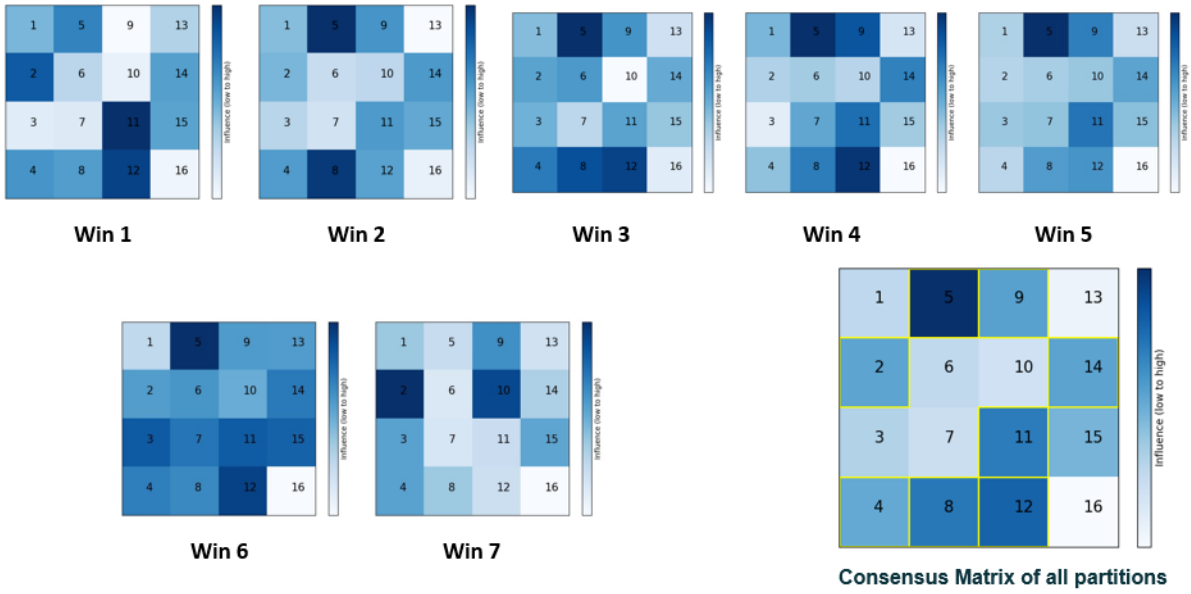

Figure A.19 Consensus matrices of each window using H2(PR)

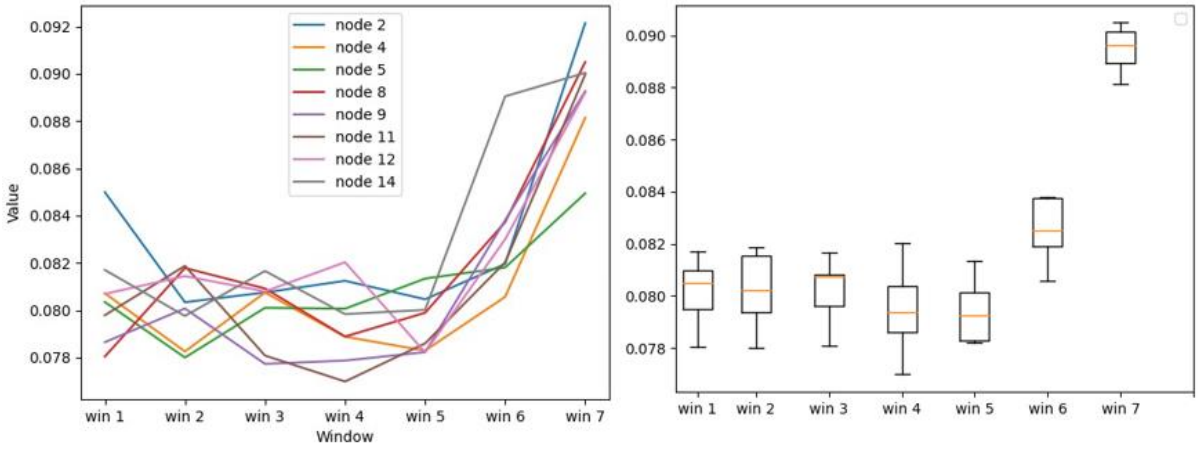

Figure A.20 Analyses of each window for the methods H2(PR)

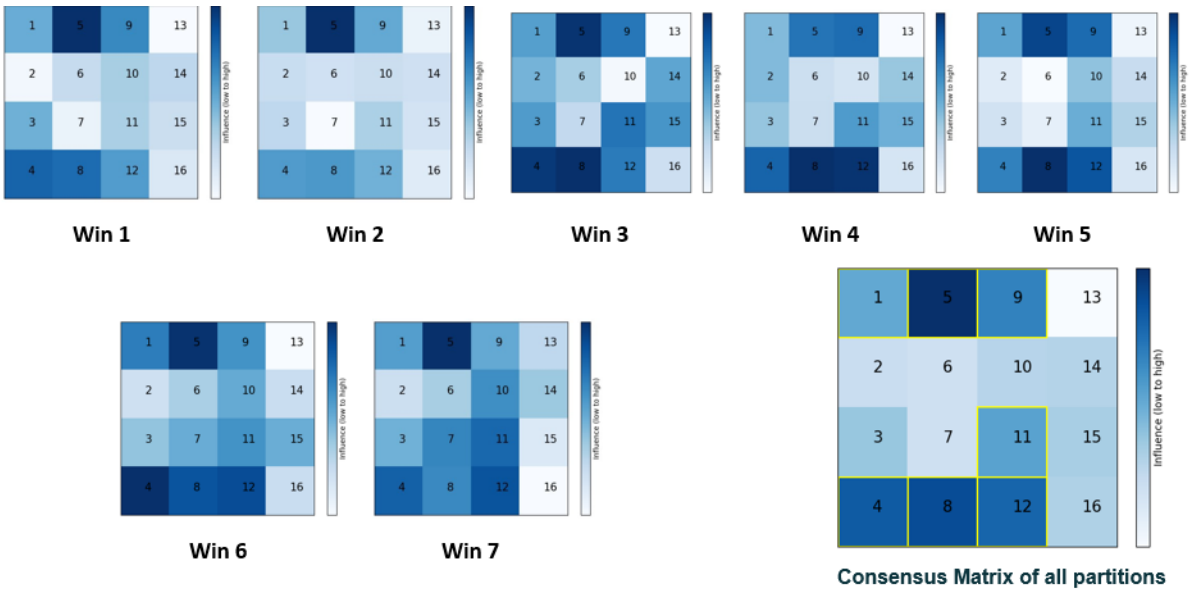

Figure A.21 Consensus matrices of each window using H2(BC)

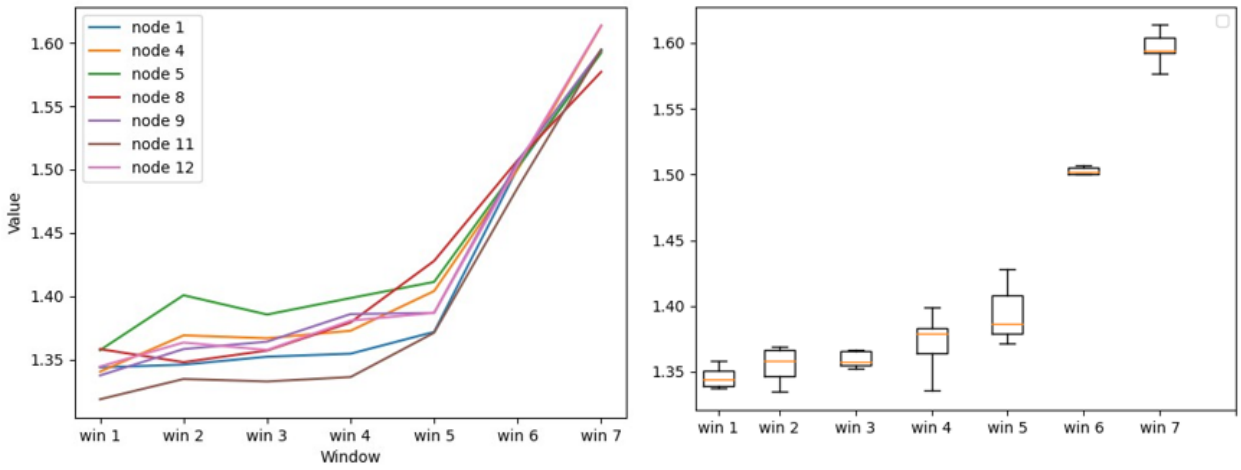

Figure A.22 Analyses of each window for the methods H2(BC)

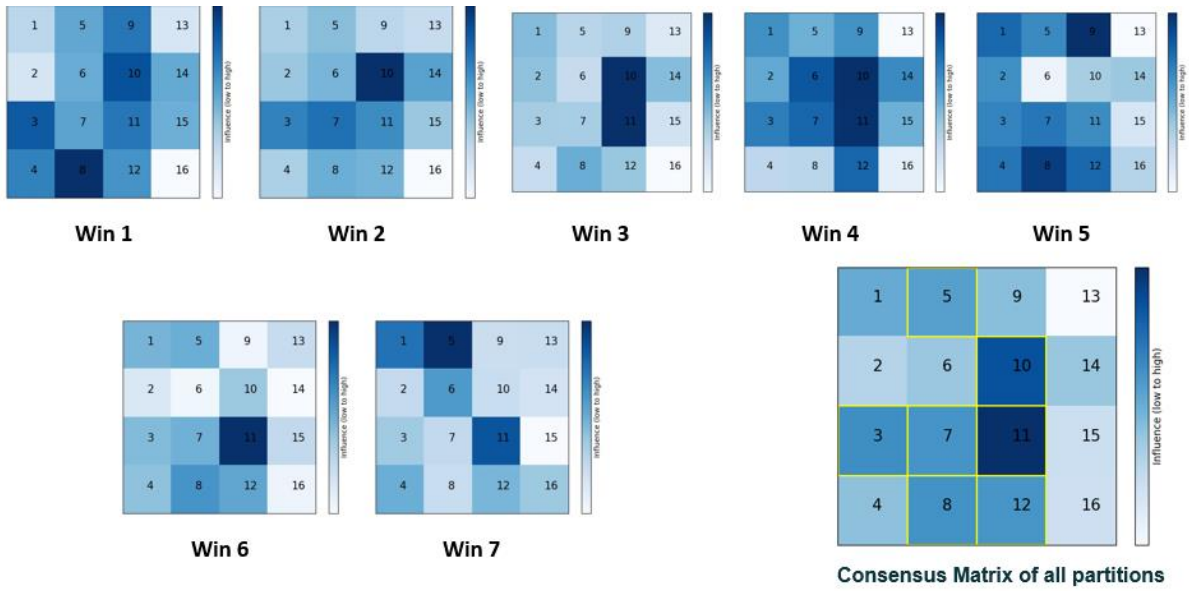

Figure A.23 Consensus matrices of each window using H2(CC)

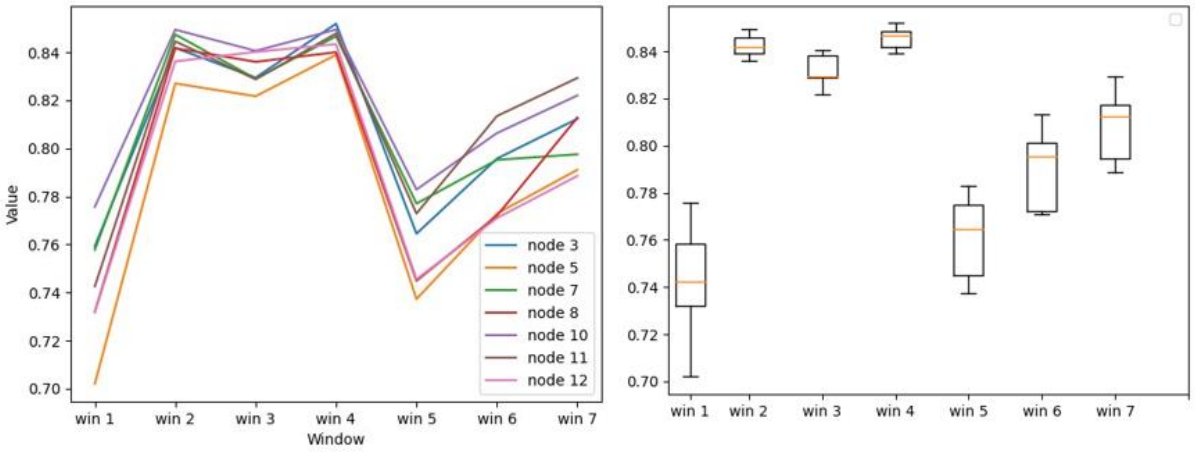

Figure A.24 Analyses of each window for the methods H2(CC)

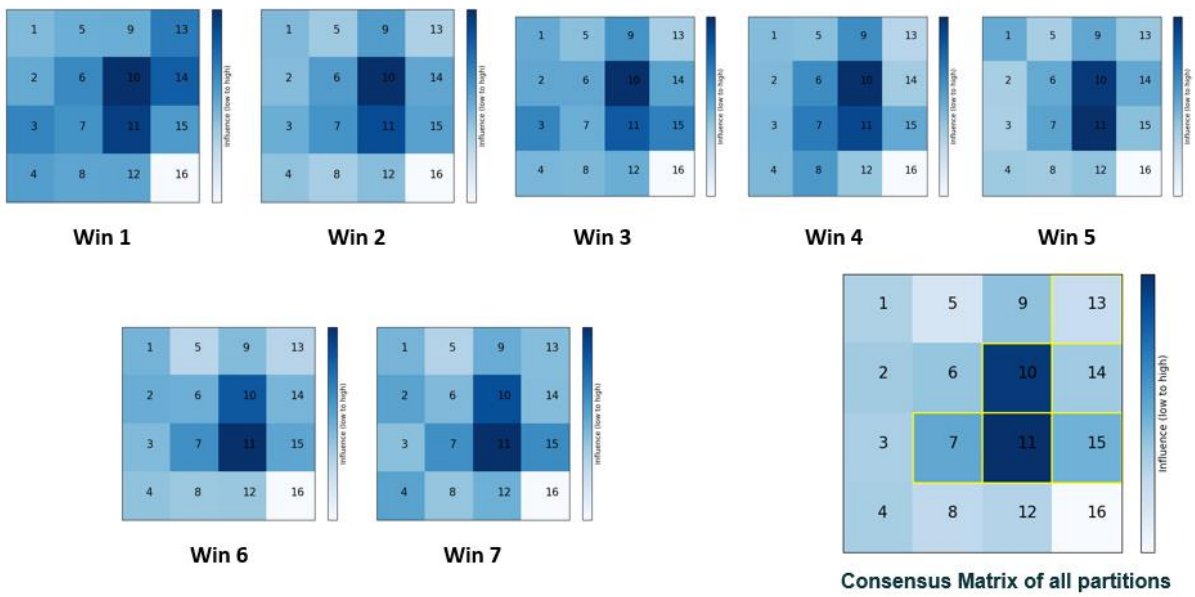

Figure A.25 Consensus matrices of each window using ICOH

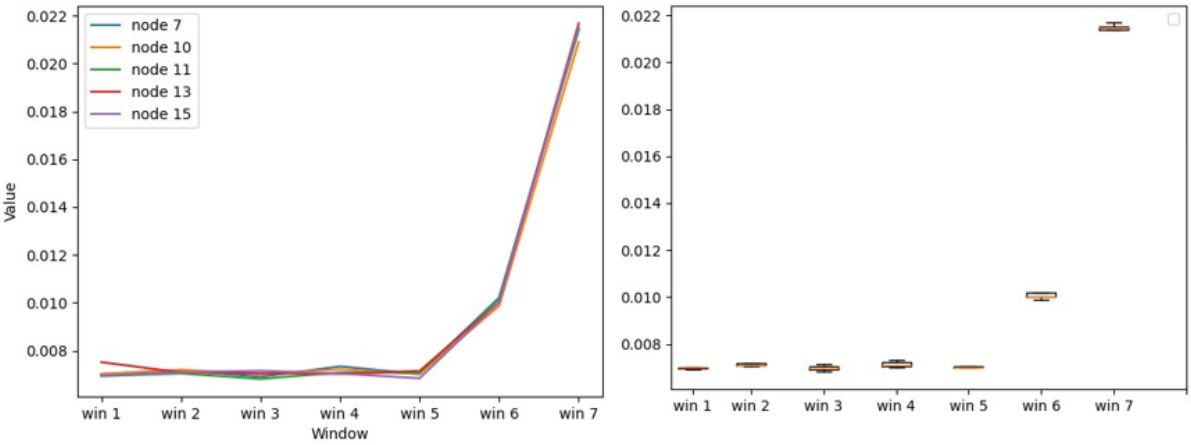

Figure A.26 Analyses of each window for the methods ICOH

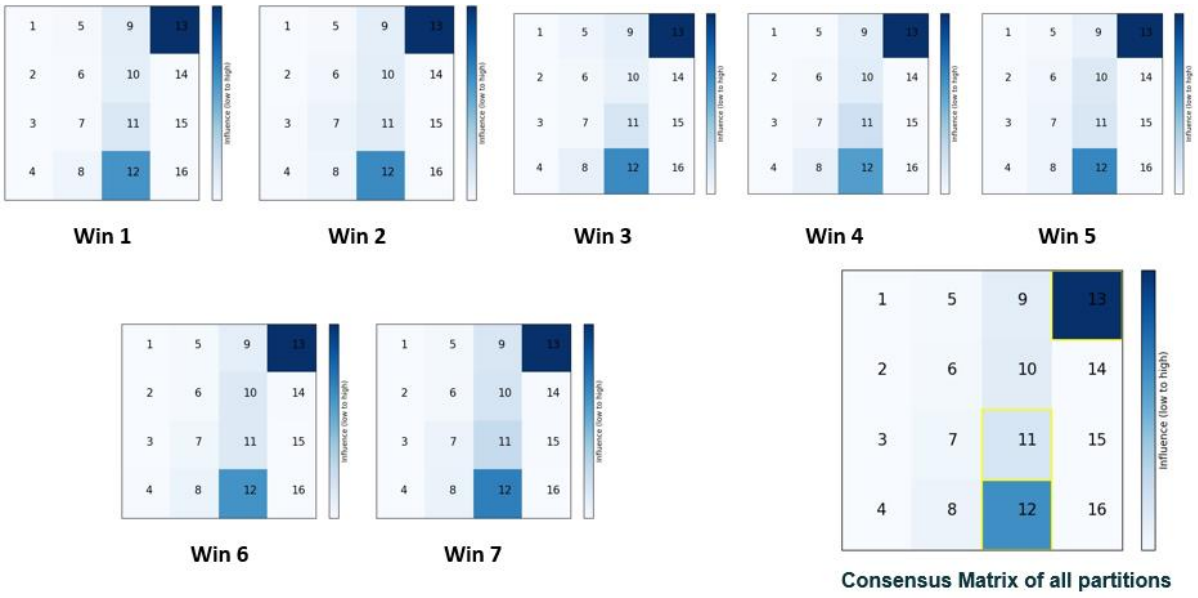

Figure A.27 Consensus matrices of each window using ICOH(Eff

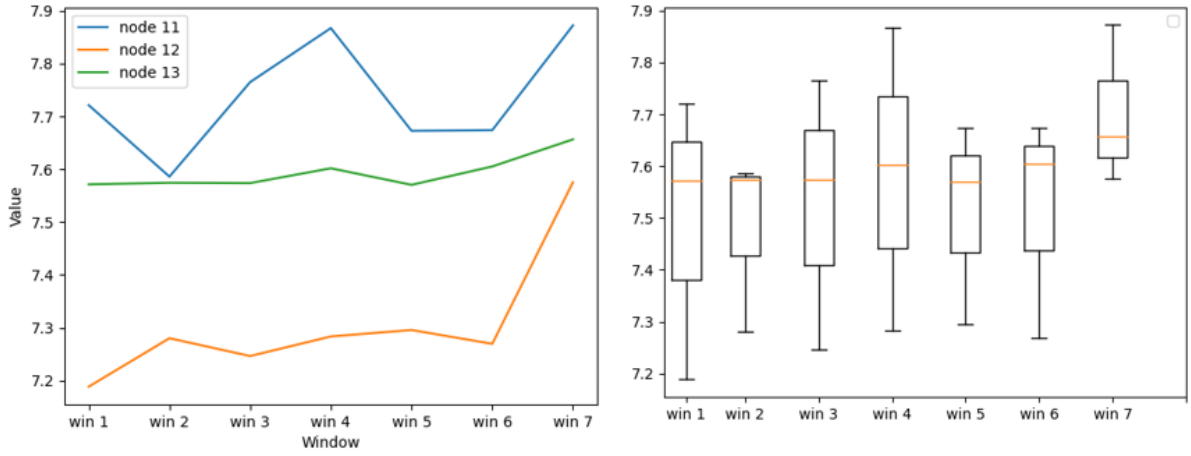

Figure A.28 Analyses of each window for the methods ICOH(Eff

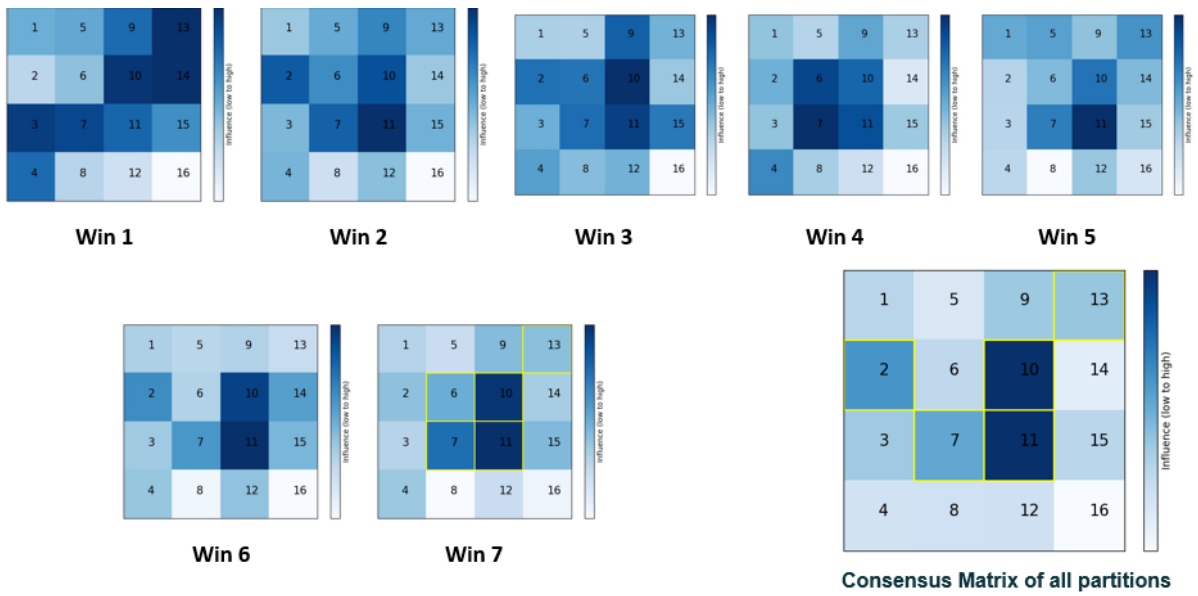

Figure A.29 Consensus matrices of each window using ICOH(Str)

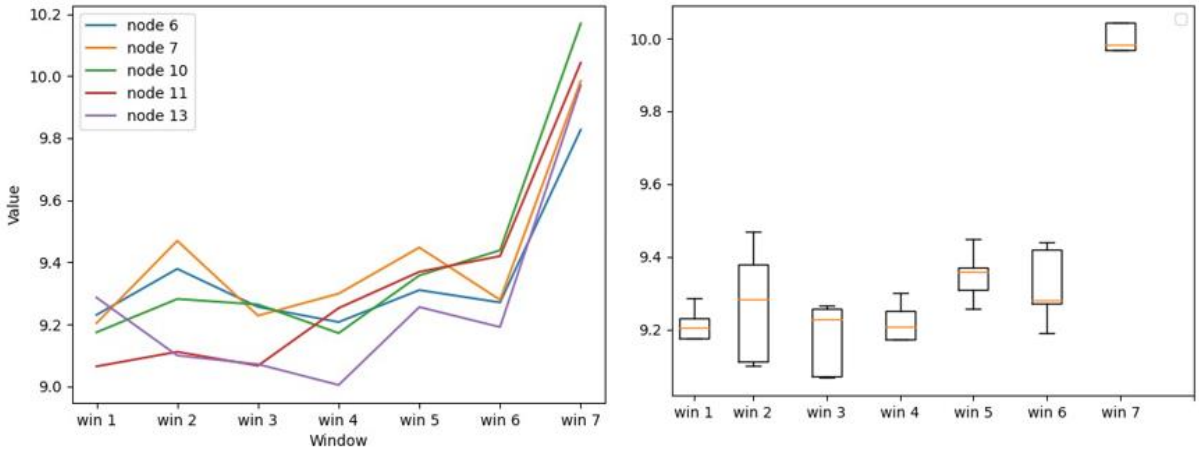

Figure A.30 Analyses of each window for the methods ICOH(Str)

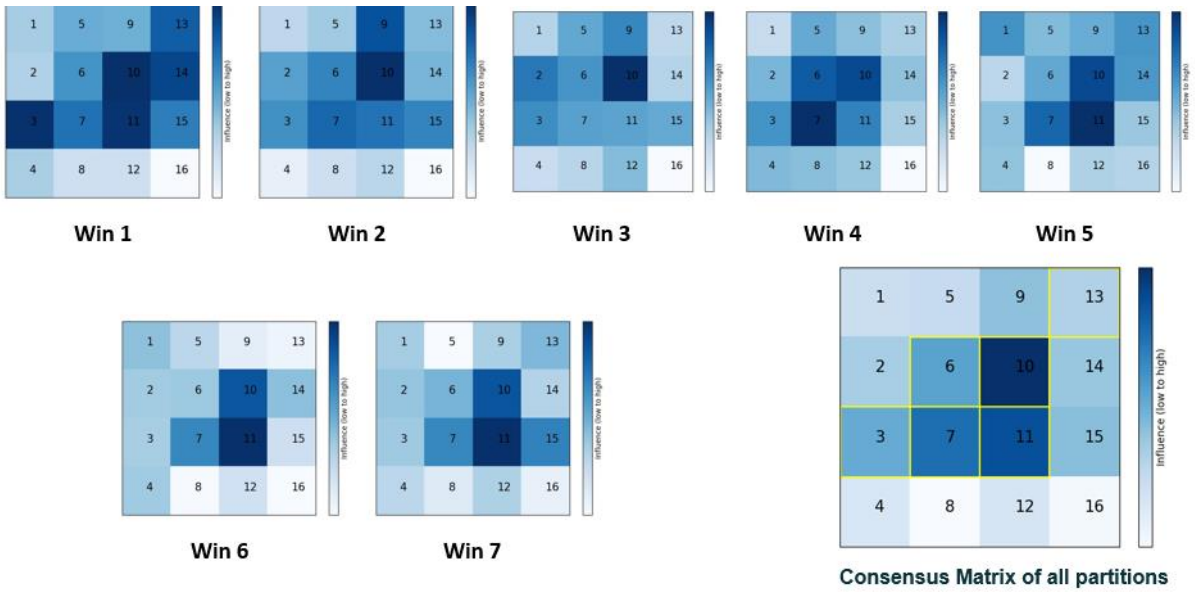

Figure A.31 Consensus matrices of each window using ICOH(PR)

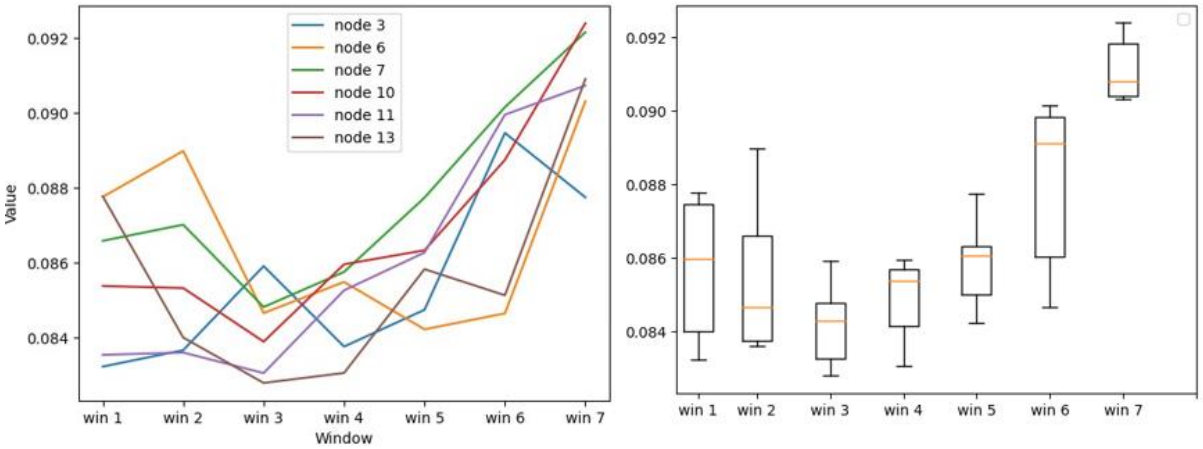

Figure A.32 Analyses of each window for the methods ICOH(PR)

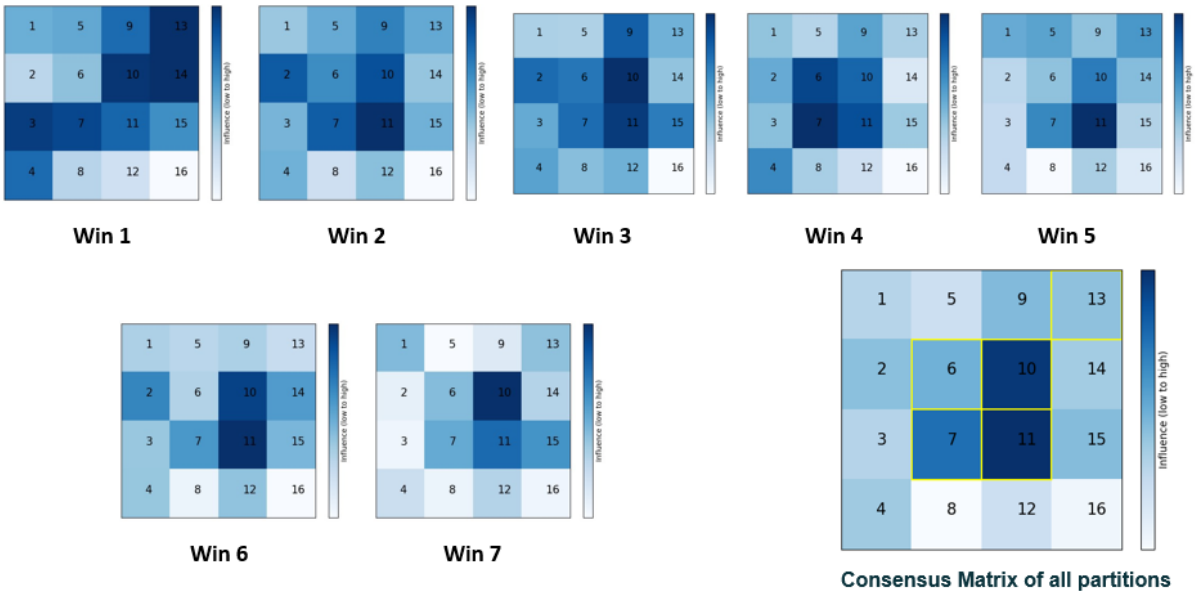

Figure A.33 Consensus matrices of each window using ICOH(BC)

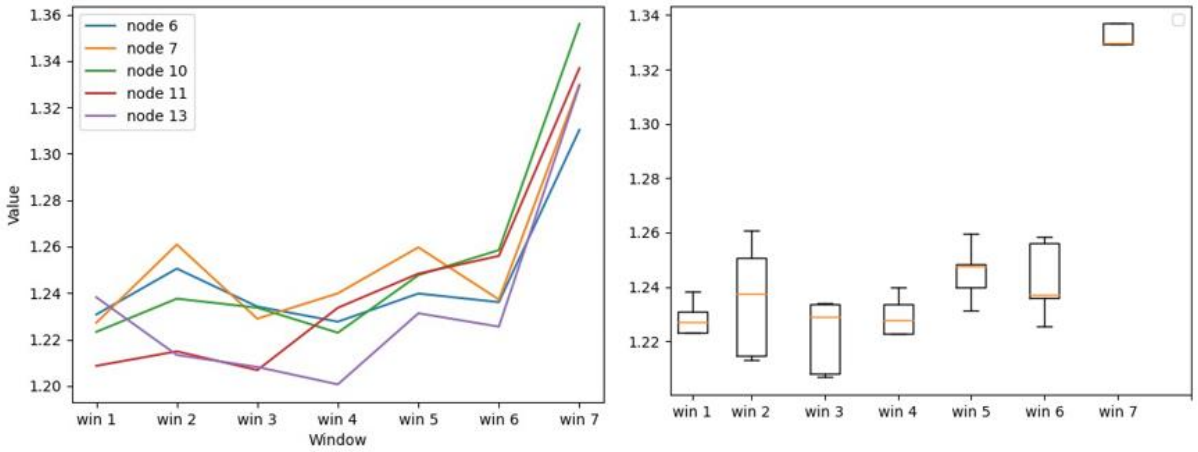

Figure A.34 Analyses of each window for the methods ICOH(BC)

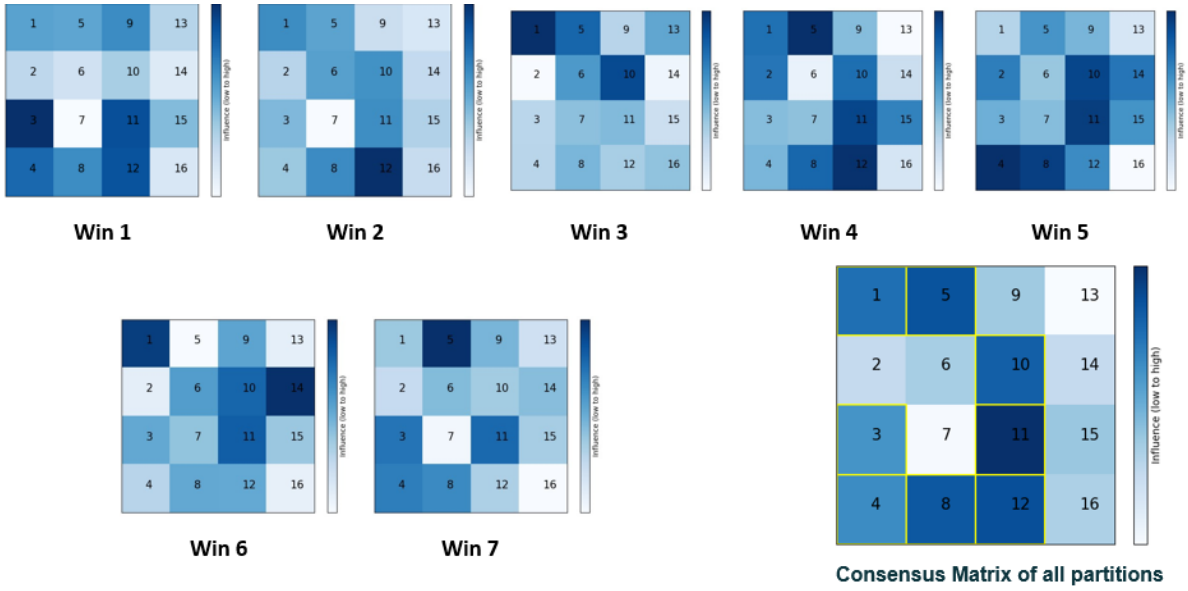

Figure A.35 Consensus matrices of each window using ICOH(CC)

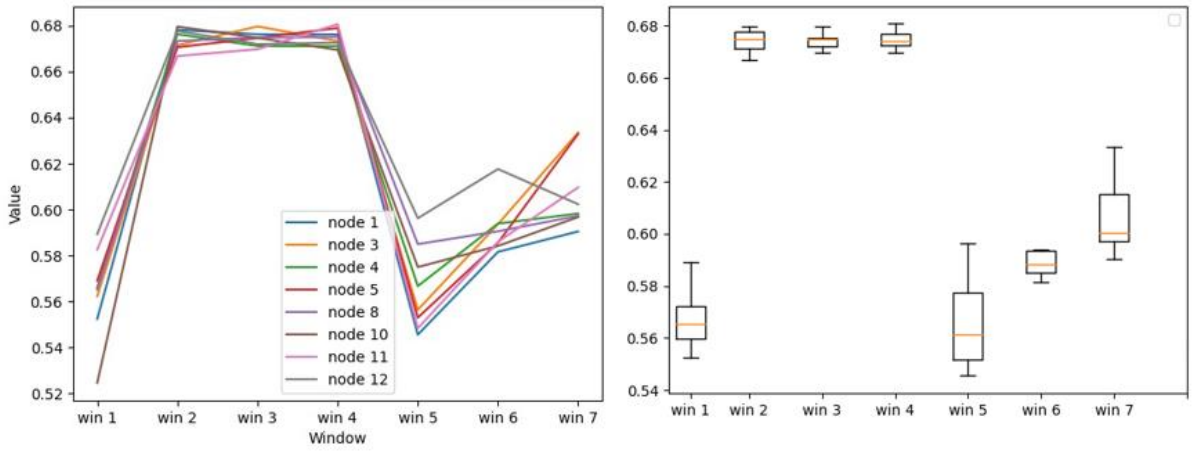

Figure A.36 Analyses of each window for the methods ICOH(CC)

Annex B: Impact of the model parameters

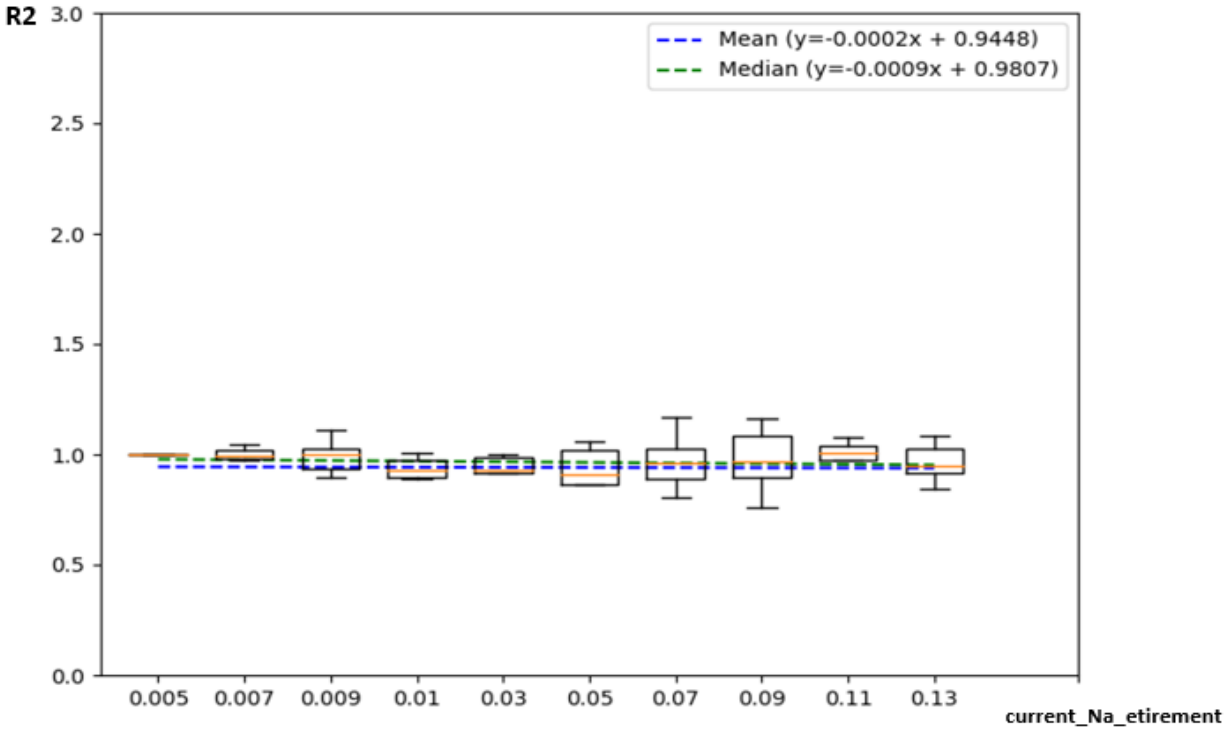

Figure B.1 Evolution of R2 function of the tissue current_Na_etirement

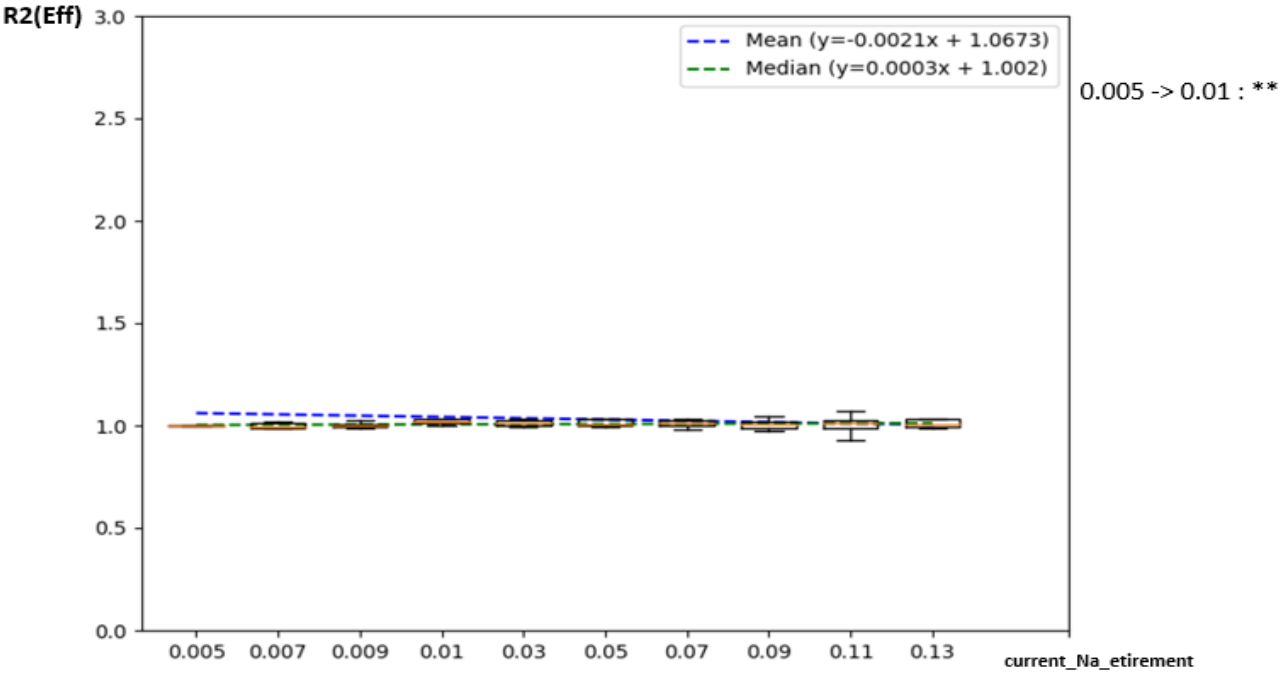

Figure B.2 Evolution of R2(Eff) function of the tissue current_Na_etirement

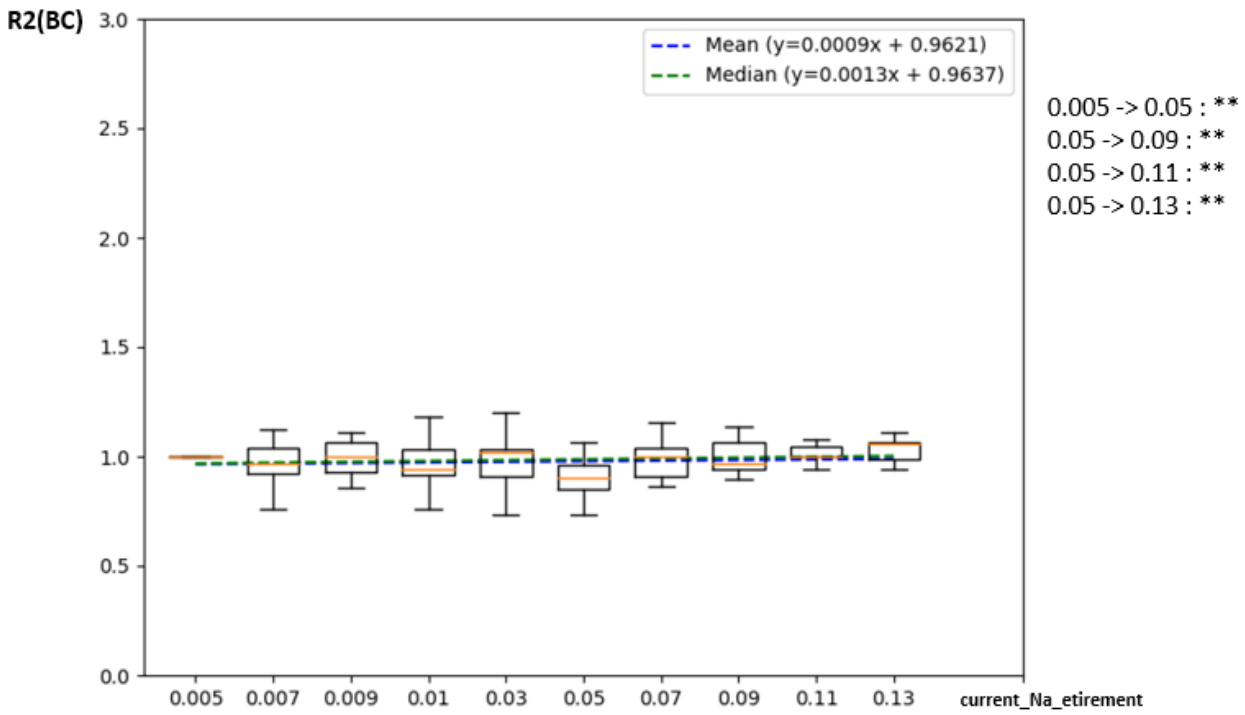

Figure B.3 Evolution of R2(BC) function of the tissue current_Na_etirement

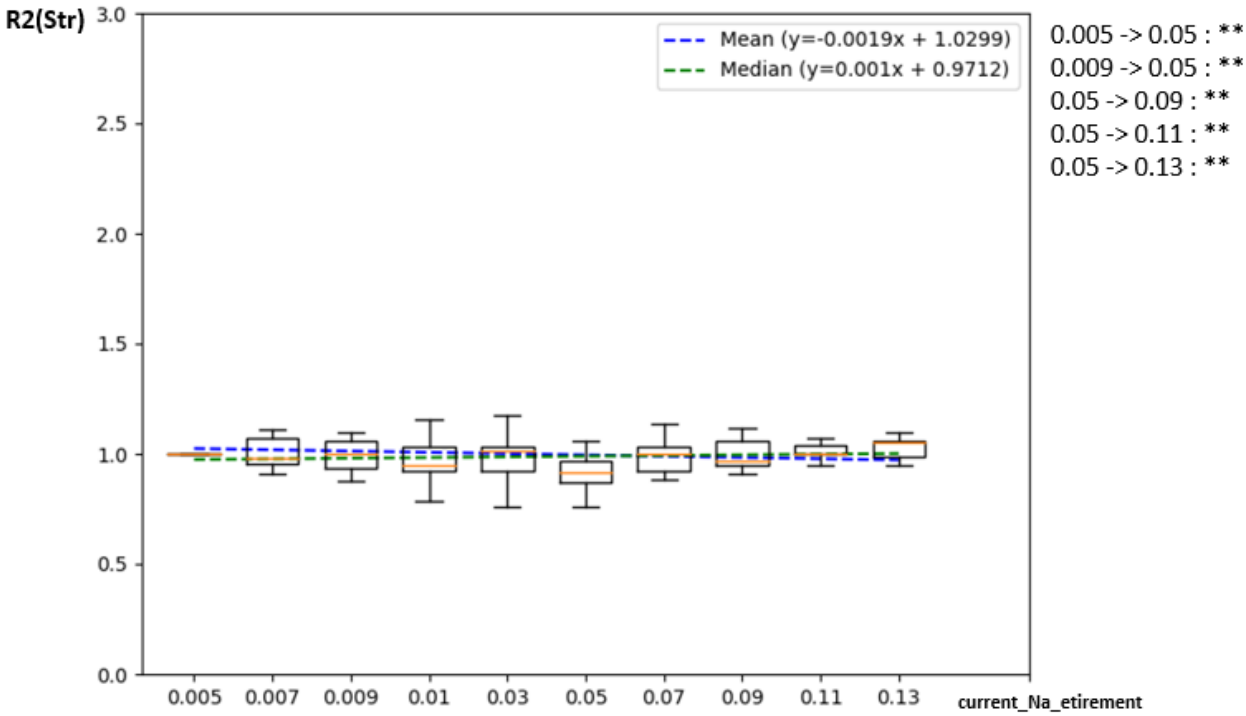

Figure B.4 Evolution of R2(Str) function of the tissue current_Na_etirement

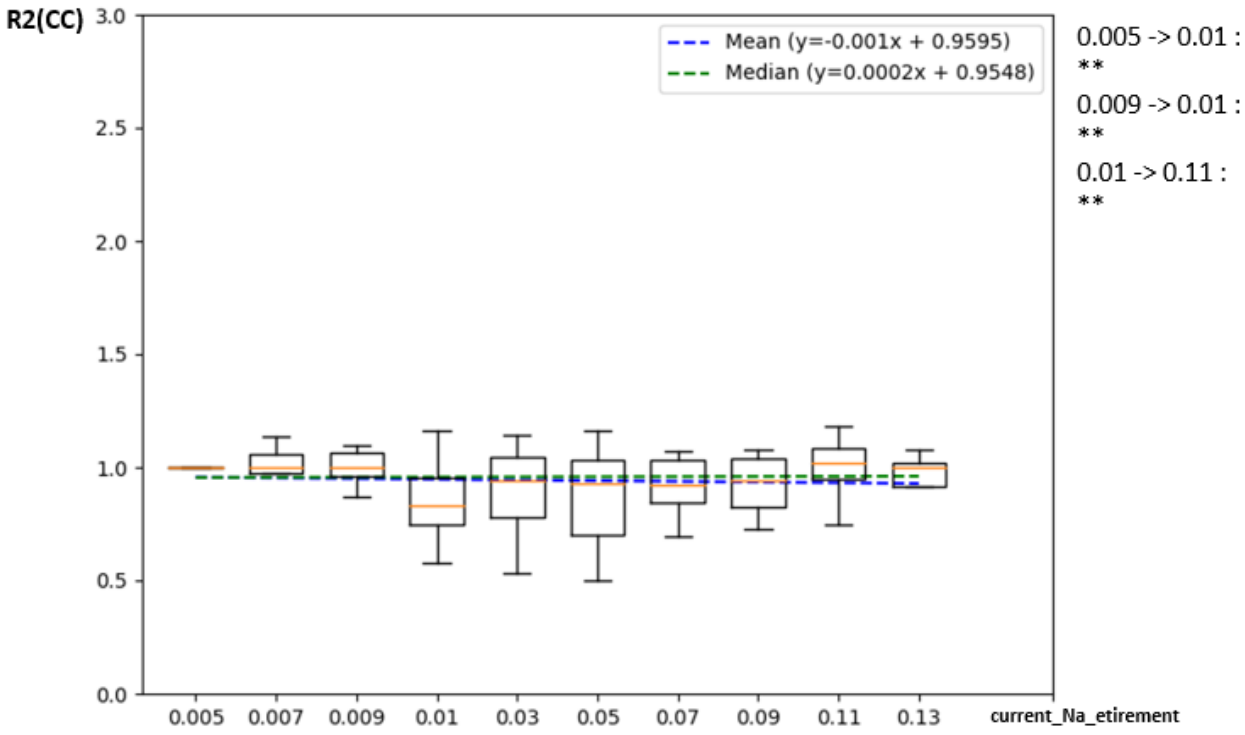

Figure B.5 Evolution of R2(CC) function of the tissue current_Na_etirement

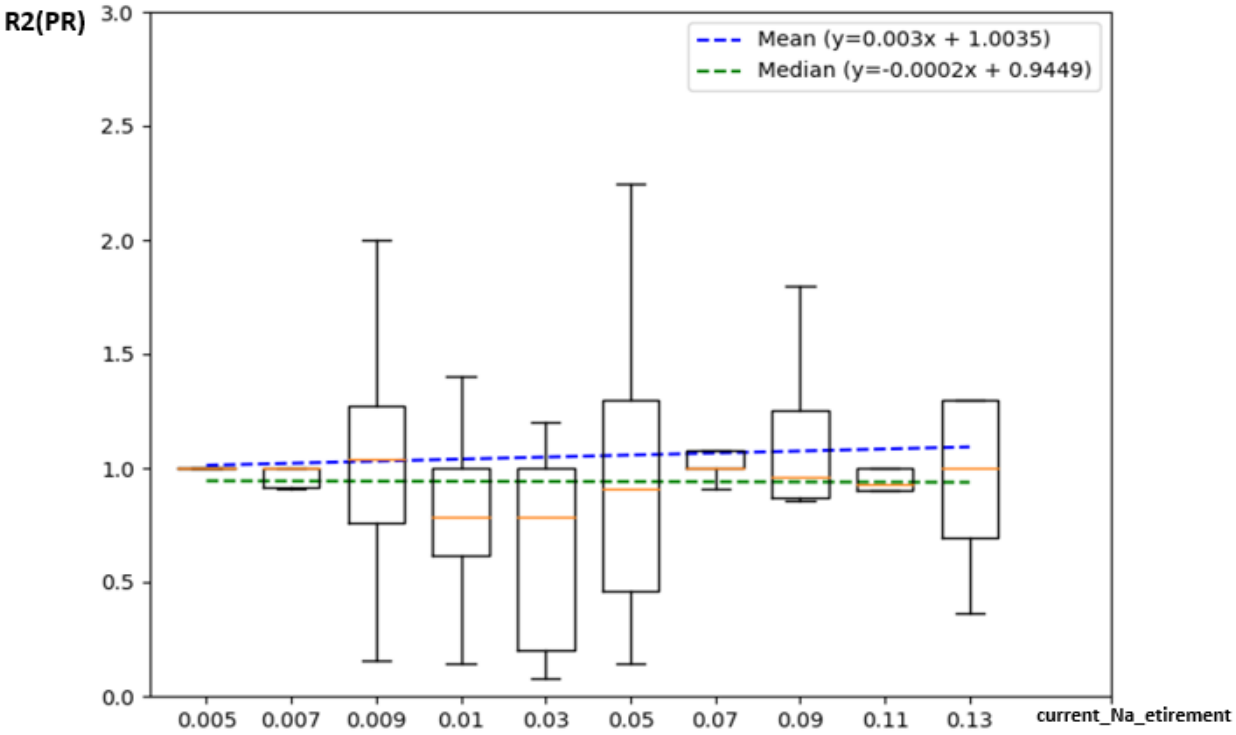

Figure B.6 Evolution of R2(PR) function of the tissue current_Na_etirement

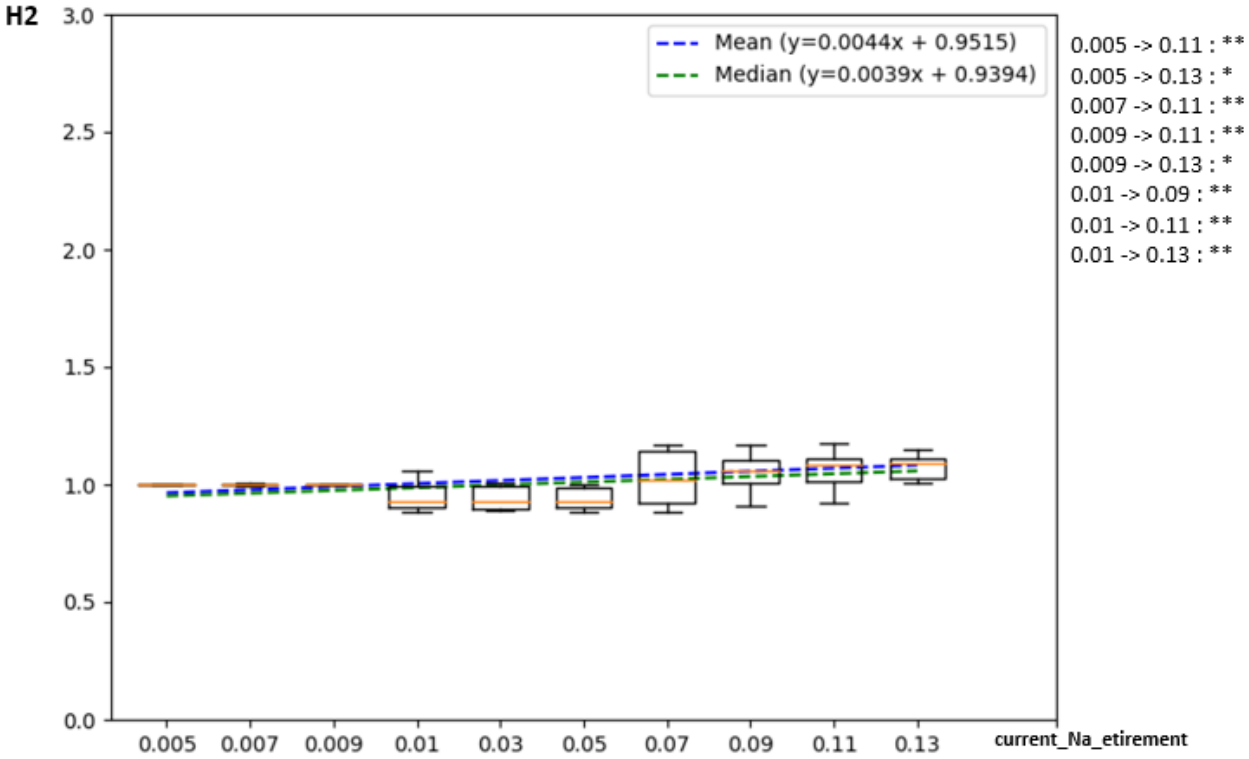

Figure B.7 Evolution of H2 function of the tissue current_Na_etirement

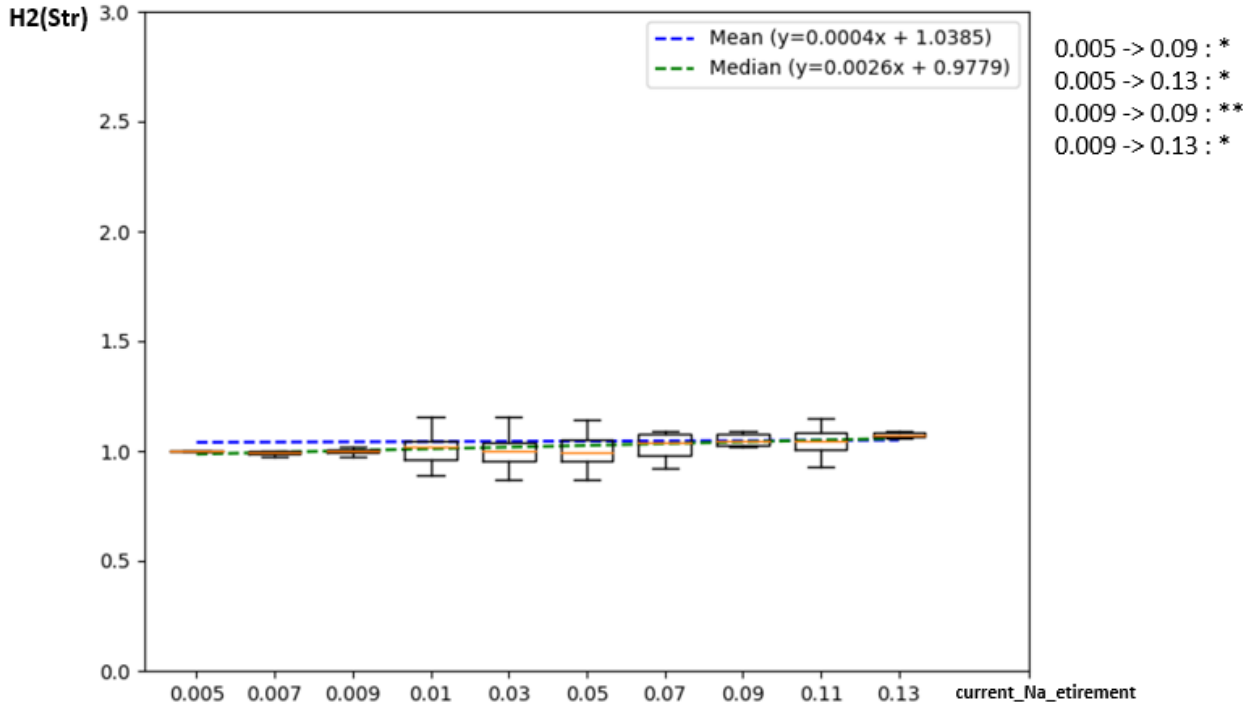

Figure B.8 Evolution of H2(Str) function of the tissue current_Na_etirement

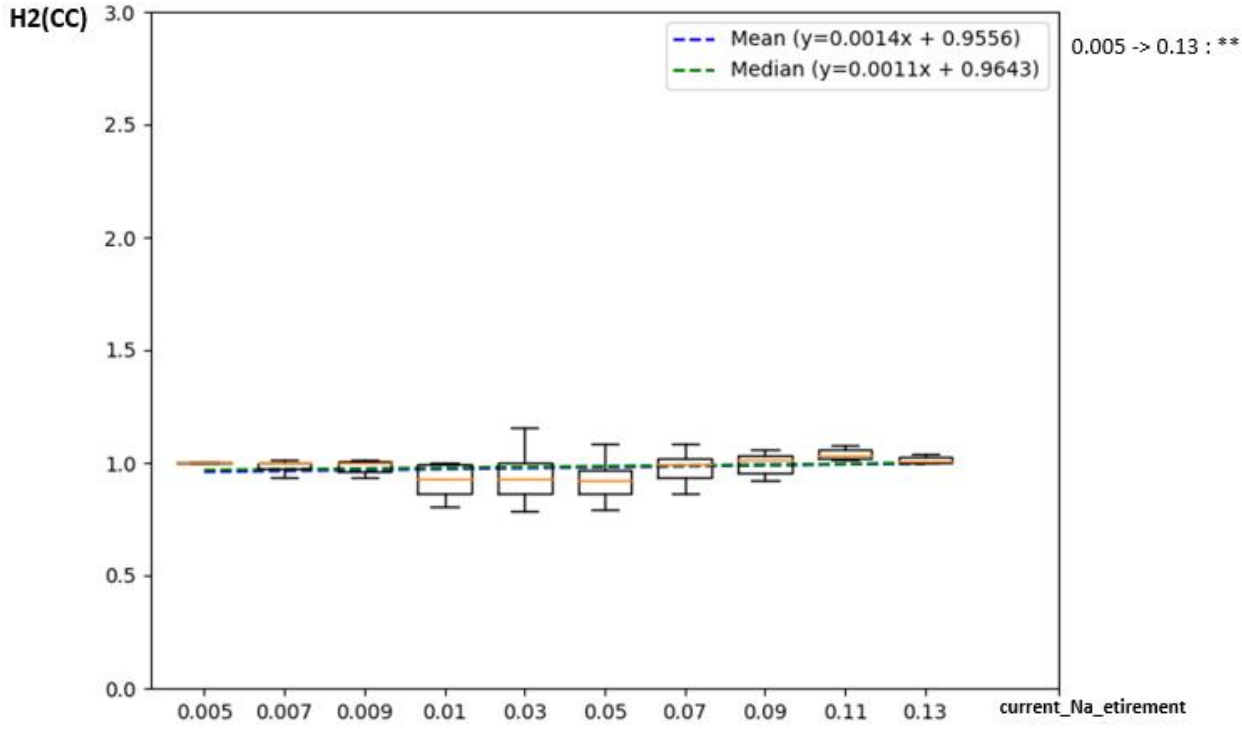

Figure B.9 Evolution of H2(CC) function of the tissue current_Na_etirement

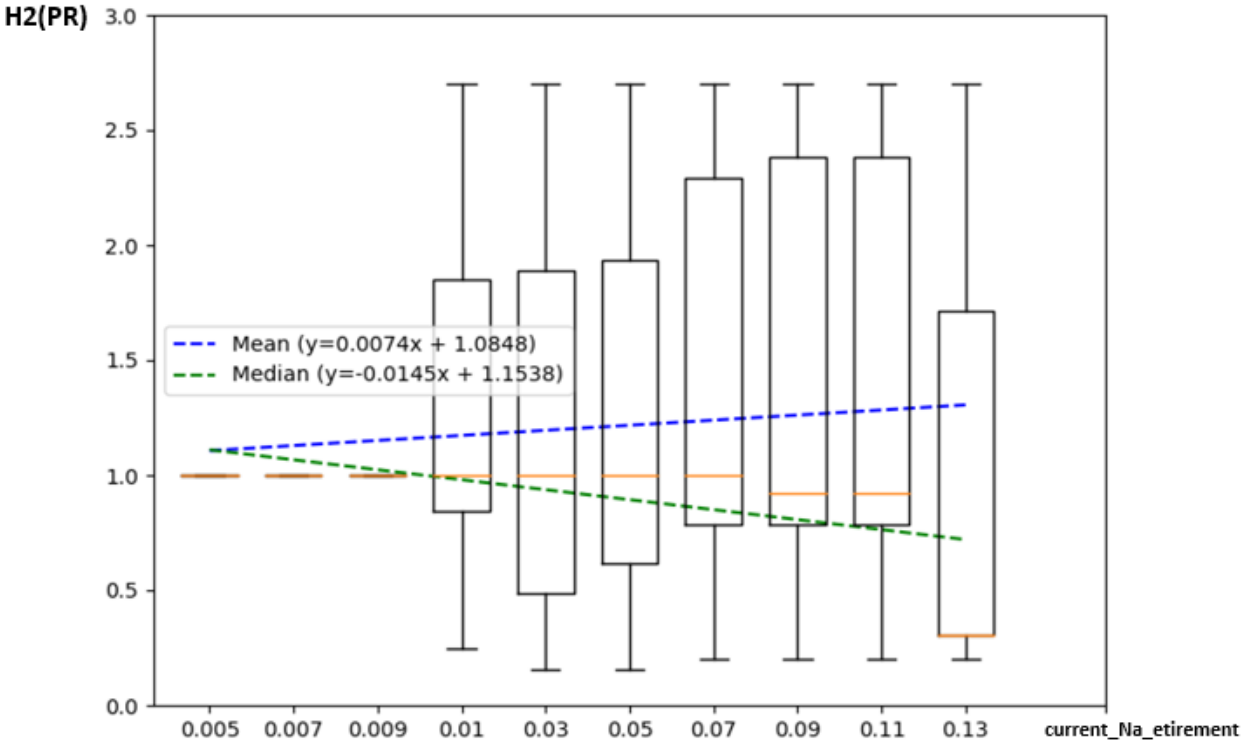

Figure B.10 Evolution of H2(PR) function of the tissue current_Na_etirement

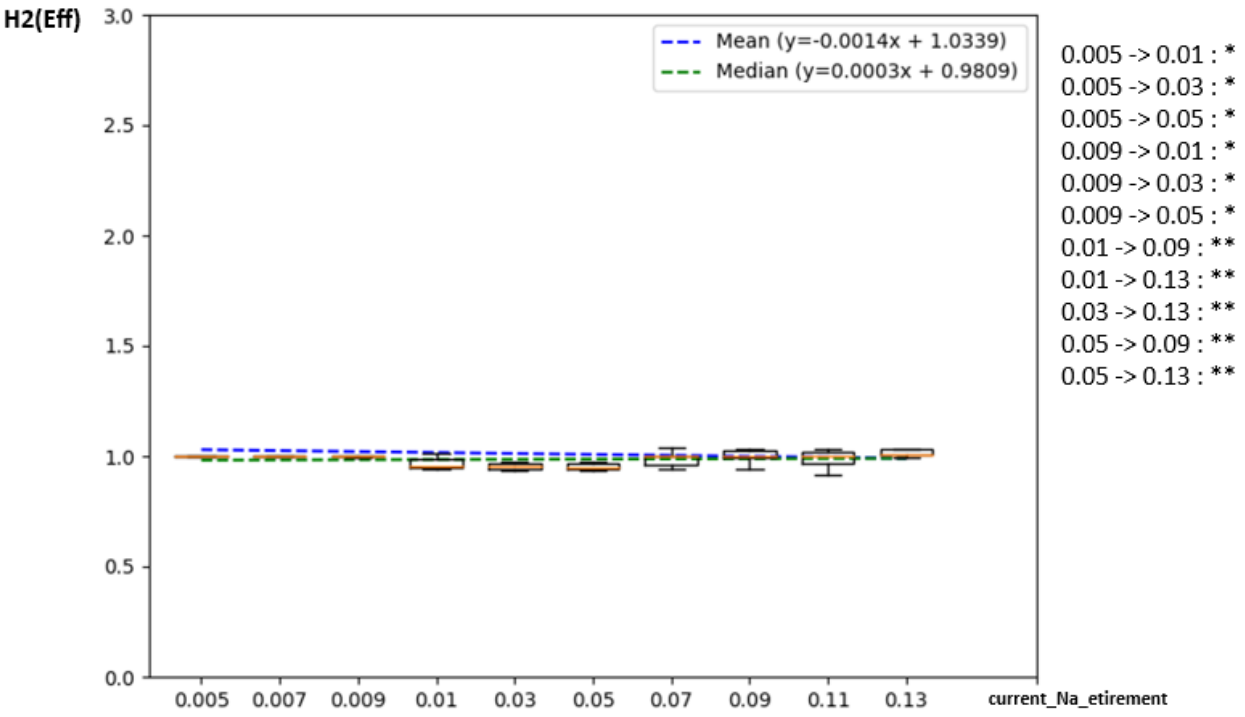

Figure B.11 Evolution of H2(Eff) function of the tissue current_Na_etirement

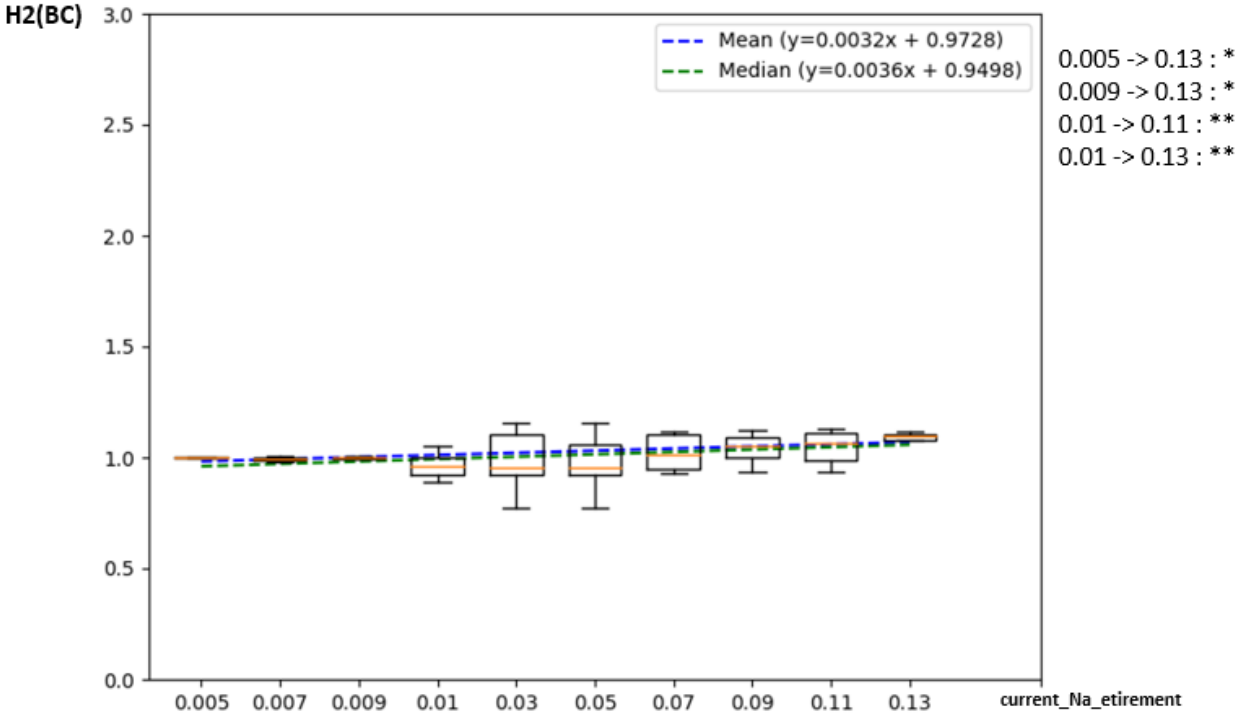

Figure B.12 Evolution of H2(BC) function of the tissue current_Na_etirement

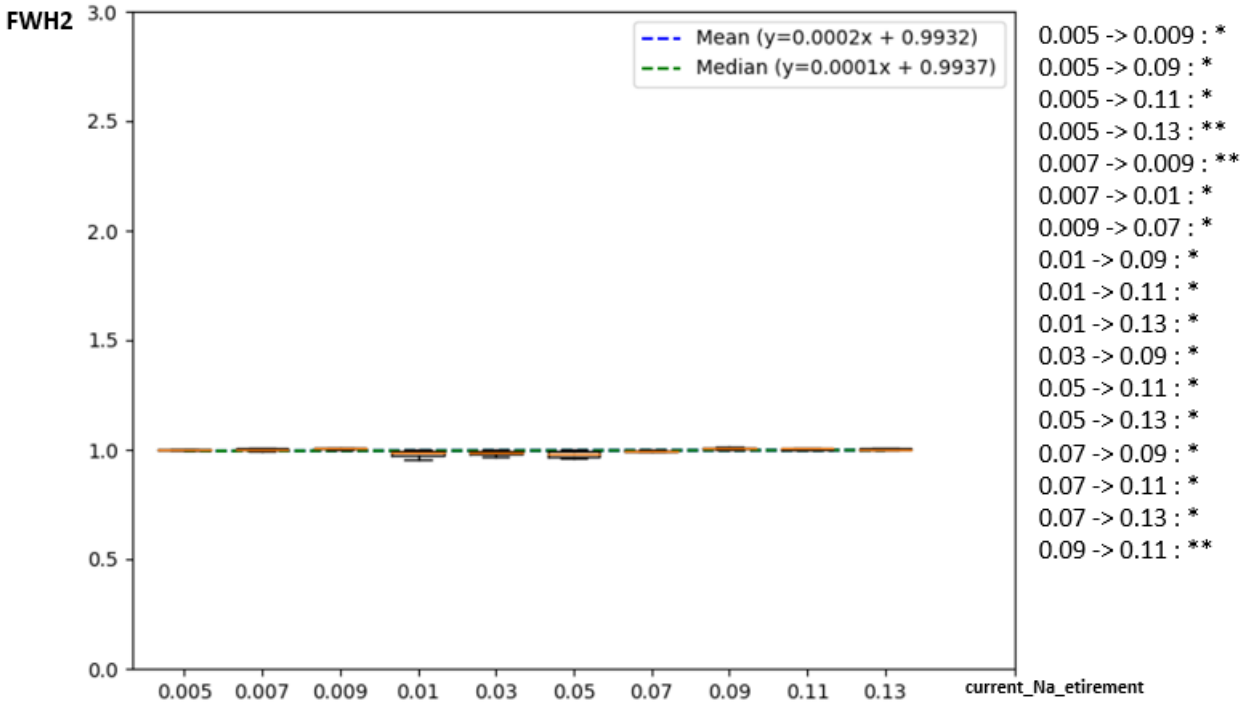

Figure B.13 Evolution of FWH2 function of the tissue current_Na_etirement

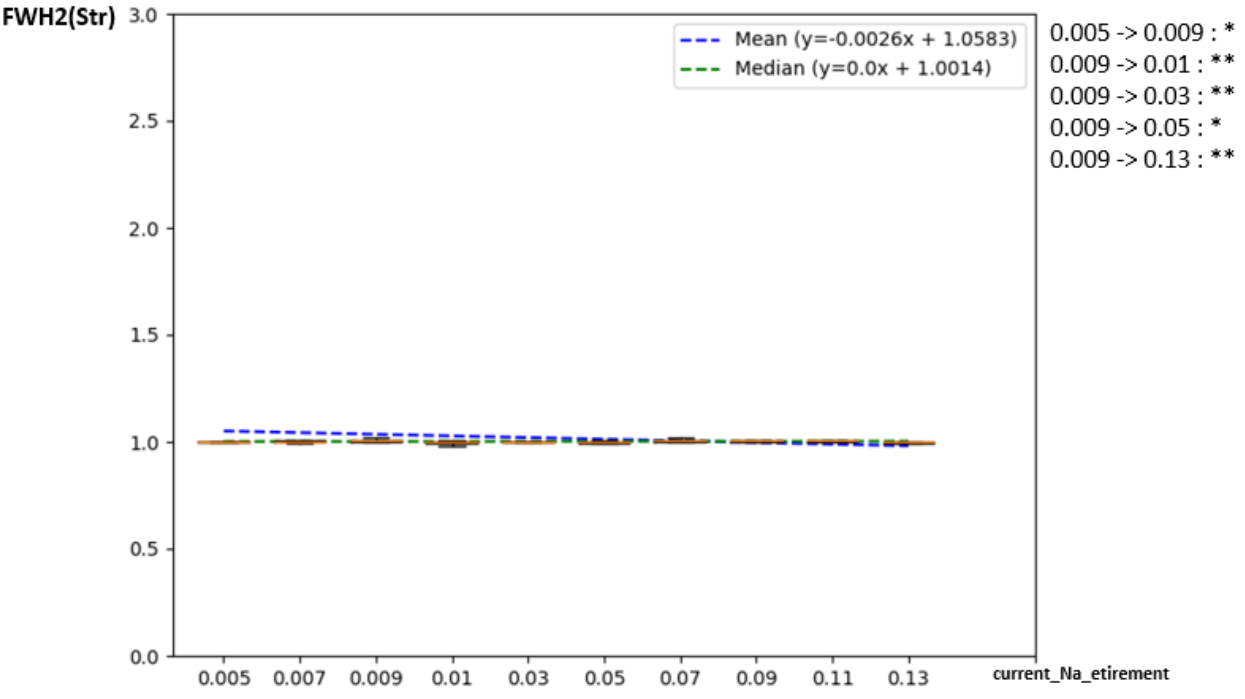

Figure B.14 Evolution of FWH2(Str) function of the tissue current_Na_etirement

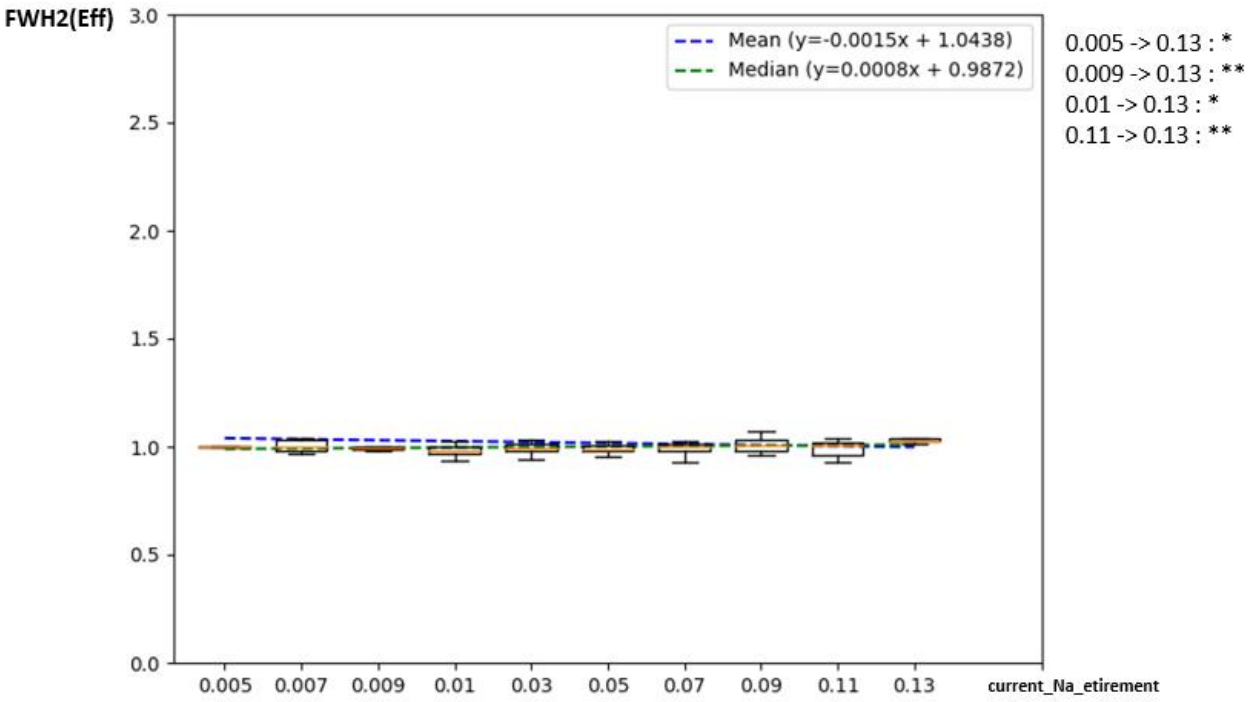

Figure B.15 Evolution of FWH2(Eff) function of the tissue current_Na_etirement

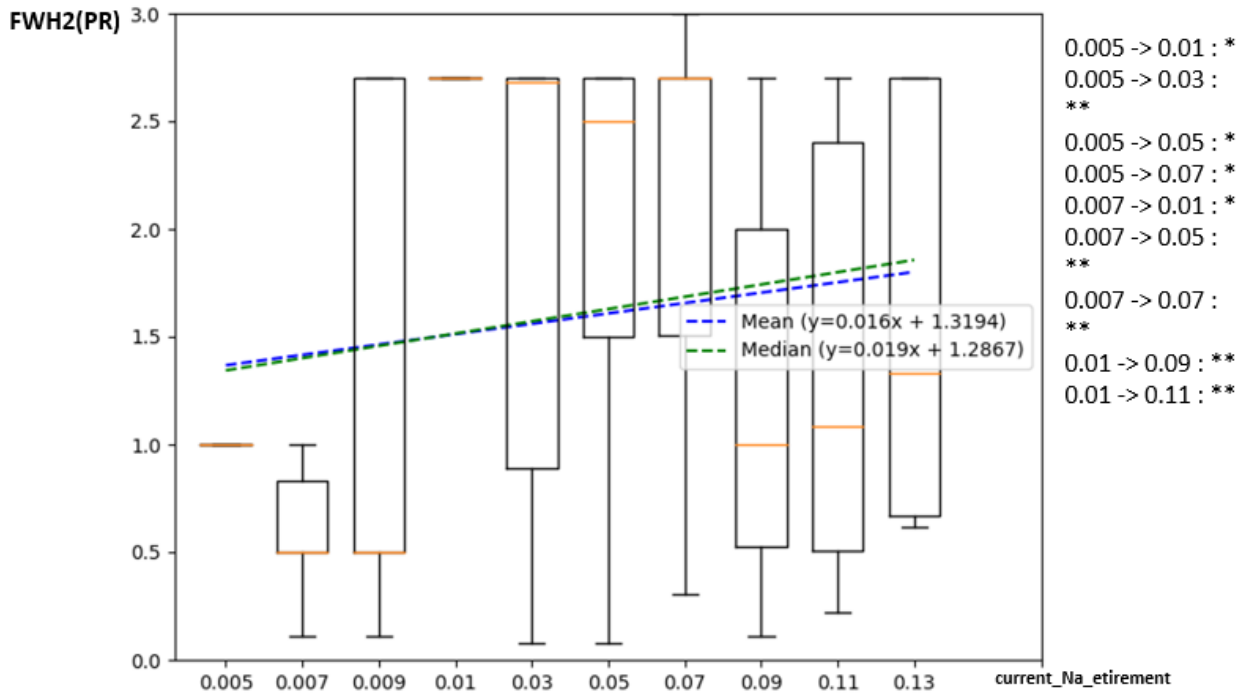

Figure B.16 Evolution of FWH2(PR) function of the tissue current_Na_etirement

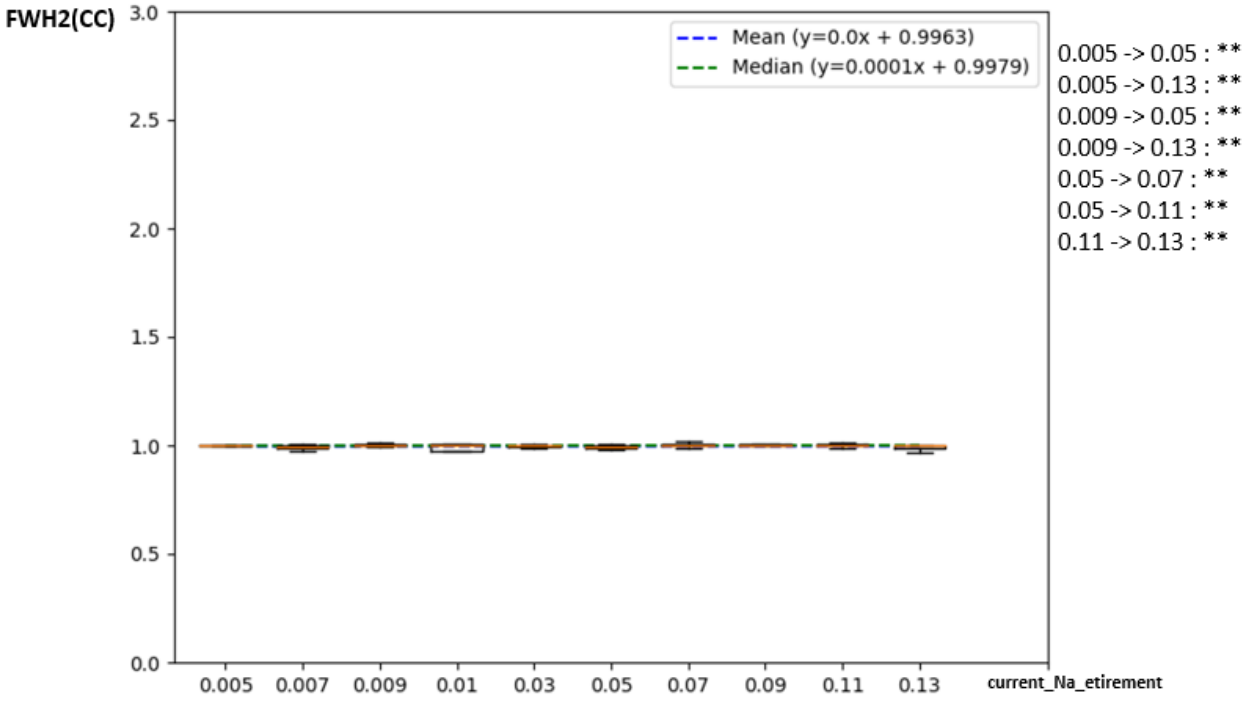

Figure B.17 Evolution of FWH2(CC) function of the tissue current_Na_etirement

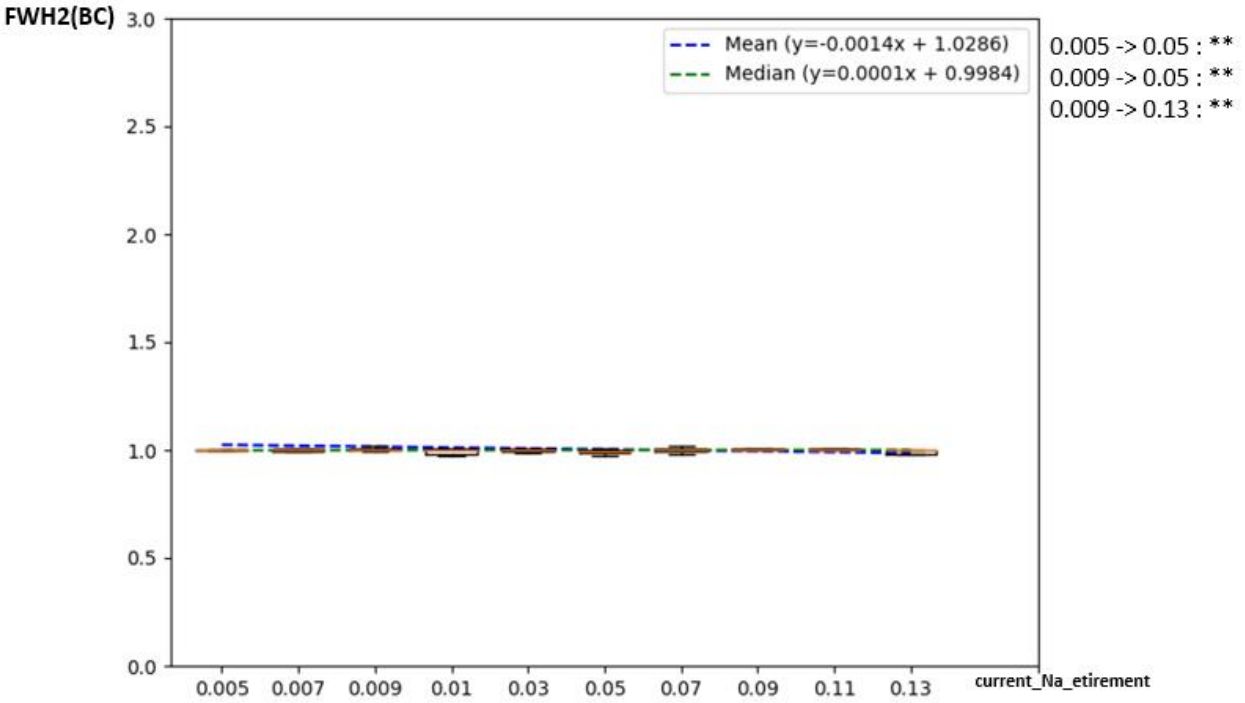

Figure B.18 Evolution of FWH2(BC) function of the tissue current_Na_etirement

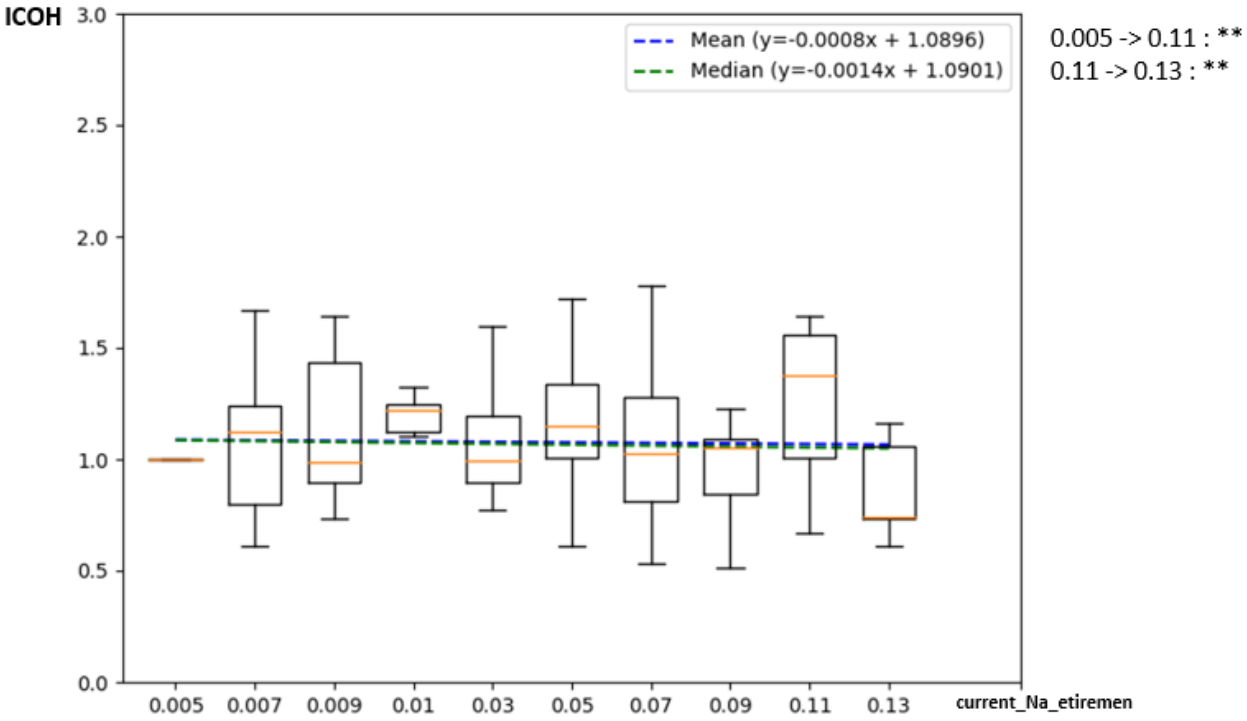

Figure B.19 Evolution of ICOH function of the tissue current_Na_etirement

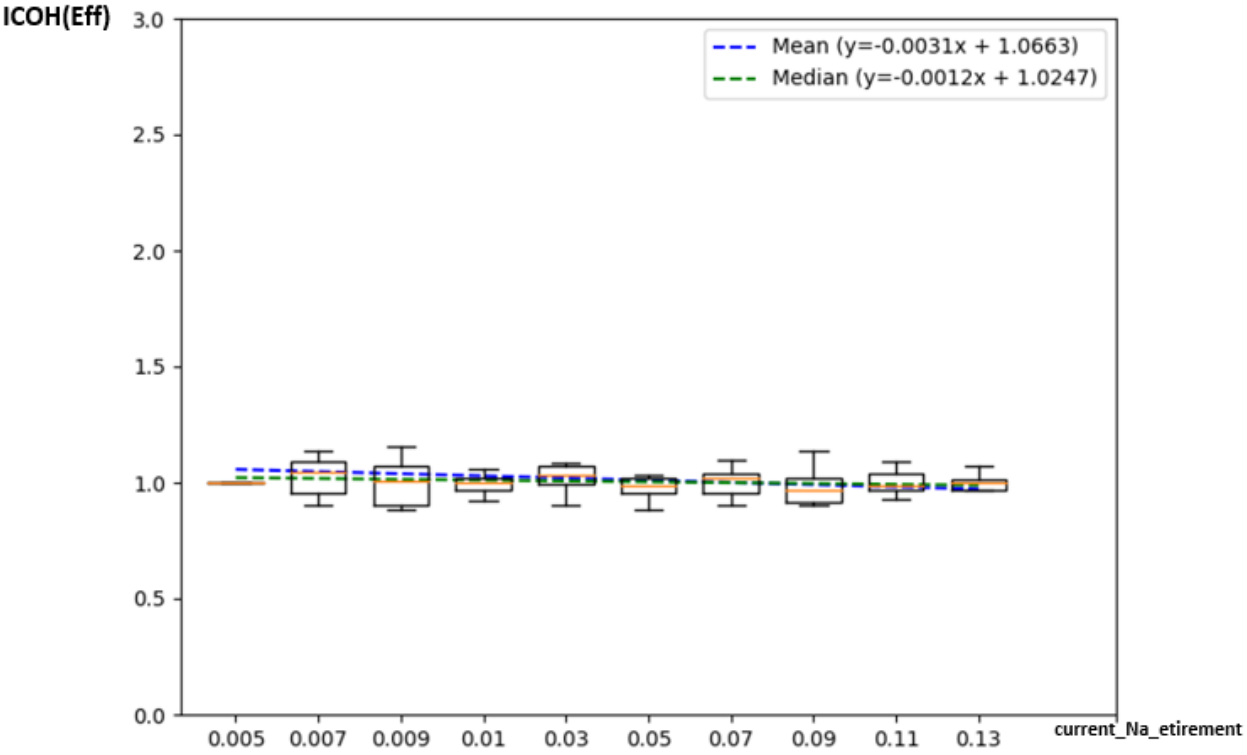

Figure B.20 Evolution of ICOH(Eff) function of the tissue current_Na_etirement

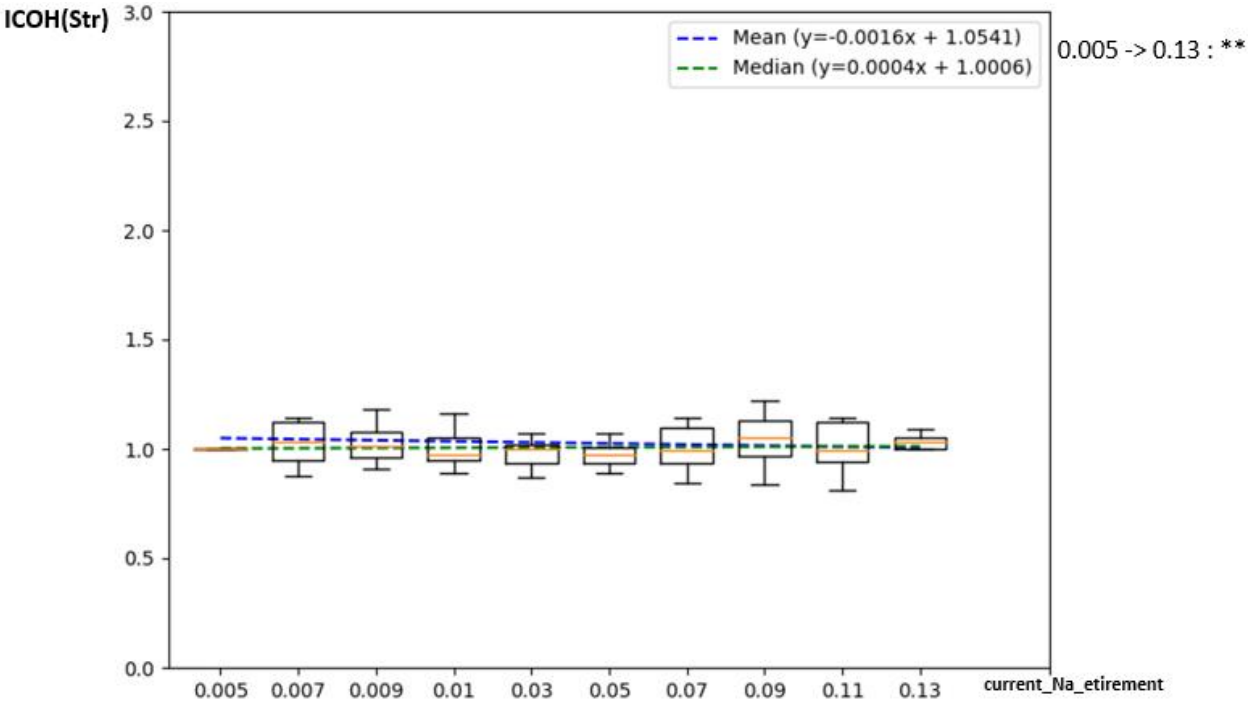

Figure B.21 Evolution of ICOH(Str) function of the tissue current_Na_etirement

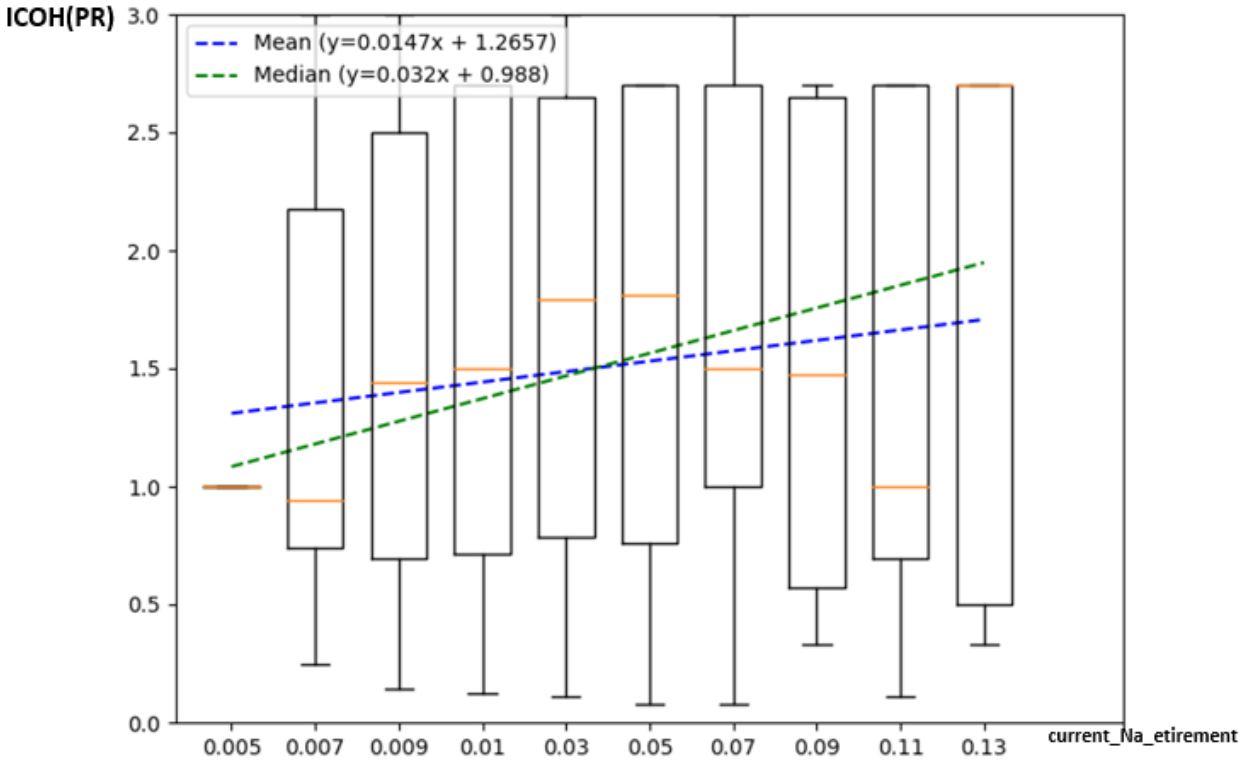

Figure B.22 Evolution of ICOH(PR) function of the tissue current_Na_etirement

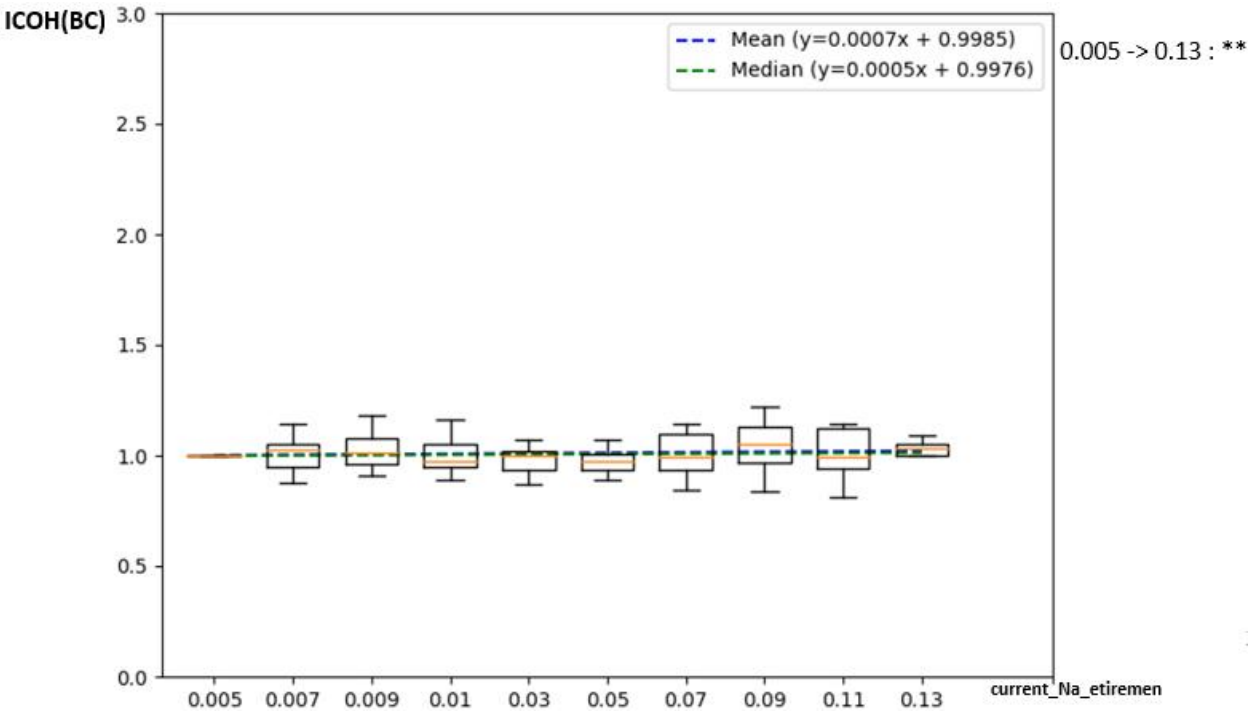

Figure B.23 Evolution of ICOH(BC) function of the tissue current_Na_etirement

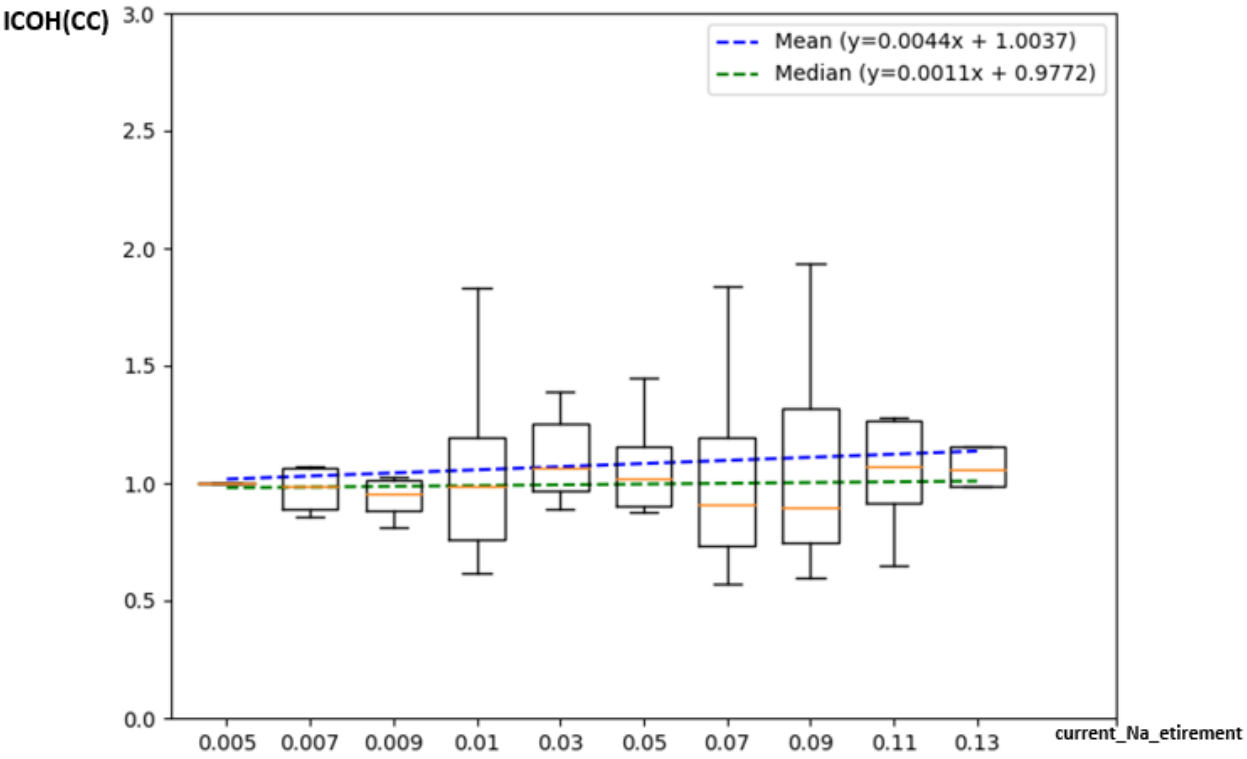

Figure B.24 Evolution of ICOH(CC) function of the tissue current_Na_etirement

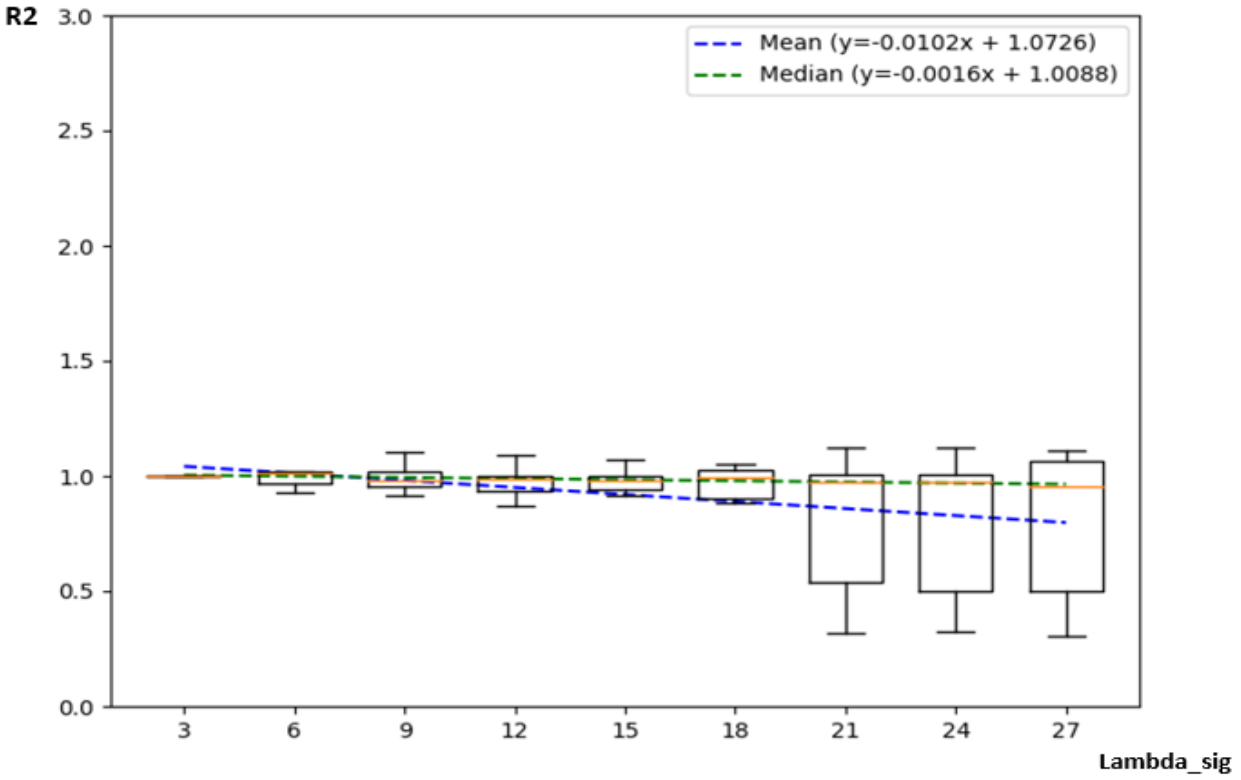

Figure B.25 Evolution of R2 function of the tissue Lambada_sig

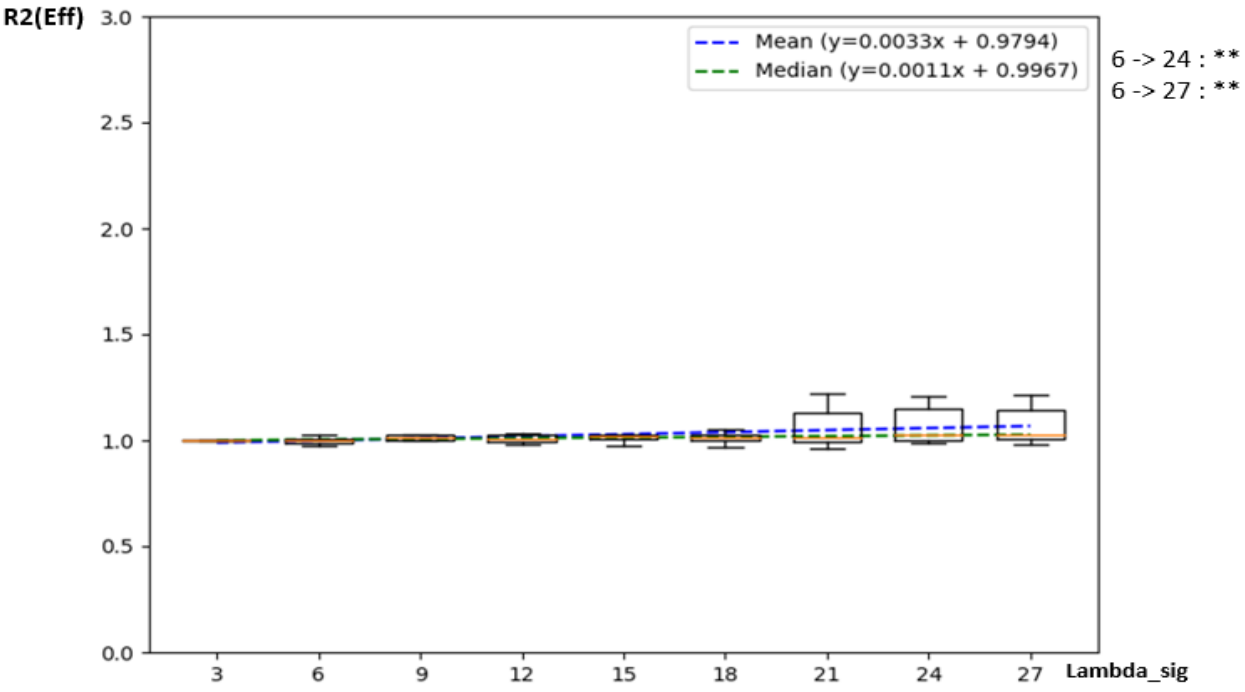

Figure B.26 Evolution of R2(Eff) function of the tissue Lambada_sig

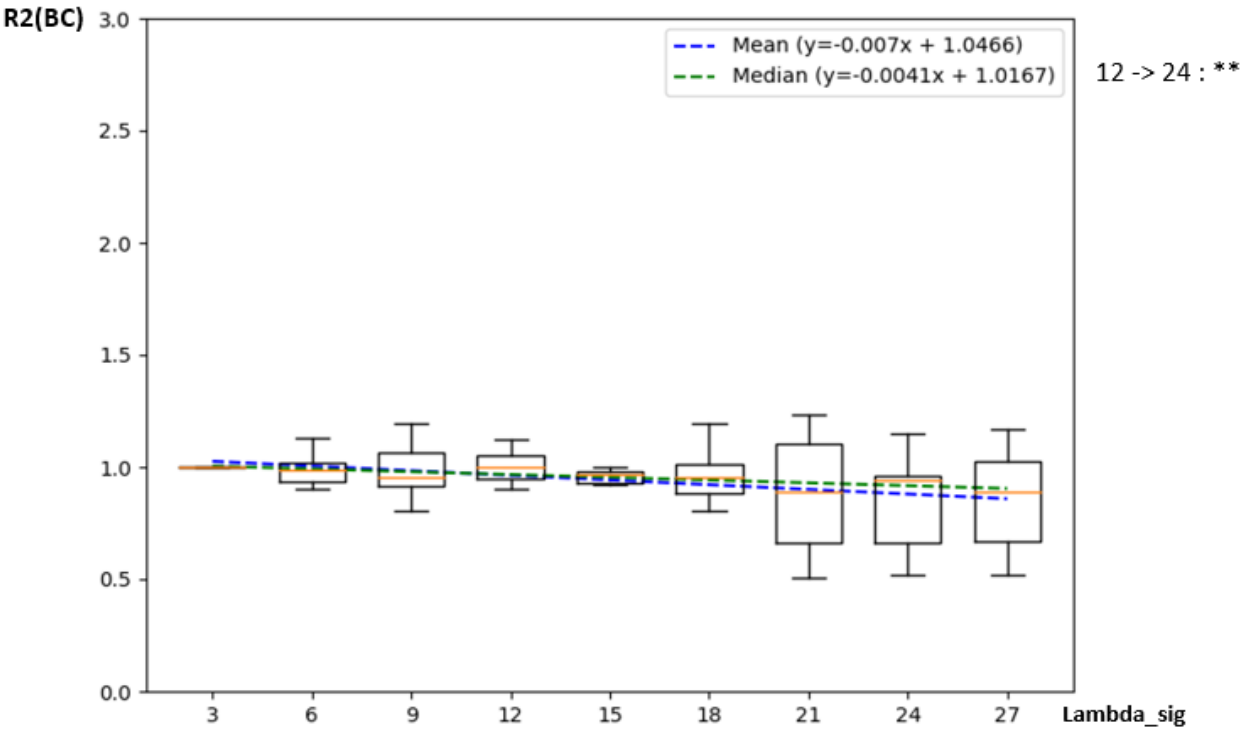

Figure B.27 Evolution of R2(BC) function of the tissue Lambada_sig

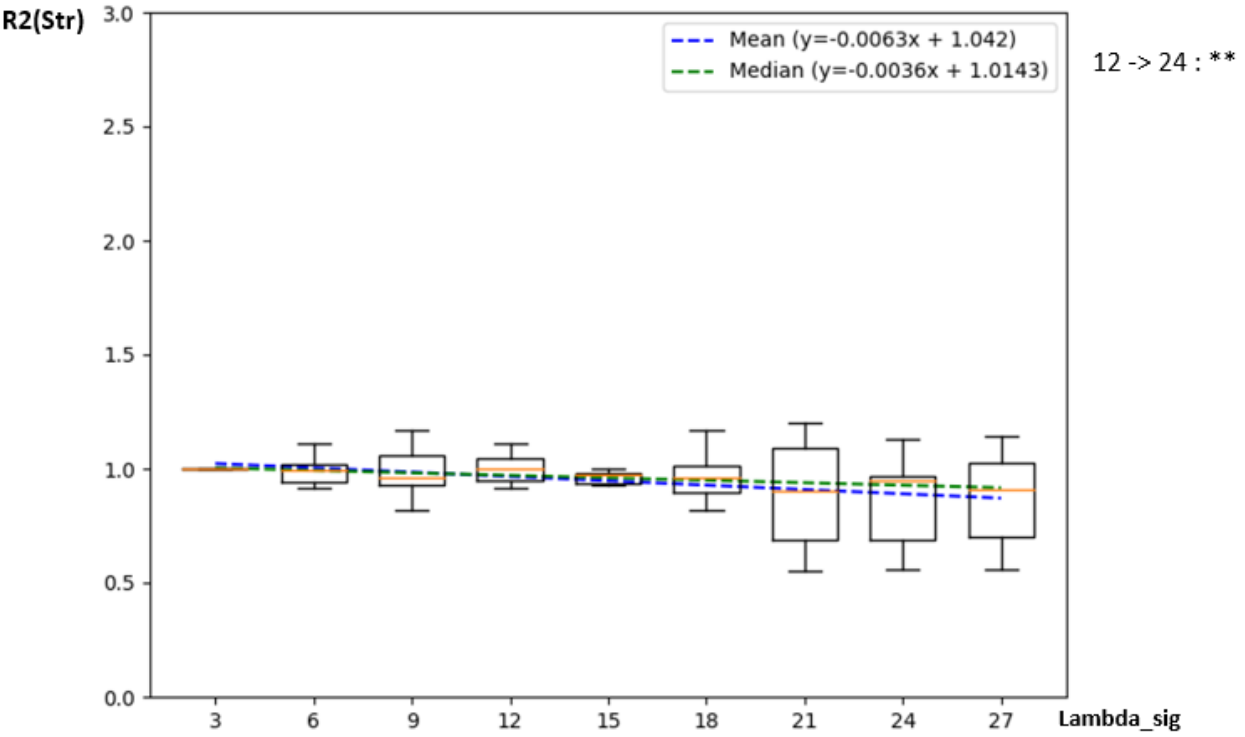

Figure B.28 Evolution of R2(Str) function of the tissue Lambada_sig

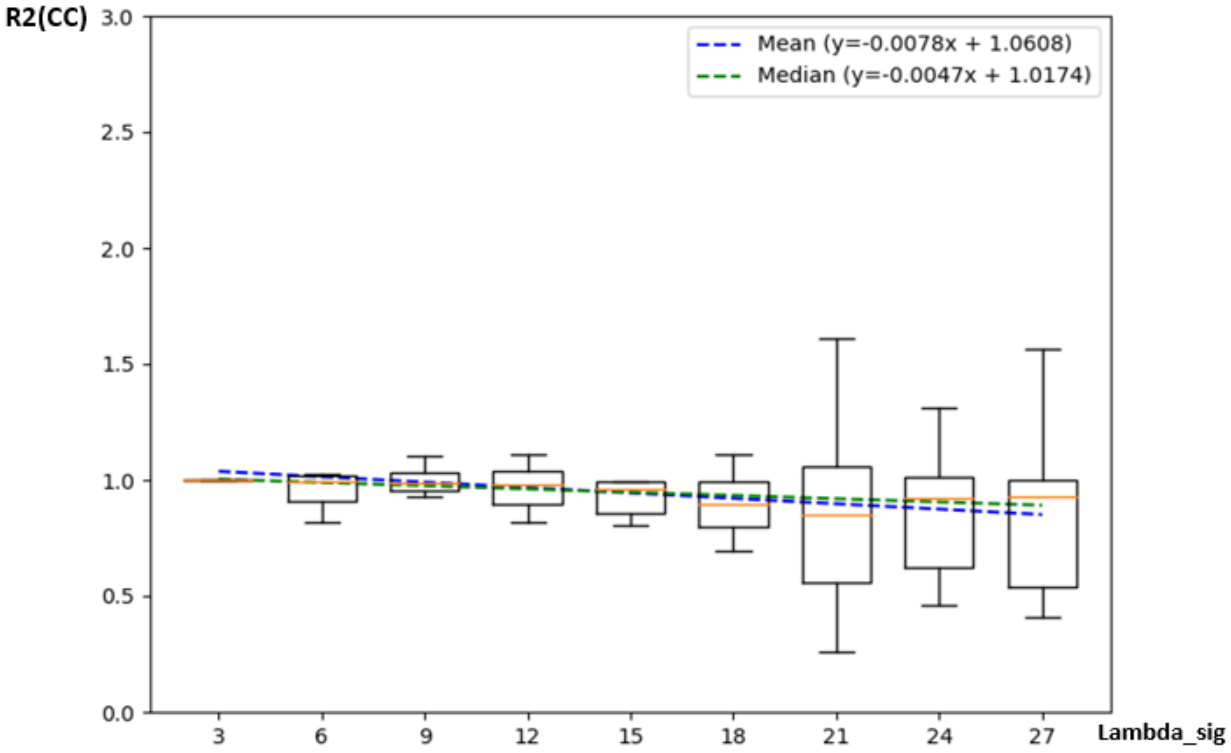

Figure B.29 Evolution of R2(CC) function of the tissue Lambada_sig

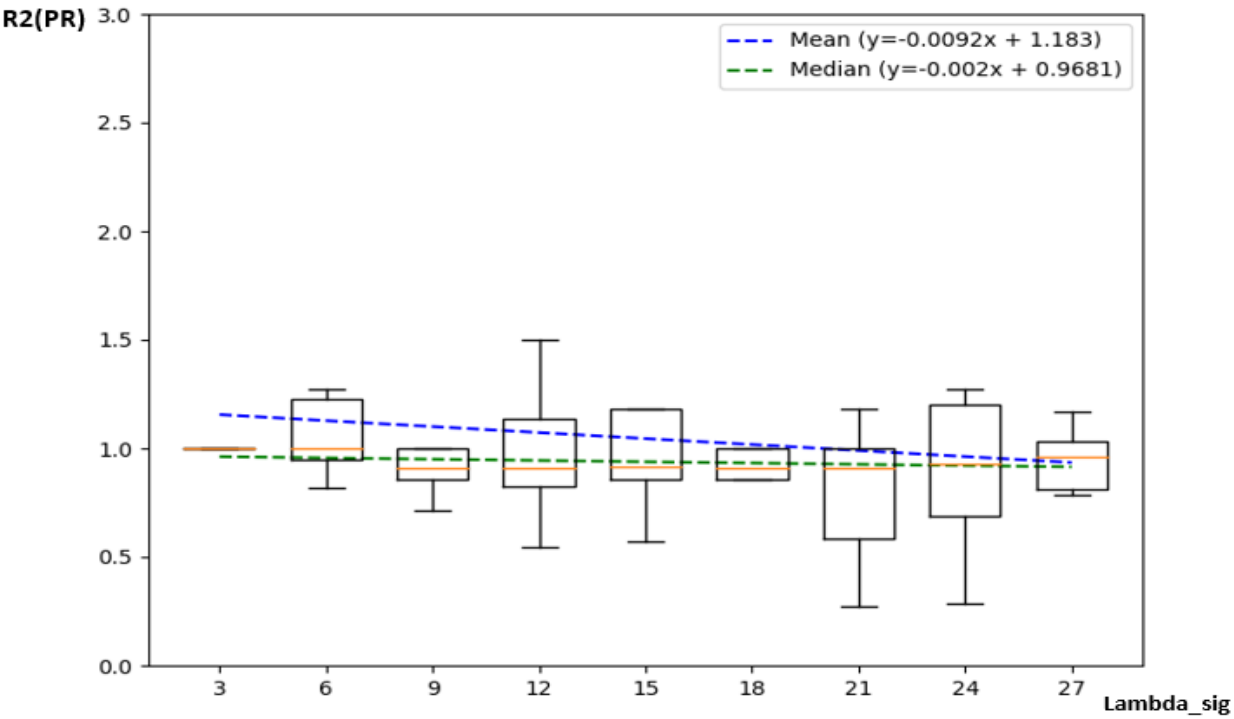

Figure B.30 Evolution of R2(BC) function of the tissue Lambada_sig

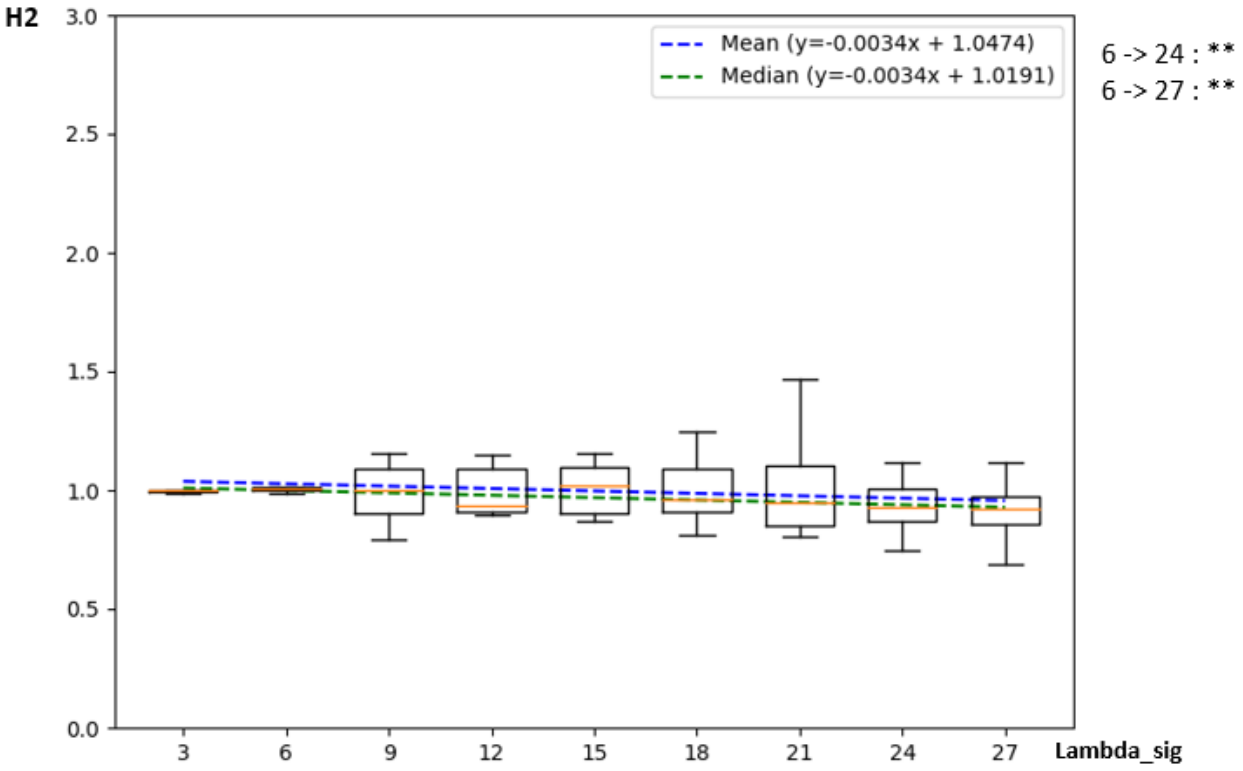

Figure B.31 Evolution of H2 function of the tissue Lambada_sig

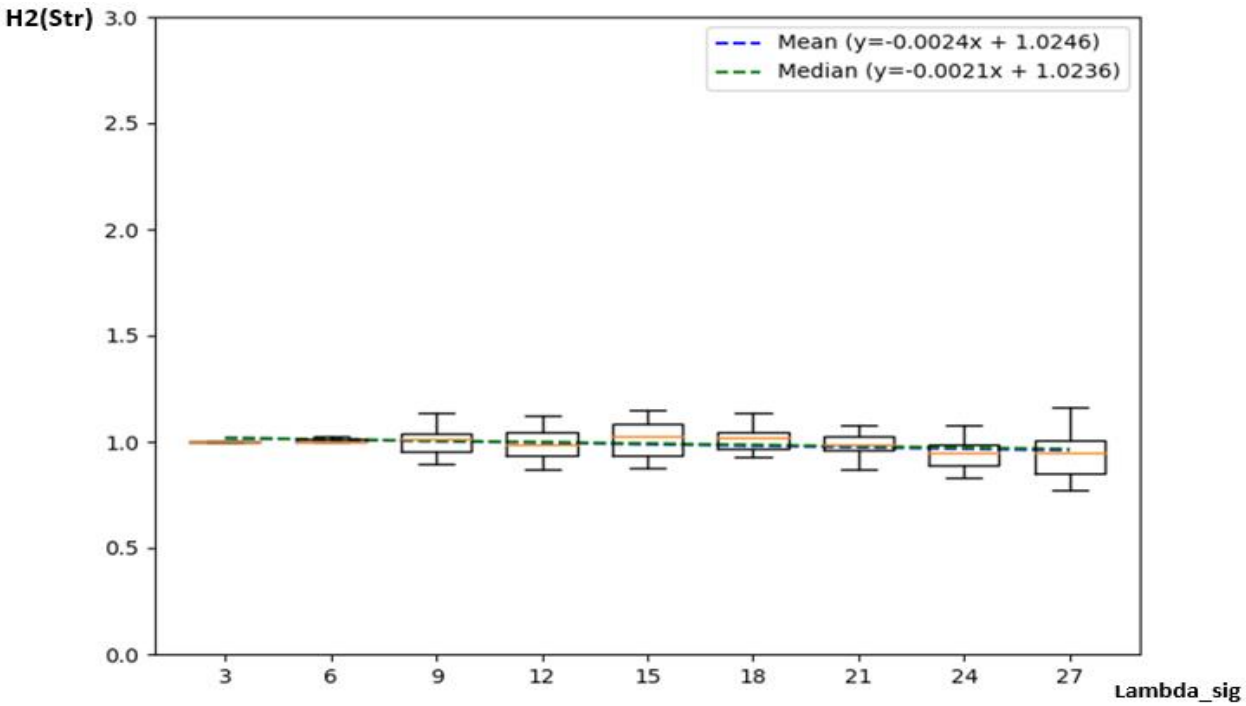

Figure B.32 Evolution of H2(Str) function of the tissue Lambada_sig

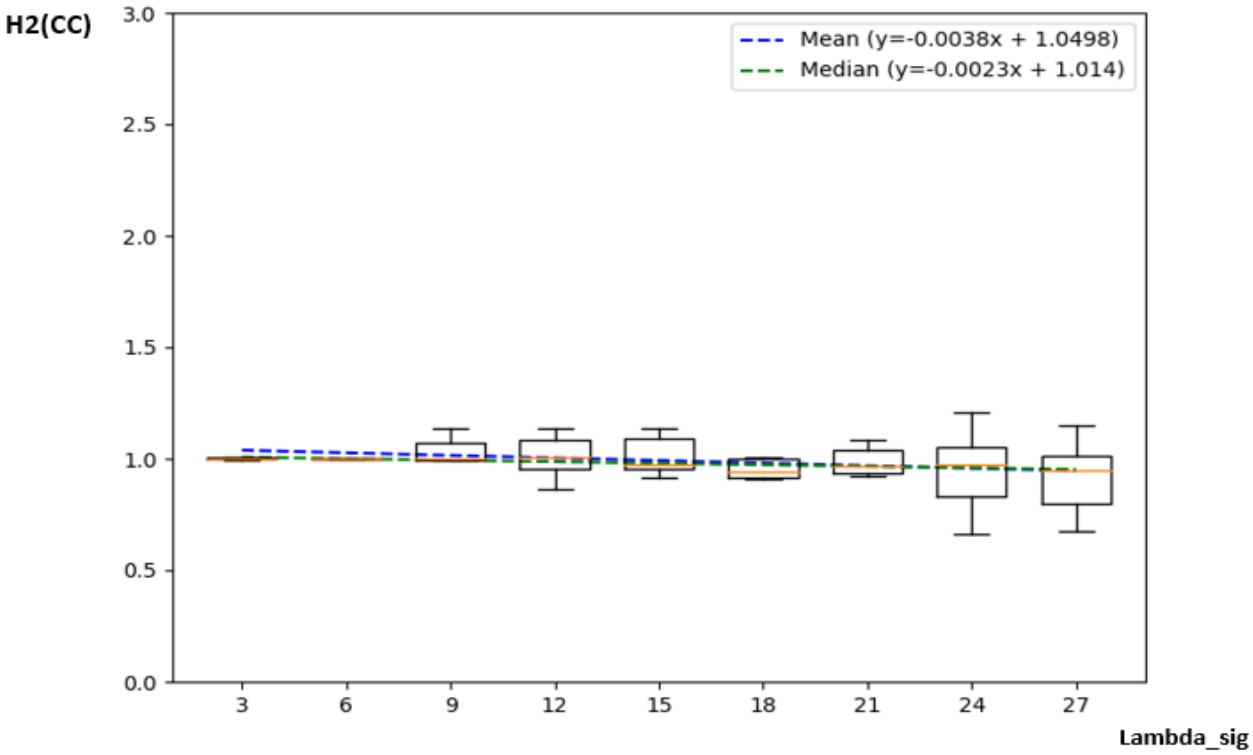

Figure B.33 Evolution of H2(CC) function of the tissue Lambada_sig

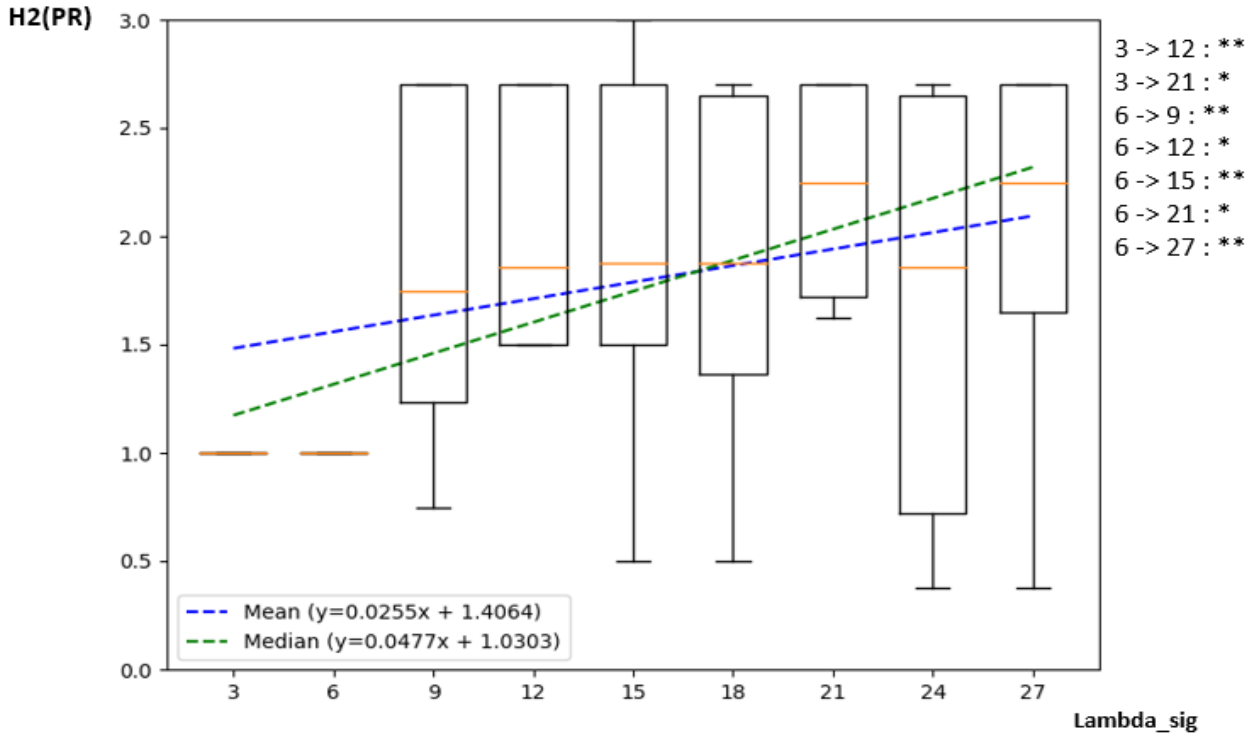

Figure B.34 Evolution of H2(PR) function of the tissue Lambada_sig

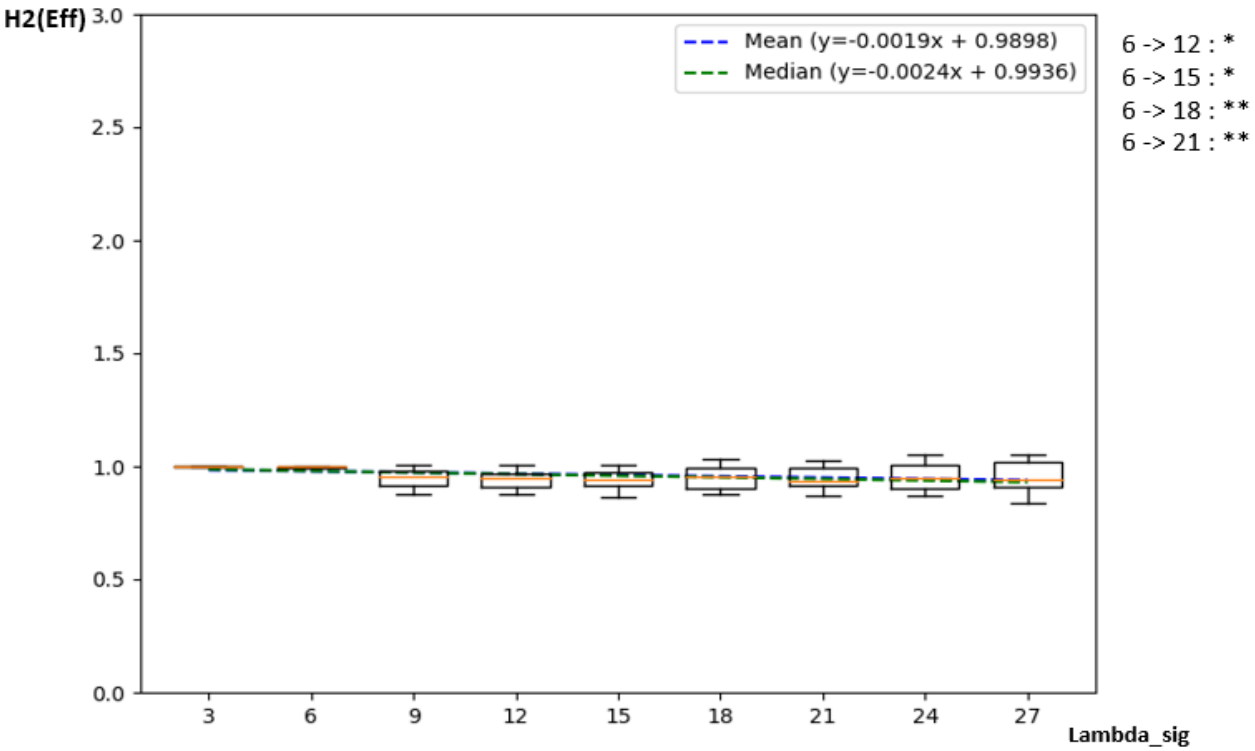

Figure B.35 Evolution of H2(Eff) function of the tissue Lambada_sig

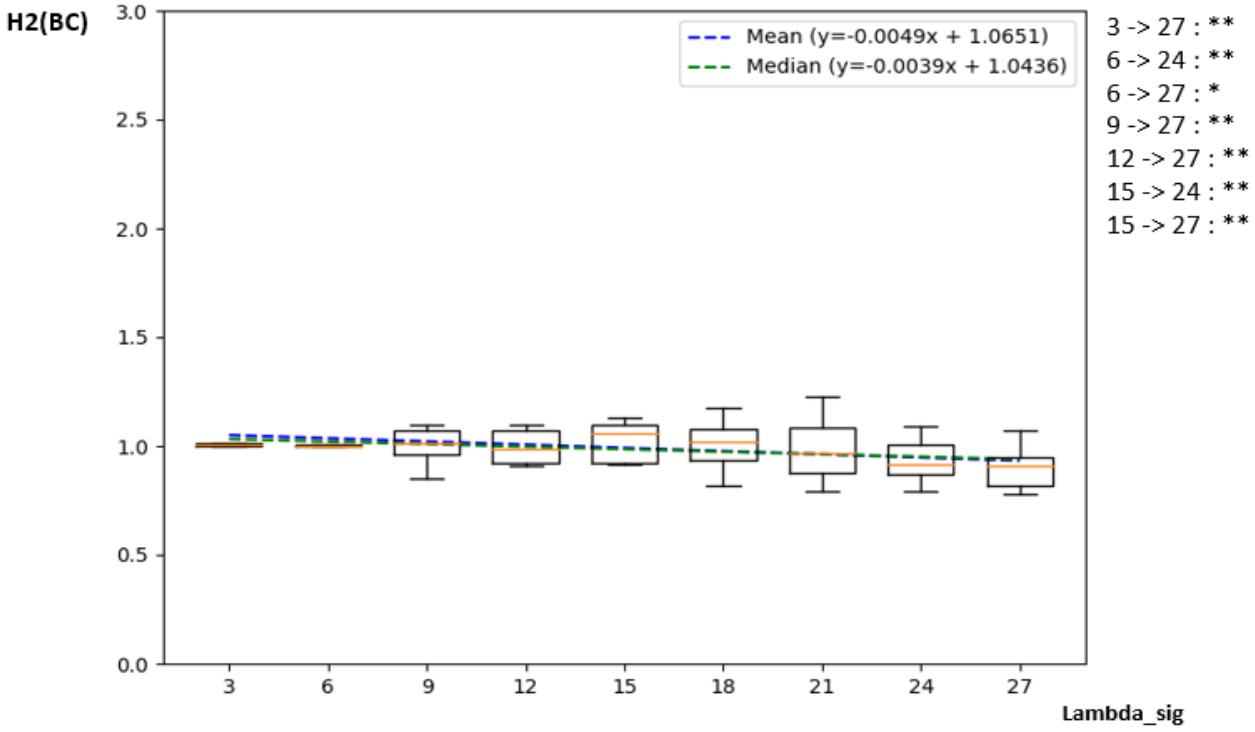

Figure B.36 Evolution of H2(BC) function of the tissue Lambada_sig

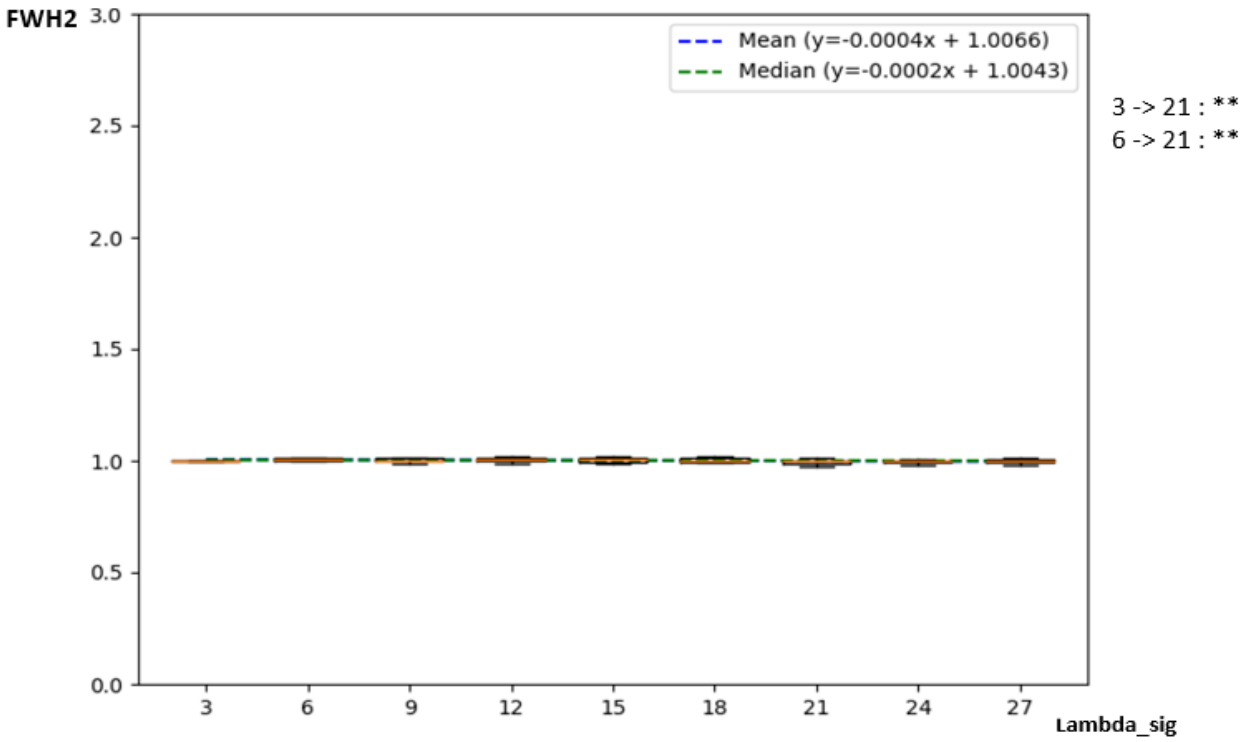

Figure B.37 Evolution of FWH2 function of the tissue Lambada_sig

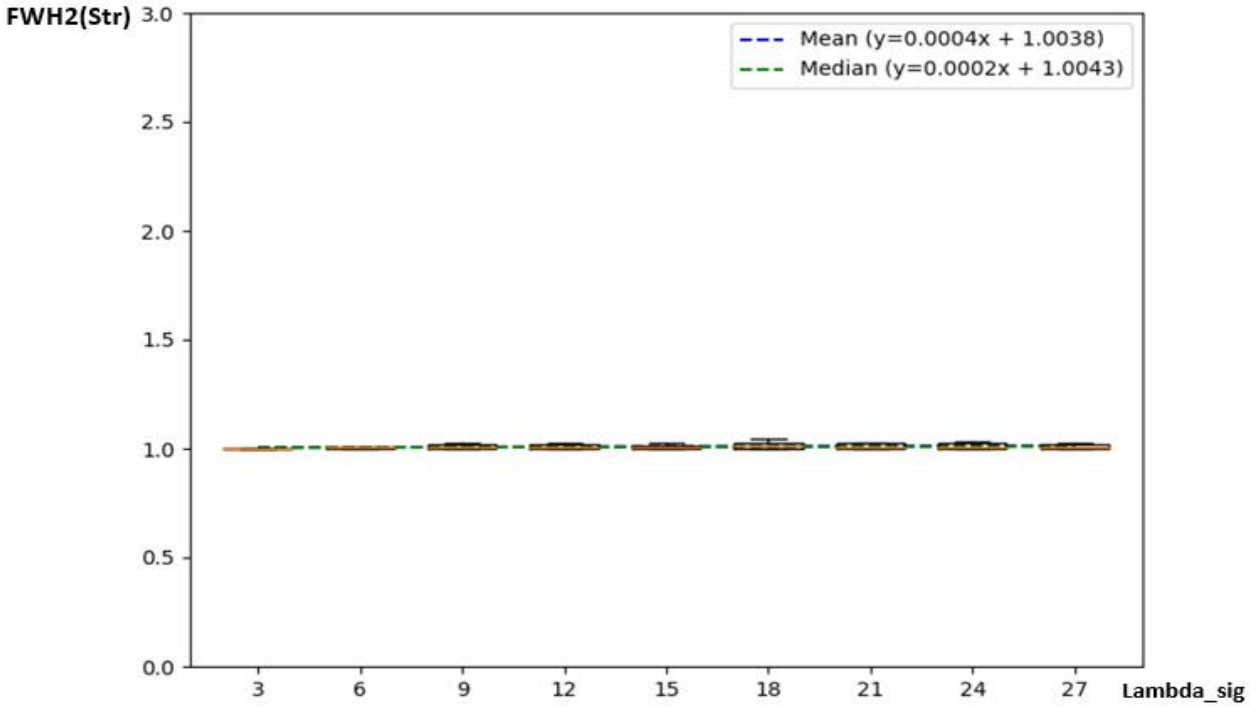

Figure B.38 Evolution of FWH2(Str) function of the tissue Lambada_sig

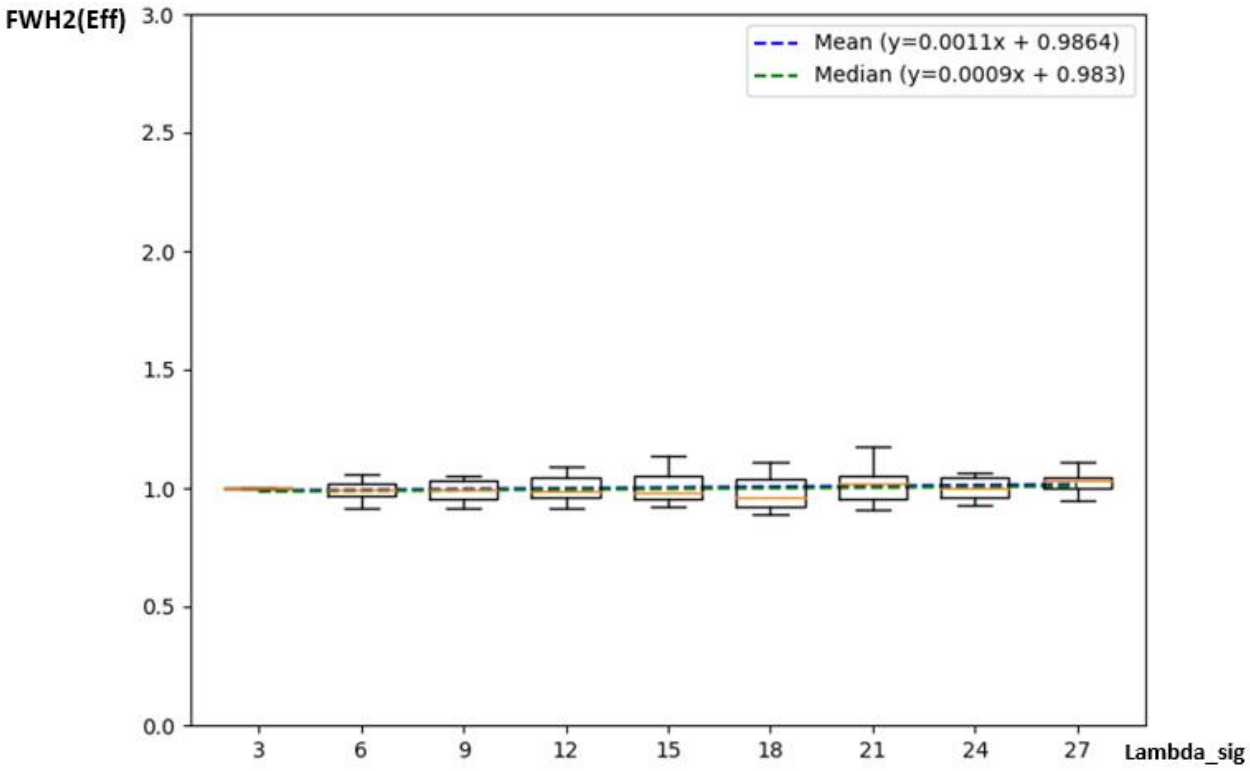

Figure B.39 Evolution of FWH2(Eff) function of the tissue Lambada_sig

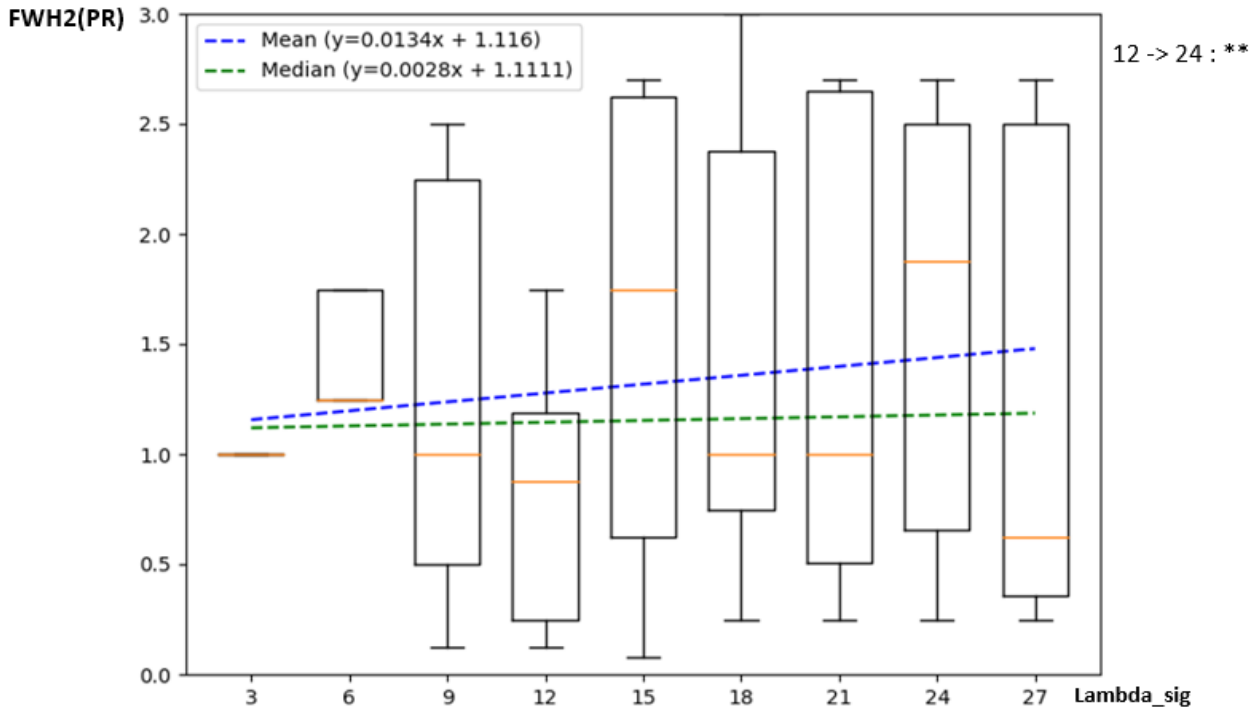

Figure B.40 Evolution of FWH2(PR) function of the tissue Lambada_sig

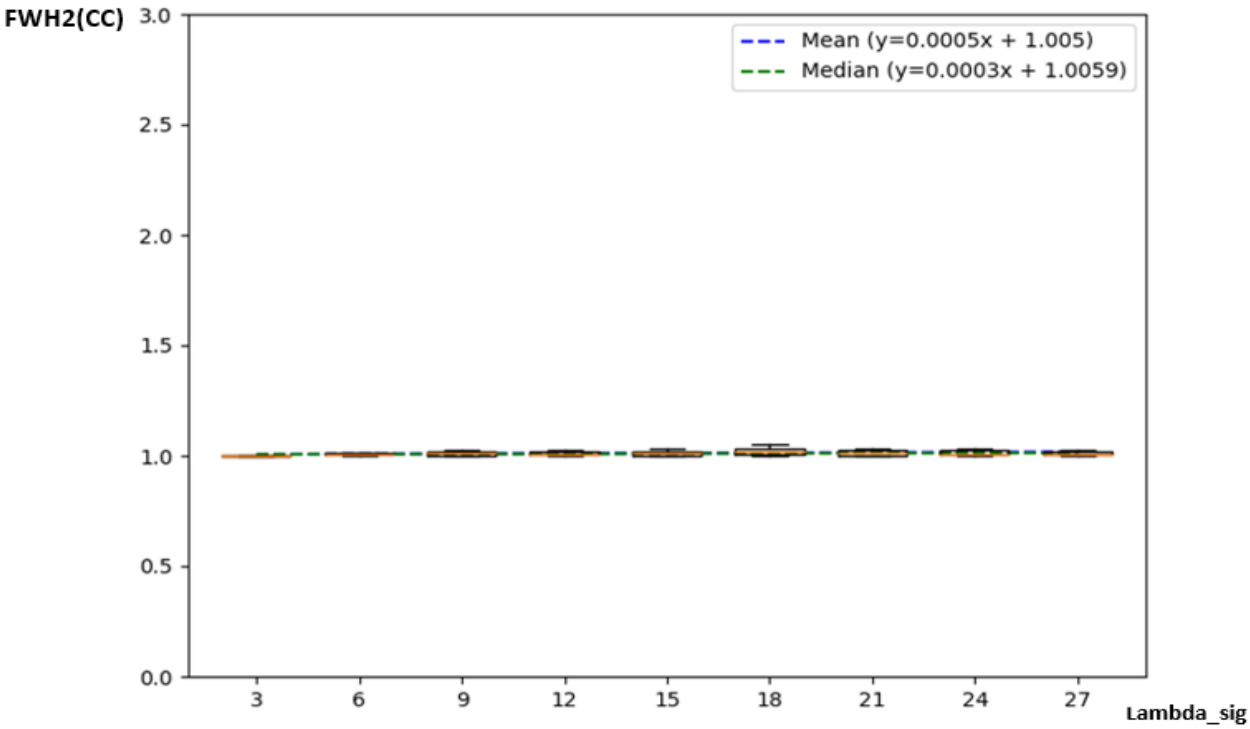

Figure B.41 Evolution of FWH2(CC) function of the tissue Lambada_sig

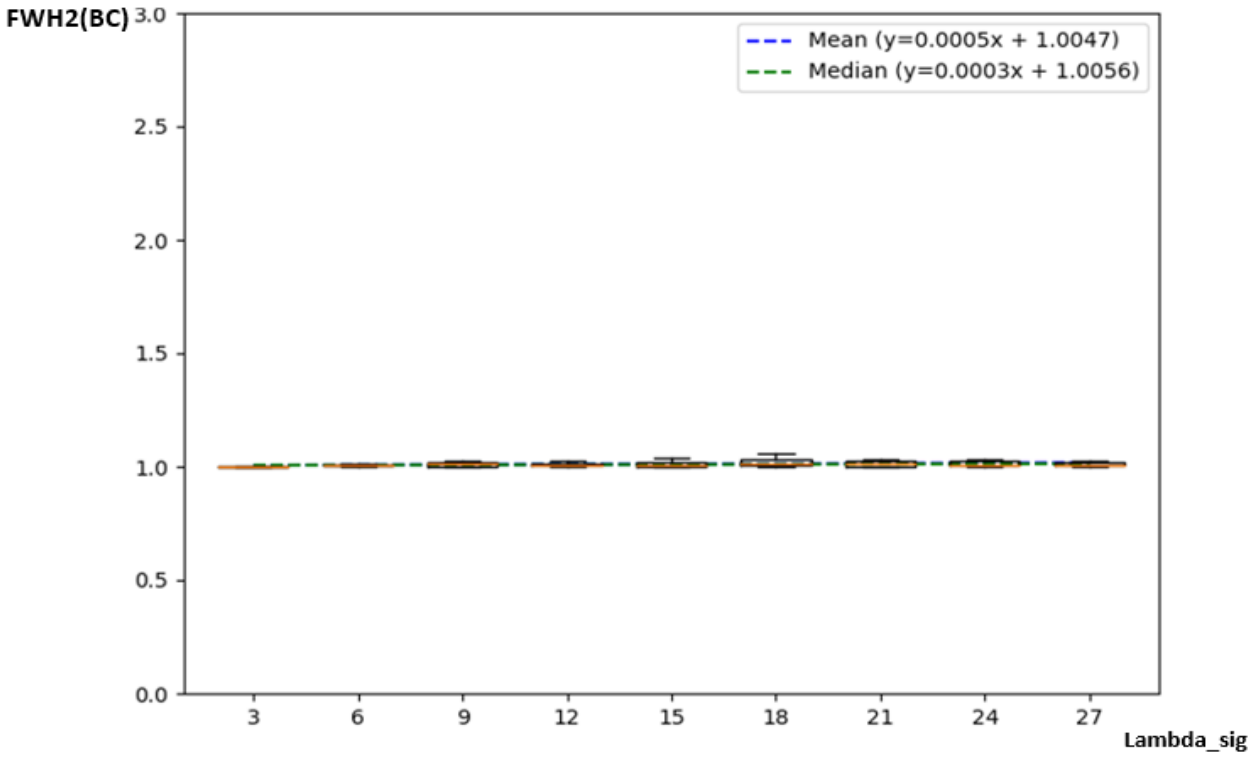

Figure B.42 Evolution of FWH2(BC) function of the tissue Lambada_sig

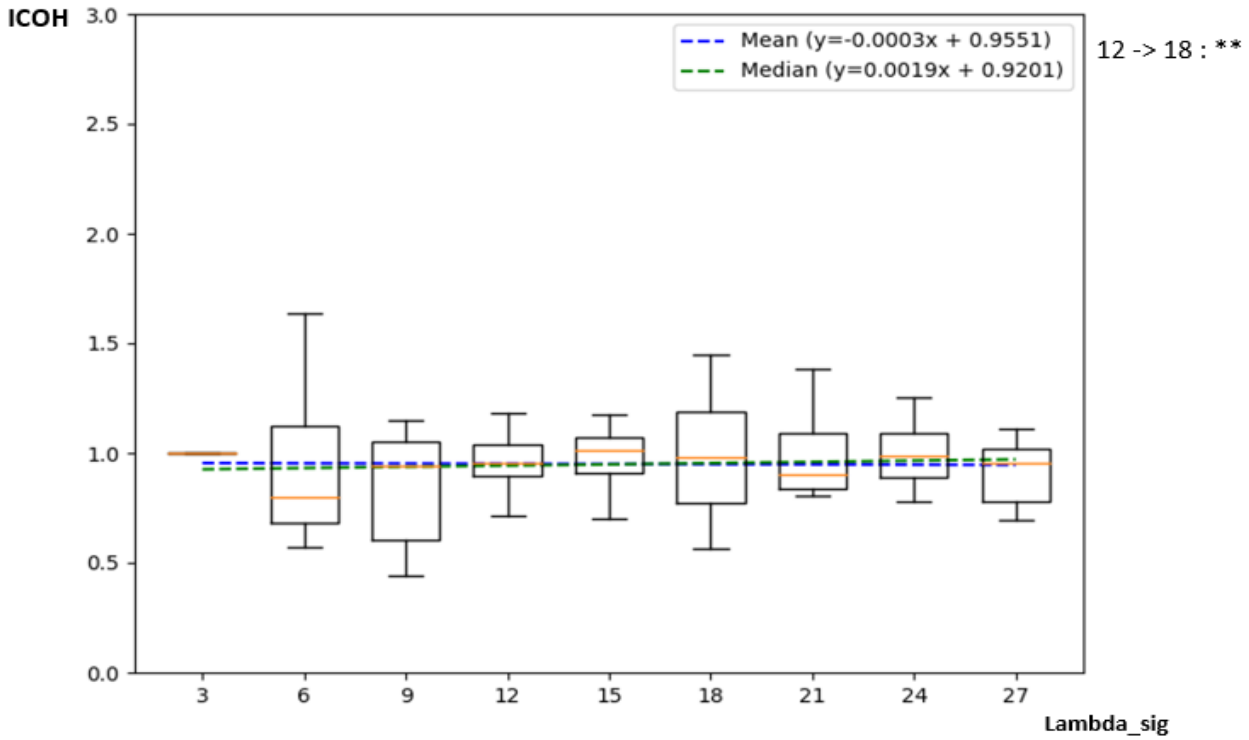

Figure B.43 Evolution of ICOH function of the tissue Lambada_sig

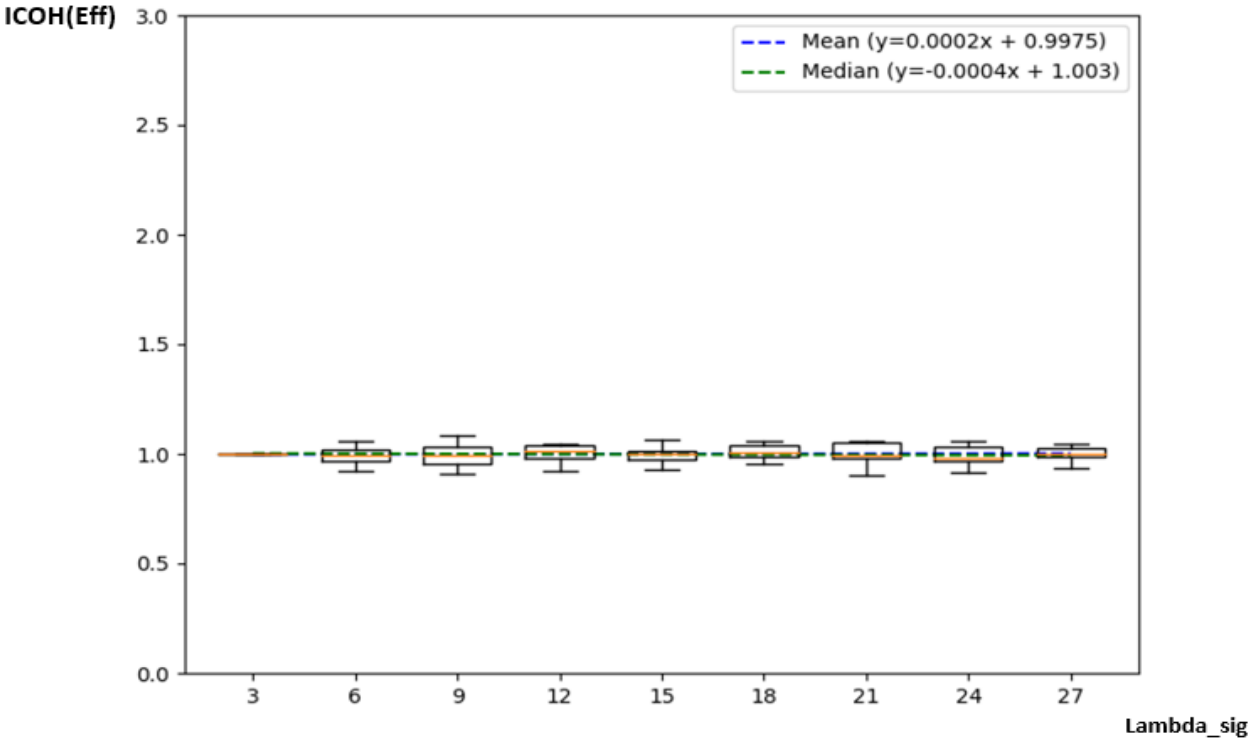

Figure B.44 Evolution of ICOH(Eff) function of the tissue Lambada_sig

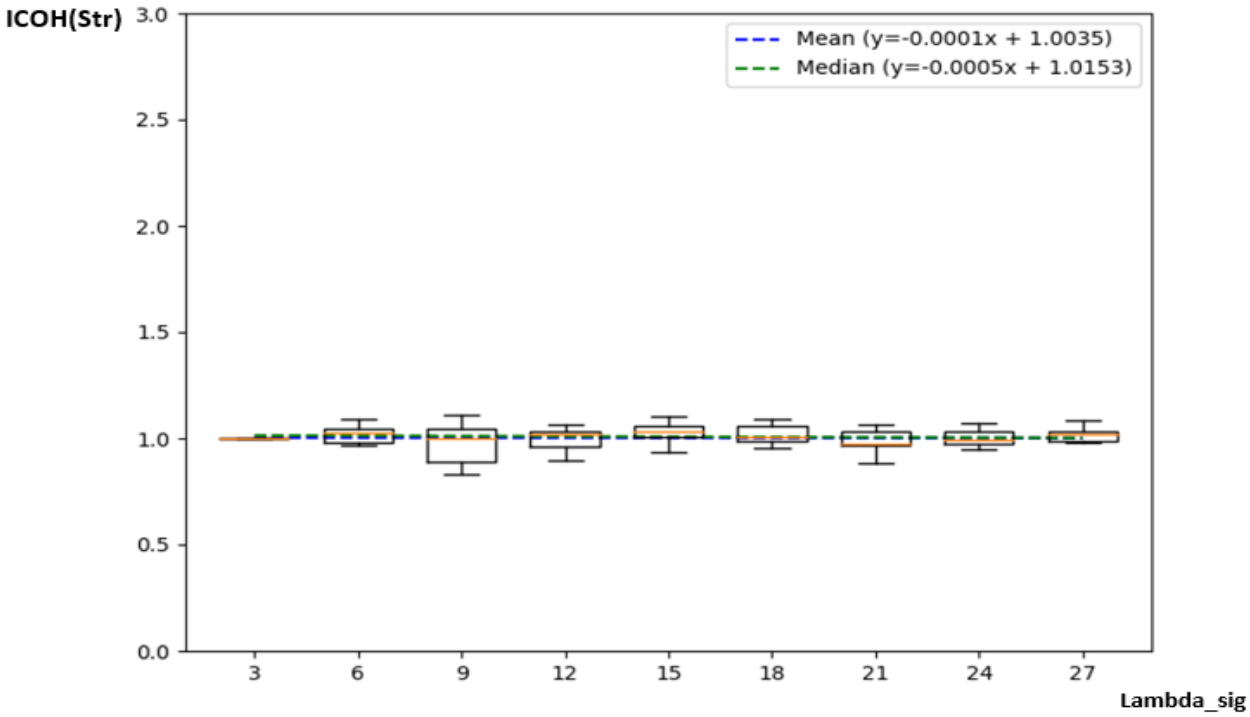

Figure B.45 Evolution of ICOH(Str) function of the tissue Lambada_sig

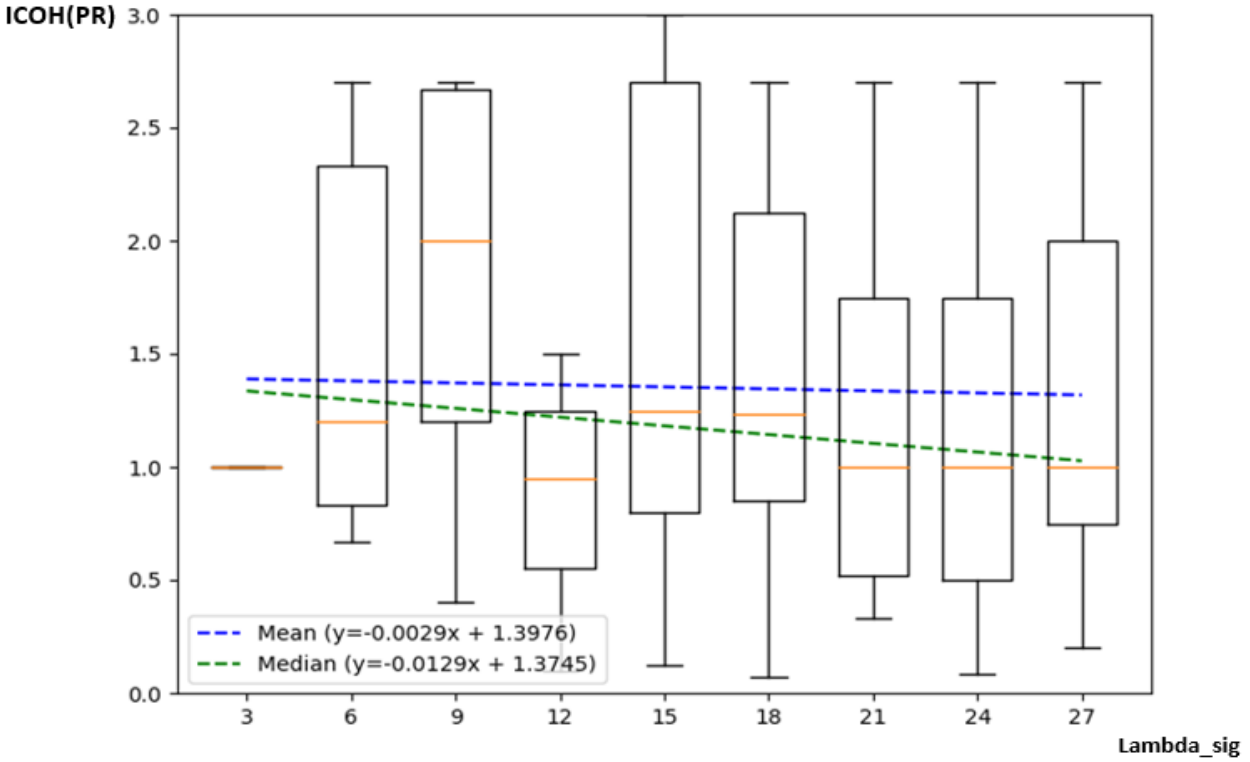

Figure B.46 Evolution of ICOH(PR) function of the tissue Lambada_sig

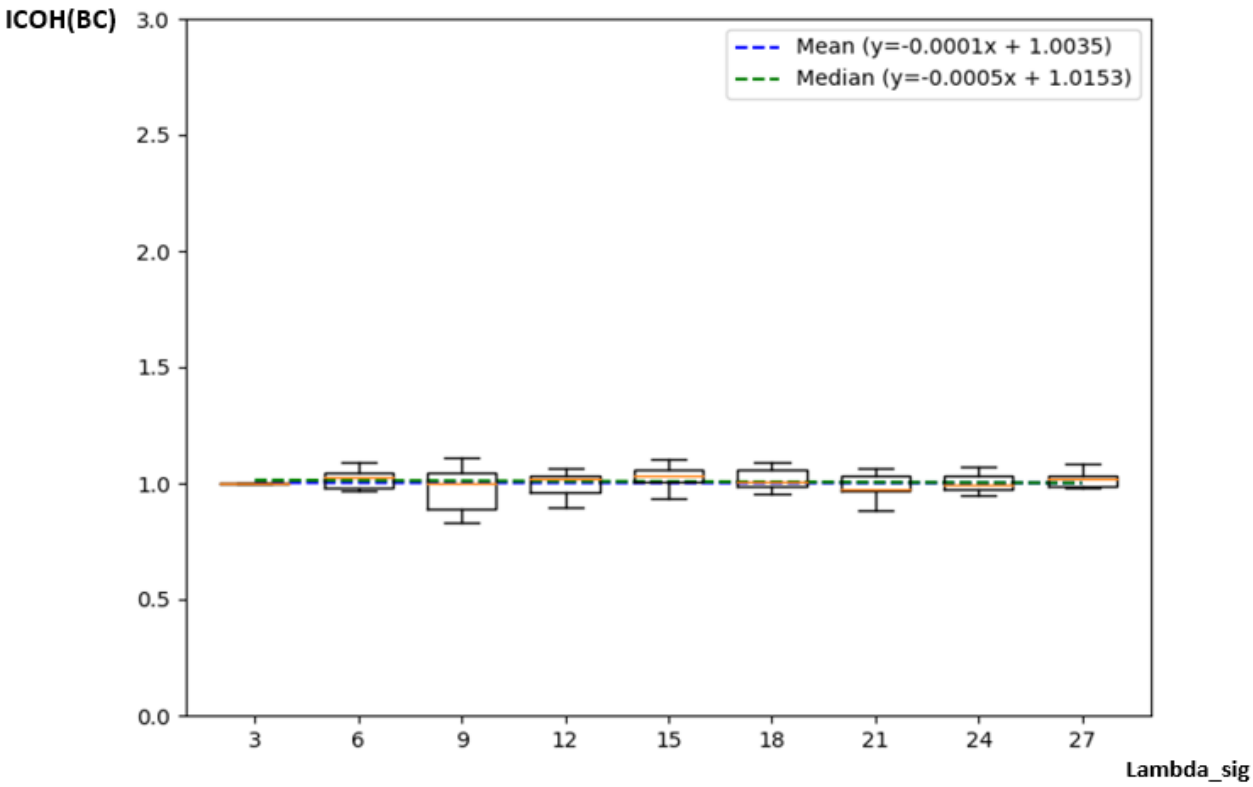

Figure B.47 Evolution of ICOH(BC) function of the tissue Lambada_sig

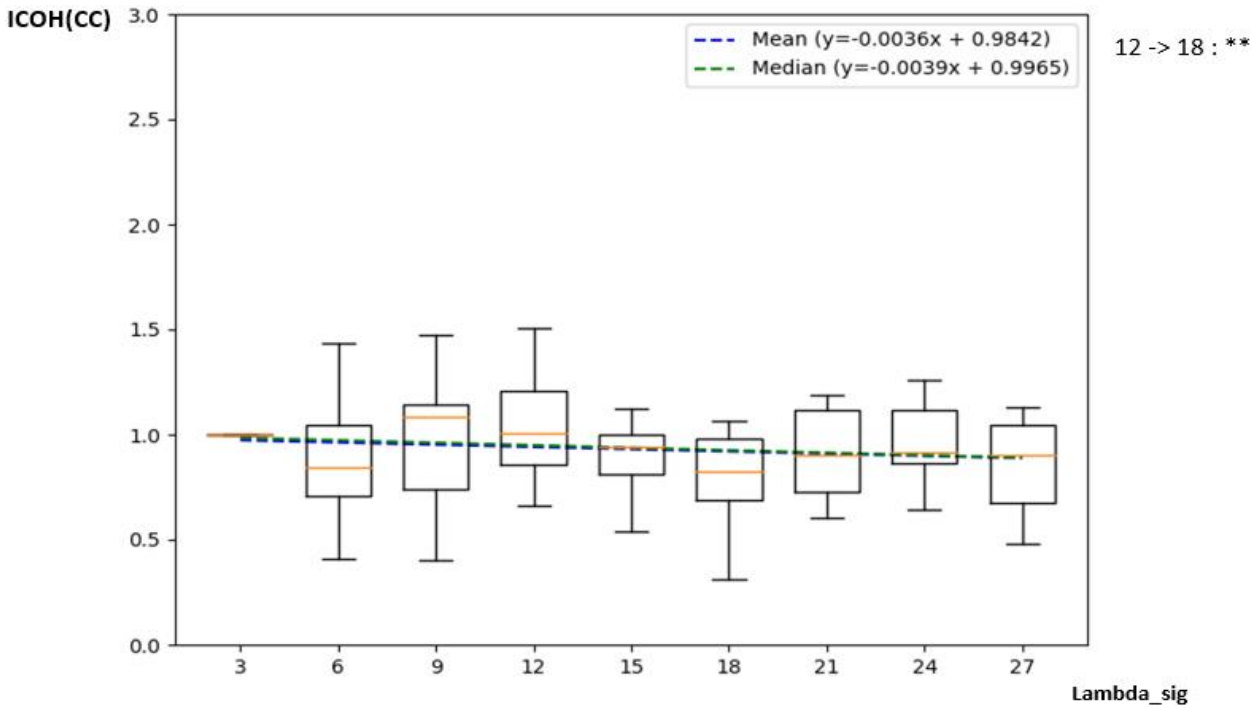

Figure B.48 Evolution of ICOH(CC) function of the tissue Lambada_sig

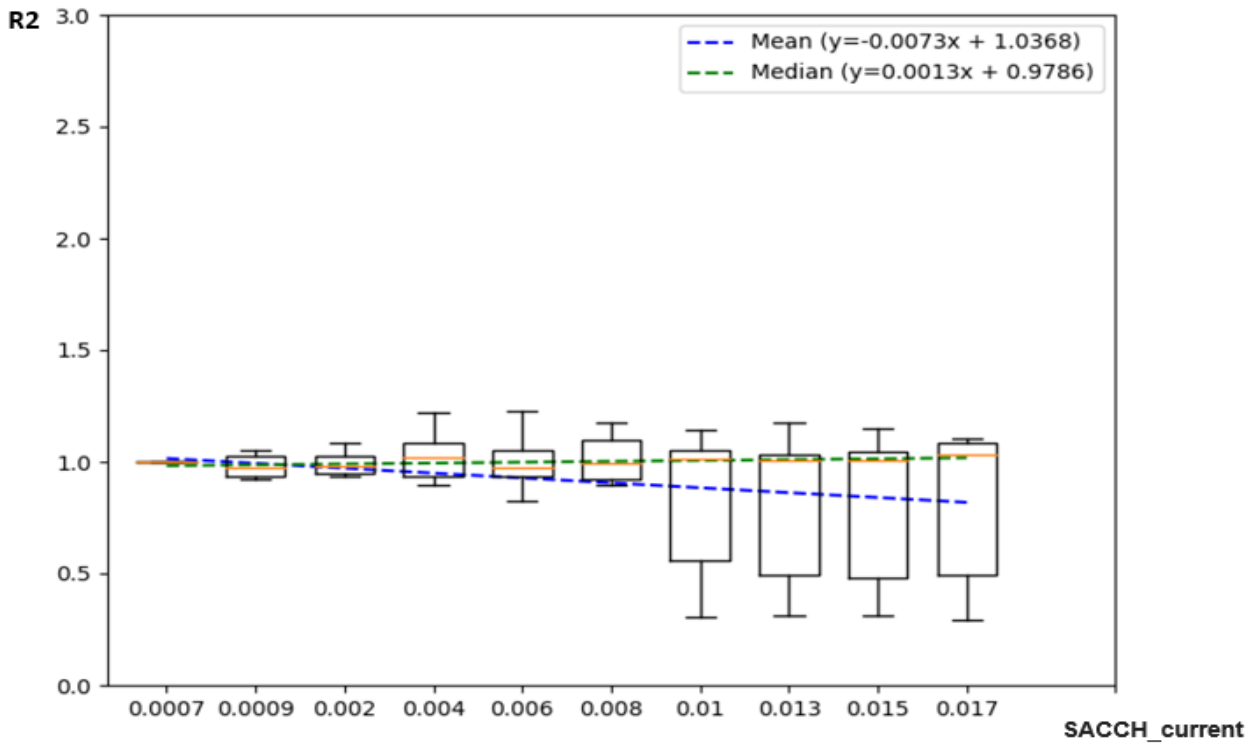

Figure B.49 Evolution of R2 function of the tissue SACCH_current

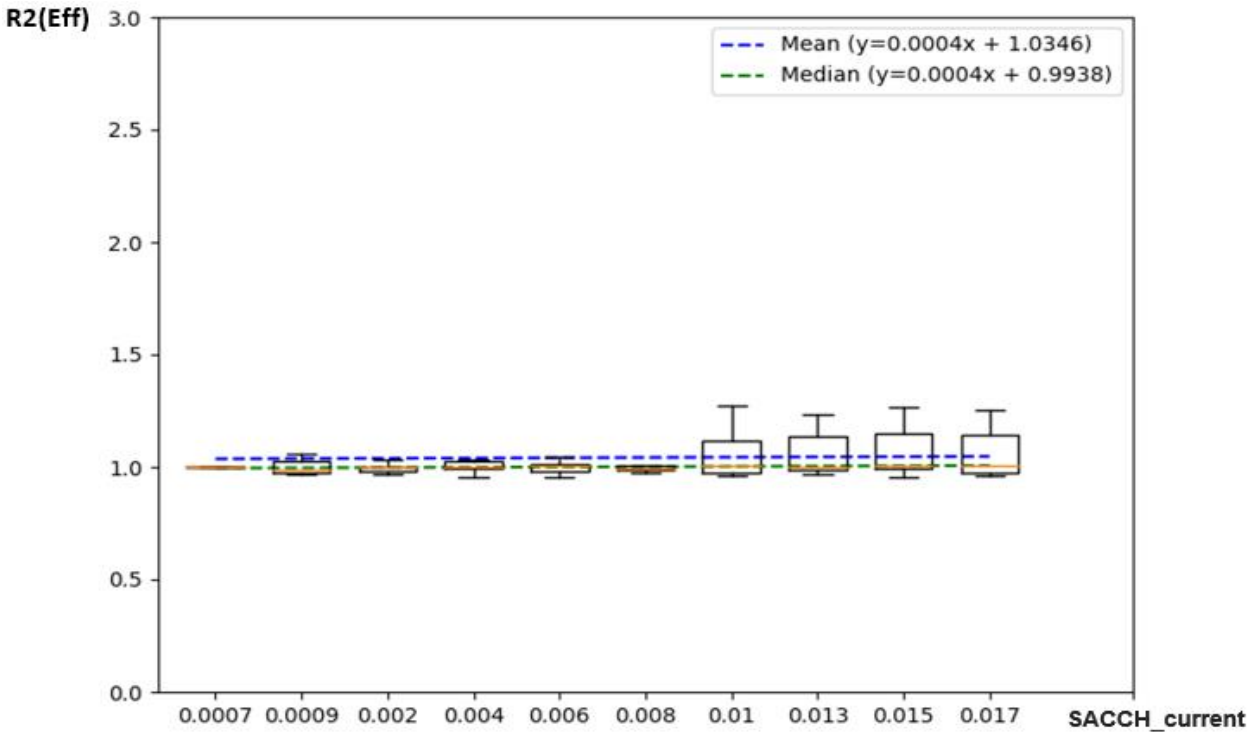

Figure B.50 Evolution of R2(Eff) function of the tissue SACCH_current

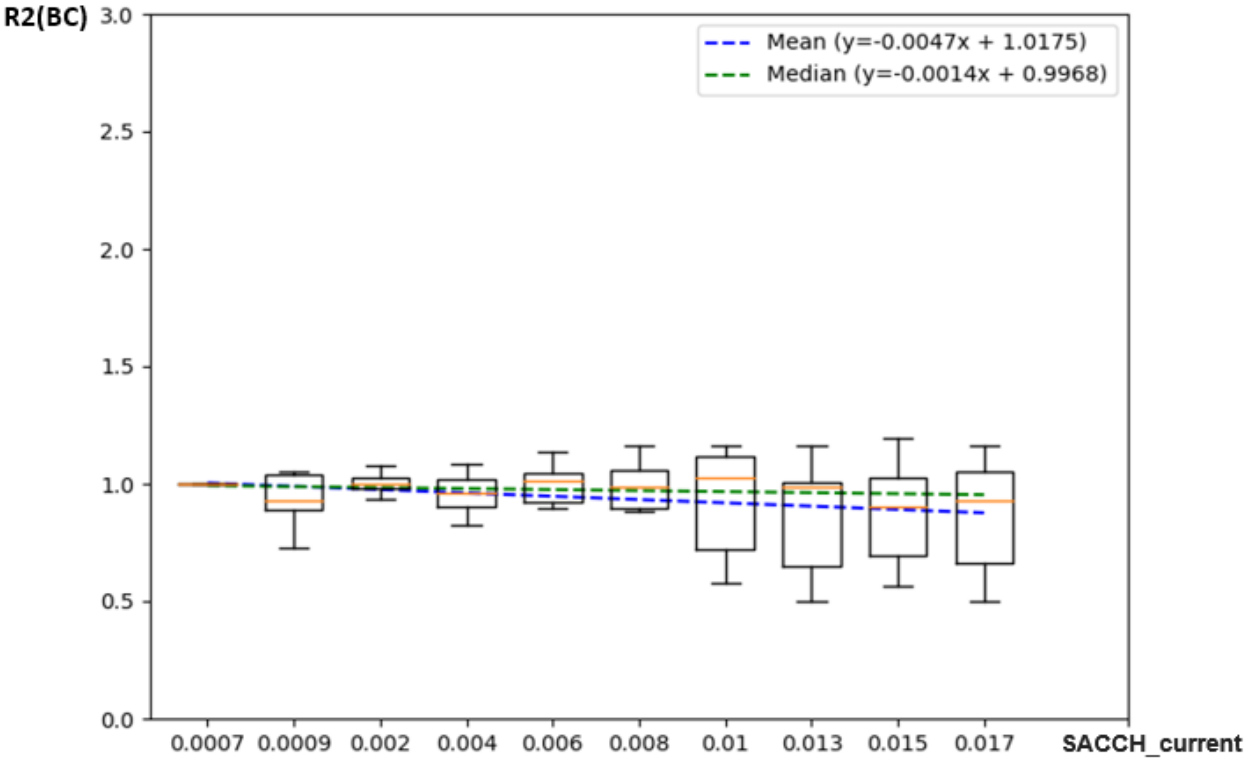

Figure B.51 Evolution of R2(BC) function of the tissue SACCH_current

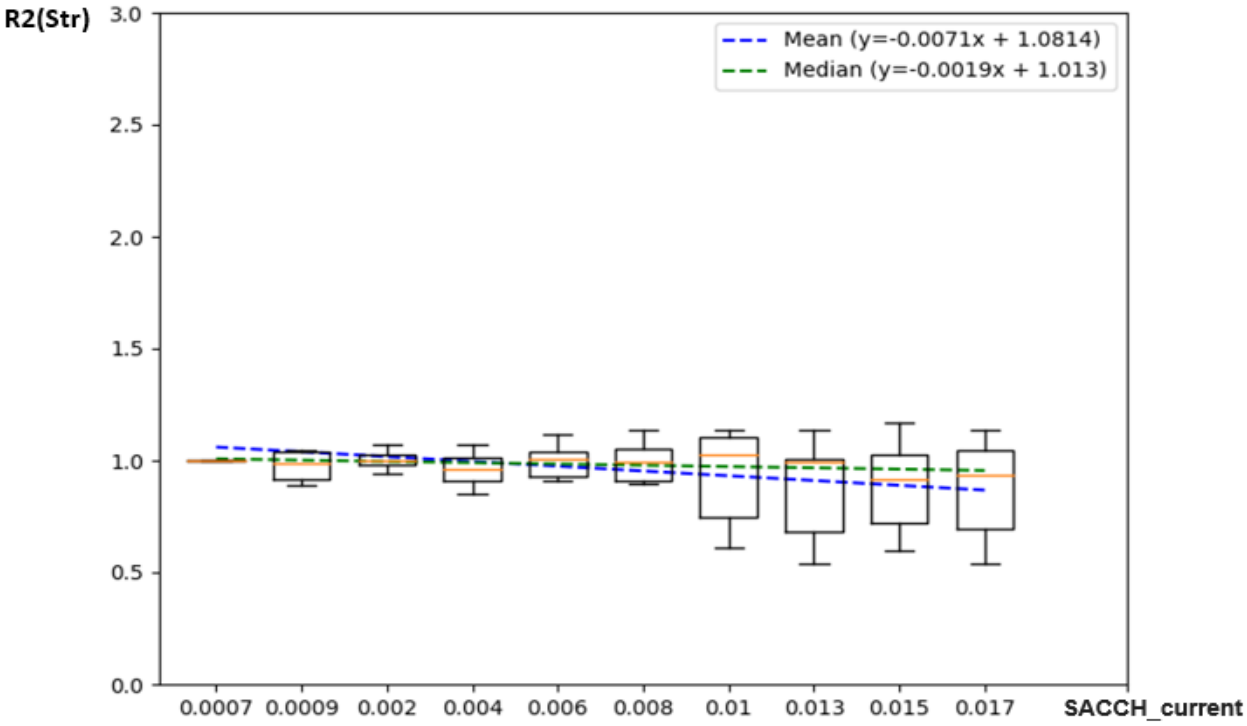

Figure B.52 Evolution of R2(Str) function of the tissue SACCH_current

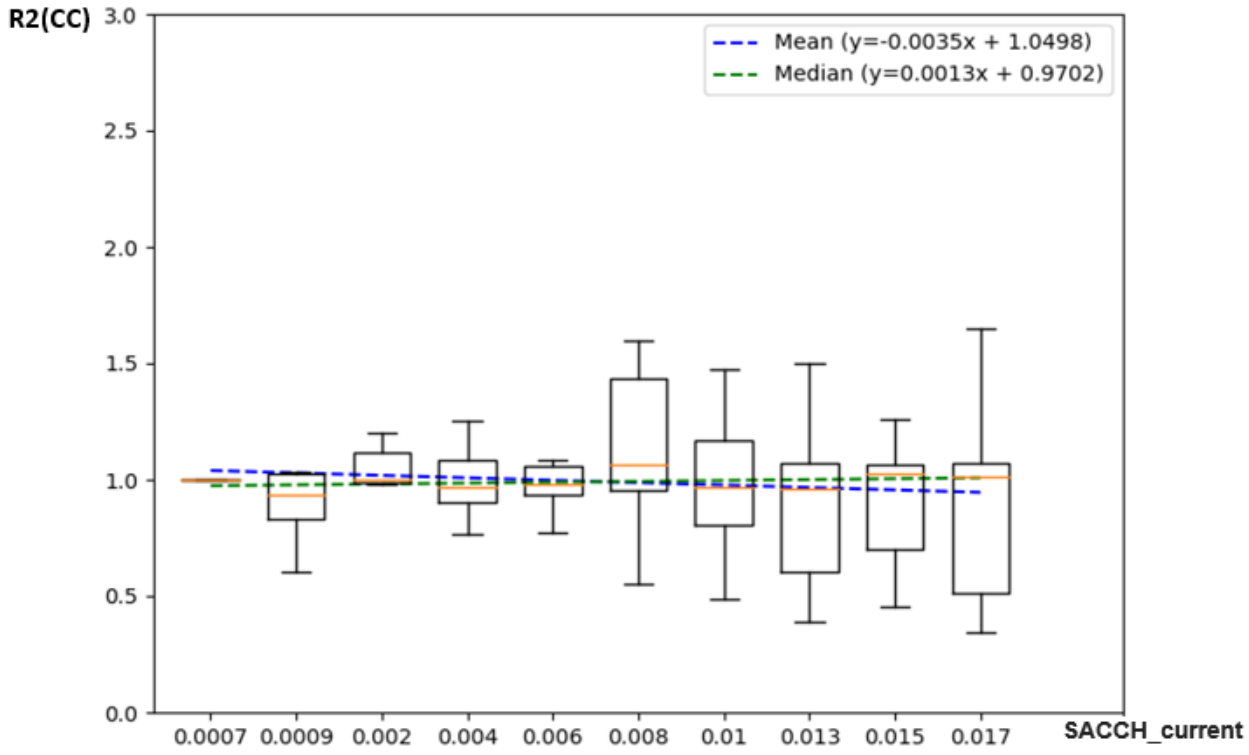

Figure B.53 Evolution of R2(CC) function of the tissue SACCH_current

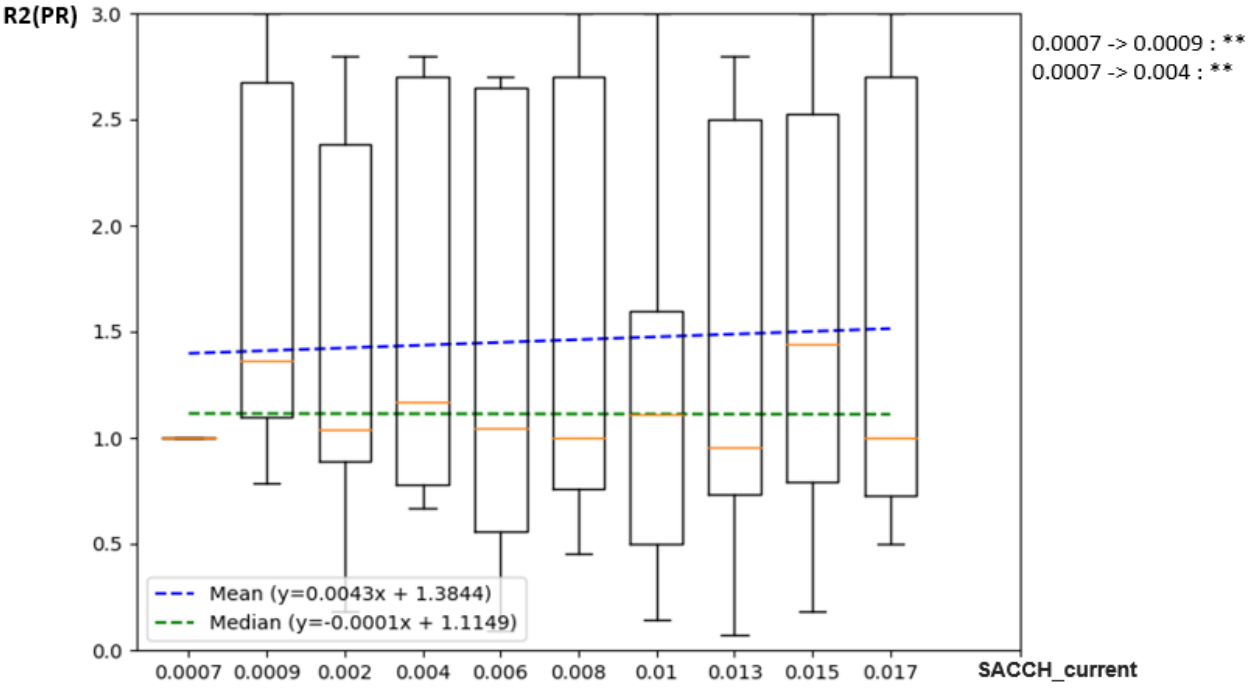

Figure B.54 Evolution of R2(PR) function of the tissue SACCH_current

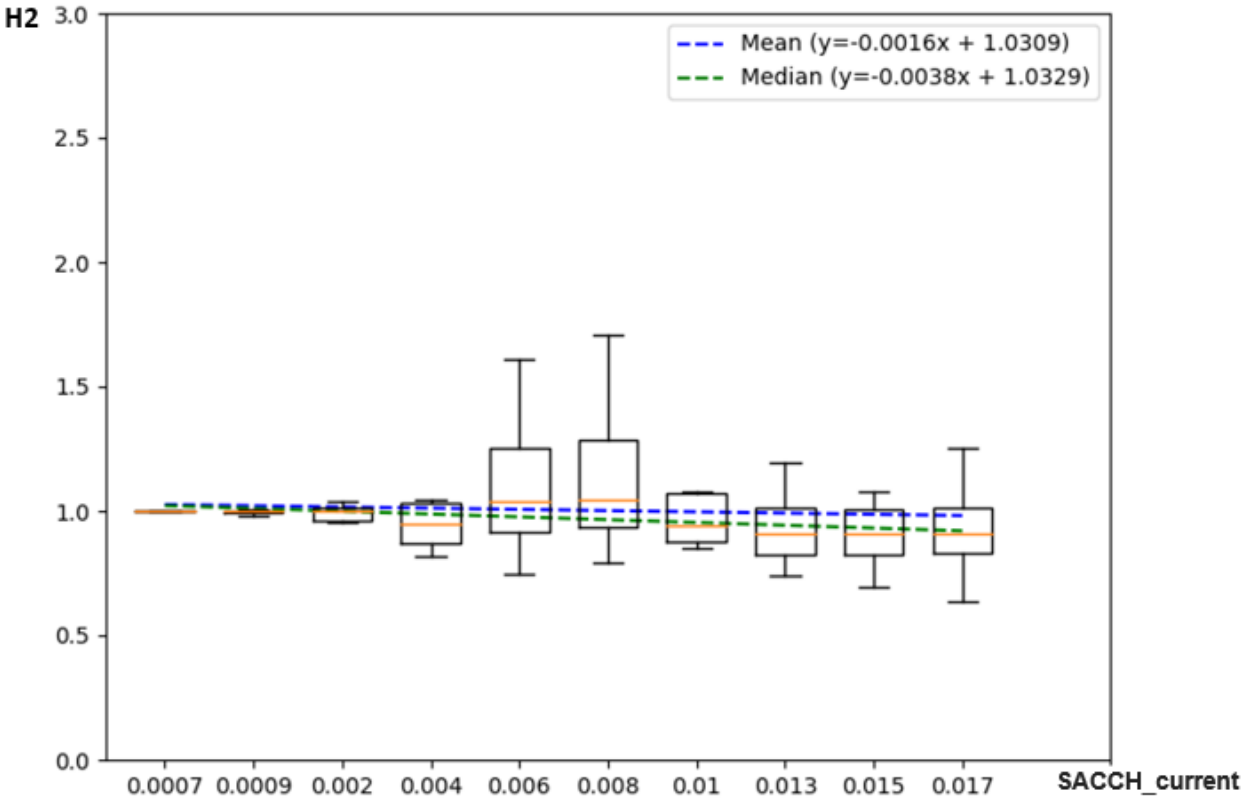

Figure B.55 Evolution of H2 function of the tissue SACCH_current

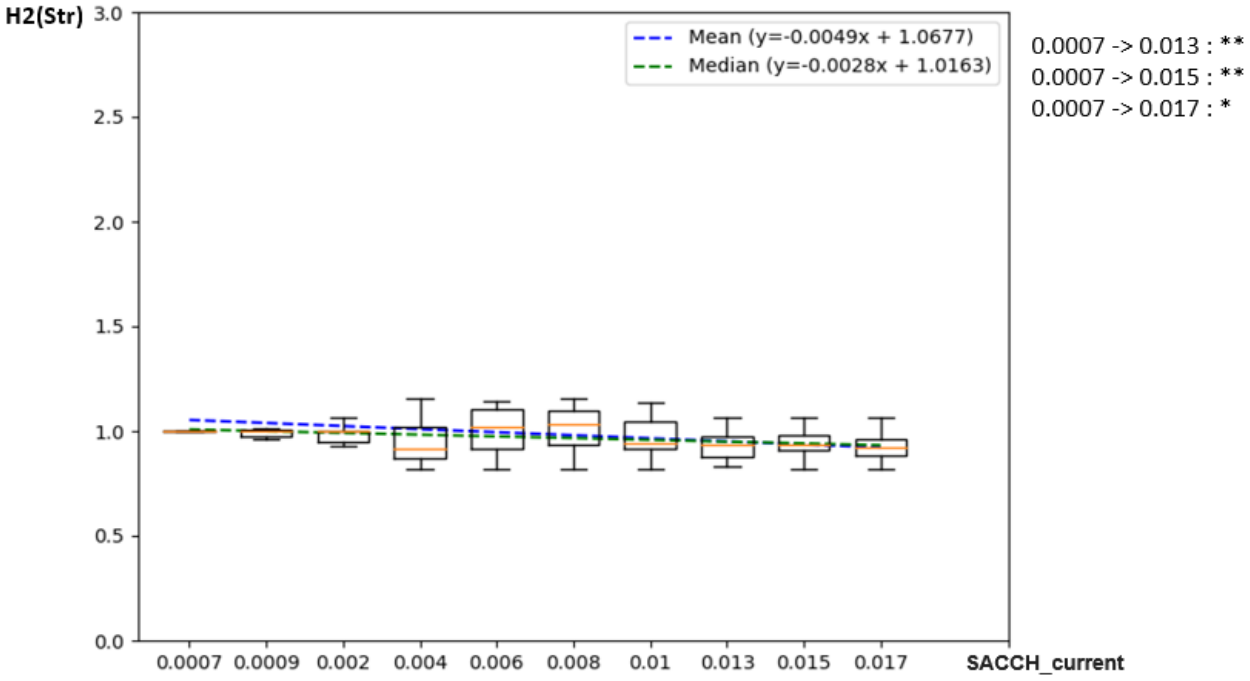

Figure B.56 Evolution of H2(Str) function of the tissue SACCH_current

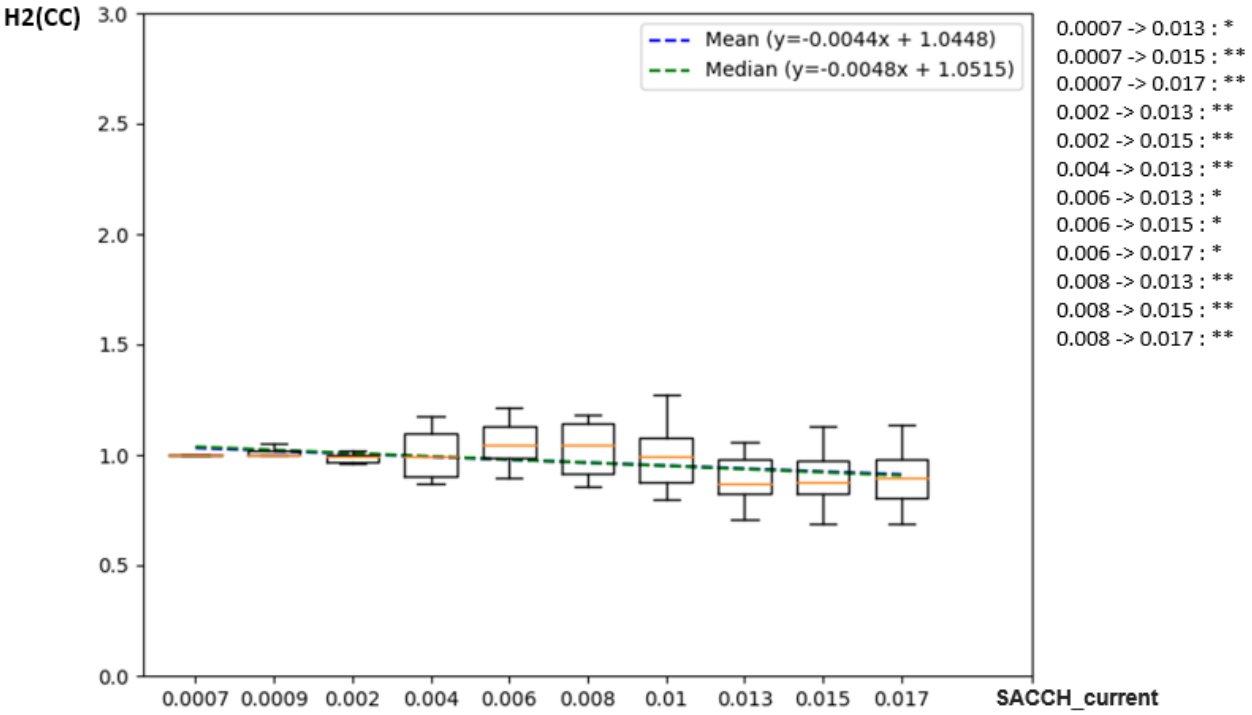

Figure B.57 Evolution of H2(CC) function of the tissue SACCH_current

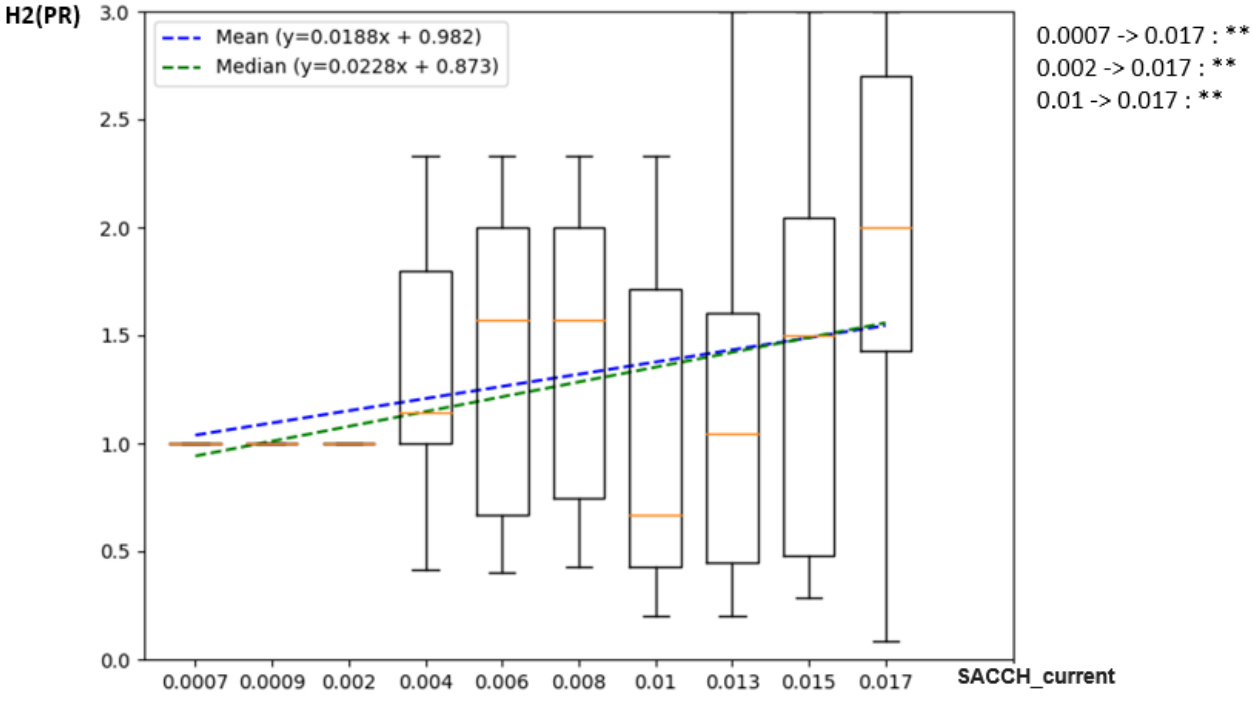

Figure B.58 Evolution of H2(PR) function of the tissue SACCH_current

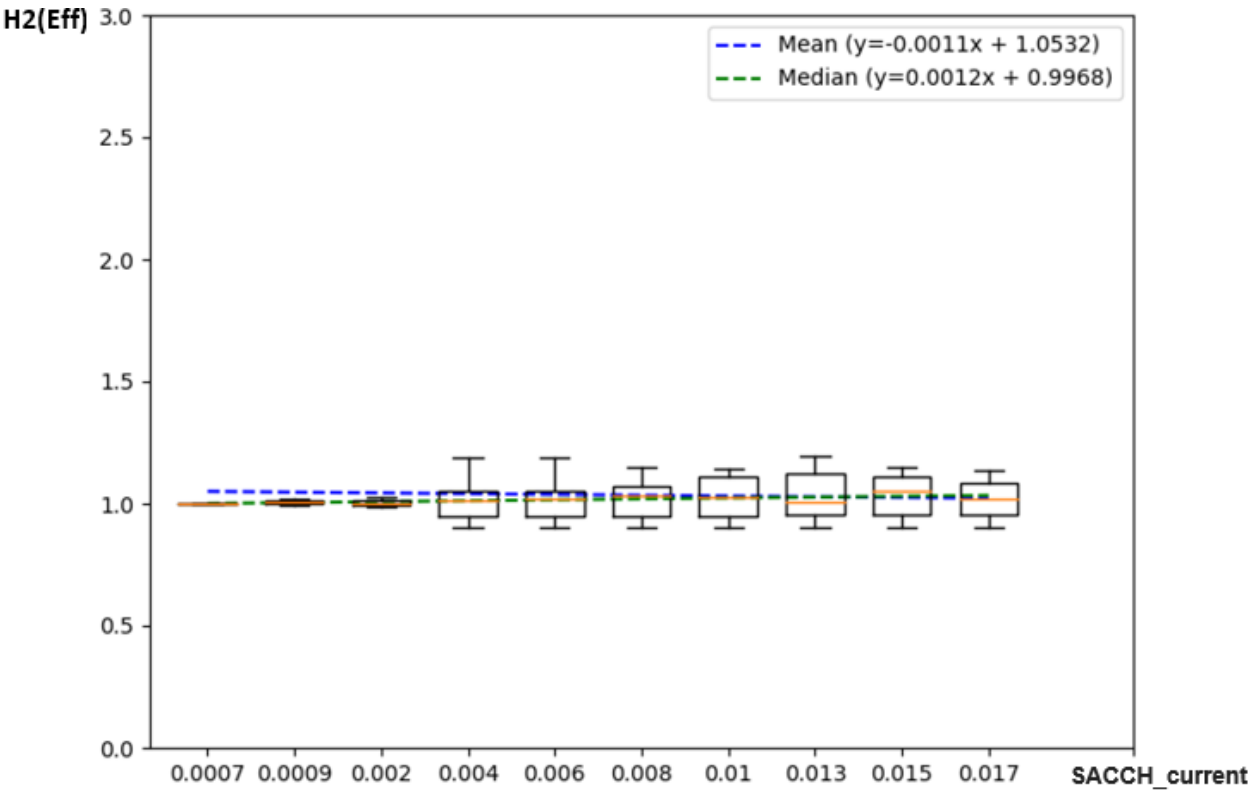

Figure B.59 Evolution of H2(Eff) function of the tissue SACCH_current

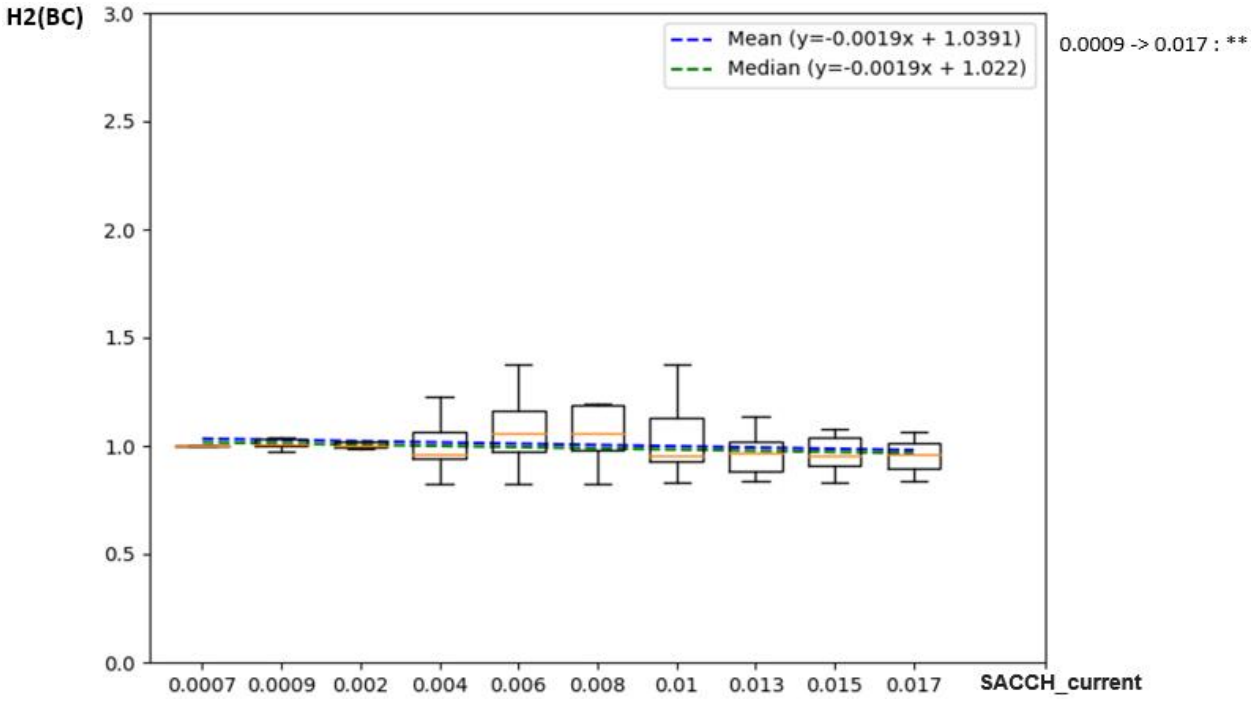

Figure B.60 Evolution of H2(BC) function of the tissue SACCH_current

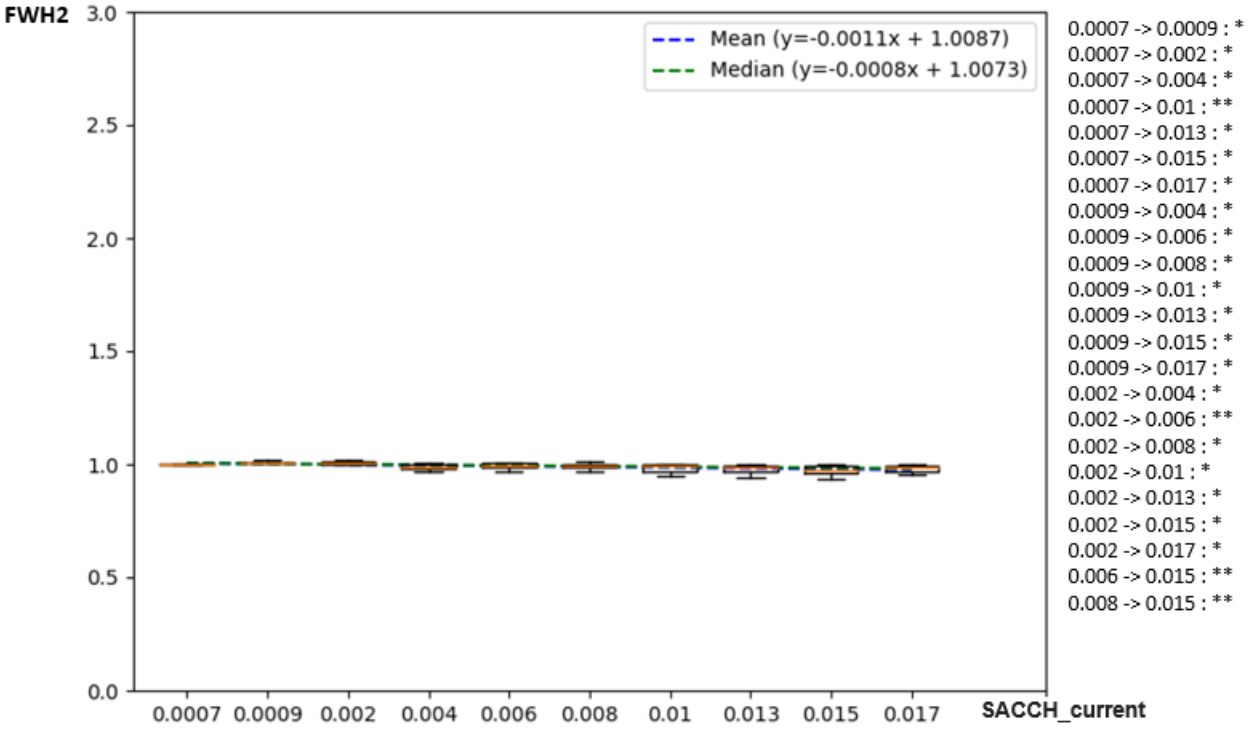

Figure B.61 Evolution of FWH2 function of the tissue SACCH_current

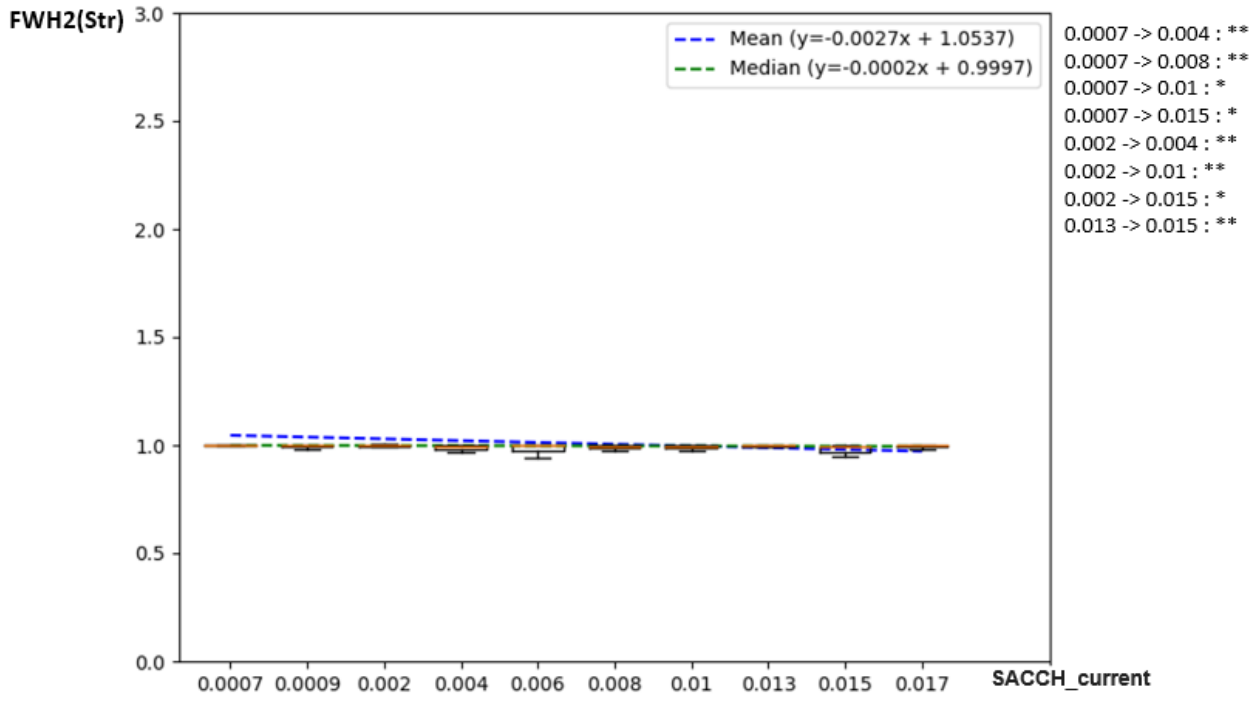

Figure B.62 Evolution of FWH2(Str) function of the tissue SACCH_current

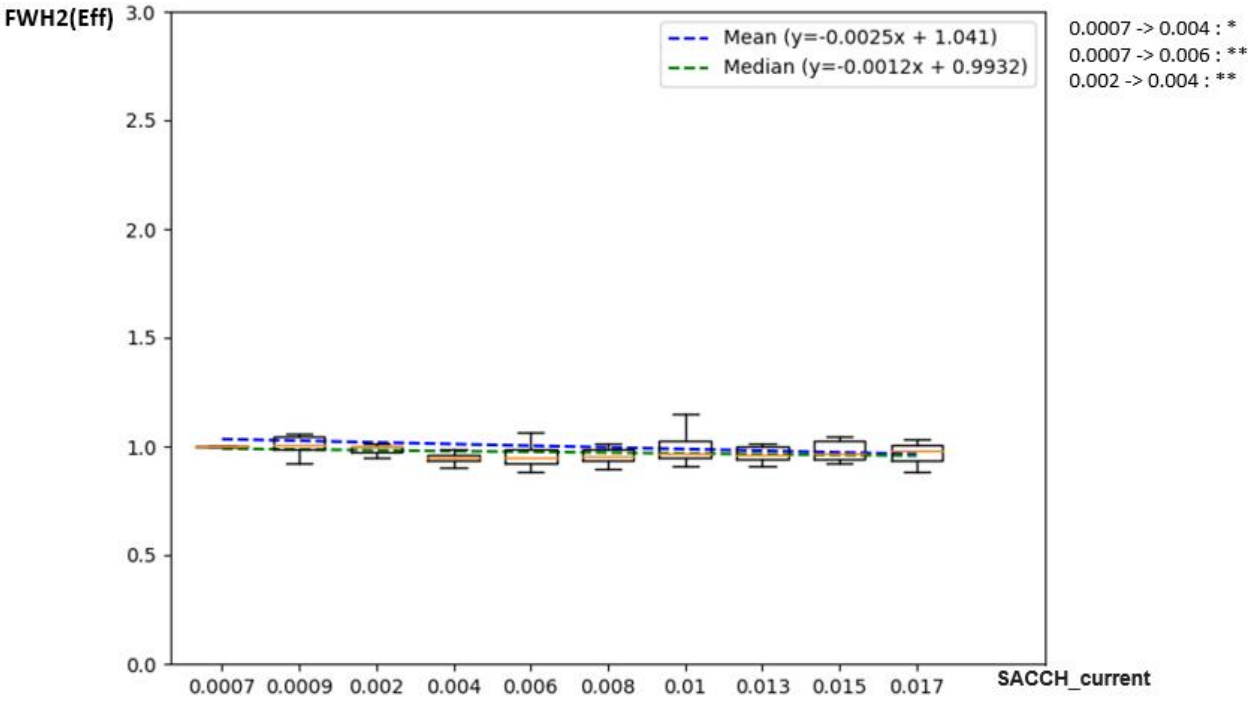

Figure B.63 Evolution of FWH2(Eff) function of the tissue SACCH_current

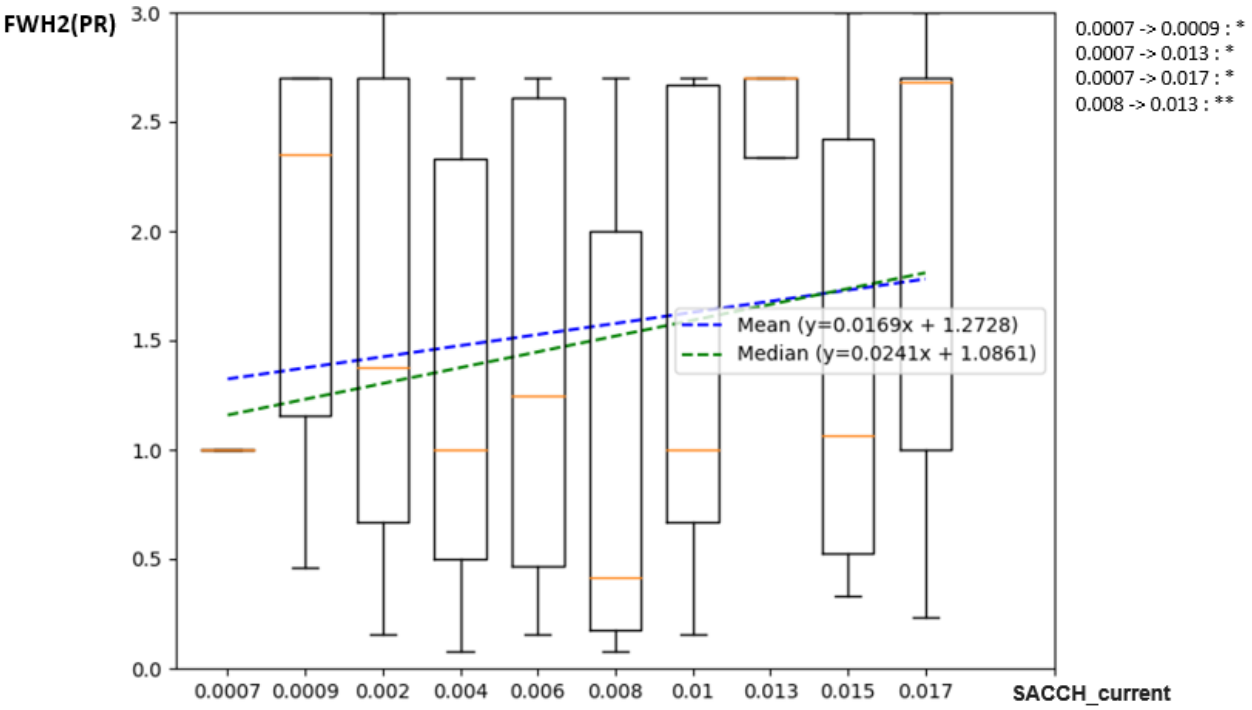

Figure B.64 Evolution of FWH2(PR) function of the tissue SACCH_current

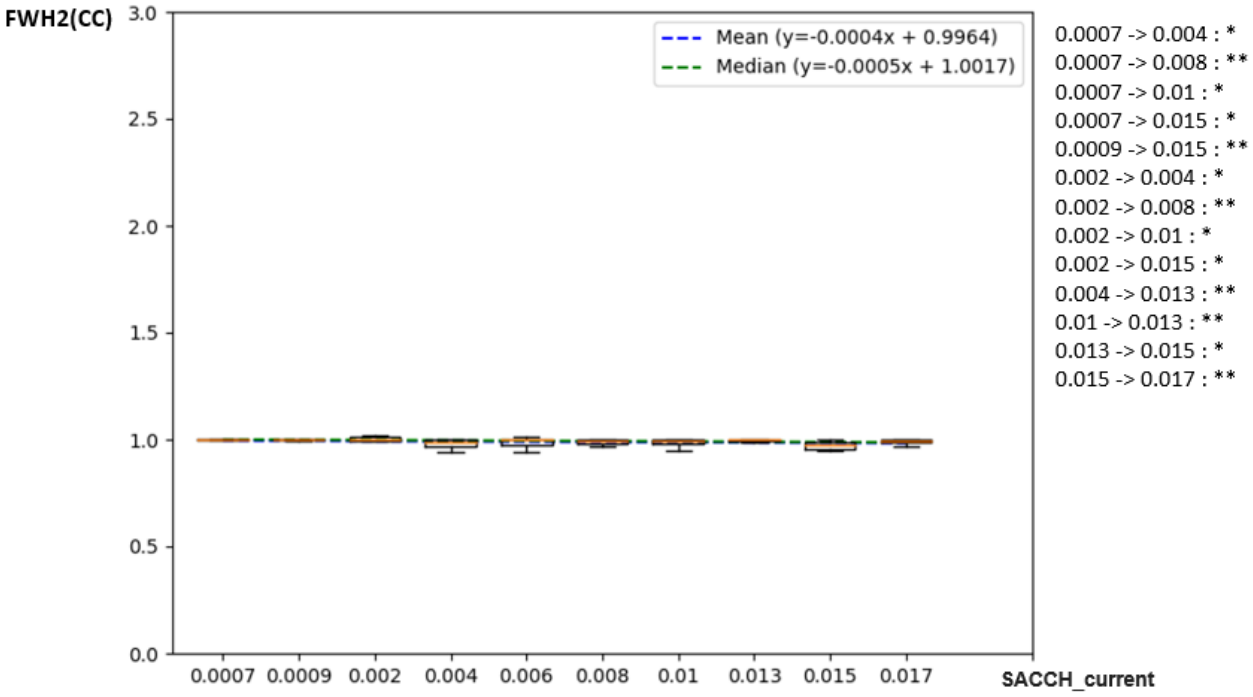

Figure B.65 Evolution of FWH2(CC) function of the tissue SACCH_current

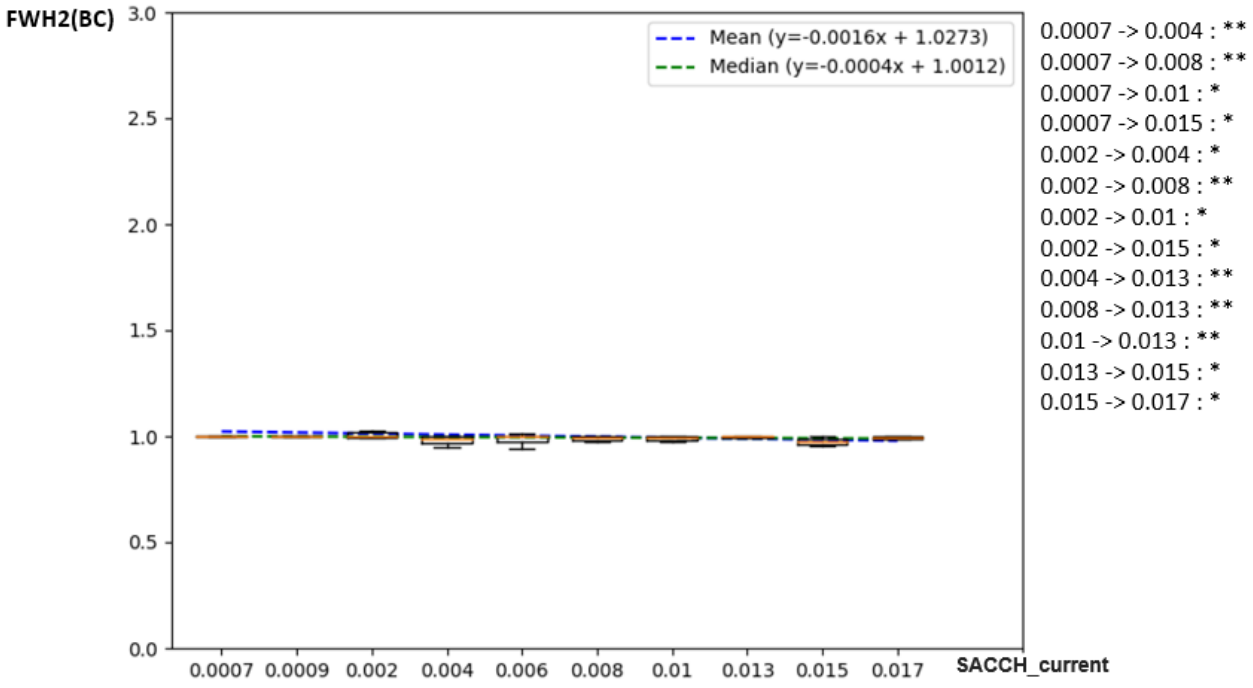

Figure B.66 Evolution of FWH2(BC) function of the tissue SACCH_current

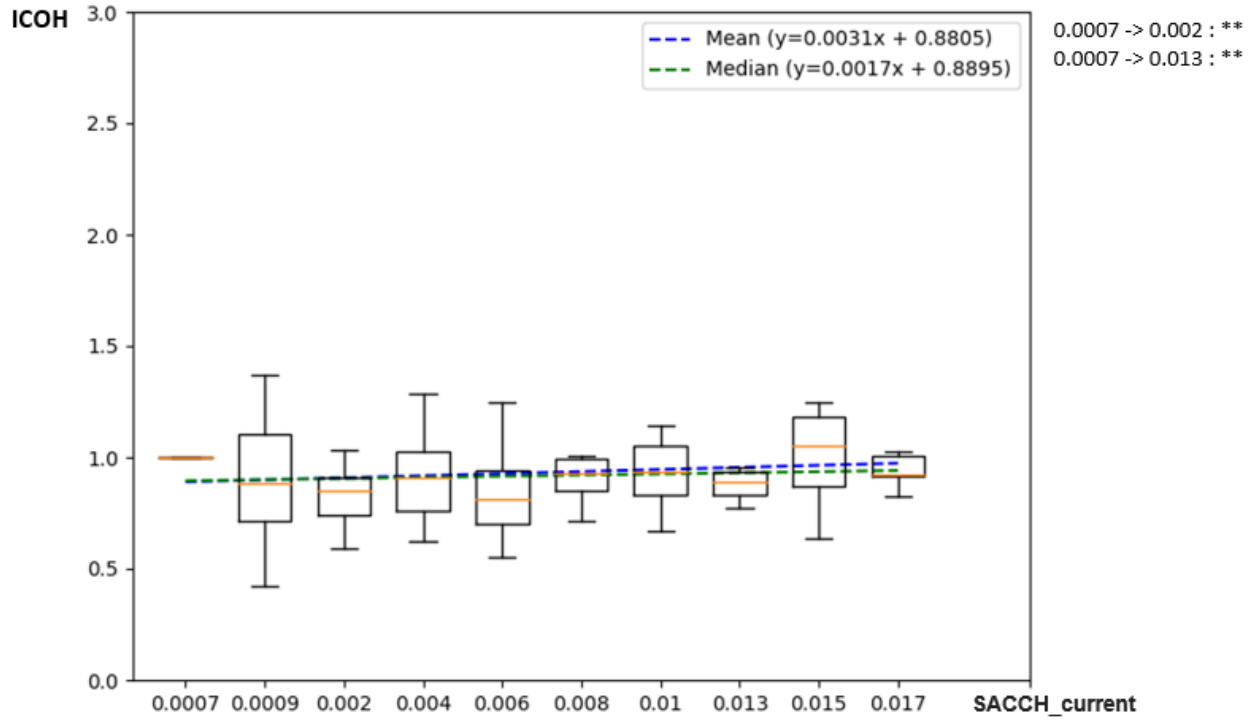

Figure B.67 Evolution of ICOH function of the tissue SACCH_current

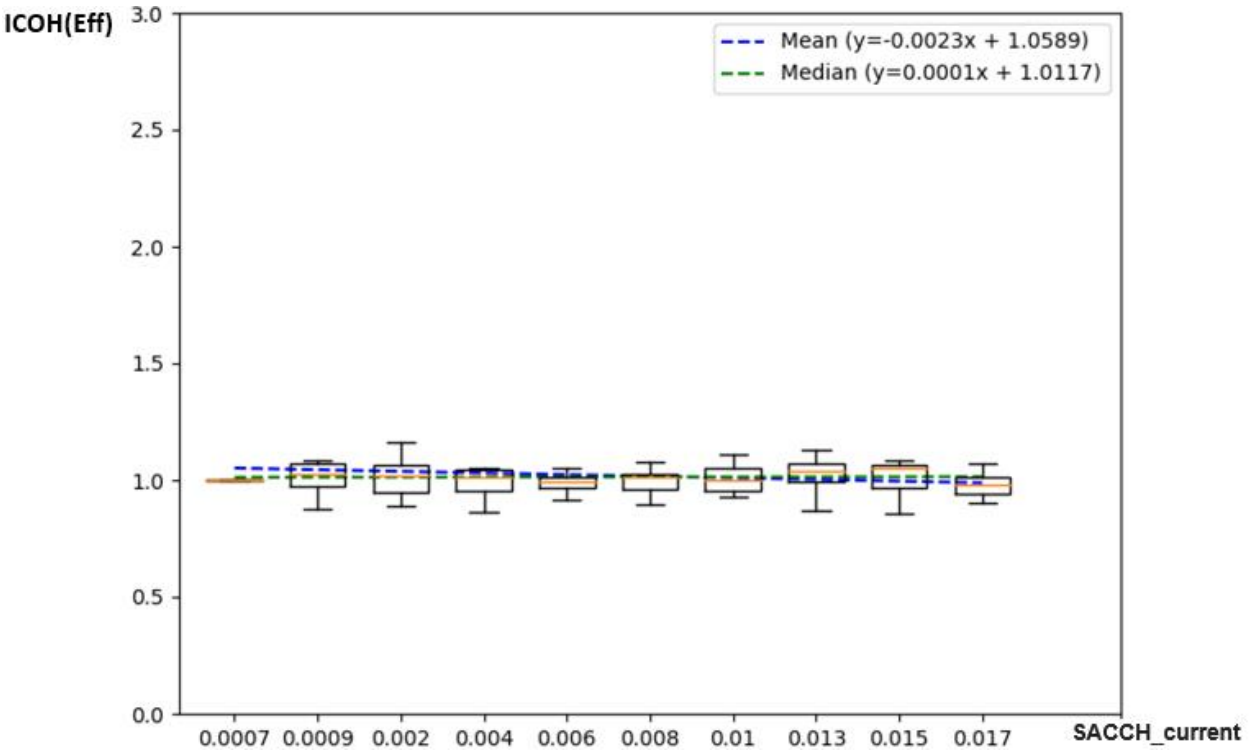

Figure B.68 Evolution of ICOH(Eff) function of the tissue SACCH_current

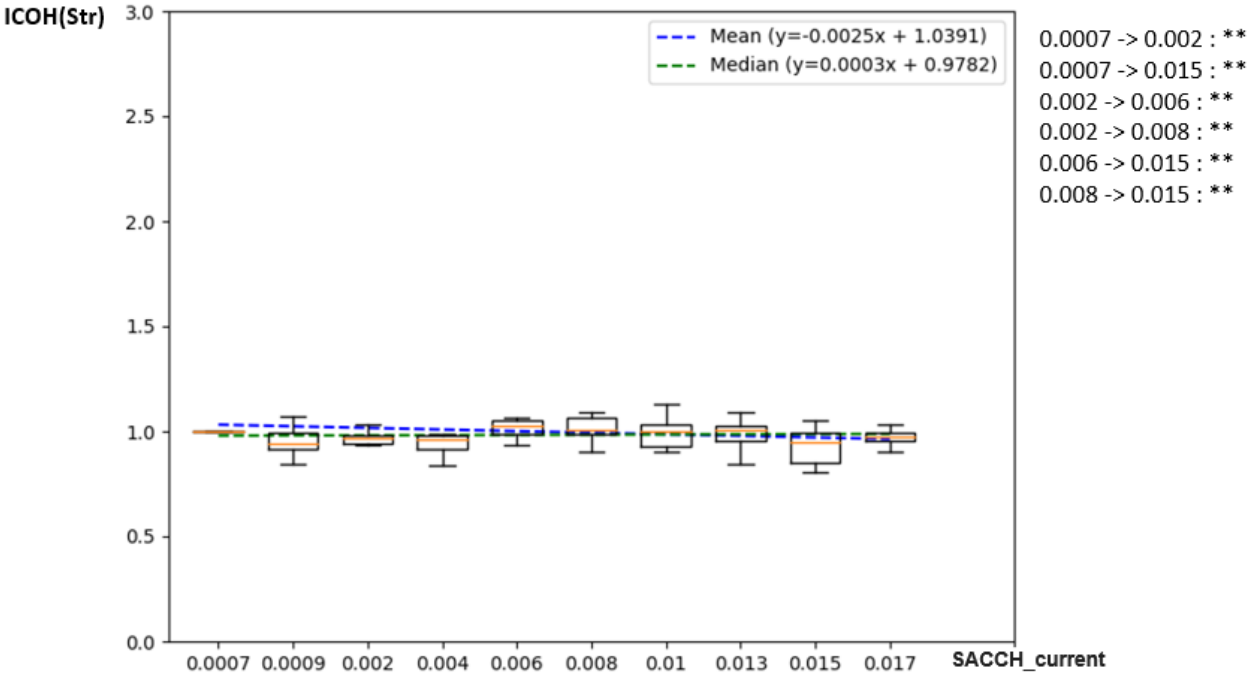

Figure B.69 Evolution of ICOH(Str) function of the tissue SACCH_current

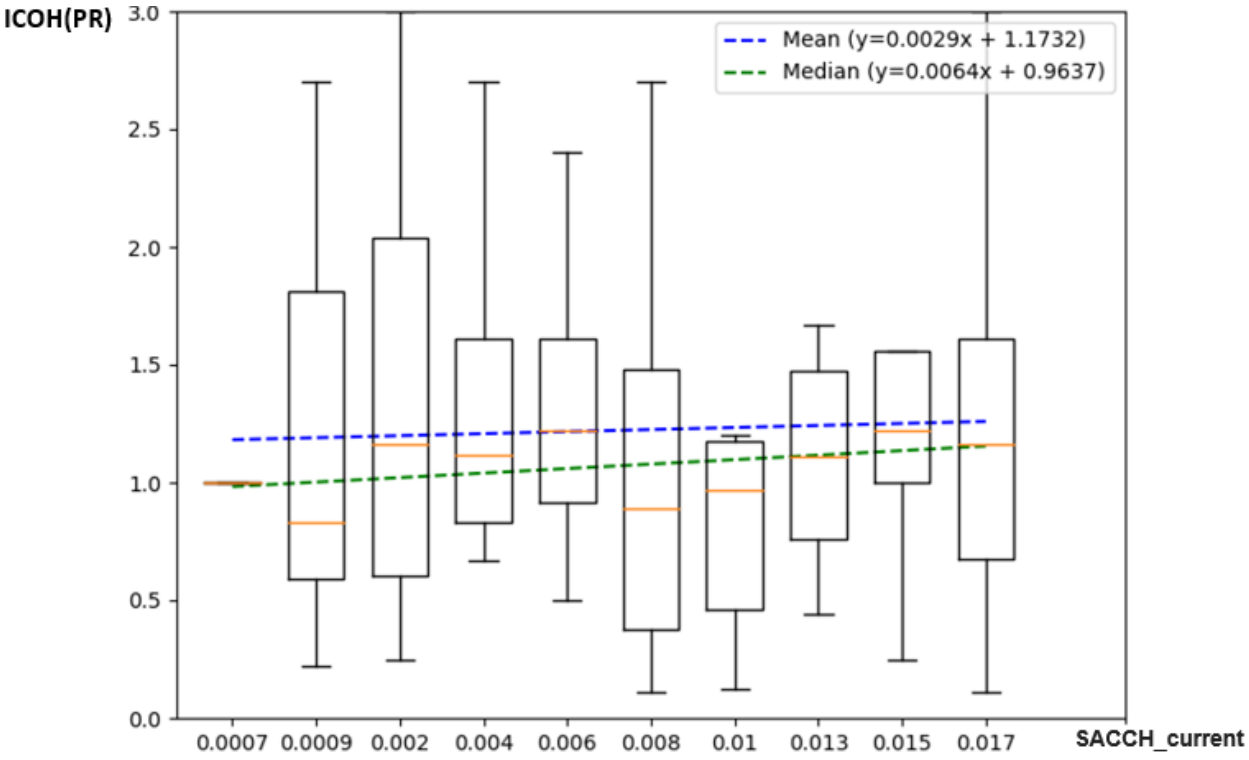

Figure B.70 Evolution of ICOH(PR) function of the tissue SACCH_current

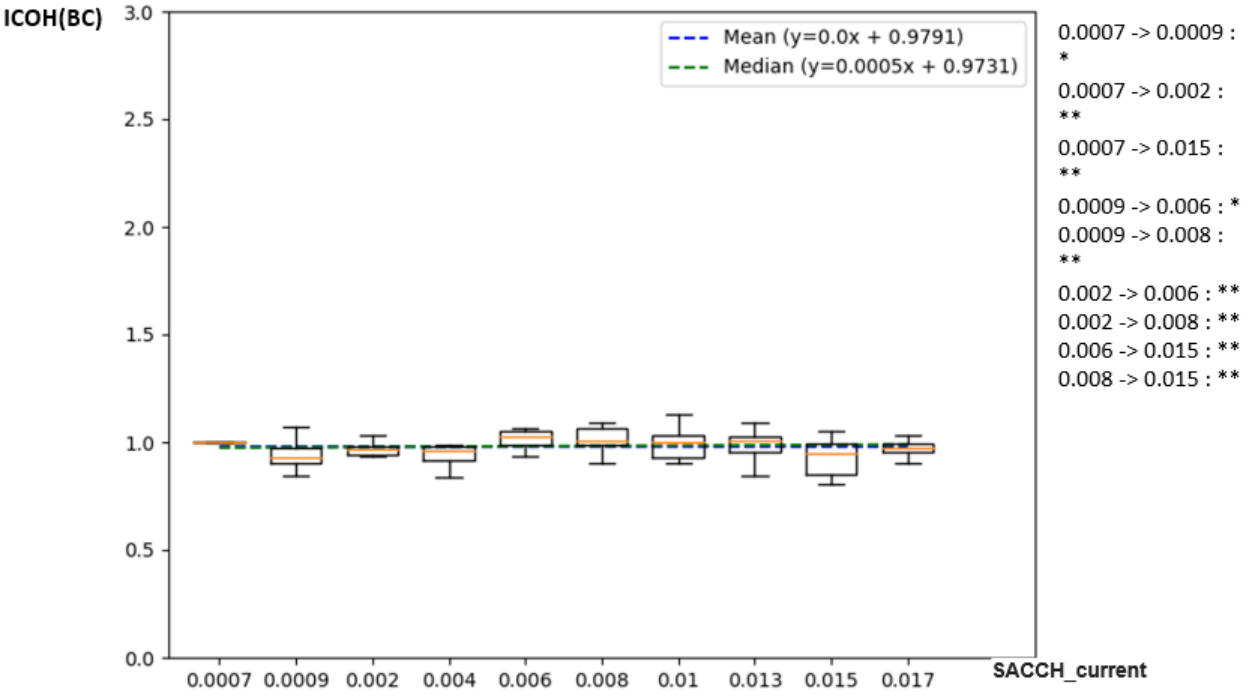

Figure B.71 Evolution of ICOH(BC) function of the tissue SACCH_current

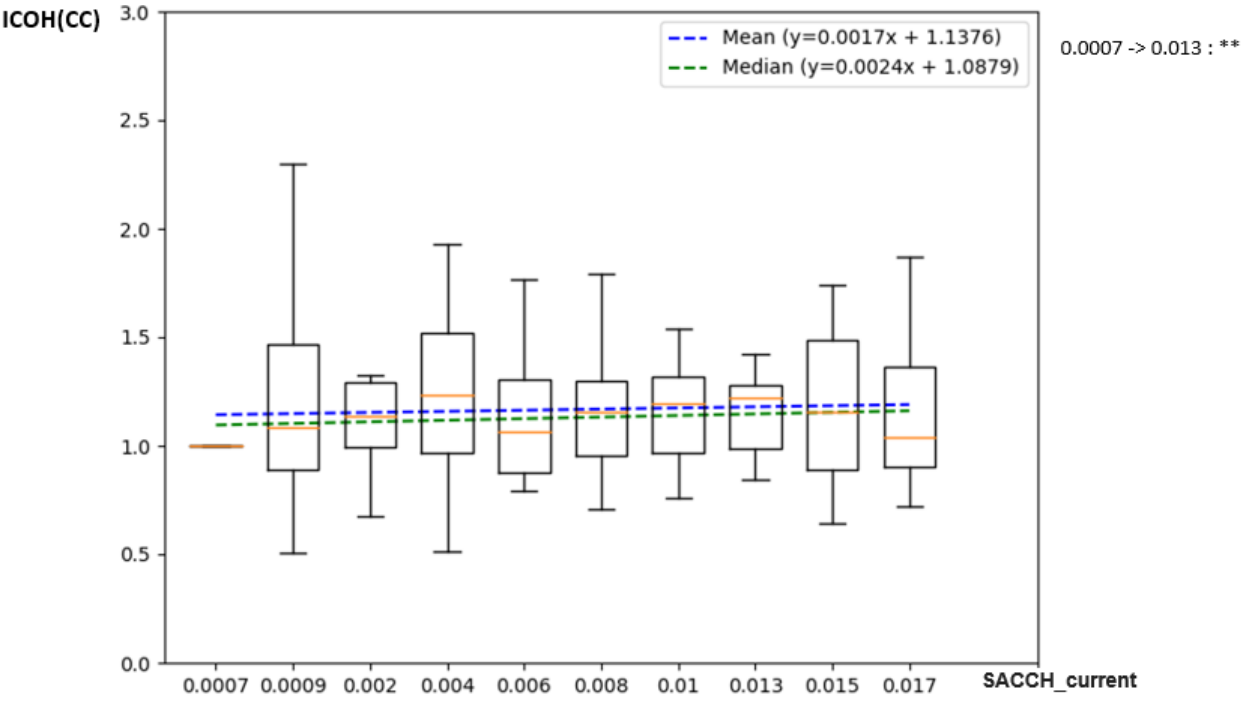

Figure B.72 Evolution of ICOH(CC) function of the tissue SACCH_current

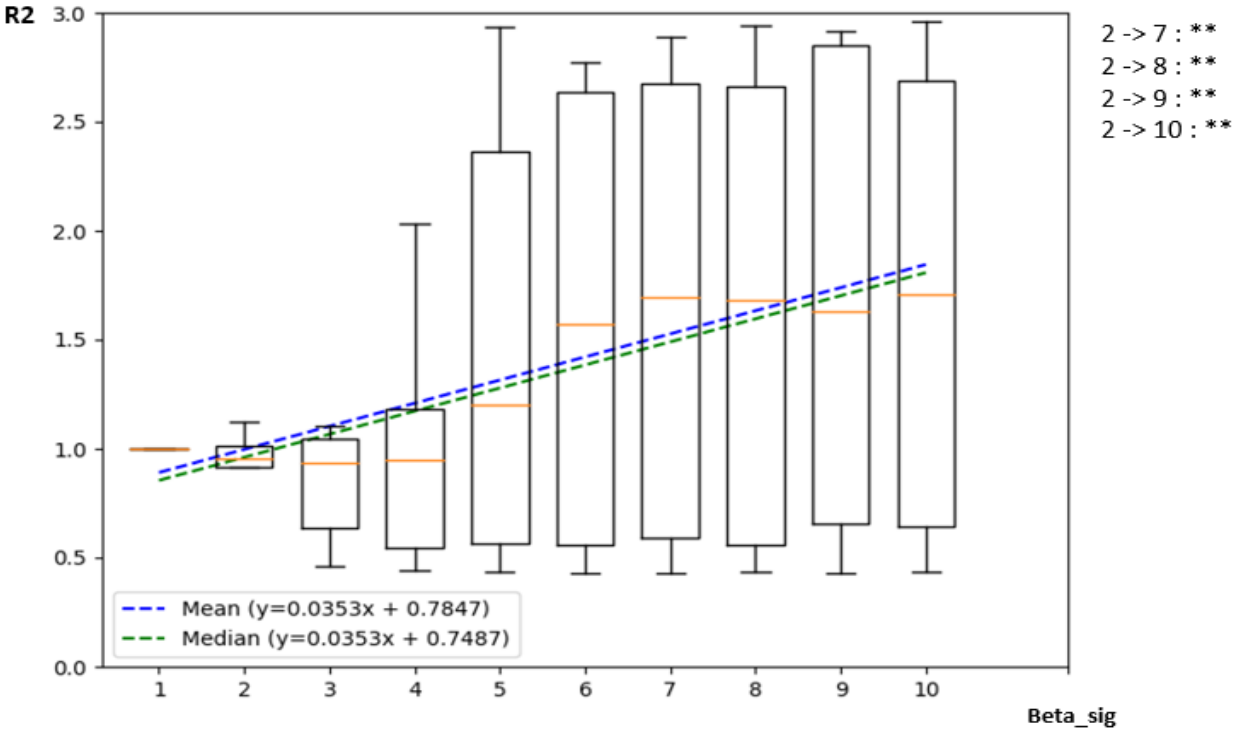

Figure B.73 Evolution of R2 function of the tissue Beta_sig

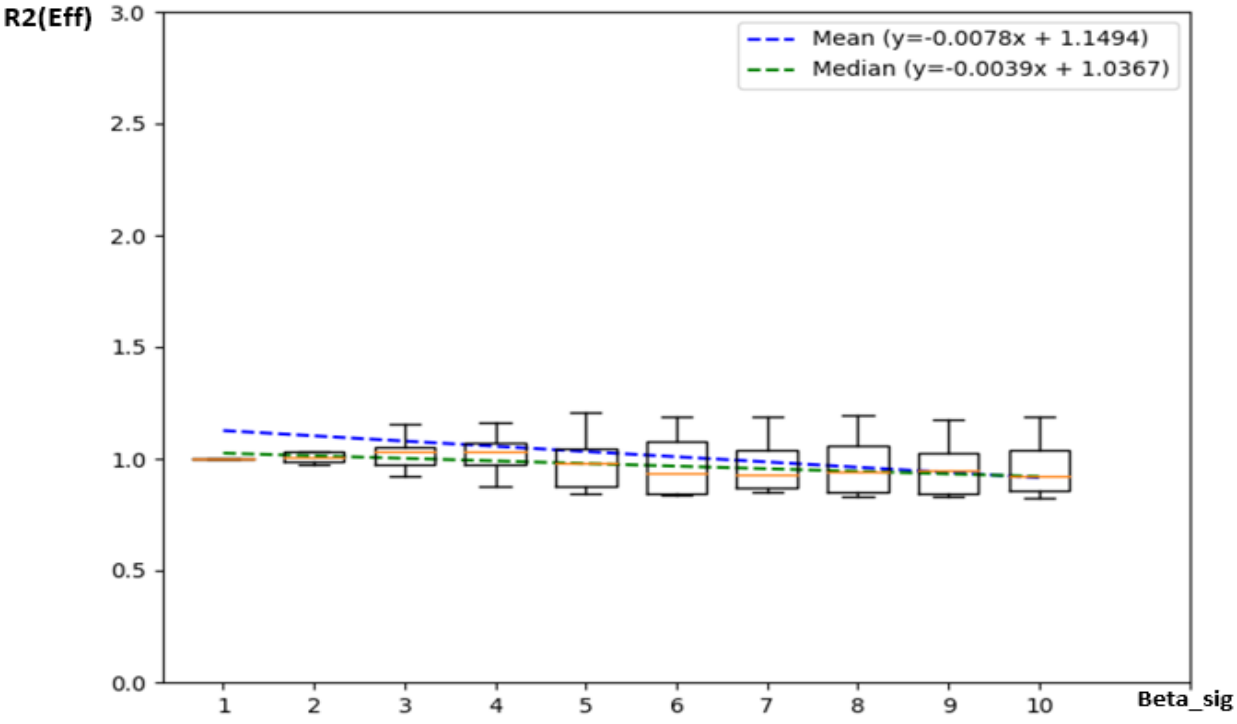

Figure B.74 Evolution of R2(Eff) function of the tissue Beta_sig

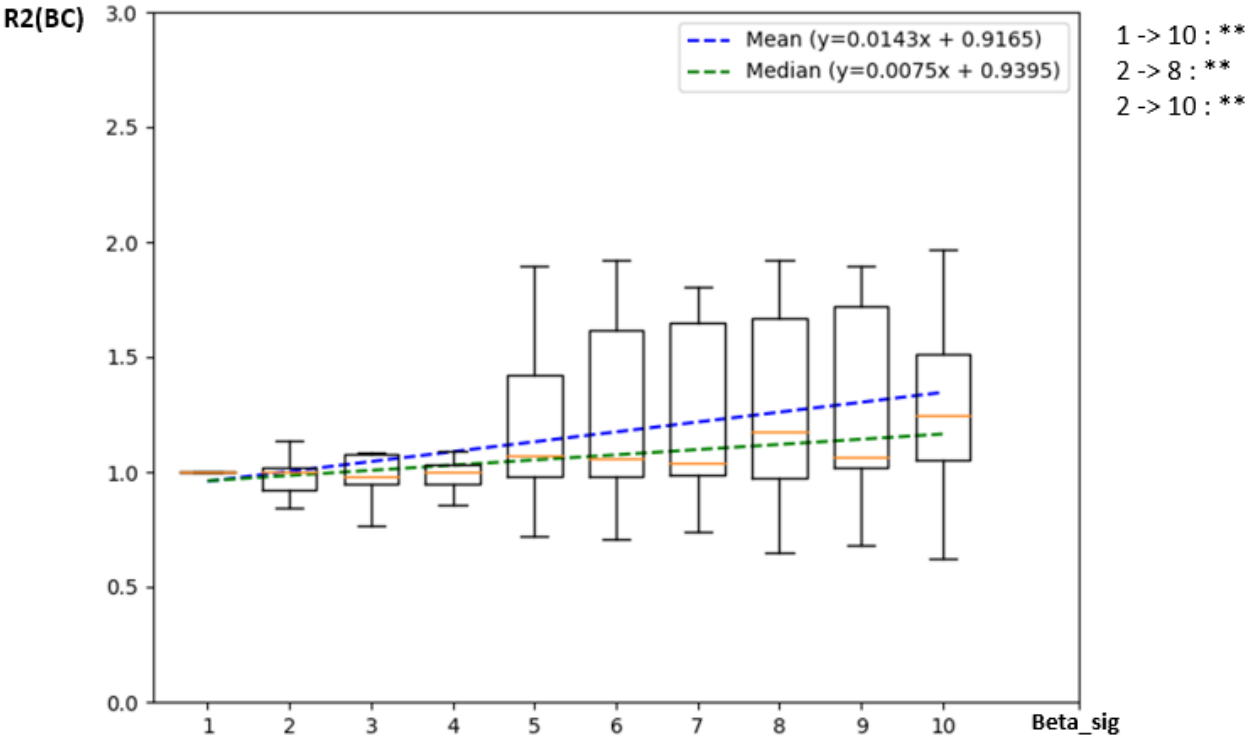

Figure B.75 Evolution of R2(BC) function of the tissue Beta_sig

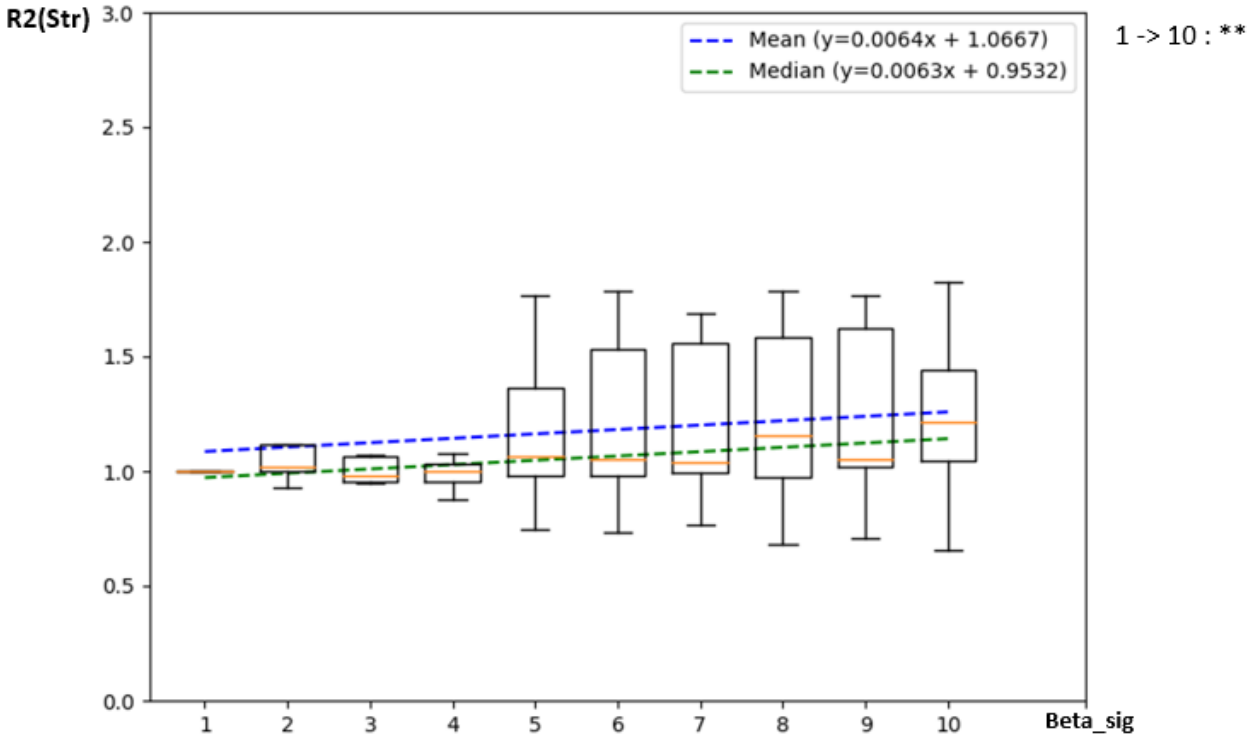

Figure B.76 Evolution of R2(Str) function of the tissue Beta_sig

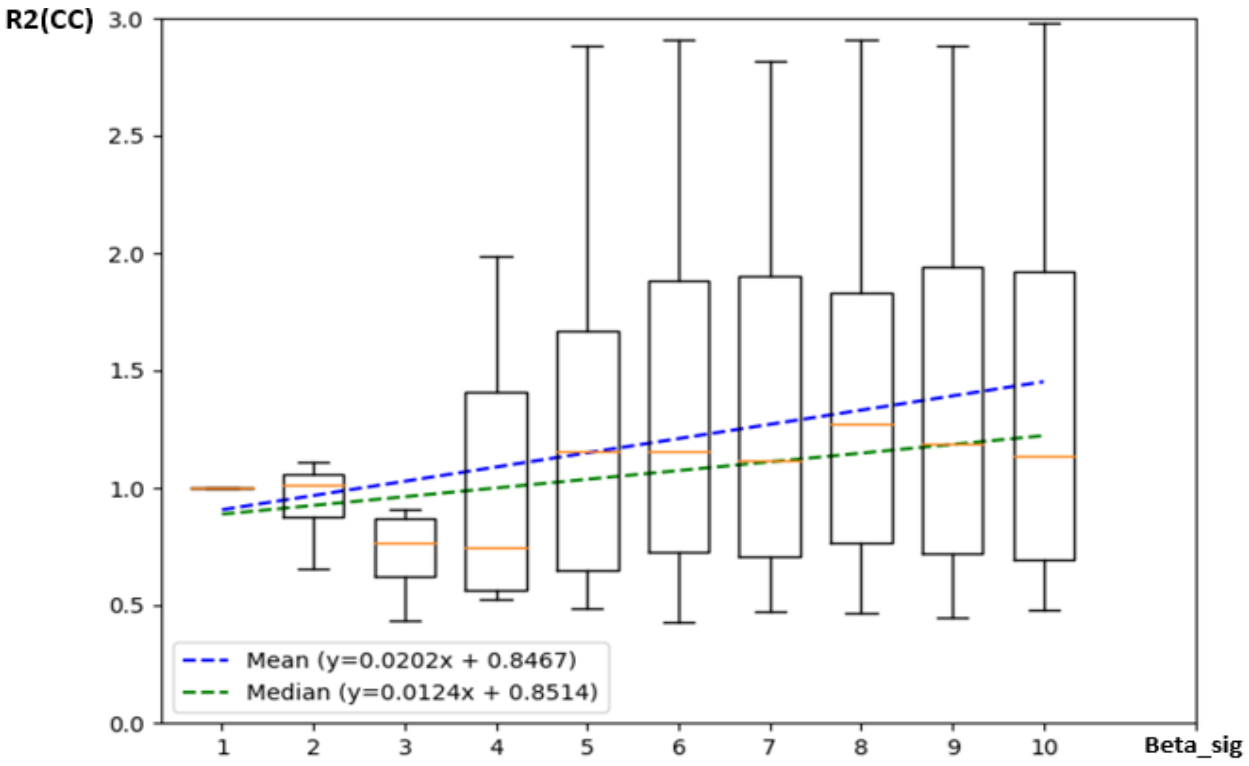

Figure B.77 Evolution of R2(CC) function of the tissue Beta_sig

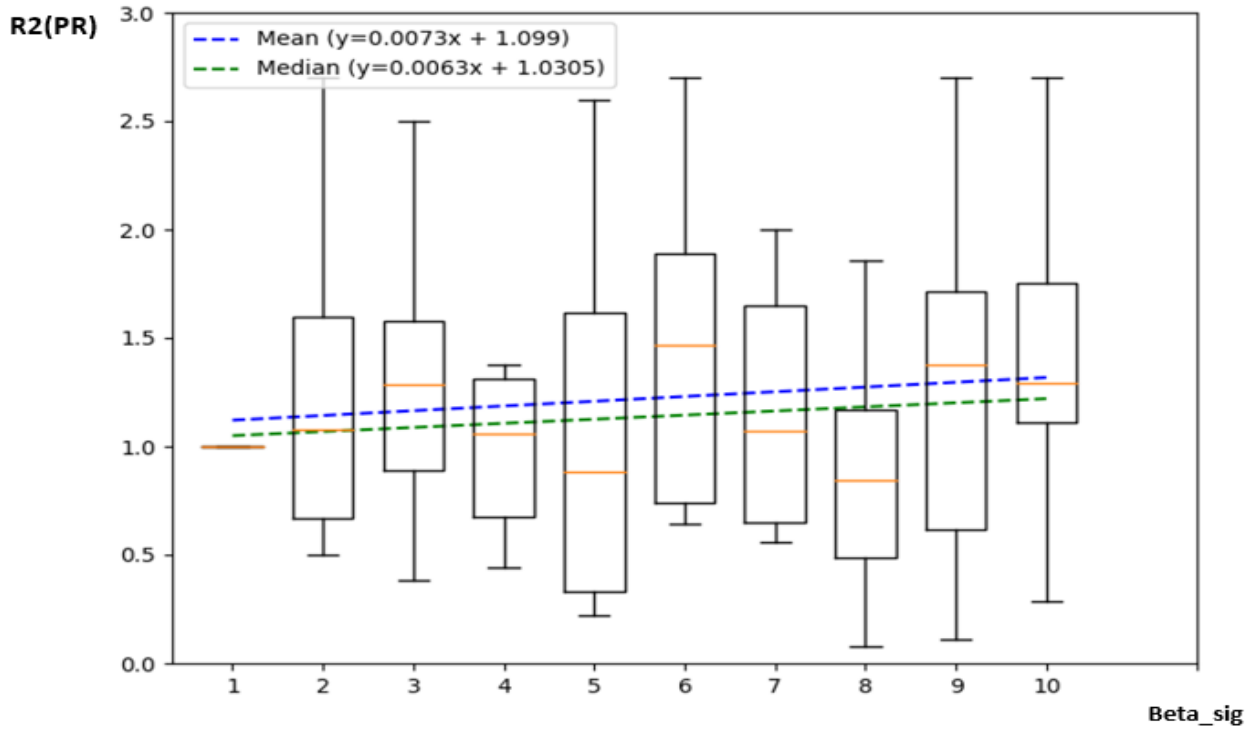

Figure B.78 Evolution of R2(PR) function of the tissue Beta_sig

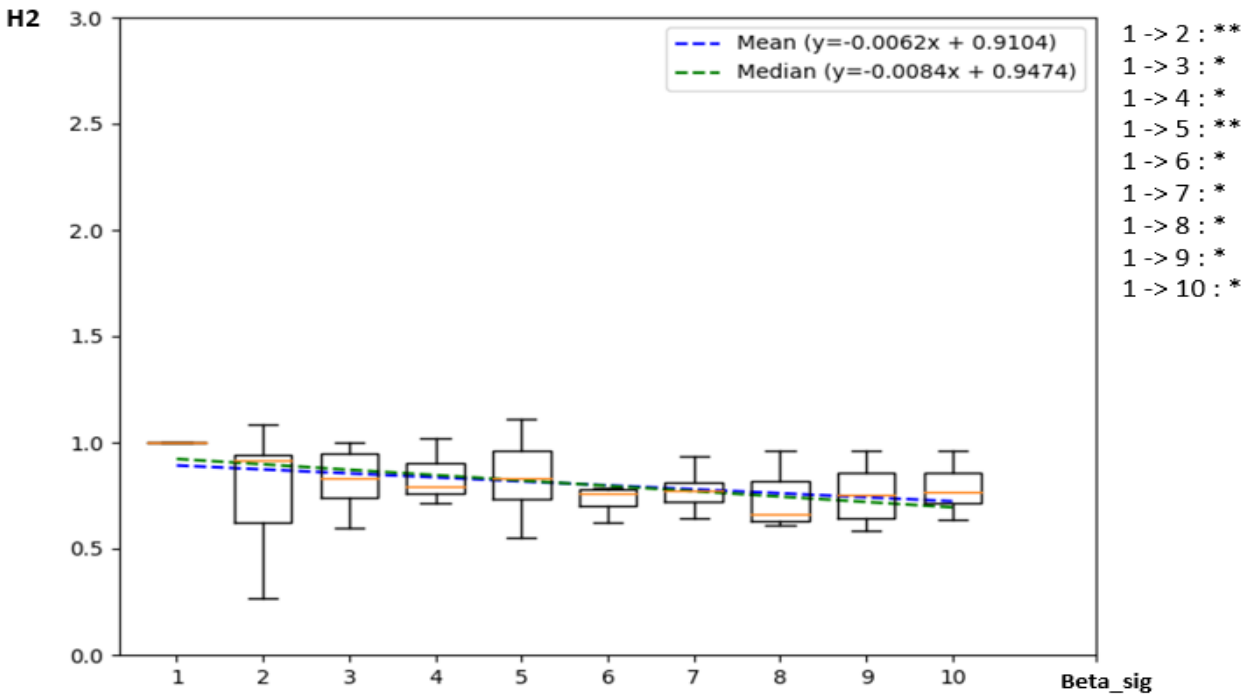

Figure B.79 Evolution of H2 function of the tissue Beta_sig

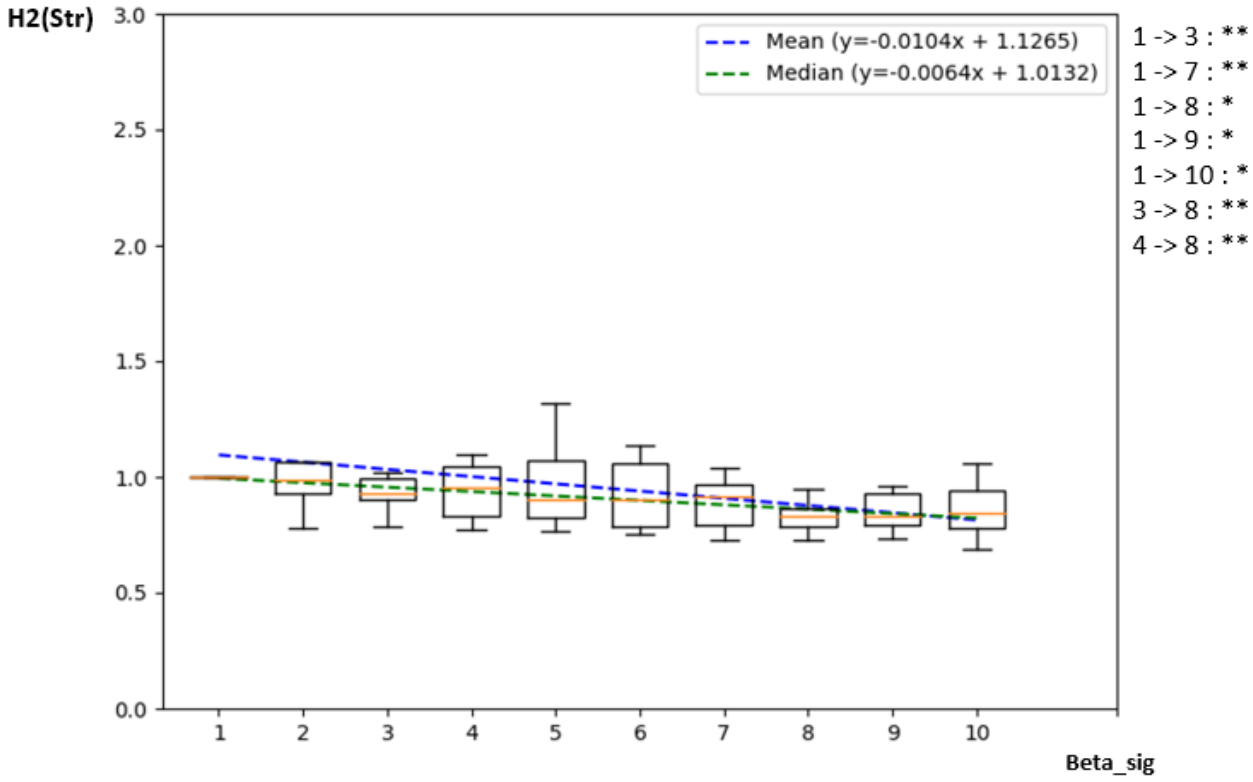

Figure B.80 Evolution of H2(Str) function of the tissue Beta_sig

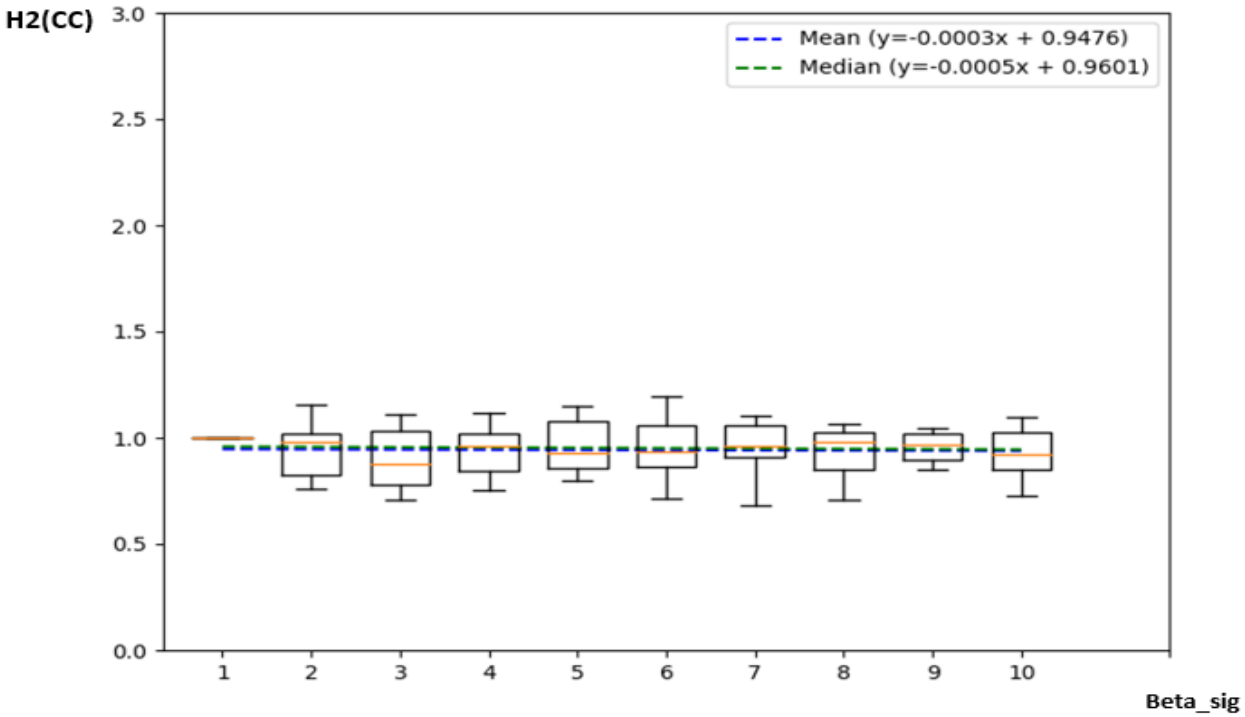

Figure B.81 Evolution of H2(CC) function of the tissue Beta_sig

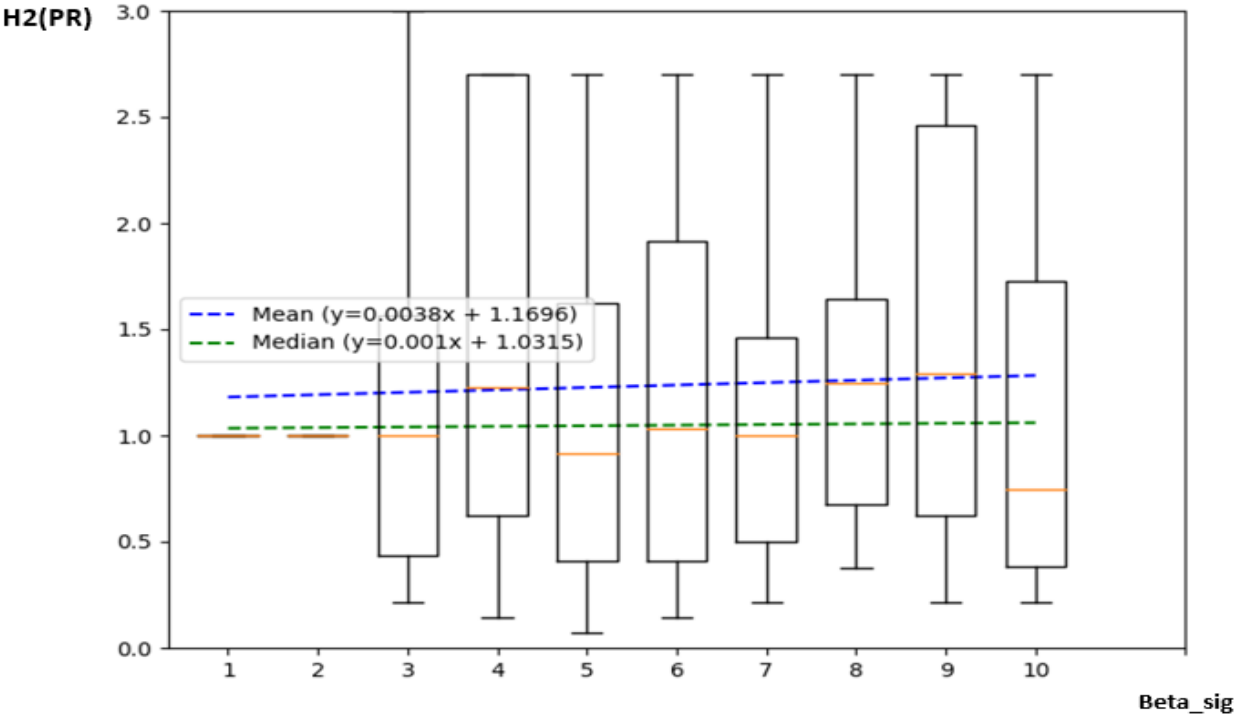

Figure B.82 Evolution of H2(PR) function of the tissue Beta_sig

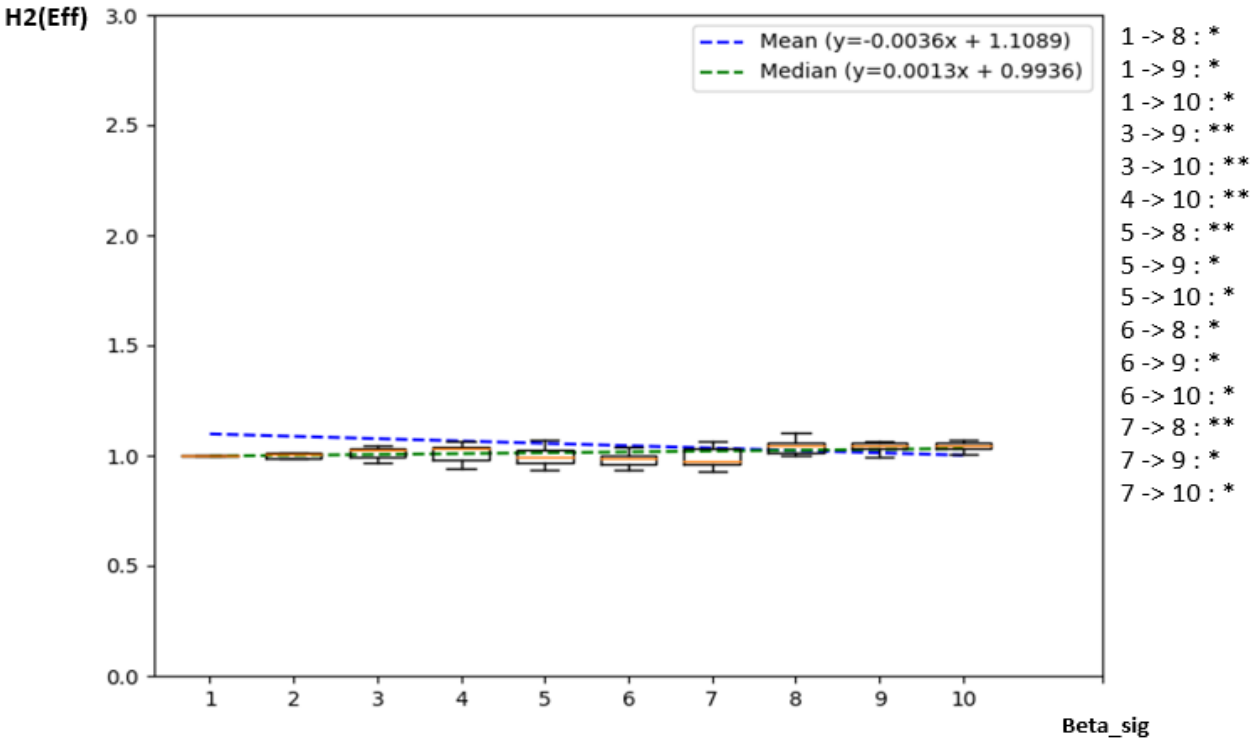

Figure B.83 Evolution of H2(Eff) function of the tissue Beta_sig

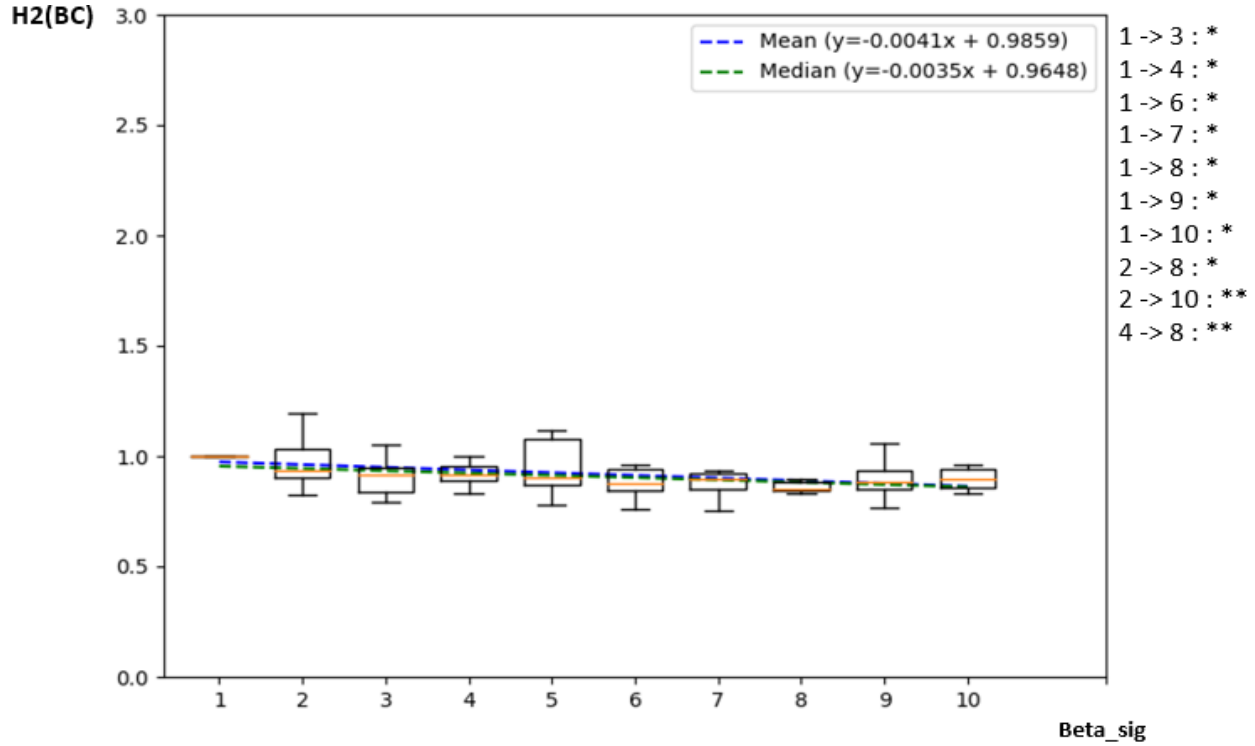

Figure B.84 Evolution of H2(BC) function of the tissue Beta_sig

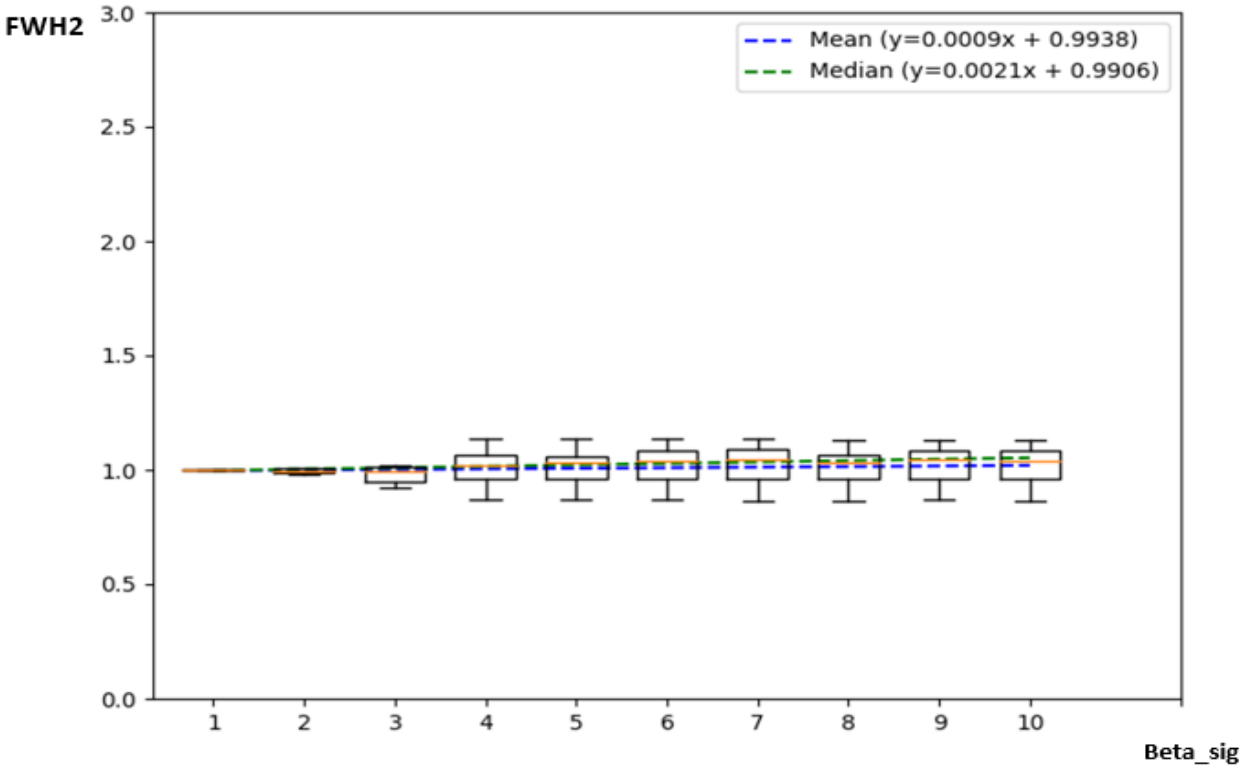

Figure B.85 Evolution of FWH2 function of the tissue Beta_sig

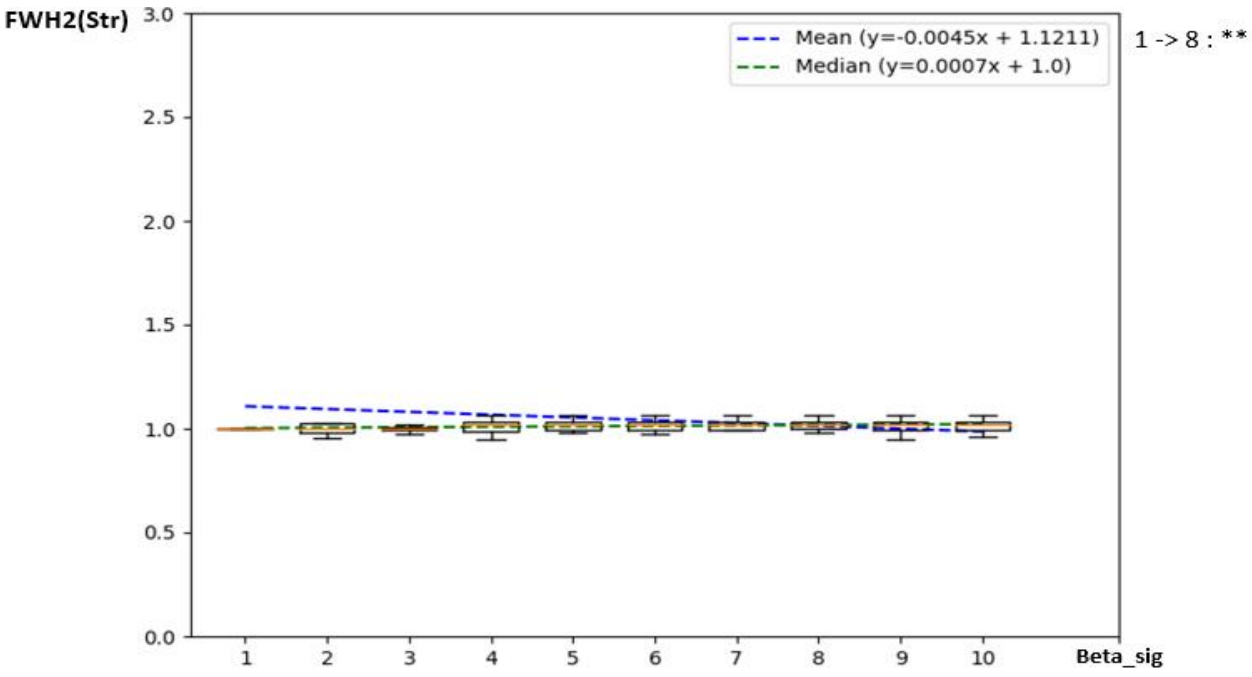

Figure B.86 Evolution of FWH2(Str) function of the tissue Beta_sig

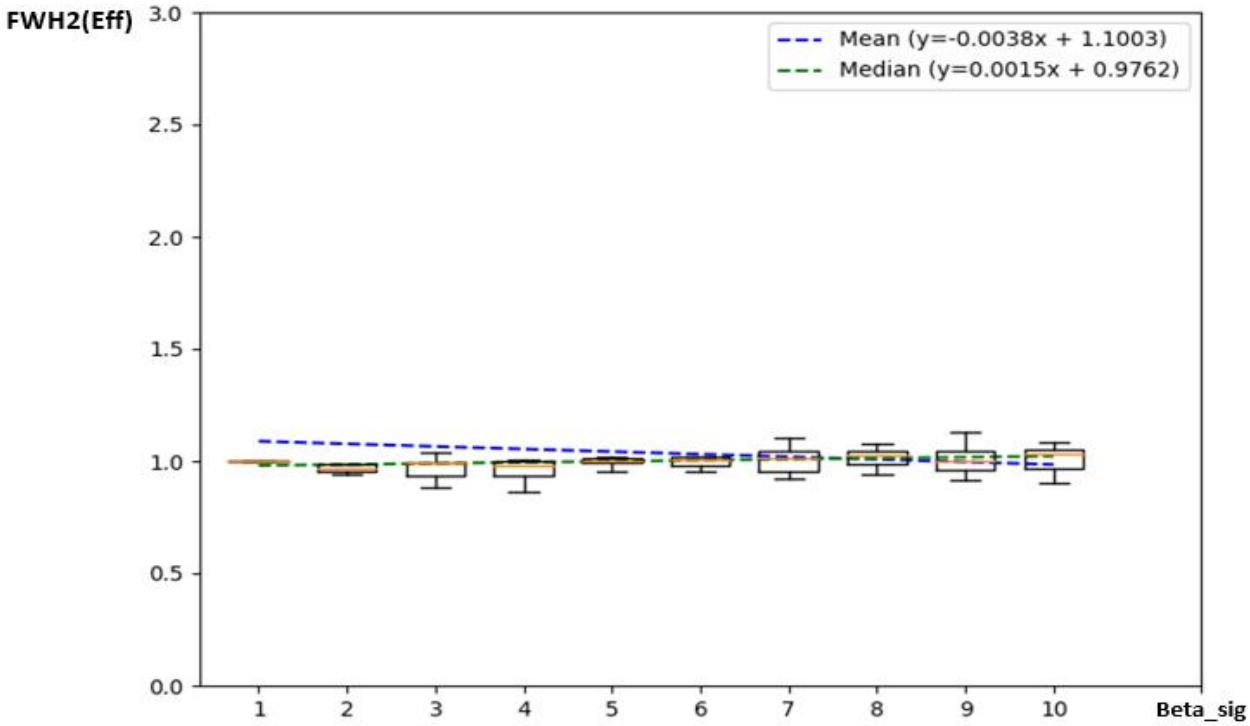

Figure B.87 Evolution of FWH2(Eff) function of the tissue Beta_sig

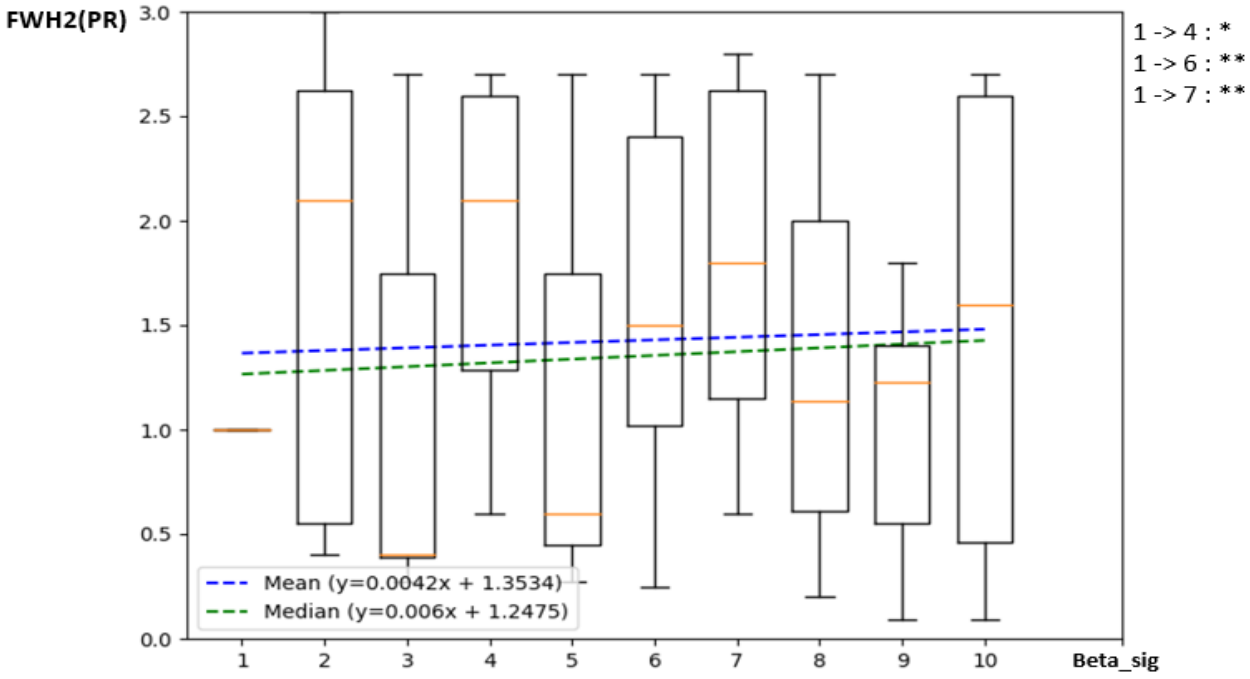

Figure B.88 Evolution of FWH2(PR) function of the tissue Beta_sig

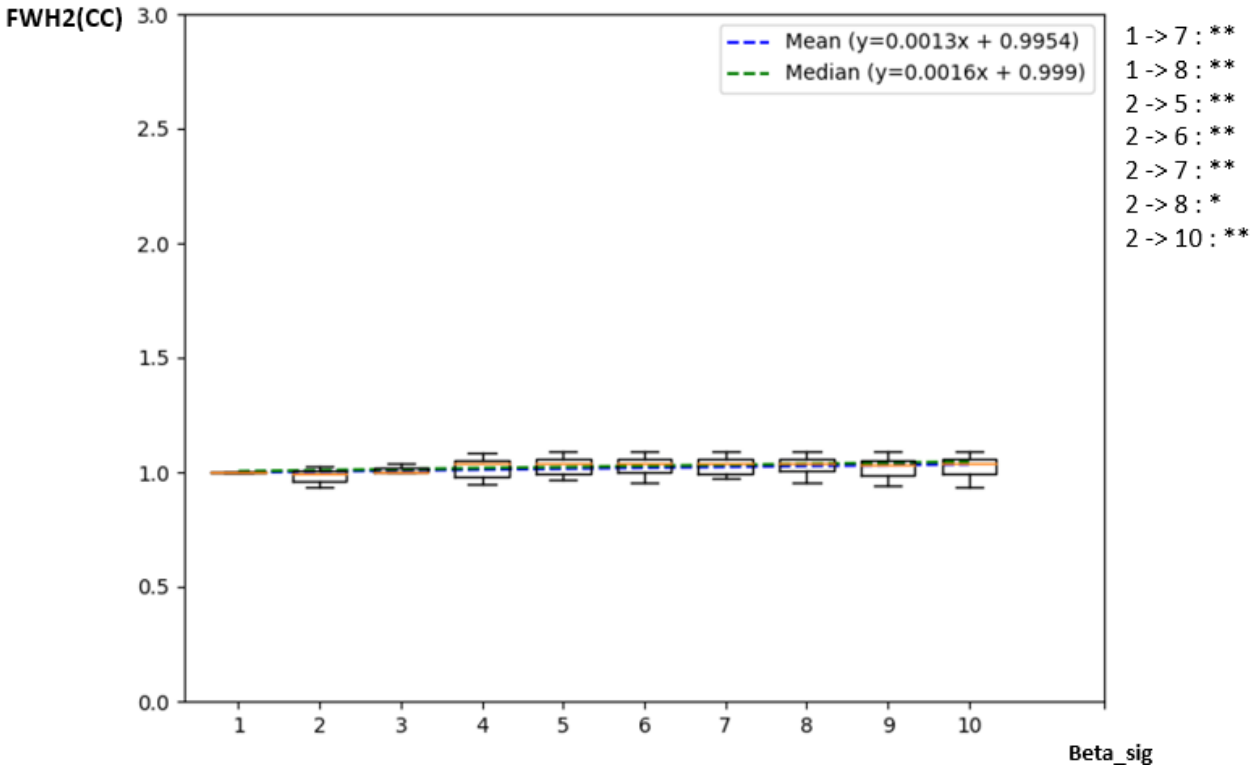

Figure B.89 Evolution of FWH2(CC) function of the tissue Beta_sig

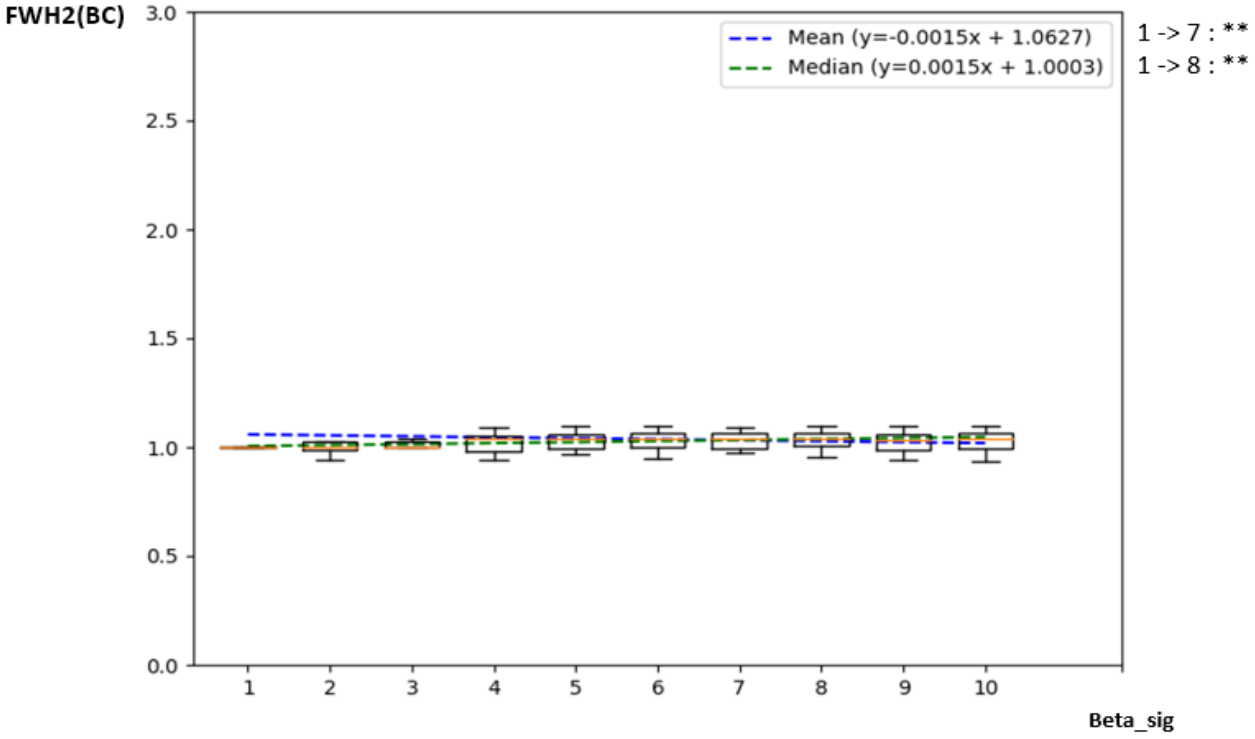

Figure B.90 Evolution of FWH2(BC) function of the tissue Beta_sig

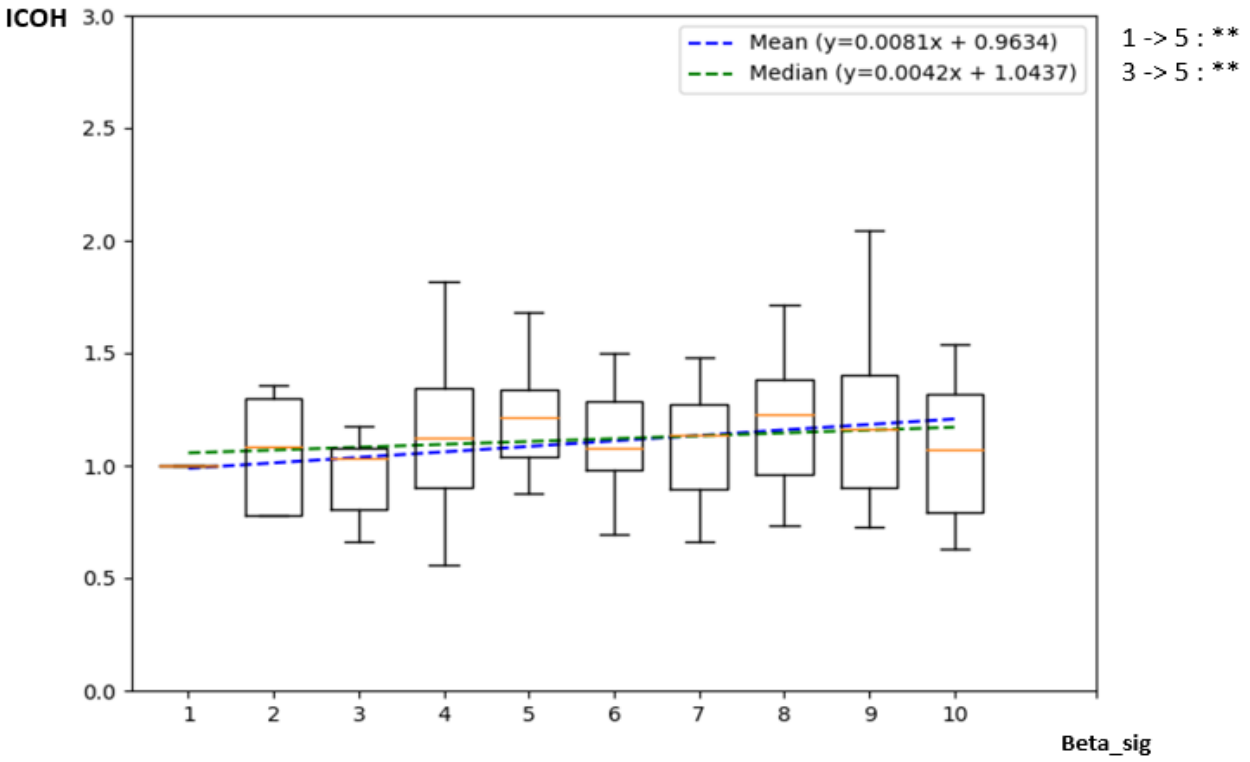

Figure B.91 Evolution of ICOH function of the tissue Beta_sig

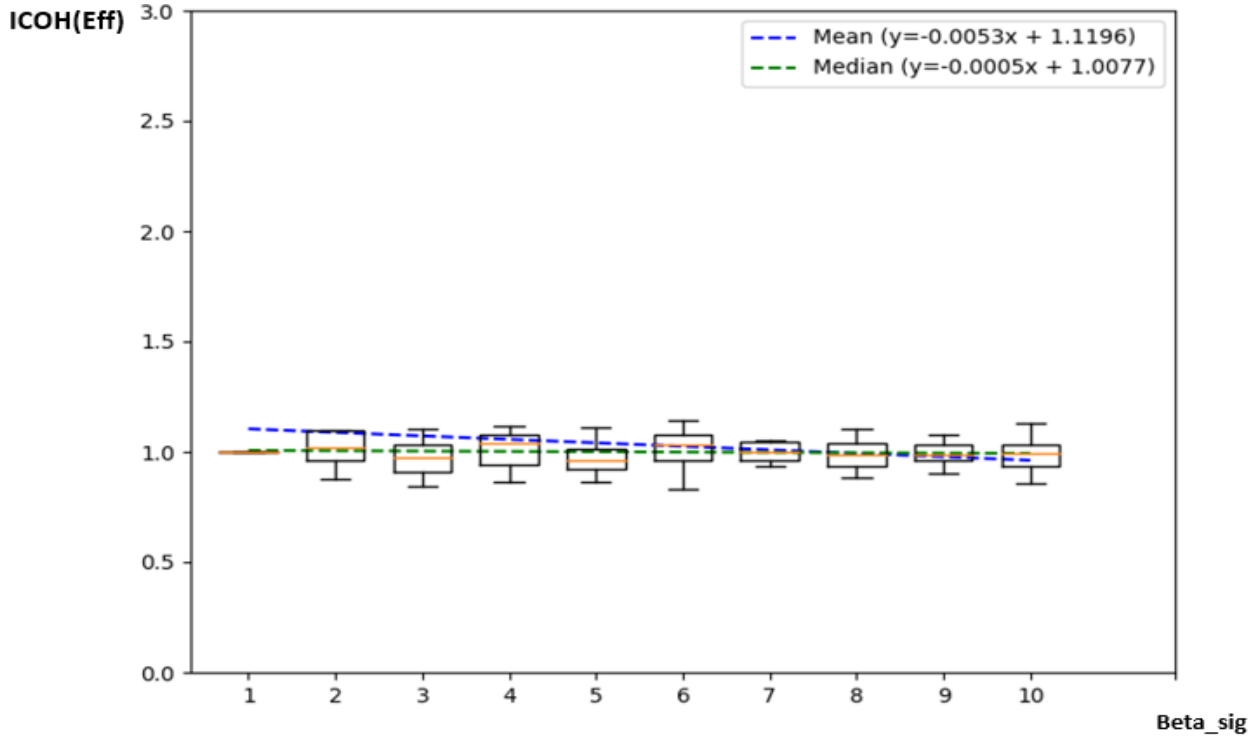

Figure B.92 Evolution of ICOH(Eff) function of the tissue Beta_sig

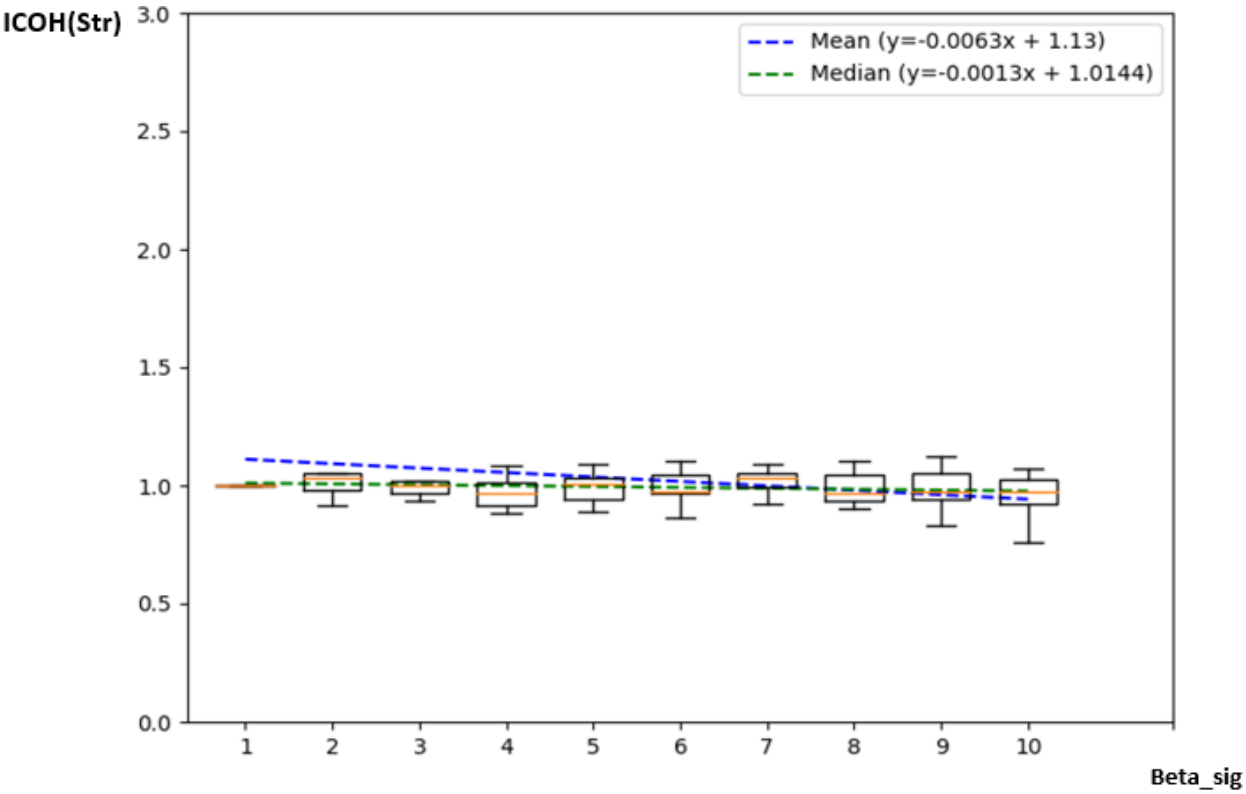

Figure B.93 Evolution of ICOH(Str) function of the tissue Beta_sig

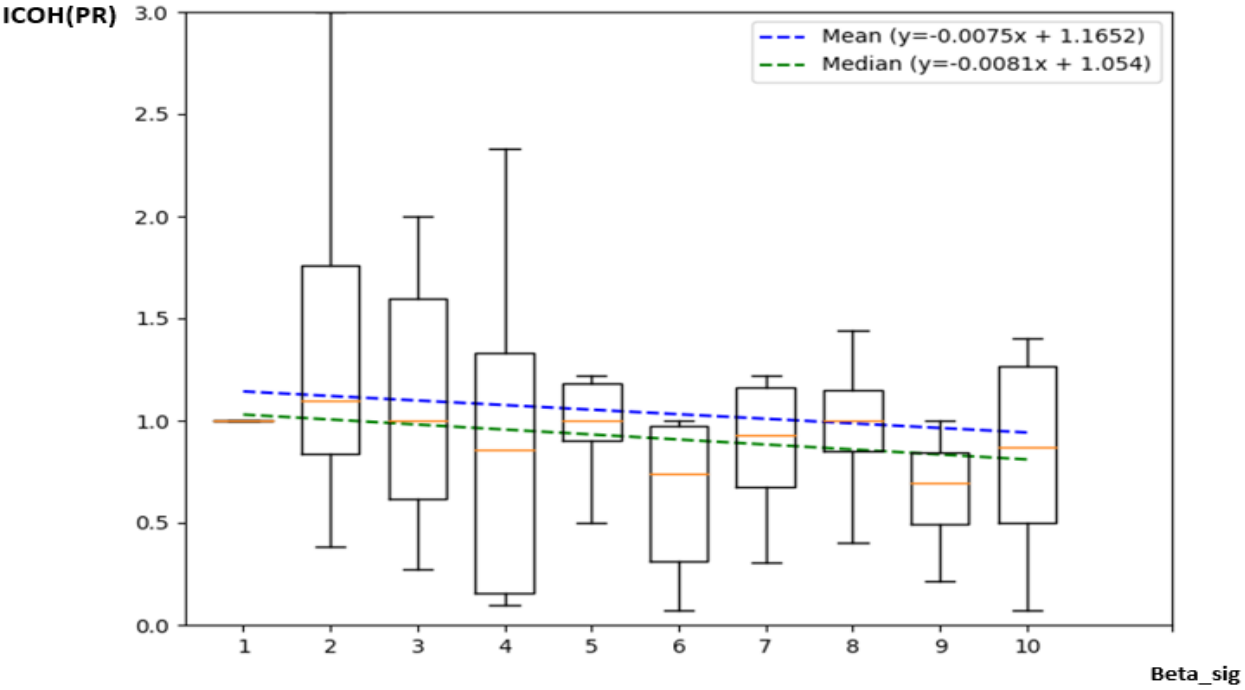

Figure B.94 Evolution of ICOH(PR) function of the tissue Beta_sig

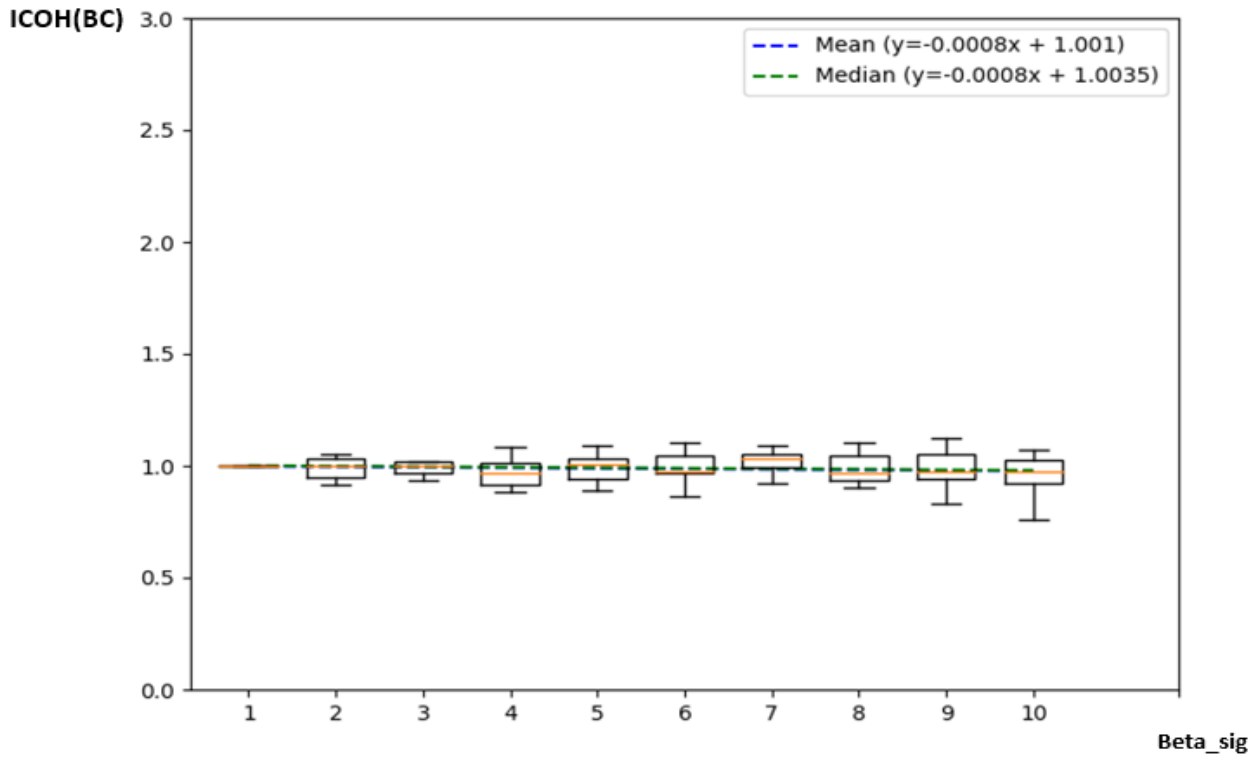

Figure B.95 Evolution of ICOH(BC) function of the tissue Beta_sig

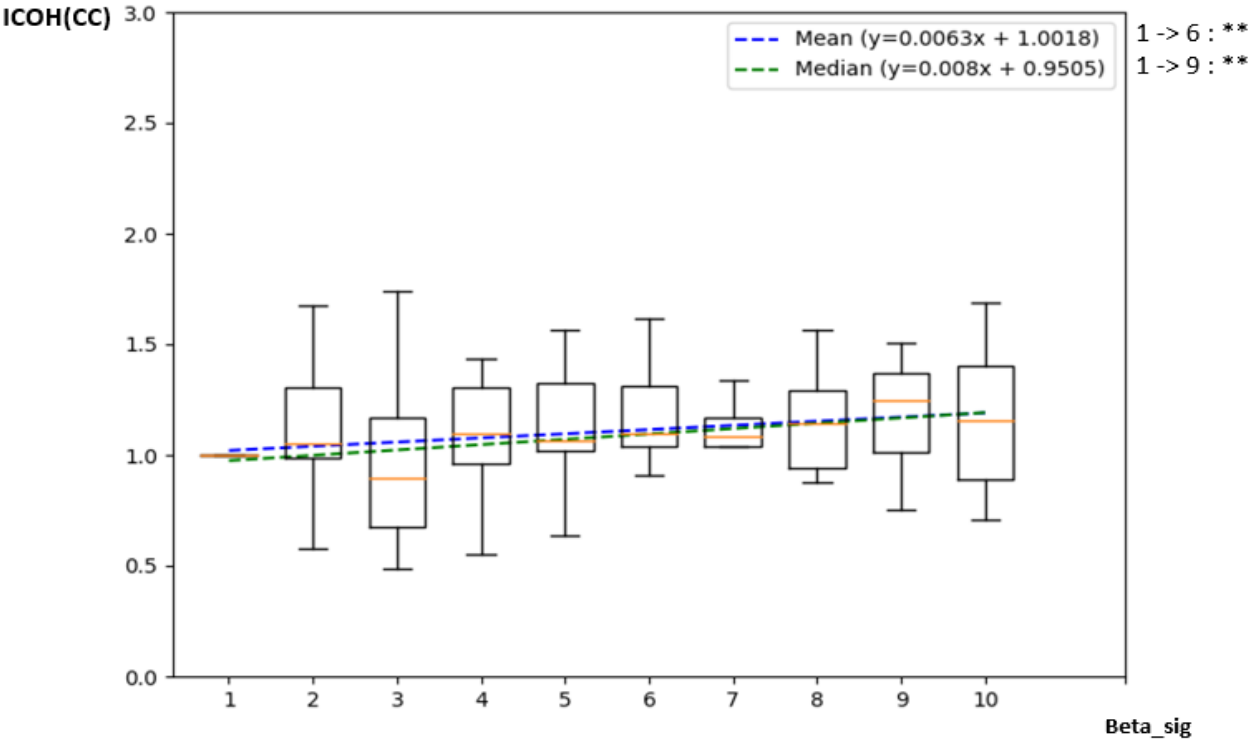

Figure B.96 Evolution of ICOH(CC) function of the tissue Beta_sig

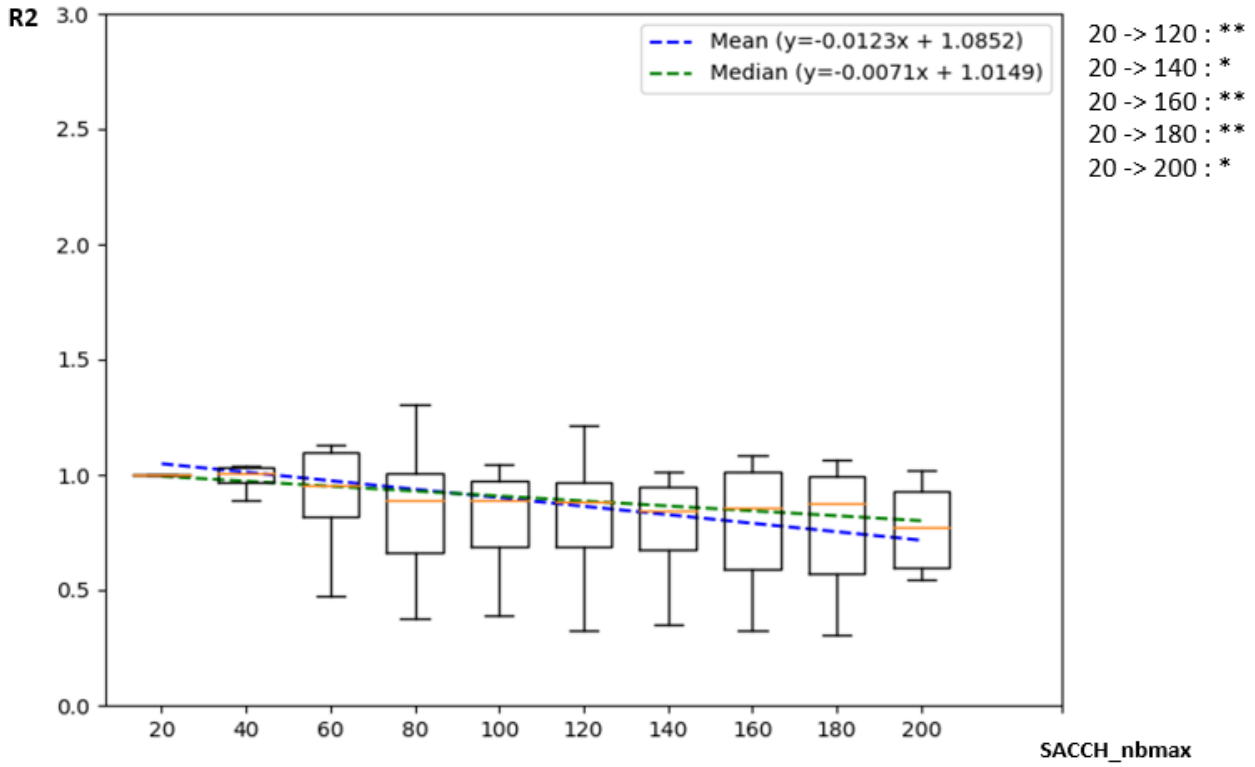

Figure B.97 Evolution of R2 function of the tissue SACCH_nbmax

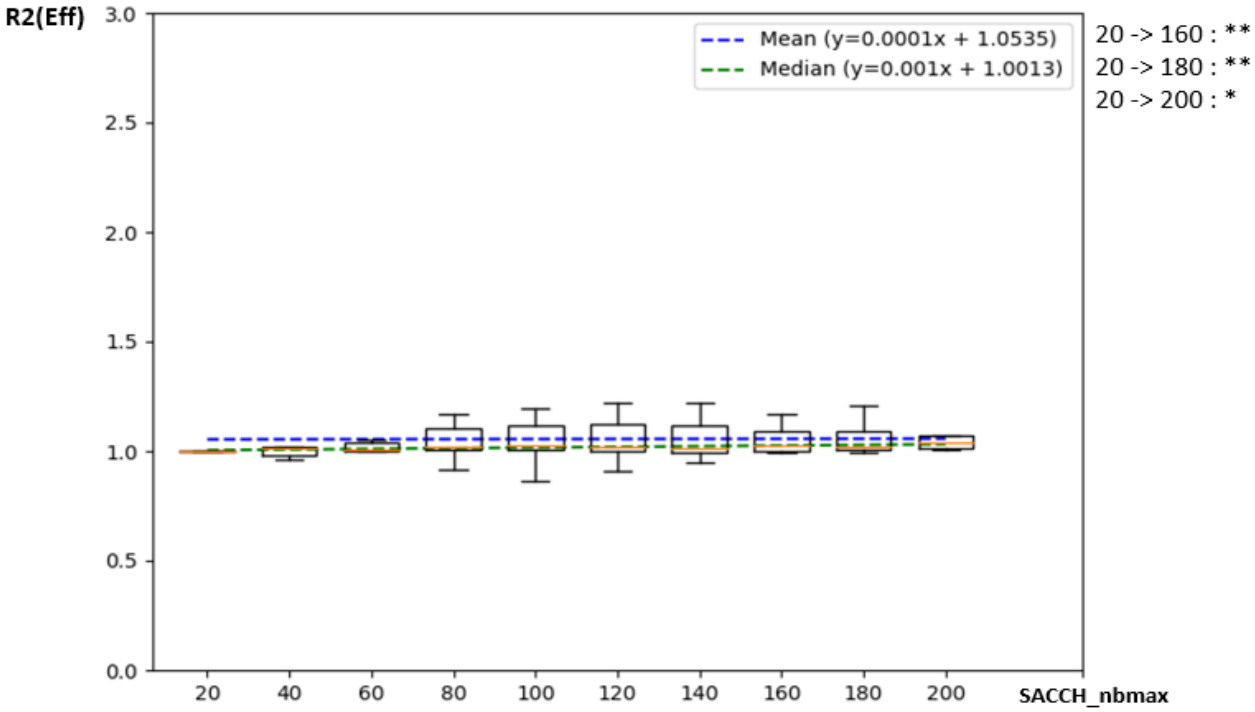

Figure B.98 Evolution of R2(Eff) function of the tissue SACCH_nbmax

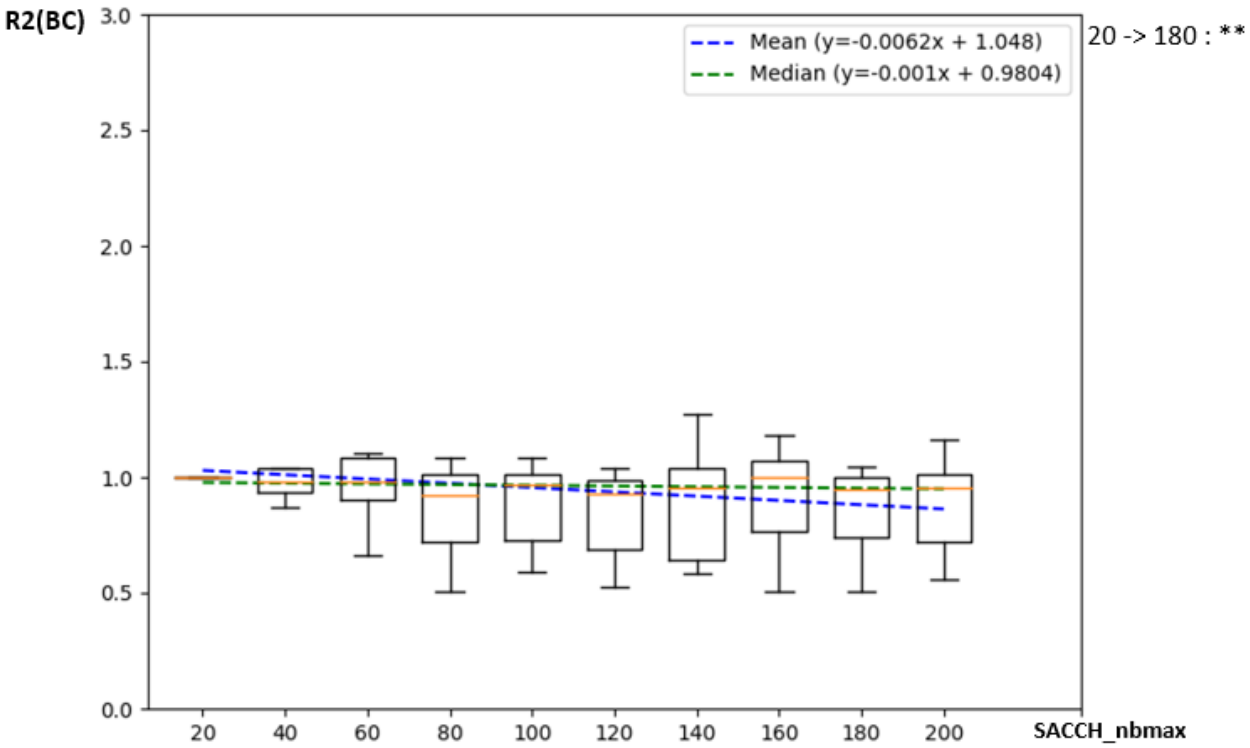

Figure B.99 Evolution of R2(BC) function of the tissue SACCH_nbmax

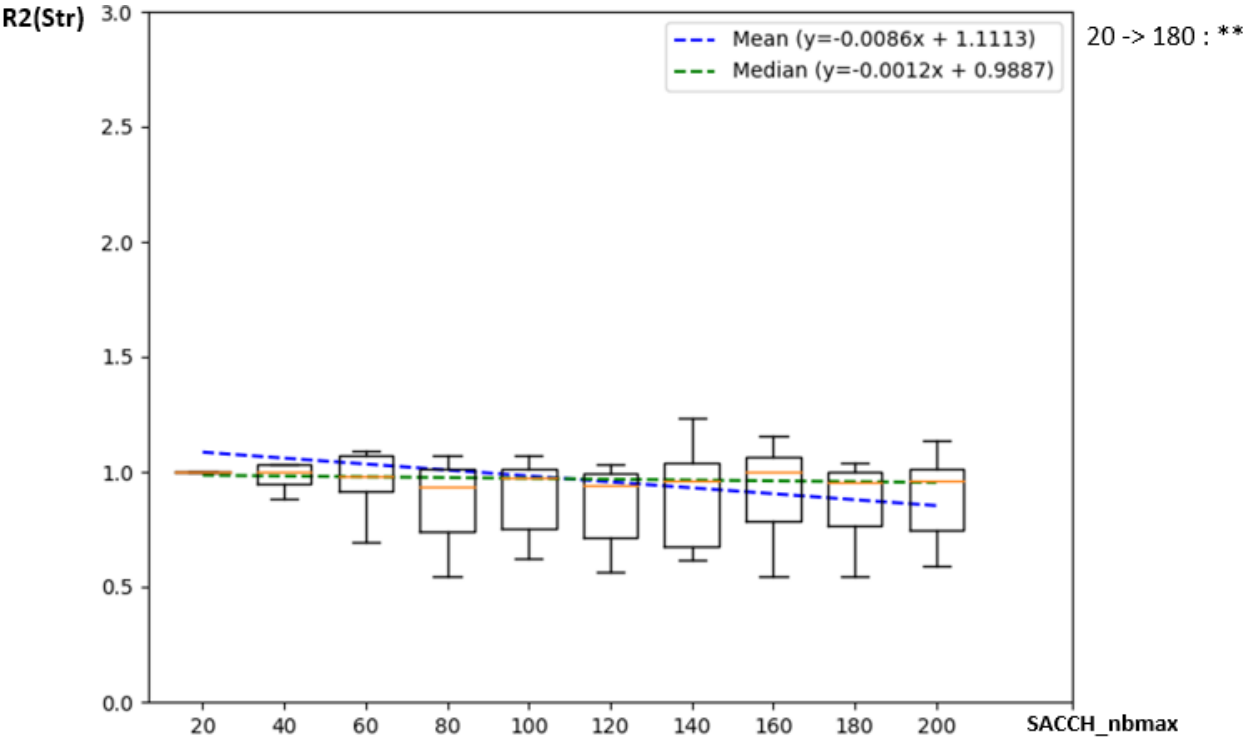

Figure B.100 Evolution of R2(Str) function of the tissue SACCH_nbmax

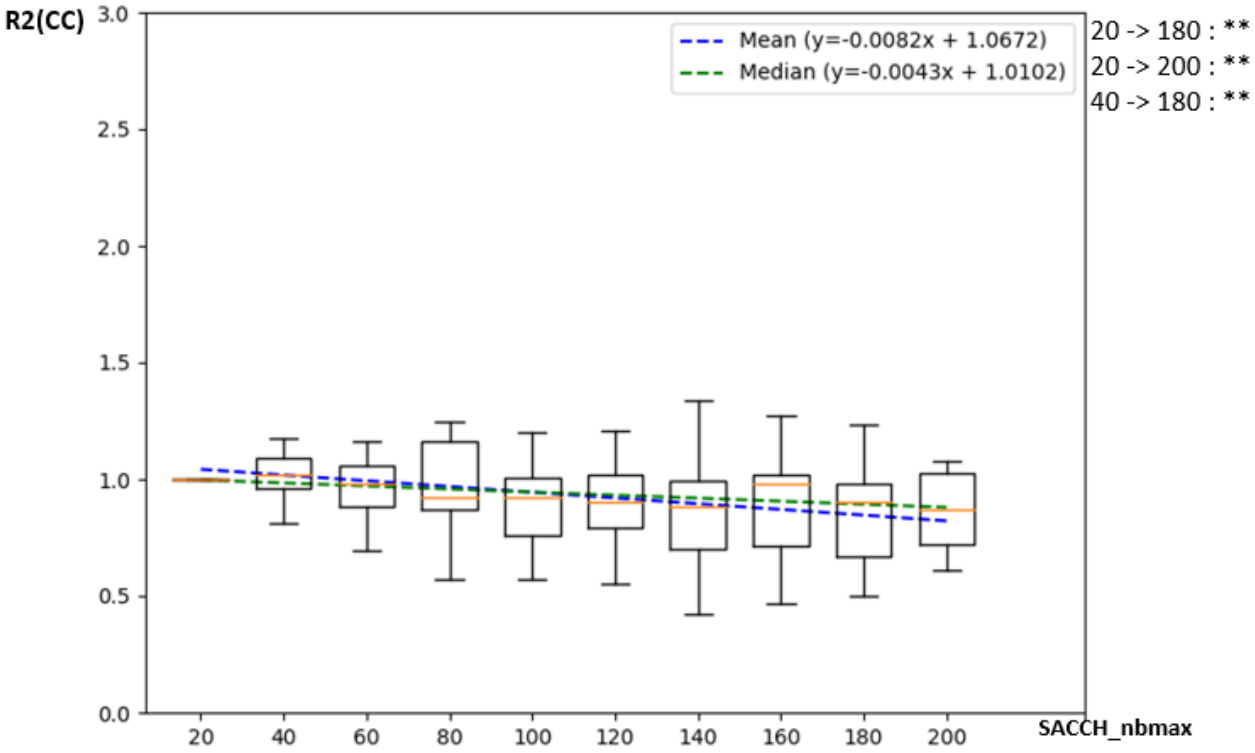

Figure B.101 Evolution of R2(CC) function of the tissue SACCH_nbmax

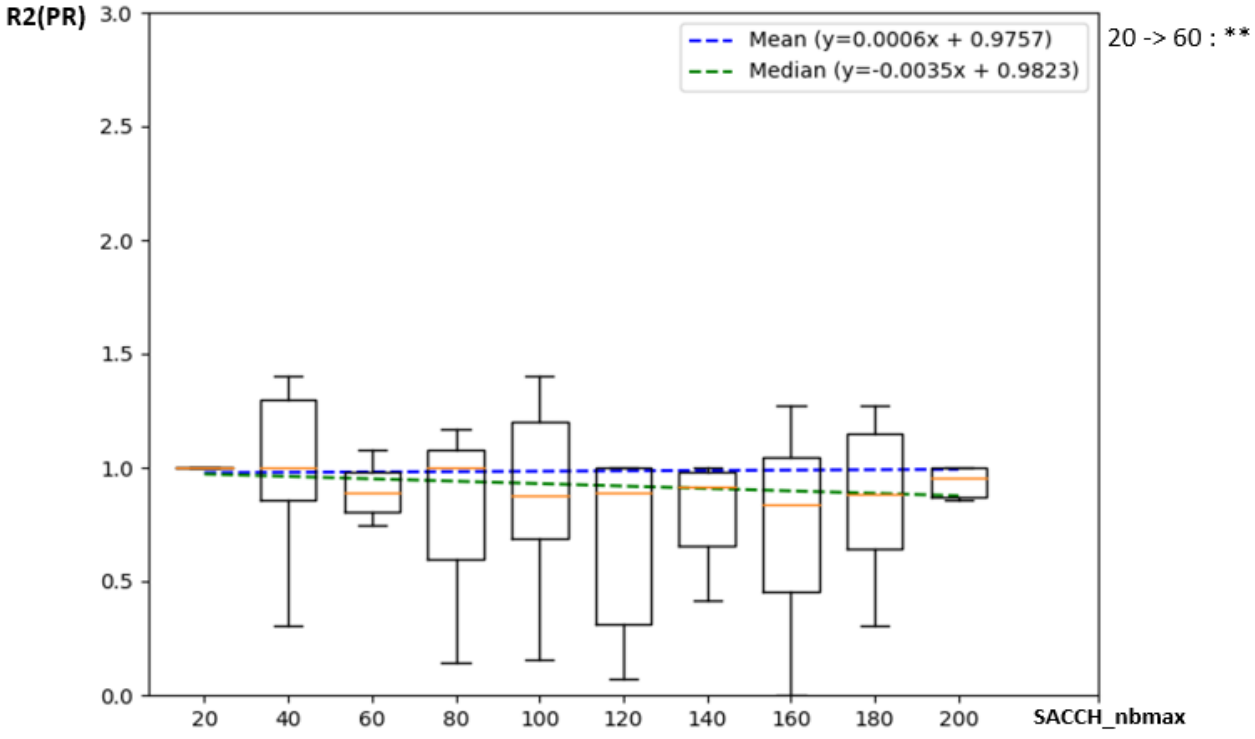

Figure B.102 Evolution of R2(PR) function of the tissue SACCH_nbmax

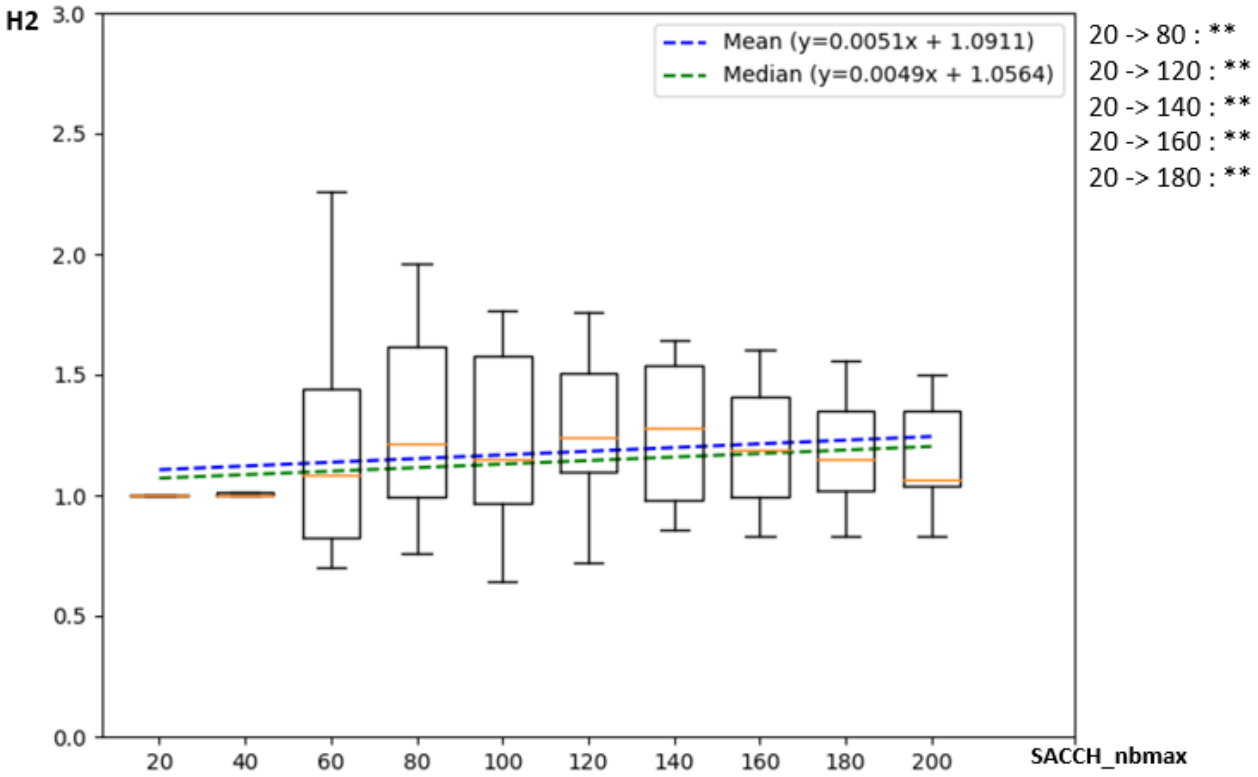

Figure B.103 Evolution of H2 function of the tissue SACCH_nbmax

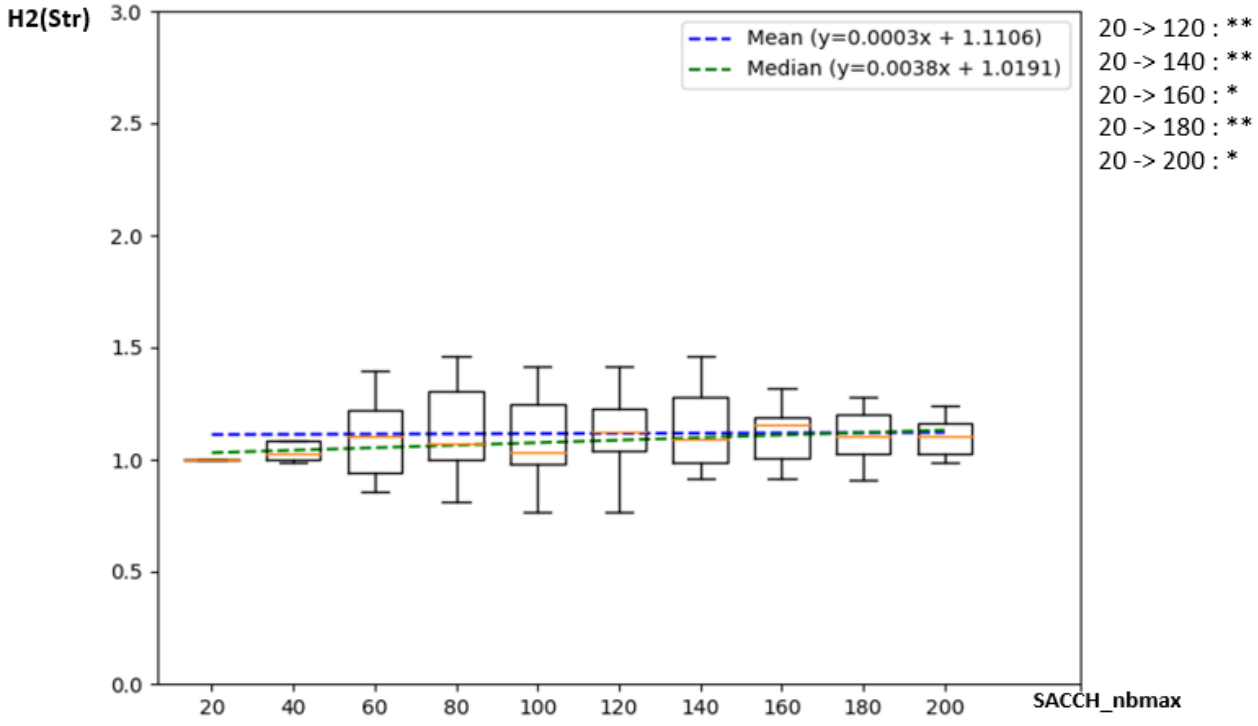

Figure B.104 Evolution of H2(Str) function of the tissue SACCH_nbmax

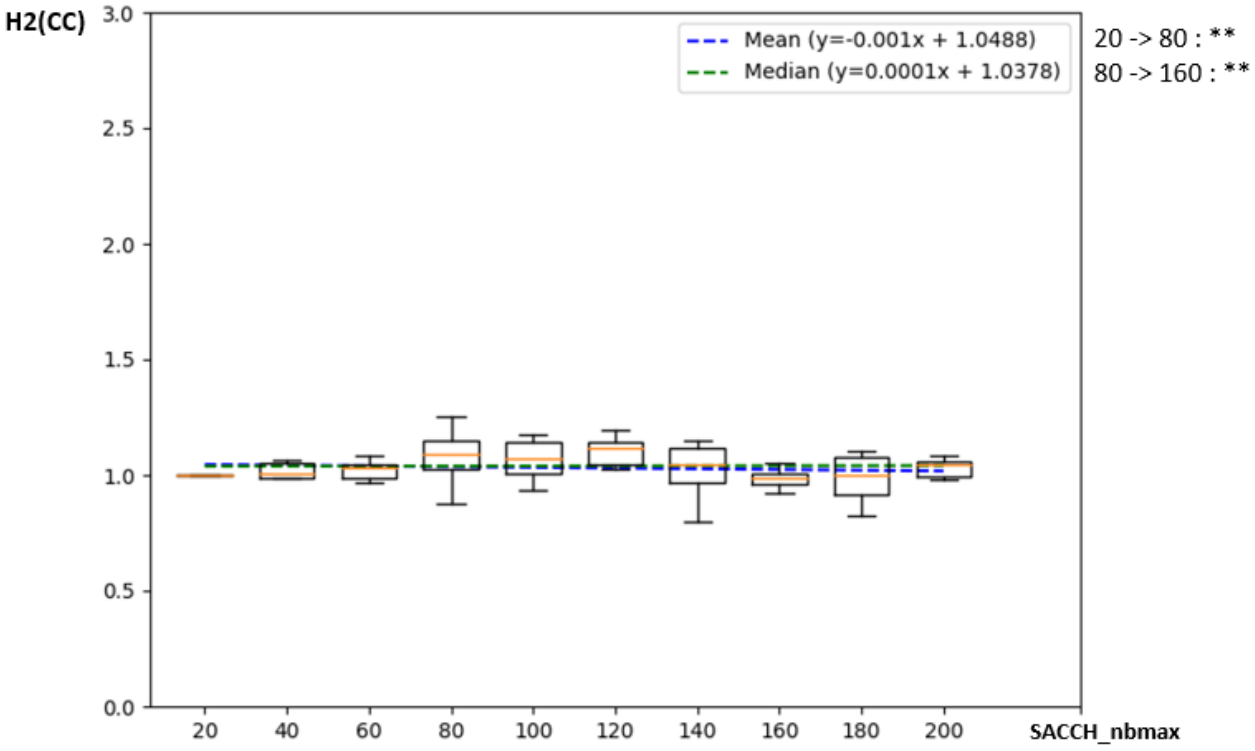

Figure B.105 Evolution of H2(CC) function of the tissue SACCH_nbmax

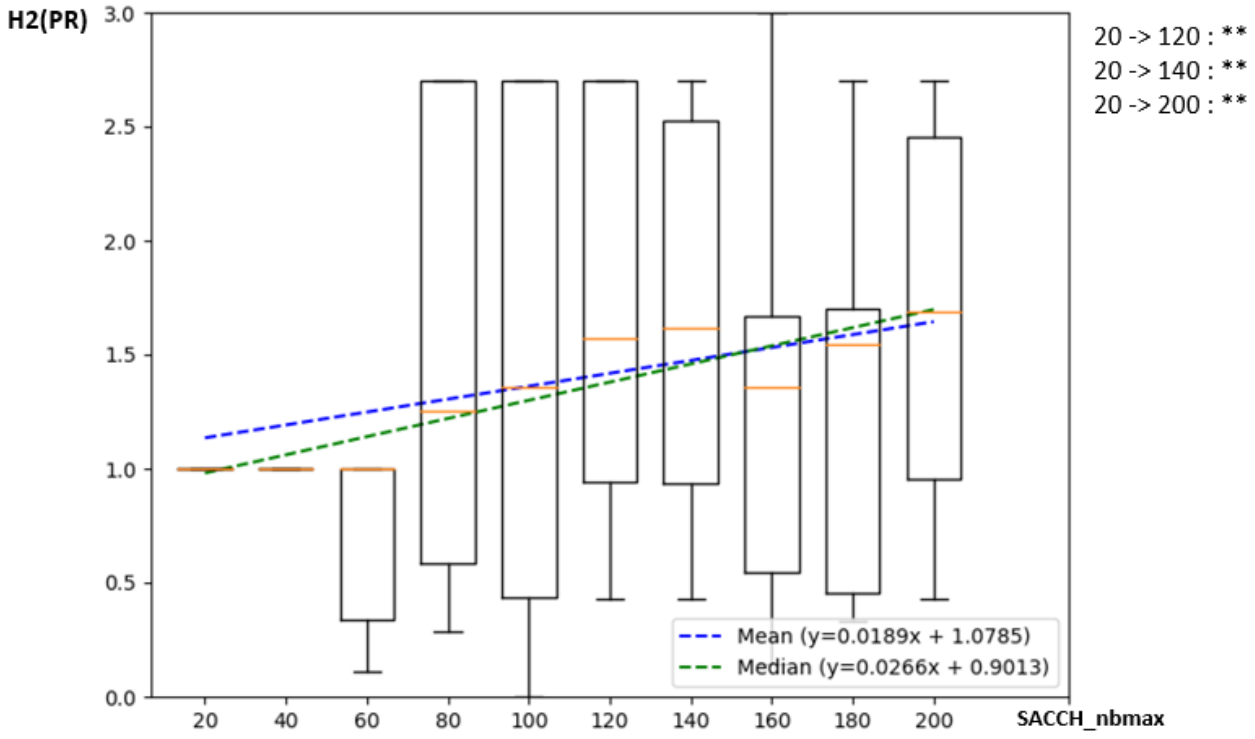

Figure B.106 Evolution of H2(PR) function of the tissue SACCH_nbmax

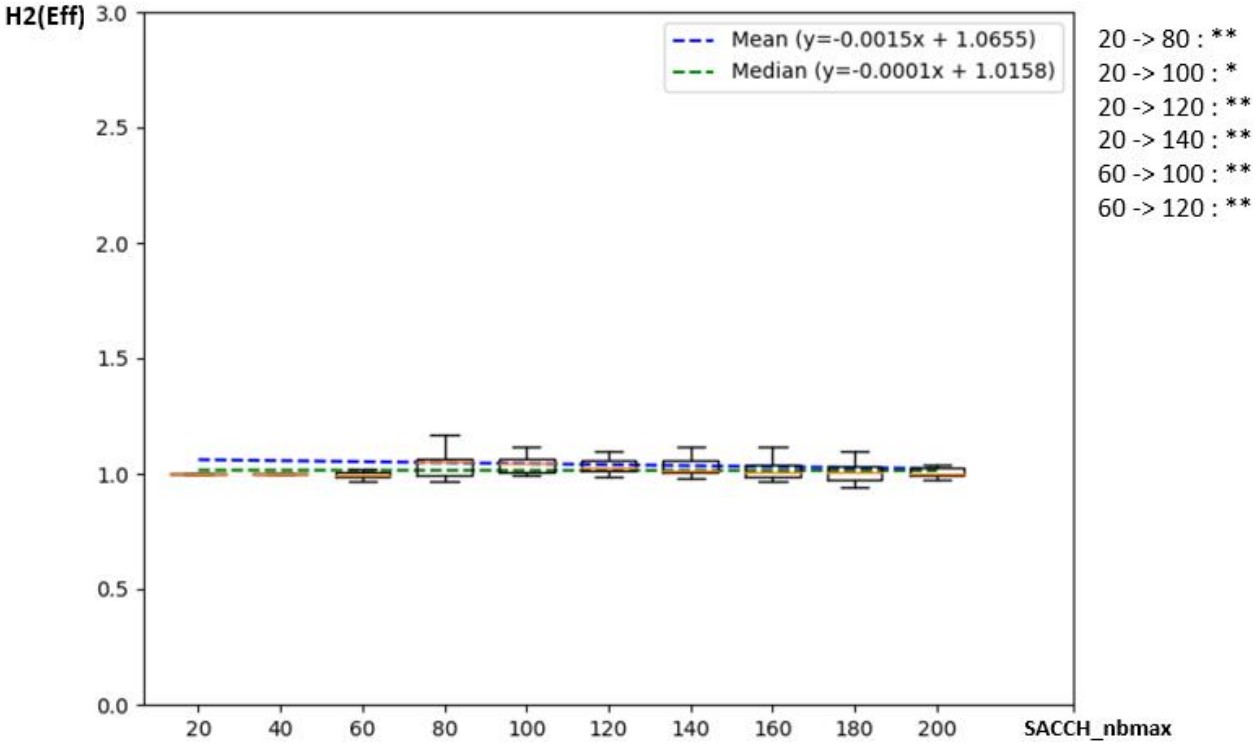

Figure B.107 Evolution of H2(Eff) function of the tissue SACCH_nbmax

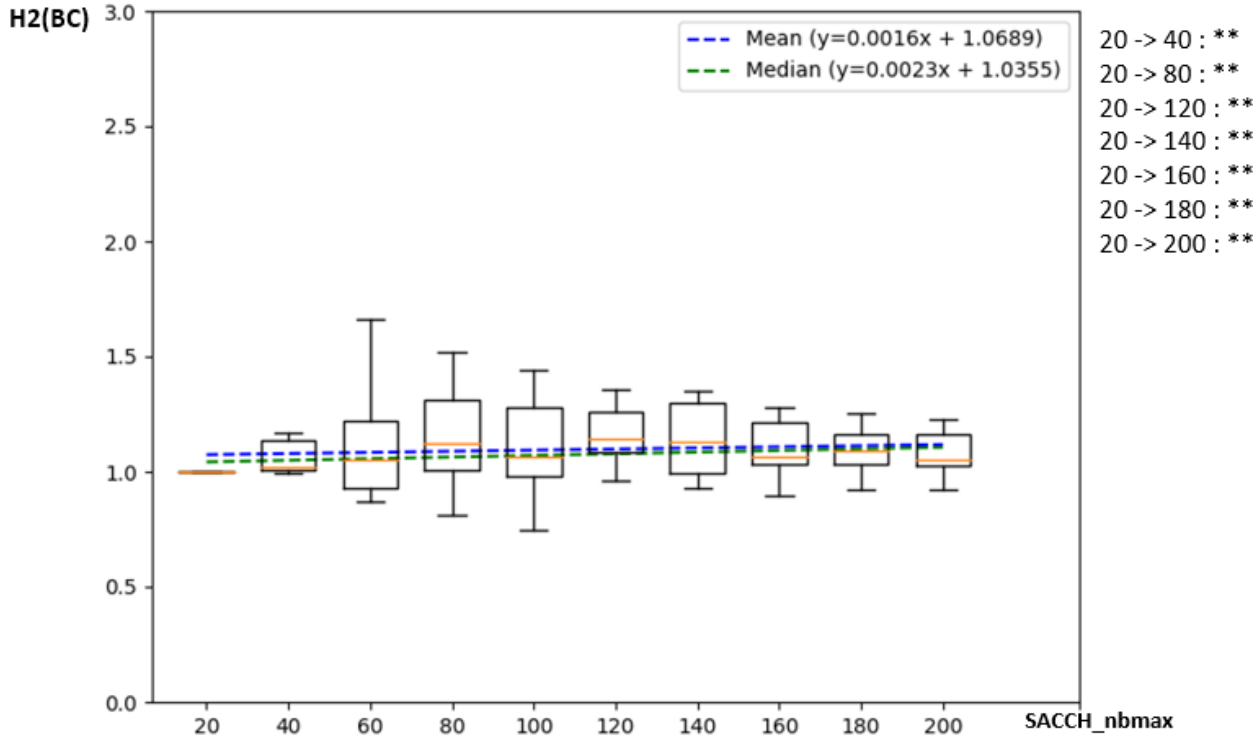

Figure B.108 Evolution of H2(BC) function of the tissue SACCH_nbmax

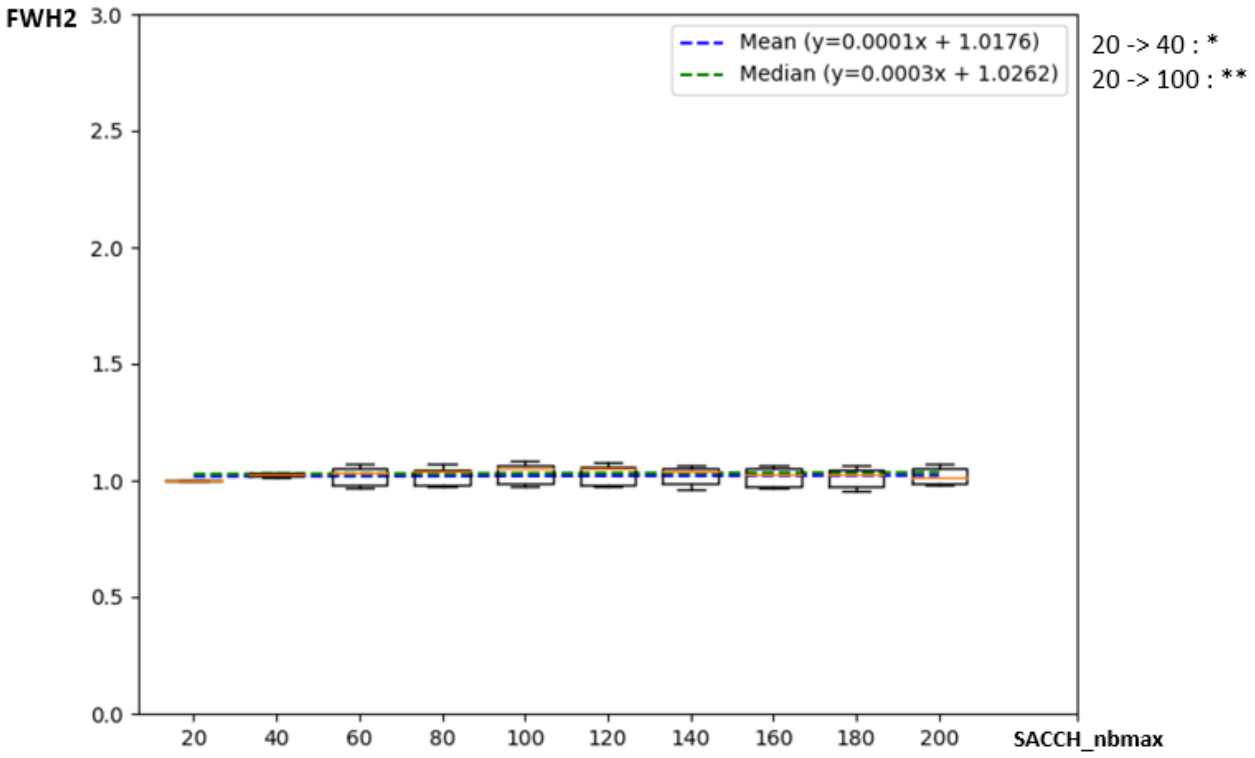

Figure B.109 Evolution of FWH2 function of the tissue SACCH_nbmax

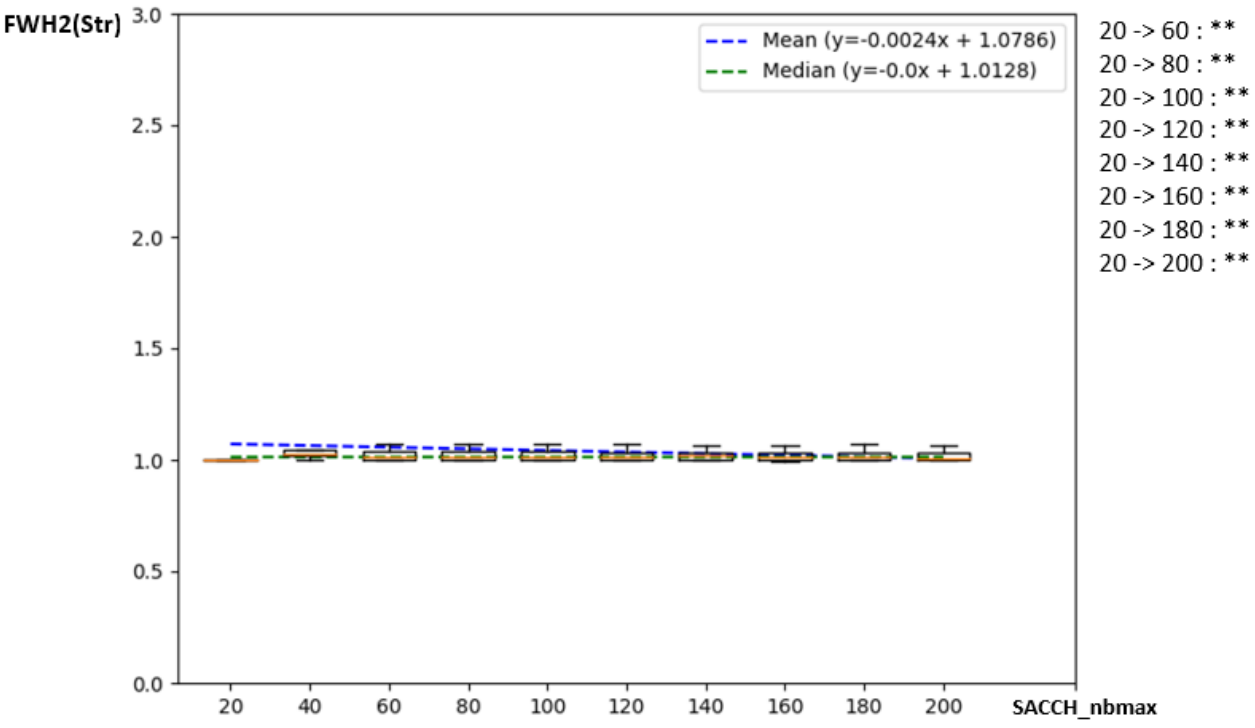

Figure B.110 Evolution of FWH2(Str) function of the tissue SACCH_nbmax

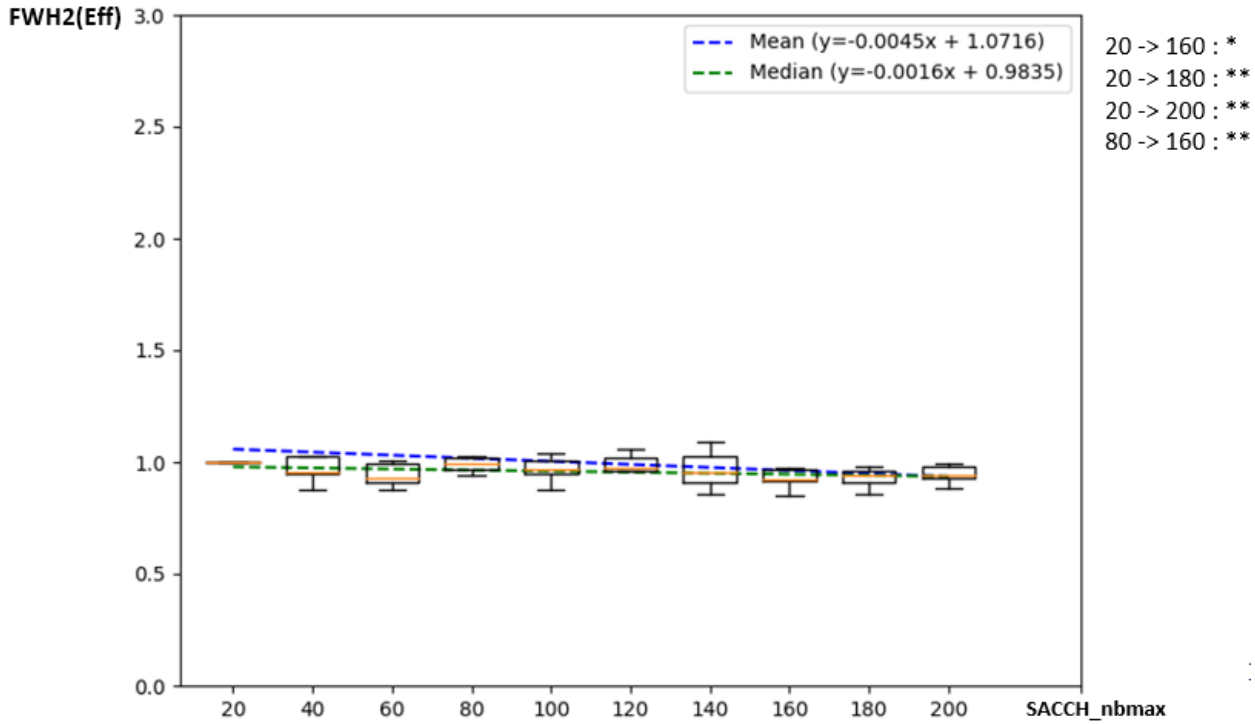

Figure B.111 Evolution of FWH2(Eff) function of the tissue SACCH_nbmax

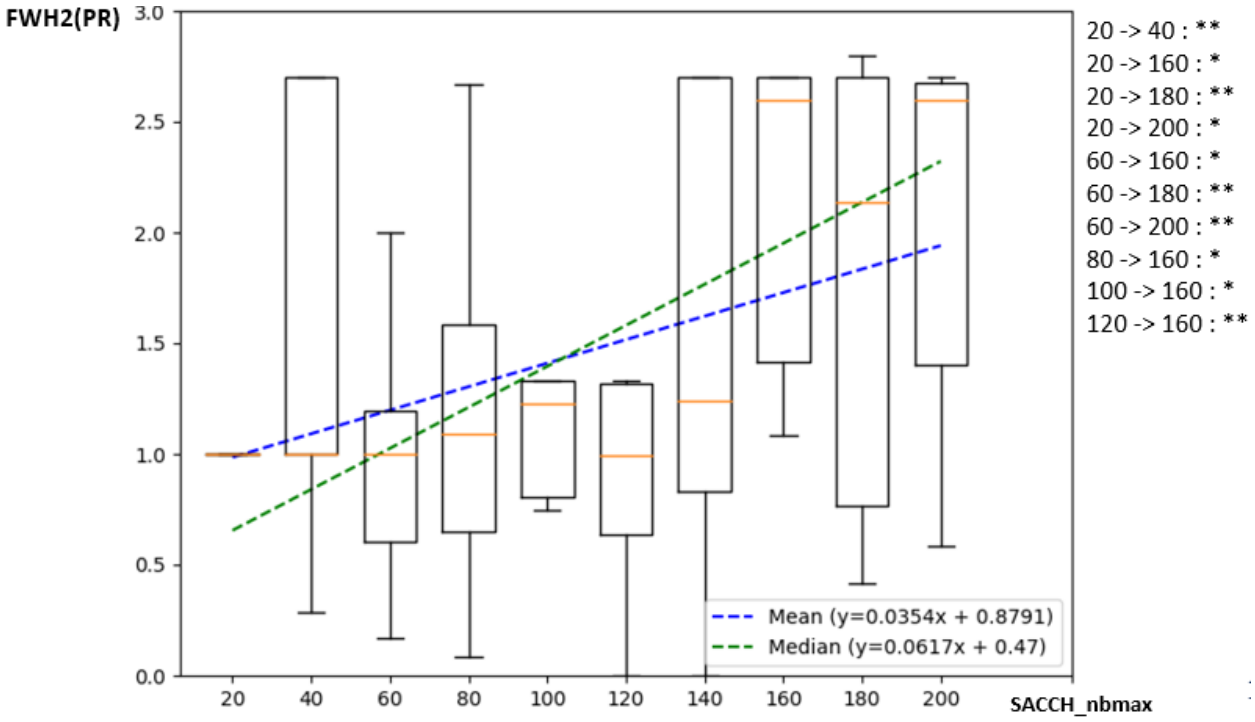

Figure B.112 Evolution of FWH2(PR) function of the tissue SACCH_nbmax

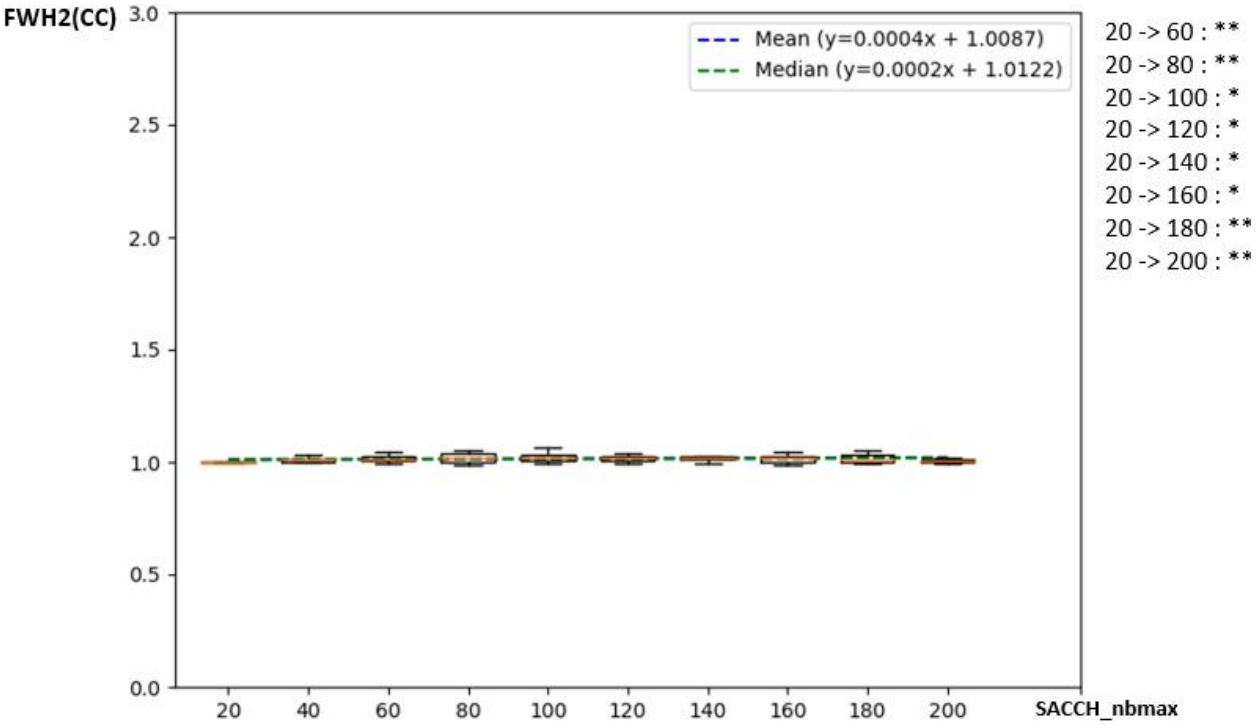

Figure B.113 Evolution of FWH2(CC) function of the tissue SACCH_nbmax

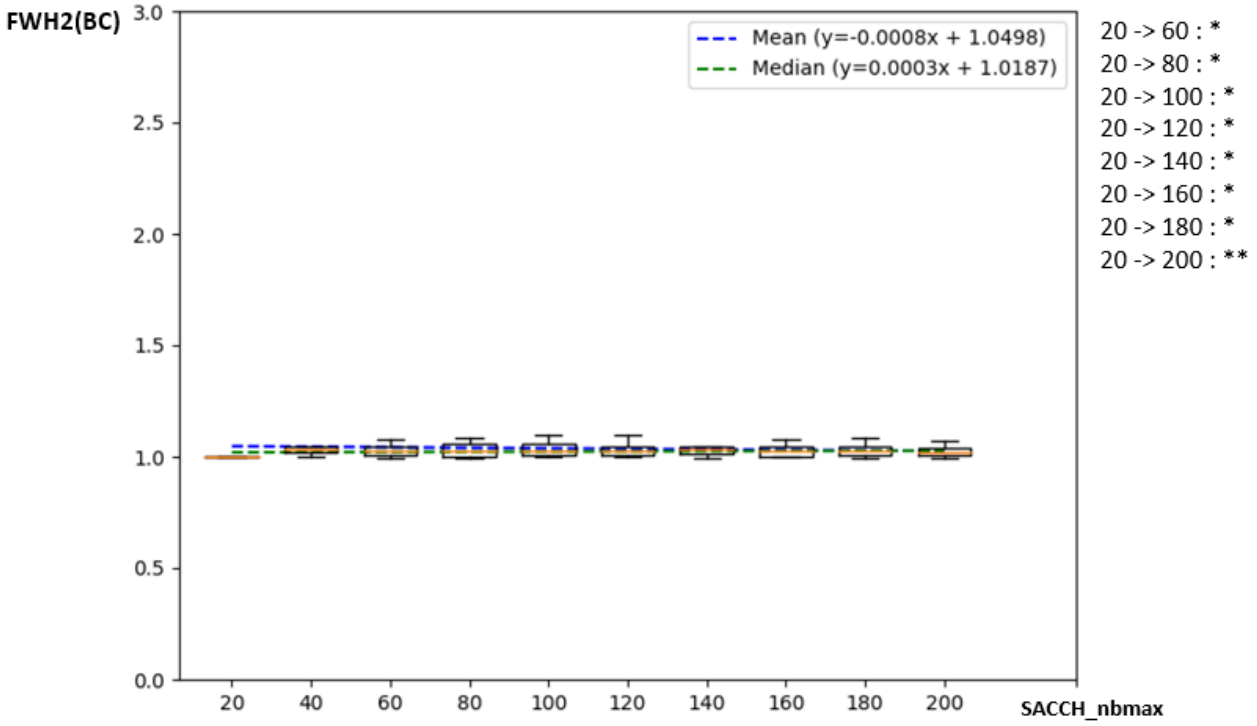

Figure B.114 Evolution of FWH2(BC) function of the tissue SACCH_nbmax

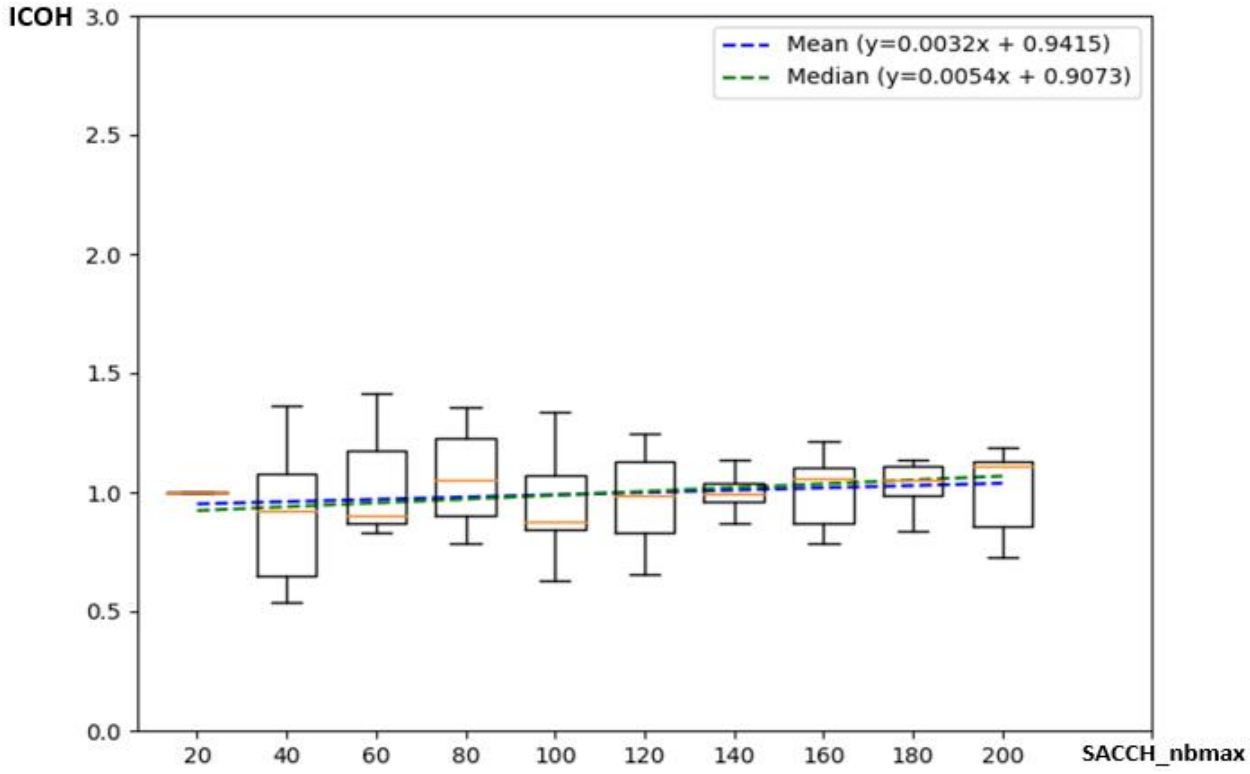

Figure B.115 Evolution of ICOH function of the tissue SACCH_nbmax

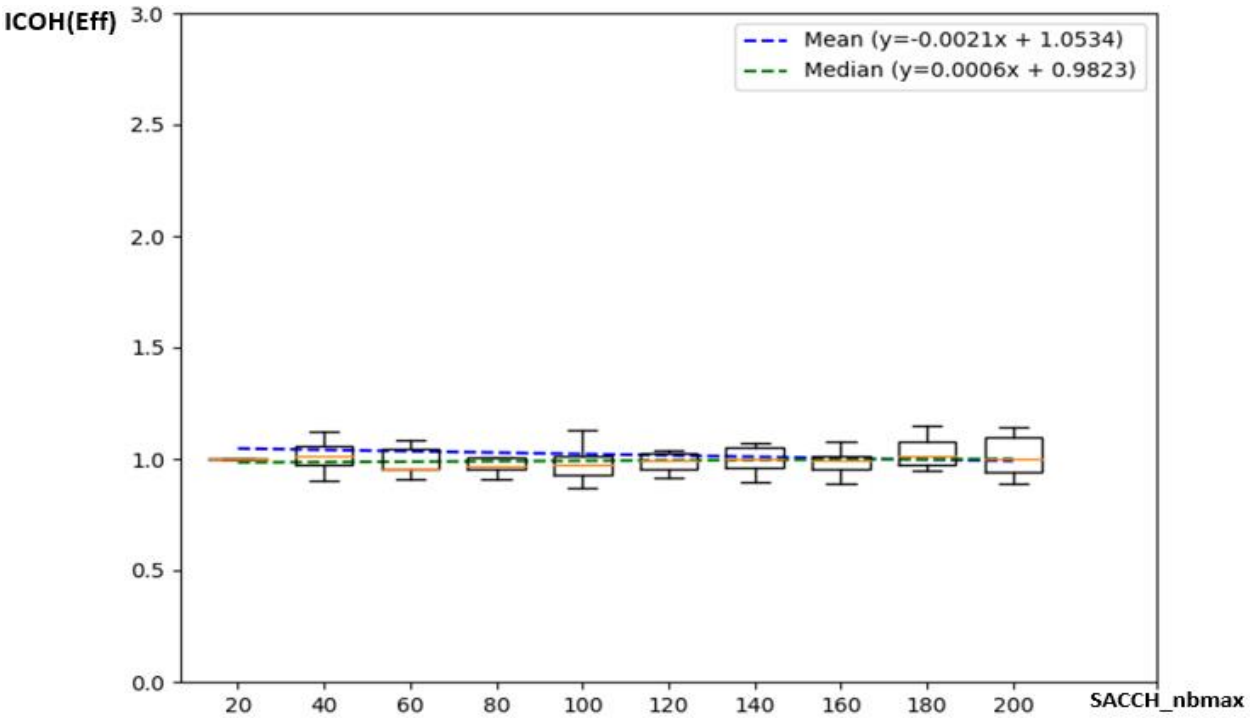

Figure B.116 Evolution of ICOH(Eff) function of the tissue SACCH_nbmax

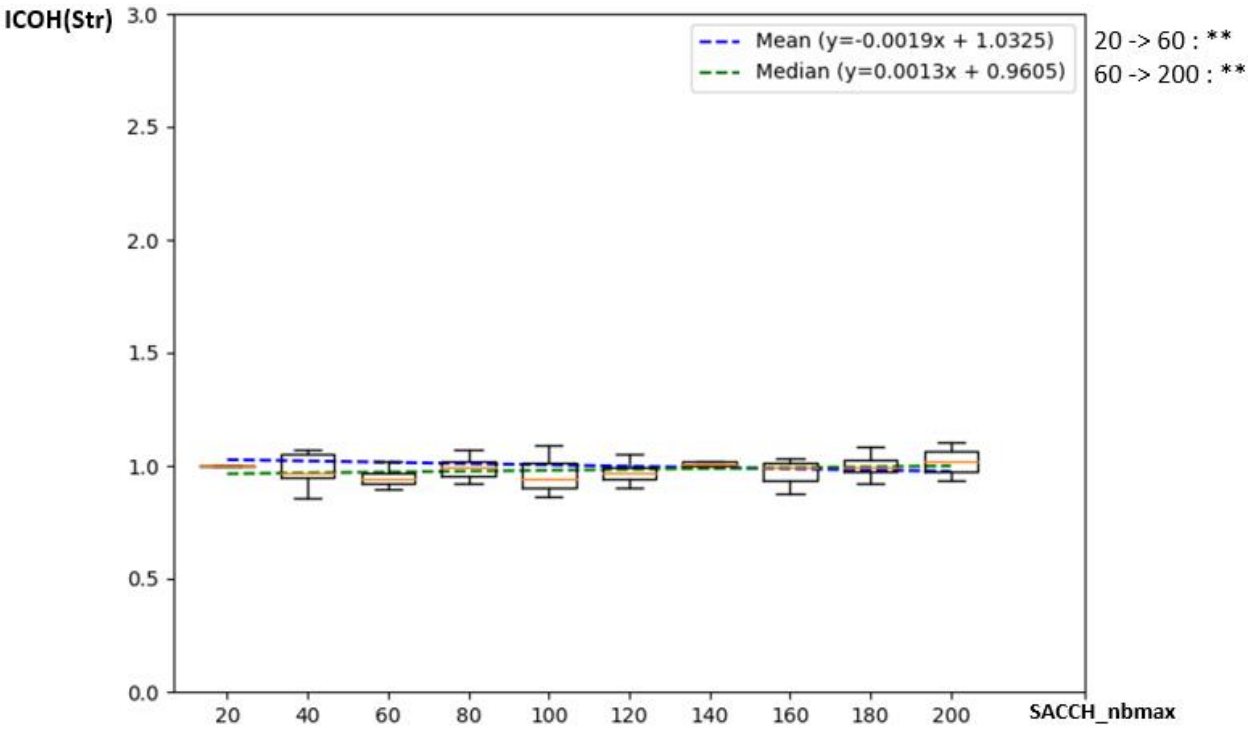

Figure B.117 Evolution of ICOH(Str) function of the tissue SACCH_nbmax

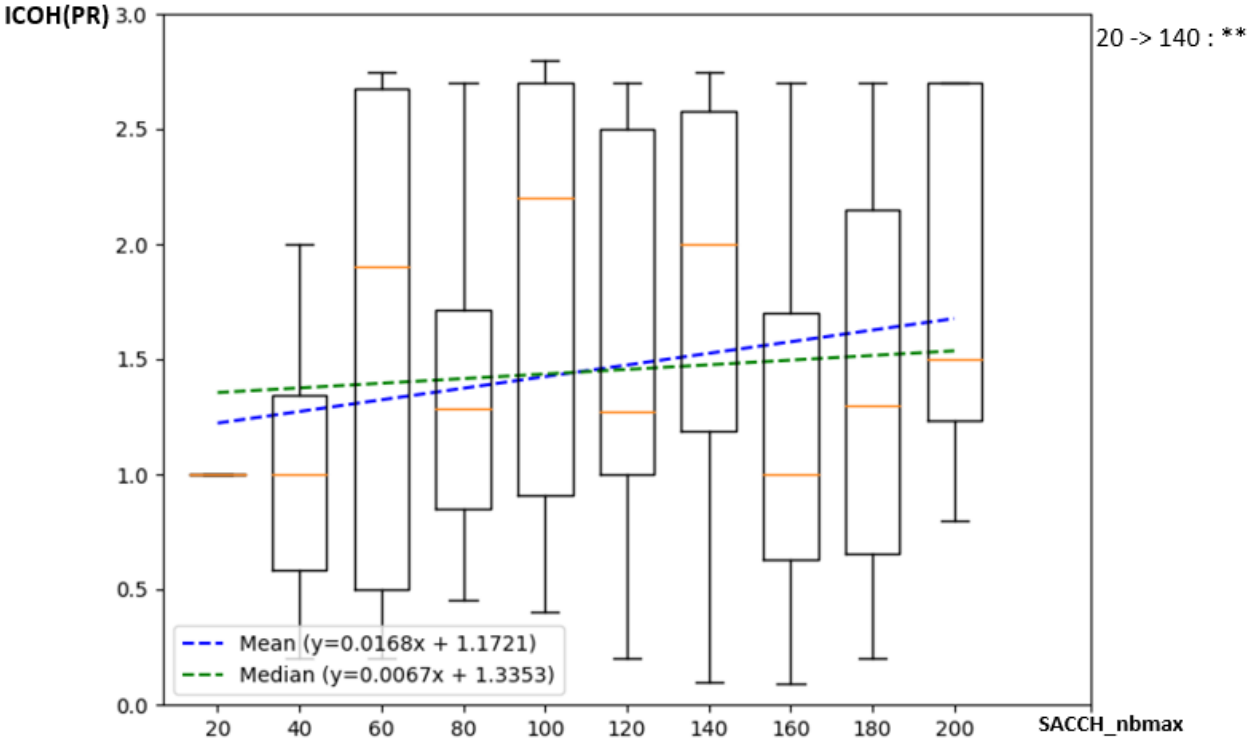

Figure B.118 Evolution of ICOH(PR) function of the tissue SACCH_nbmax

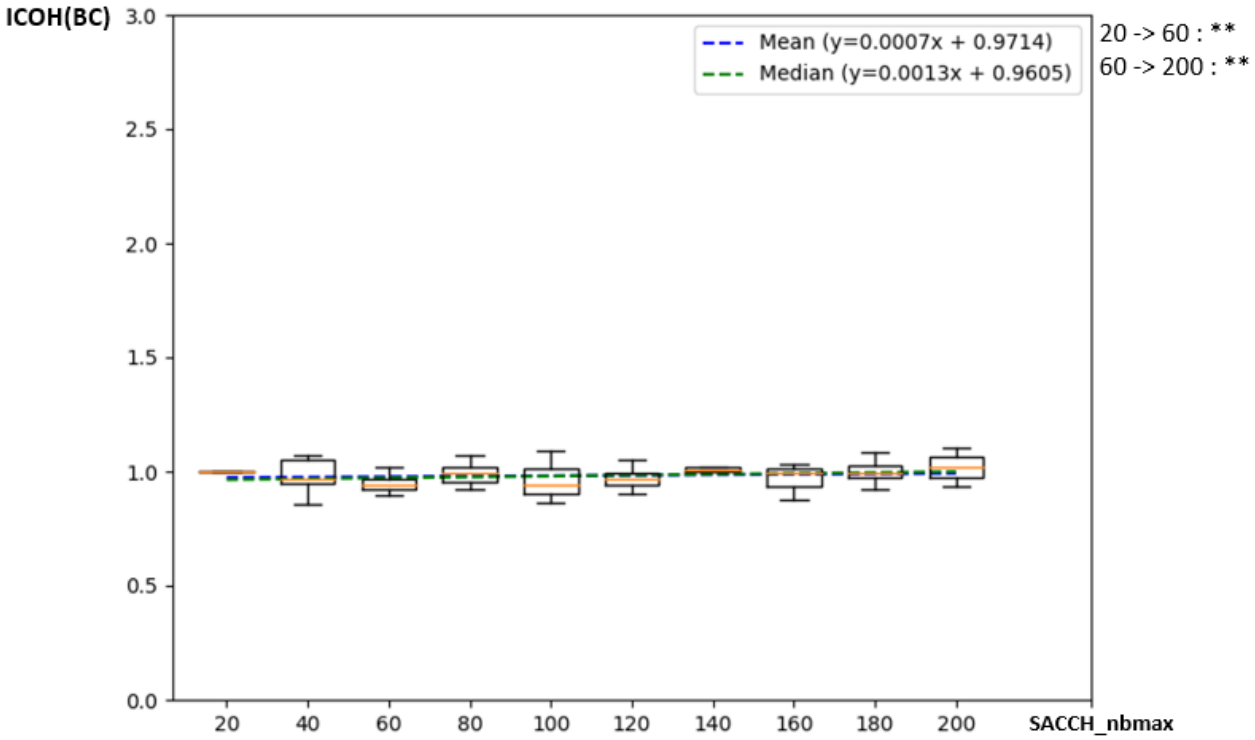

Figure B.119 Evolution of ICOH(BC) function of the tissue SACCH_nbmax

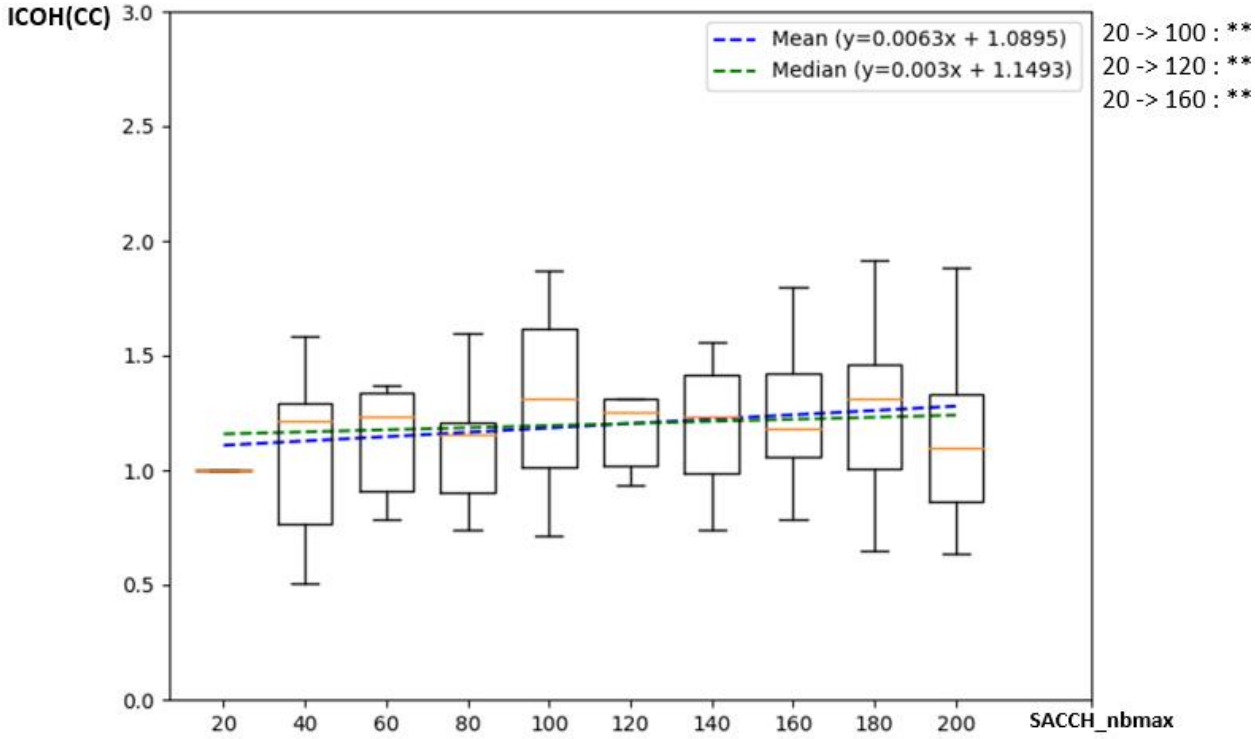

Figure B.120 Evolution of ICOH(CC) function of the tissue SACCH_nbmax

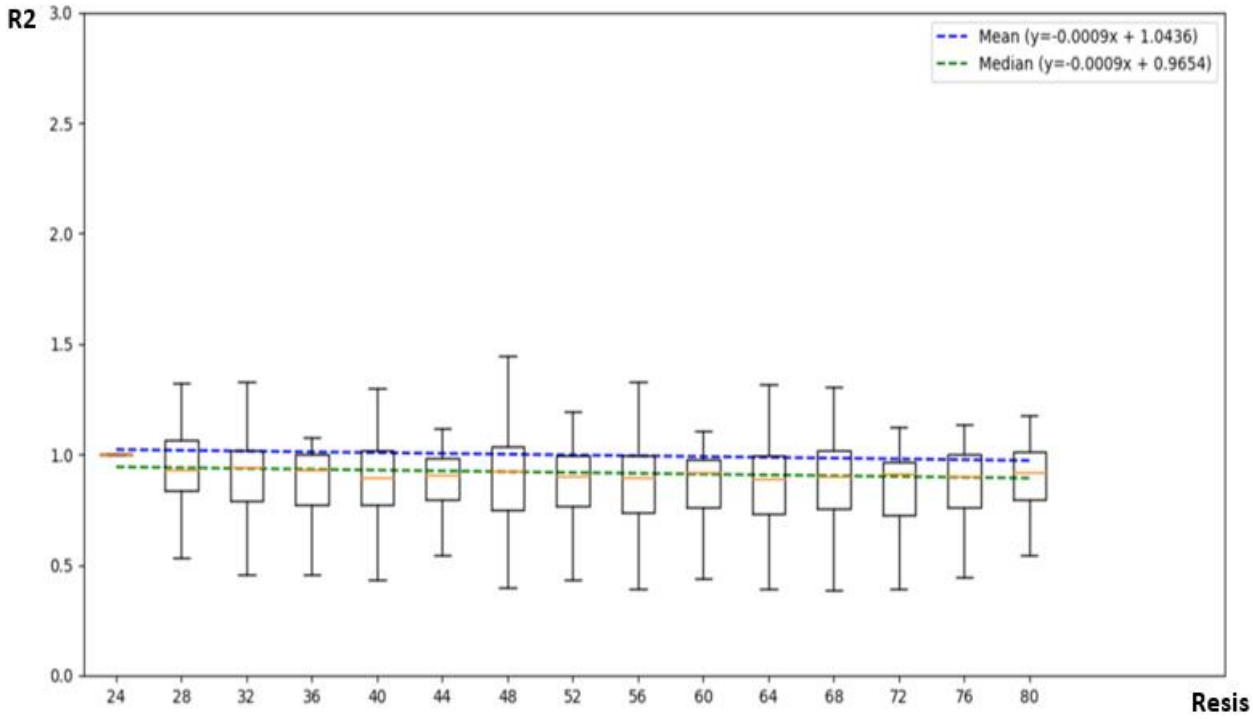

Figure B.121 Evolution of R2 function of the tissue Resistance

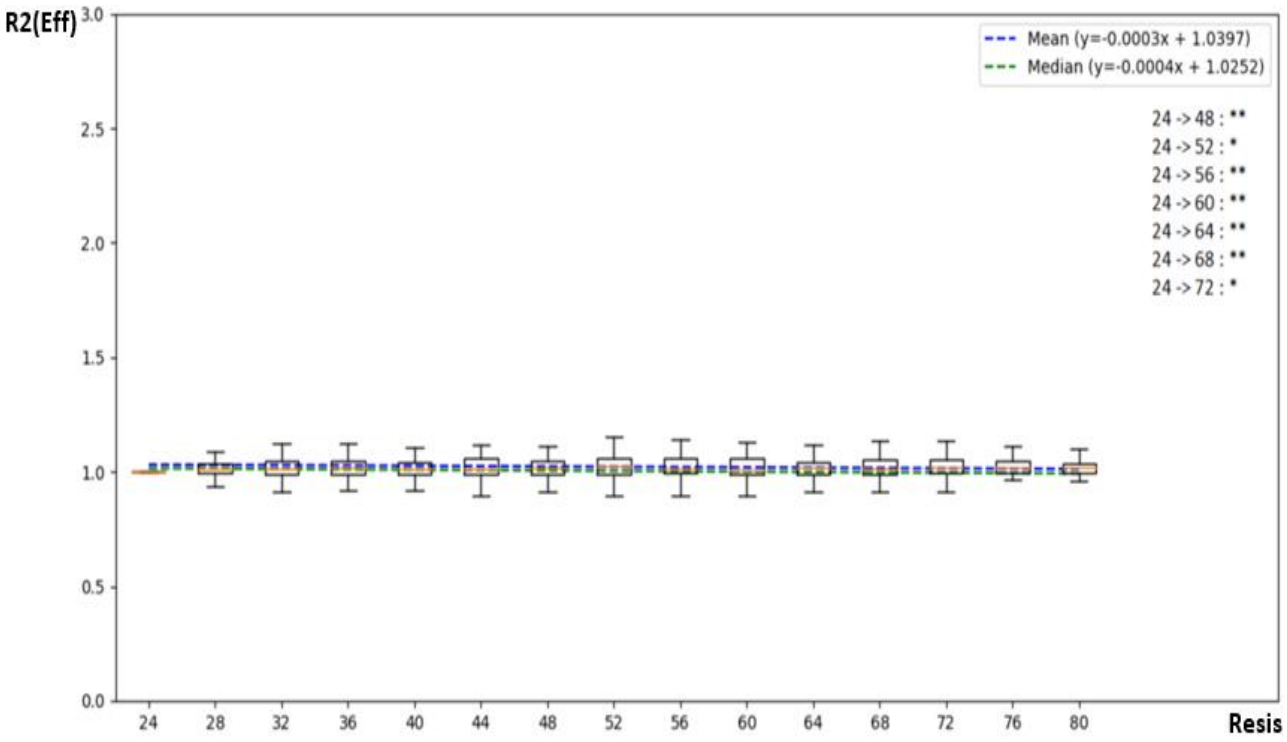

Figure B.122 Evolution of R2(Eff) function of the tissue Resistance

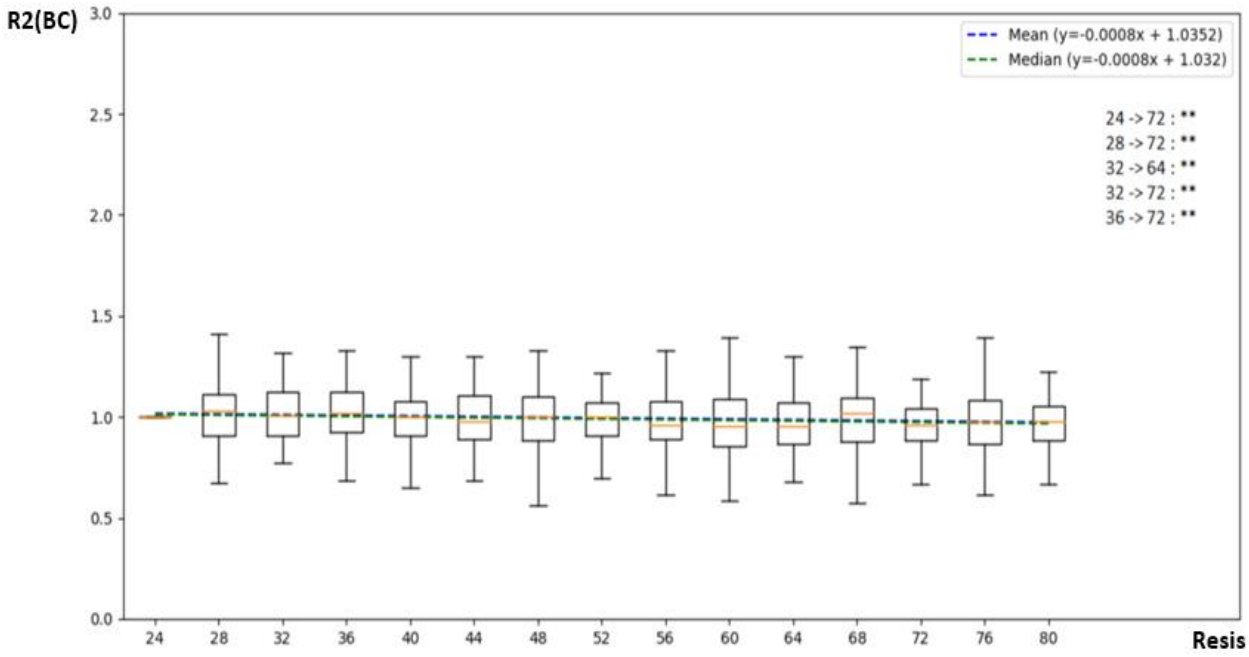

Figure B.123 Evolution of R2(BC) function of the tissue Resistance

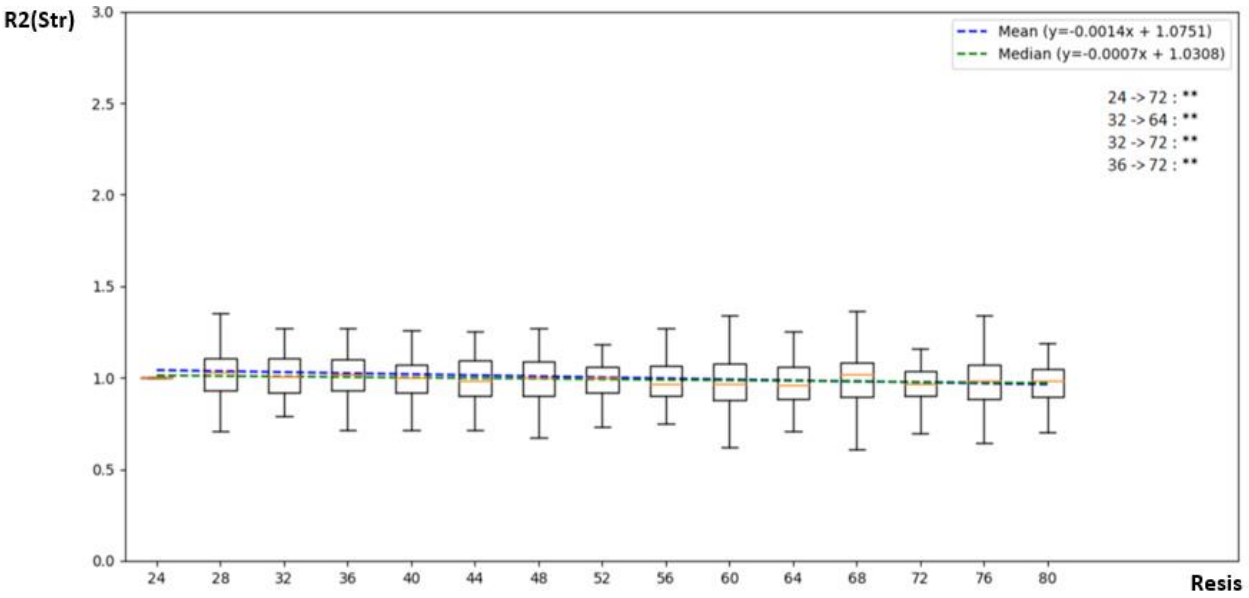

Figure B.124 Evolution of R2(Str) function of the tissue Resistance

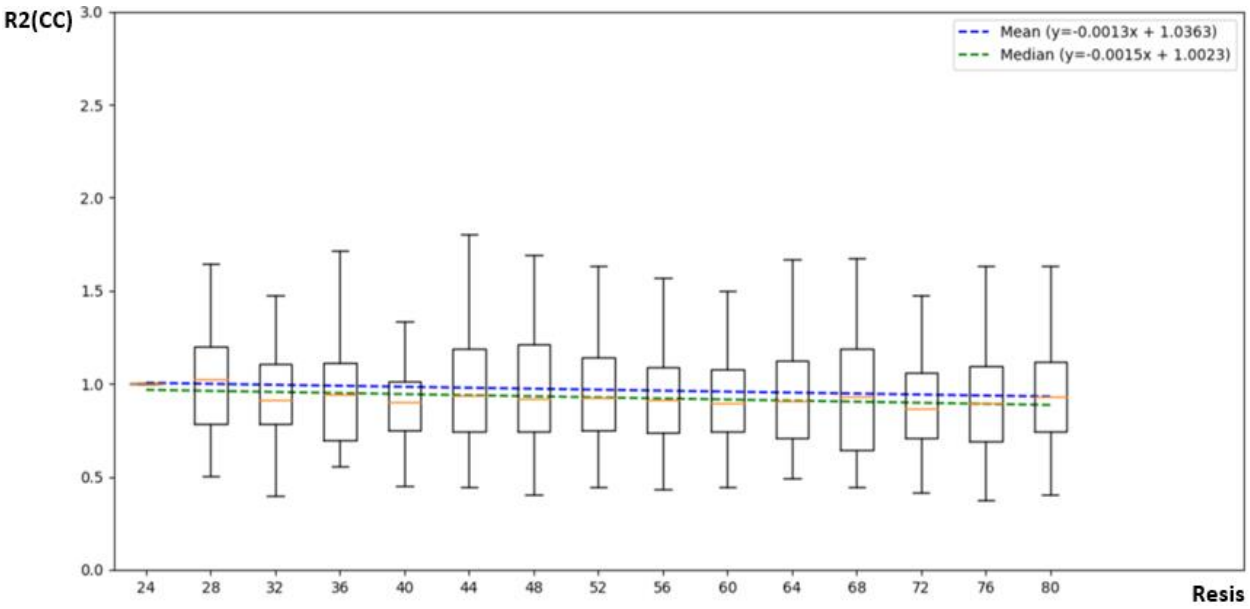

Figure B.125 Evolution of R2(CC) function of the tissue Resistance

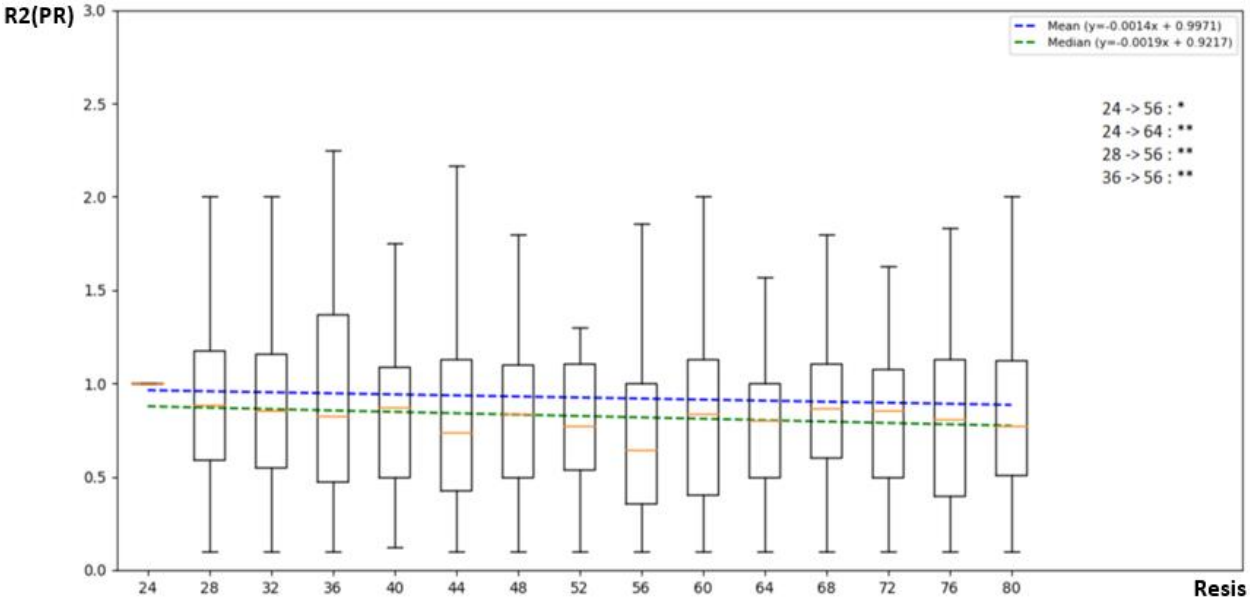

Figure B.126 Evolution of R2(PR) function of the tissue Resistance

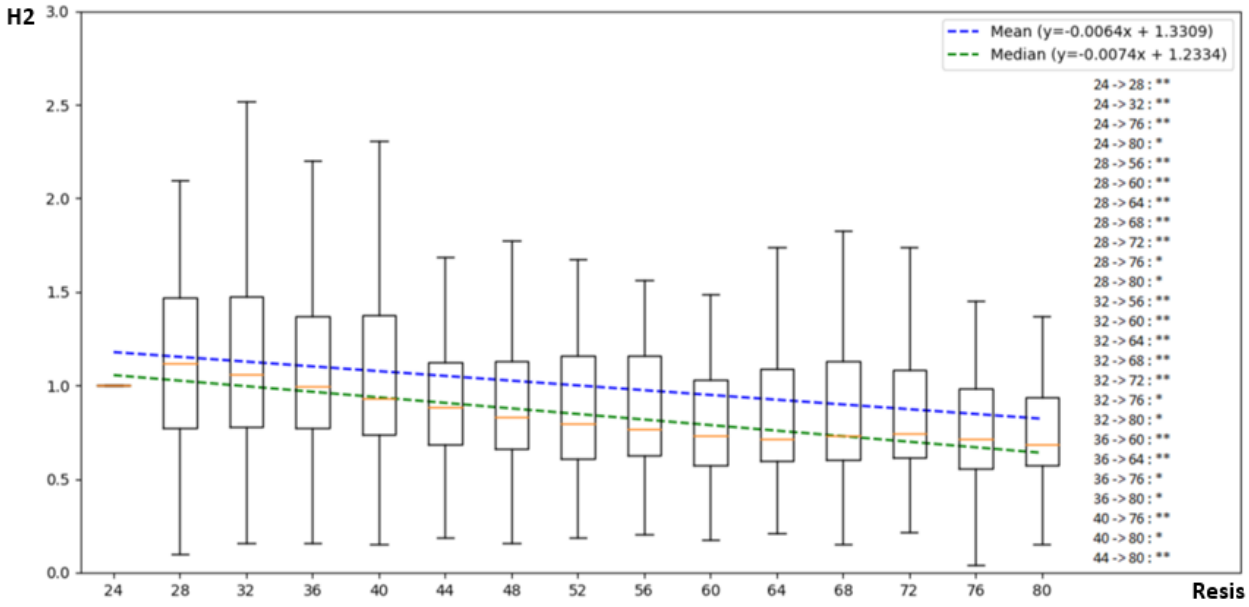

Figure B.127 Evolution of H2 function of the tissue Resistance

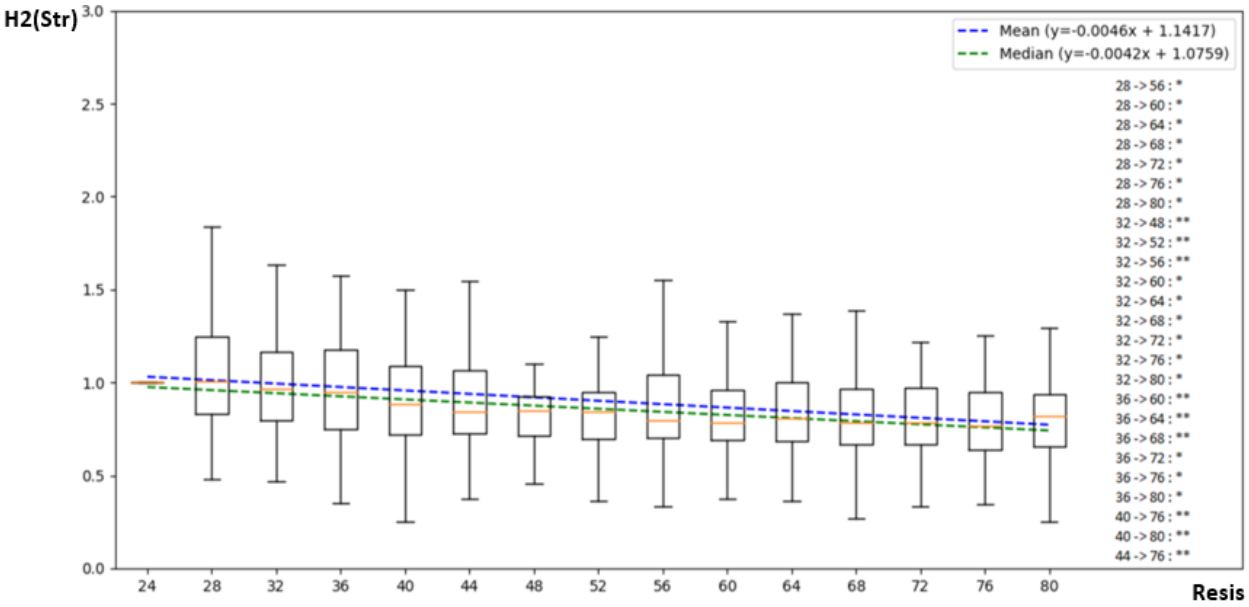

Figure B.128 Evolution of H2(Str) function of the tissue Resistance

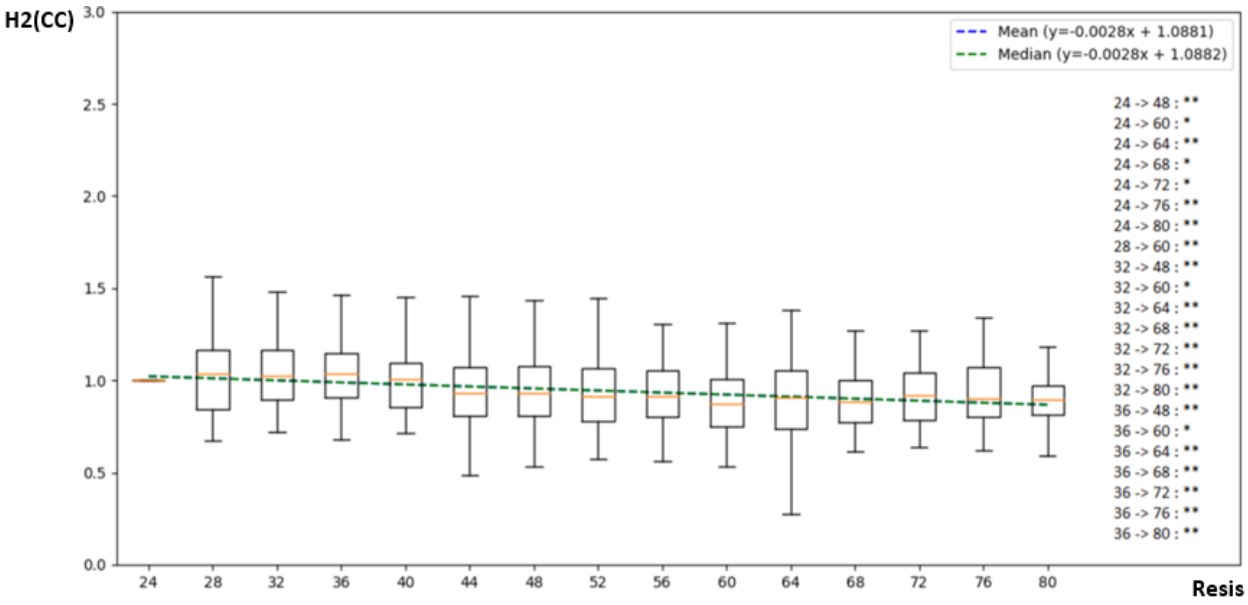

Figure B.129 Evolution of H2(CC) function of the tissue Resistance

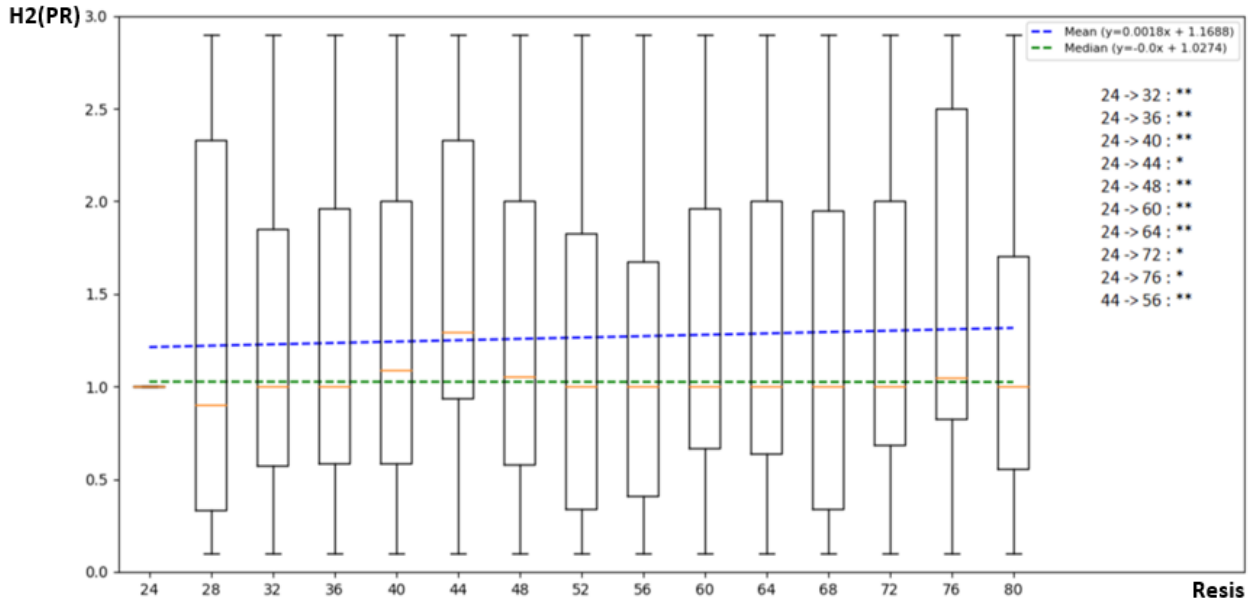

Figure B.130 Evolution of H2(PR) function of the tissue Resistance

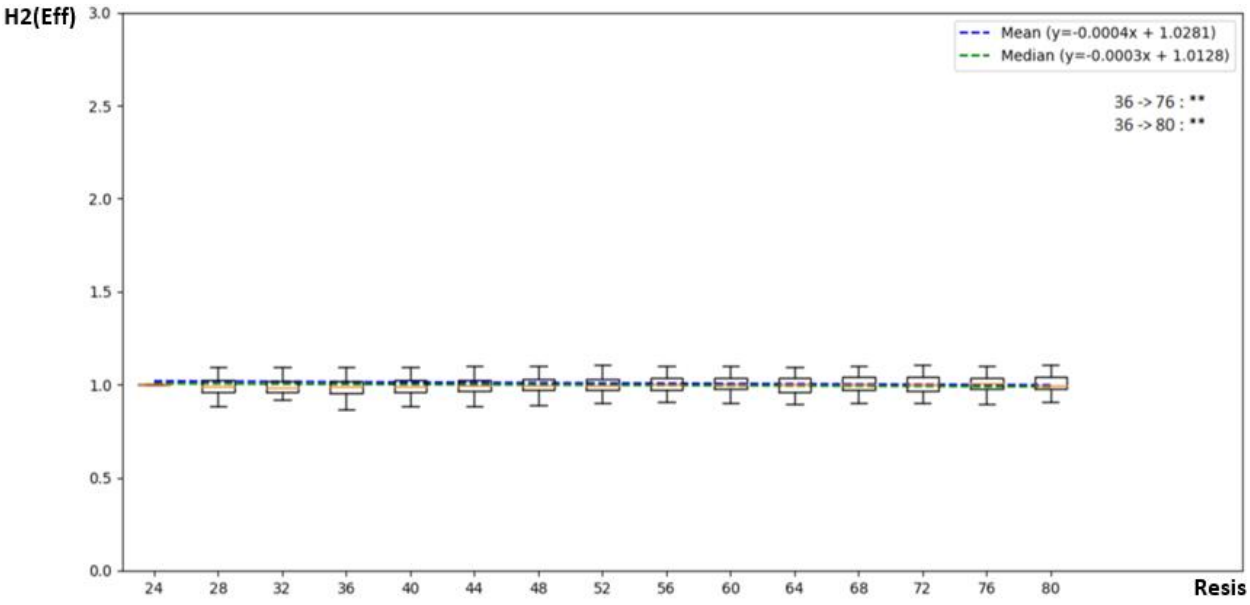

Figure B.131 Evolution of H2(Eff) function of the tissue Resistance

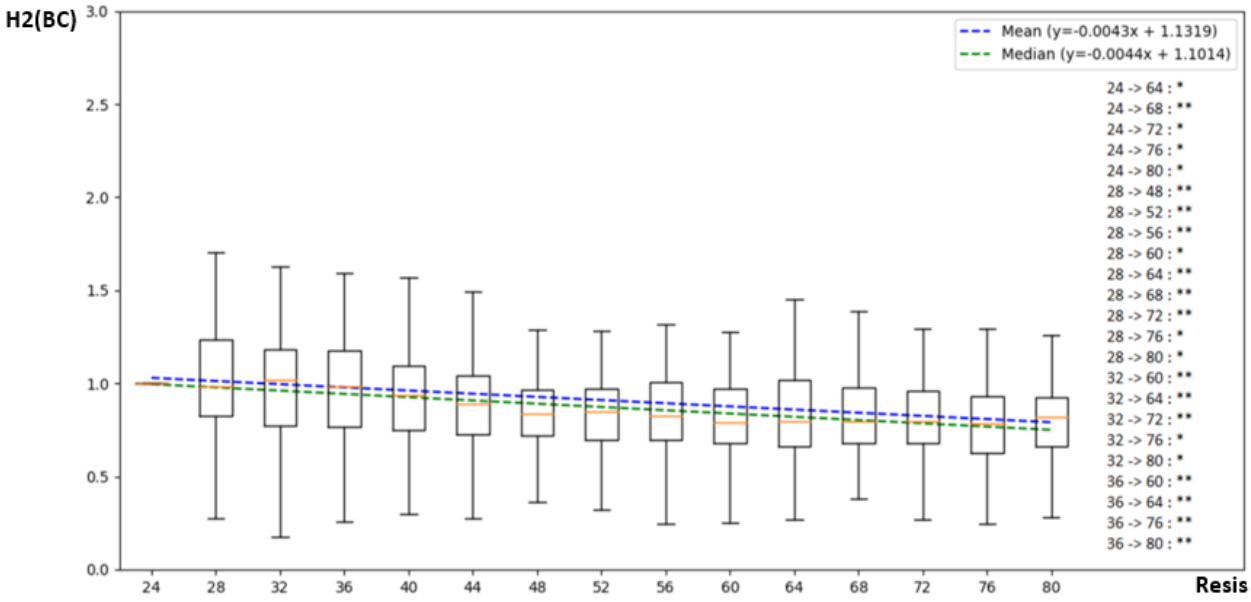

Figure B.132 Evolution of H2(BC) function of the tissue Resistance

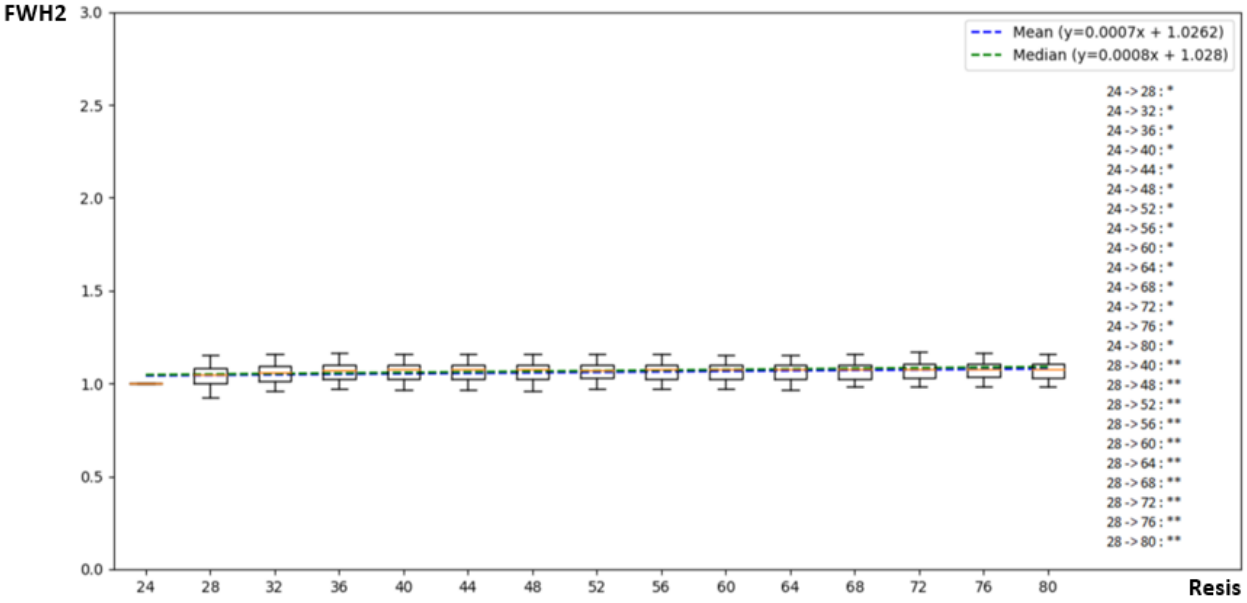

Figure B.133 Evolution of FWH2 function of the tissue Resistance

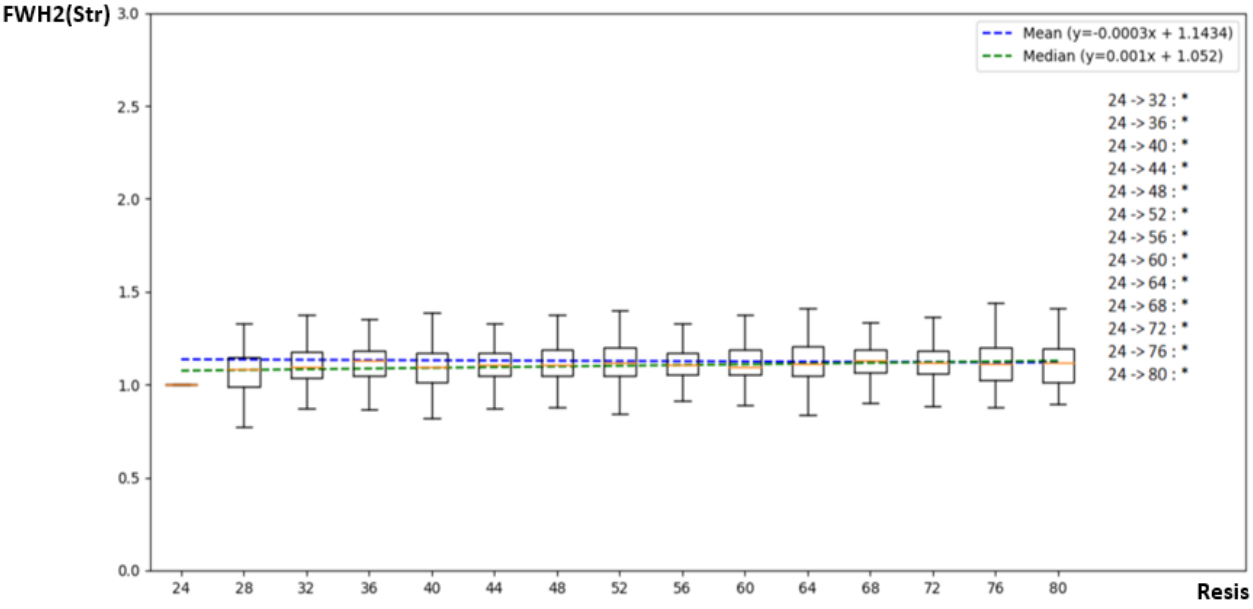

Figure B.134 Evolution of FWH2(Str) function of the tissue Resistance

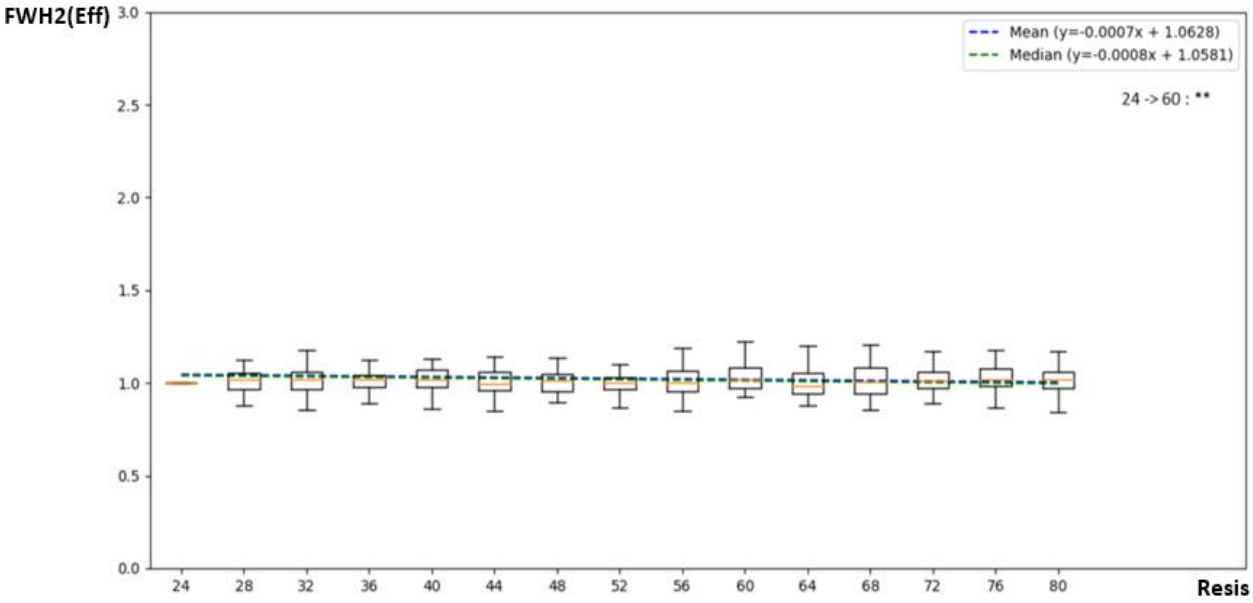

Figure B.135 Evolution of FWH2(Eff) function of the tissue Resistance

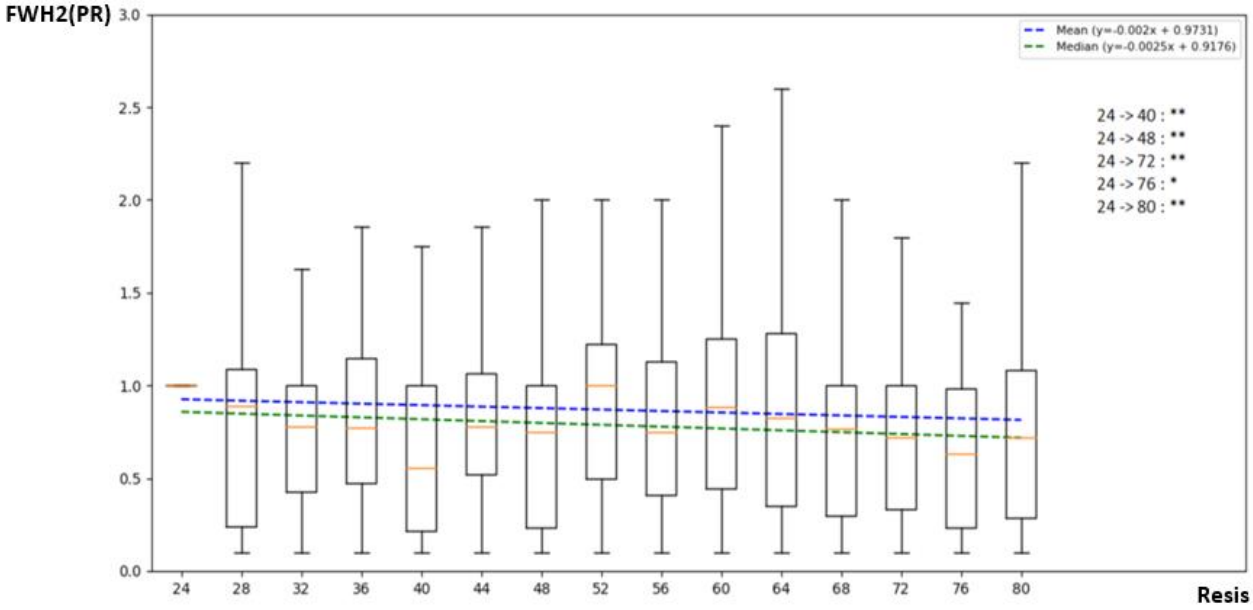

Figure B.136 Evolution of FWH2(PR) function of the tissue Resistance

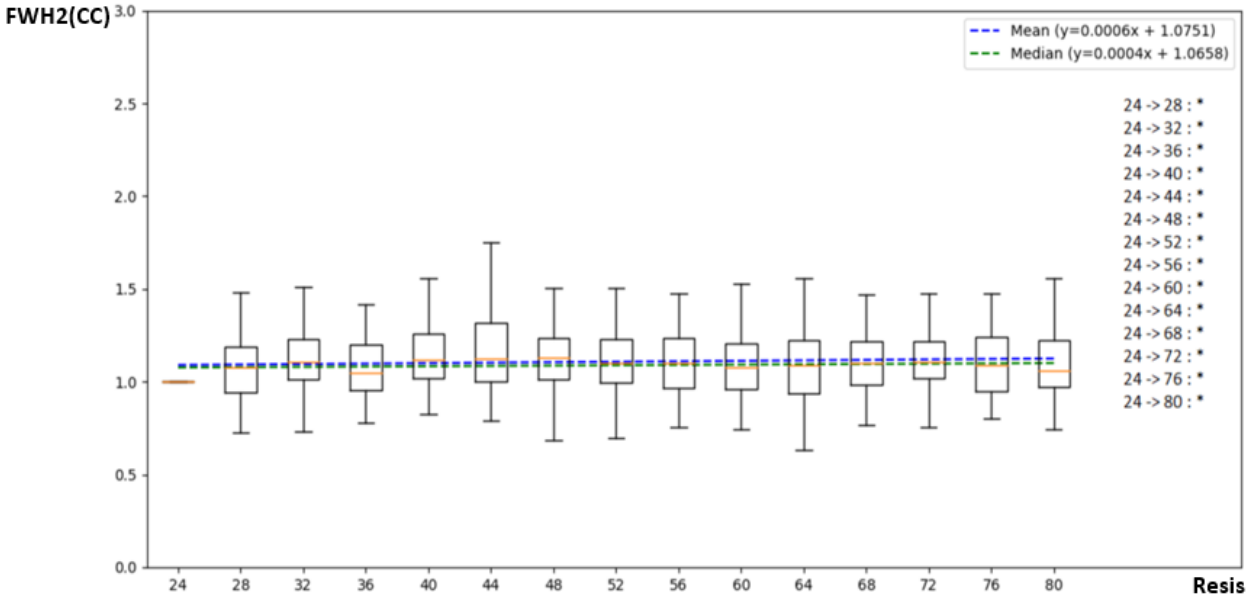

Figure B.137 Evolution of FWH2(CC) function of the tissue Resistance

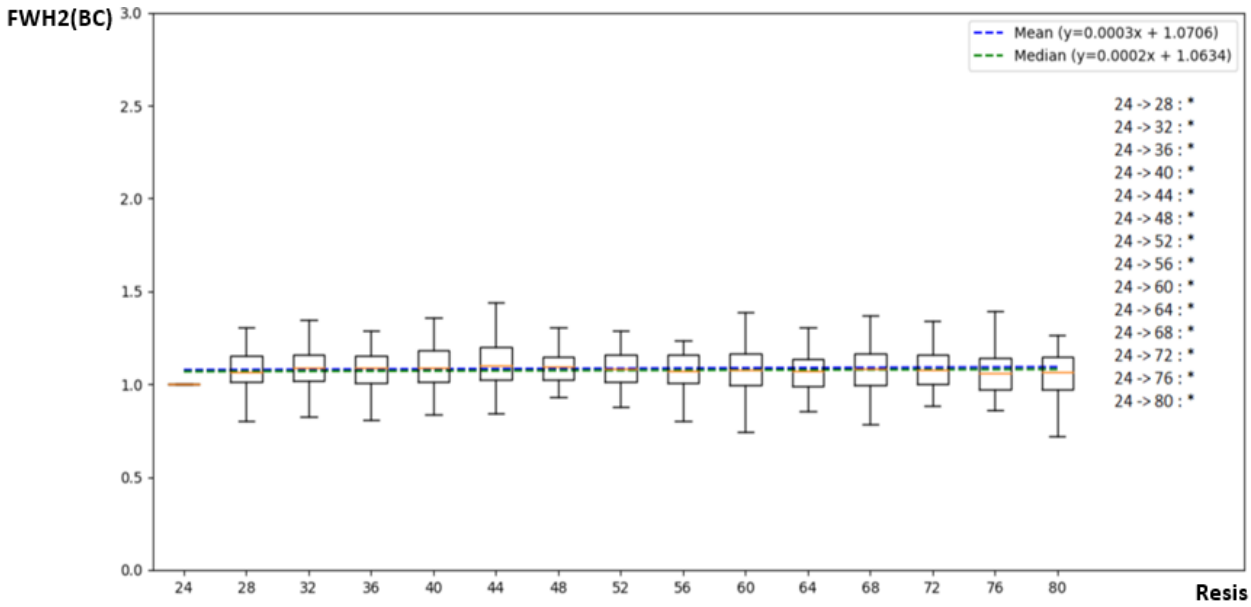

Figure B.138 Evolution of FWH2(BC) function of the tissue Resistance

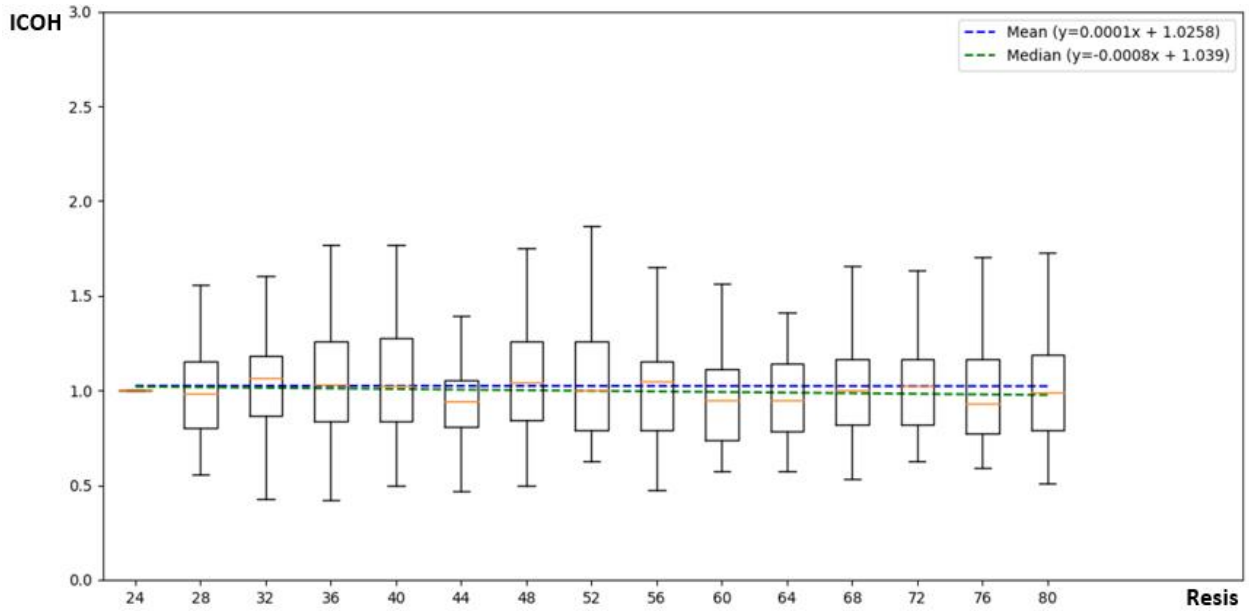

Figure B.139 Evolution of ICOH function of the tissue Resistance

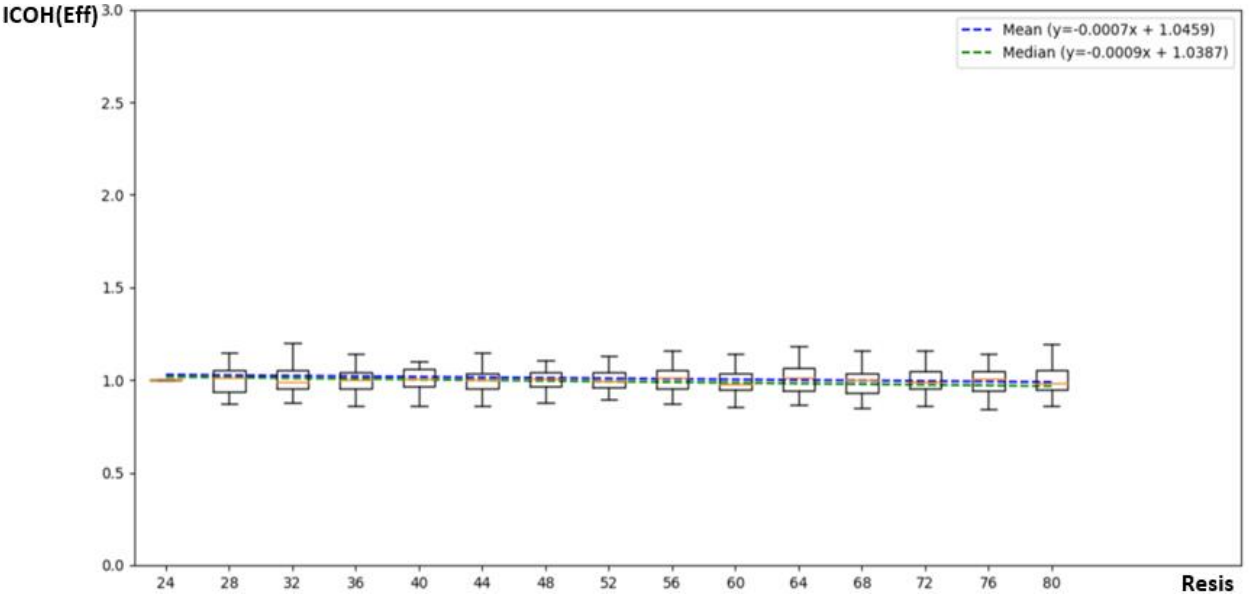

Figure B.140 Evolution of ICOH(Eff) function of the tissue Resistance

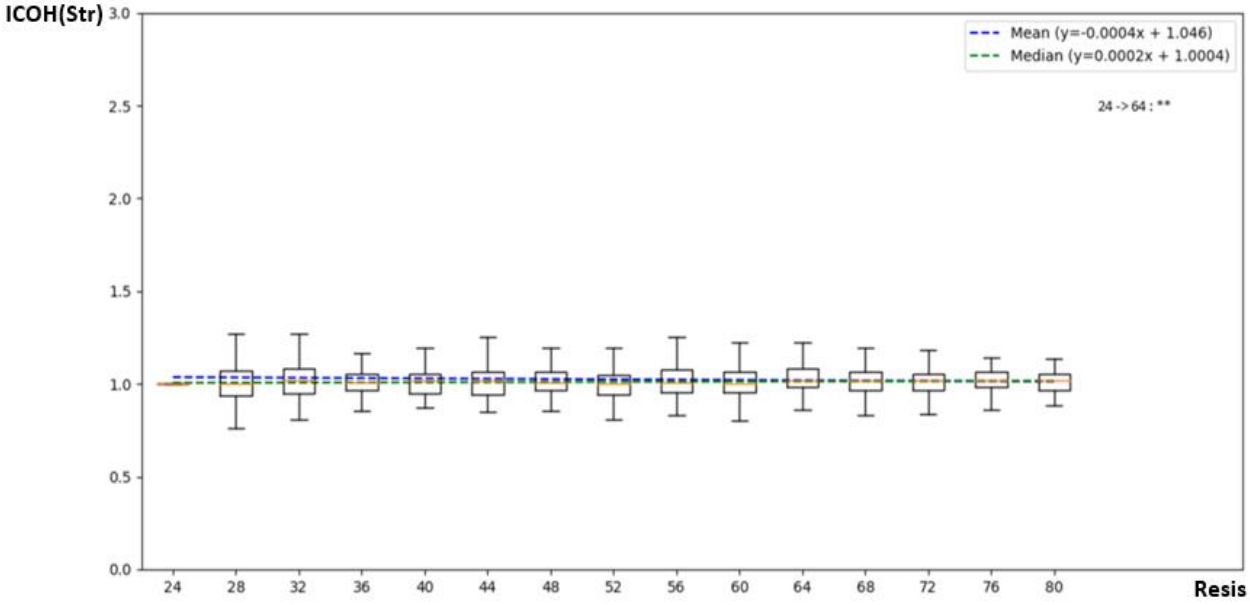

Figure B.141 Evolution of ICOH(Str) function of the tissue Resistance

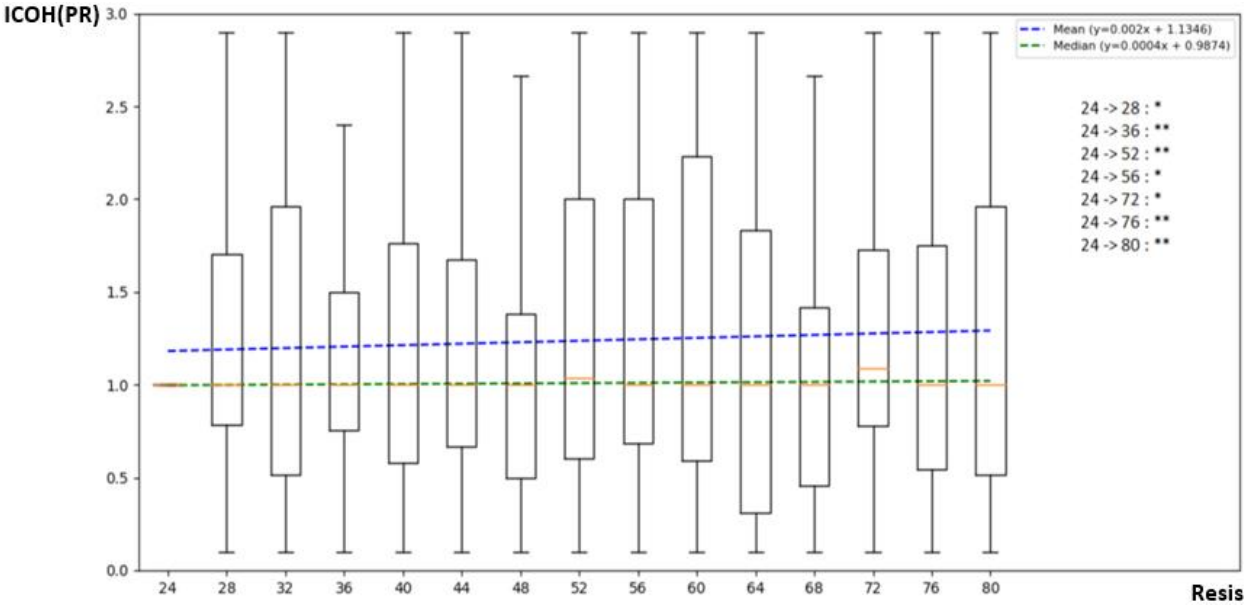

Figure B.142 Evolution of ICOH(PR) function of the tissue Resistance

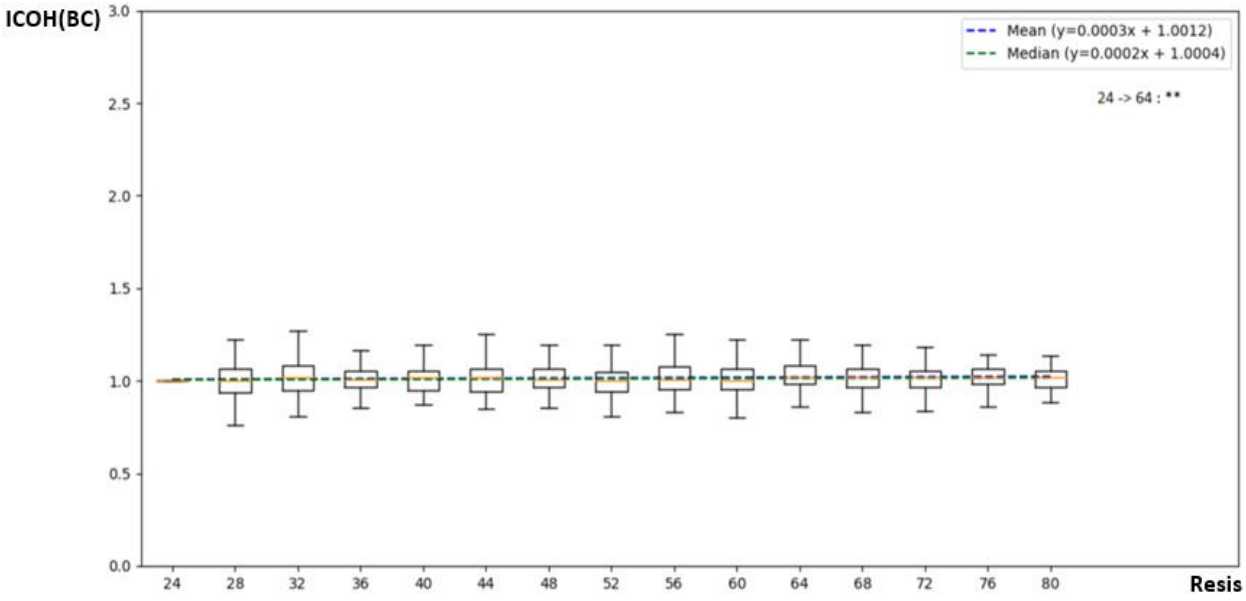

Figure B.143 Evolution of ICOH(BC) function of the tissue Resistance

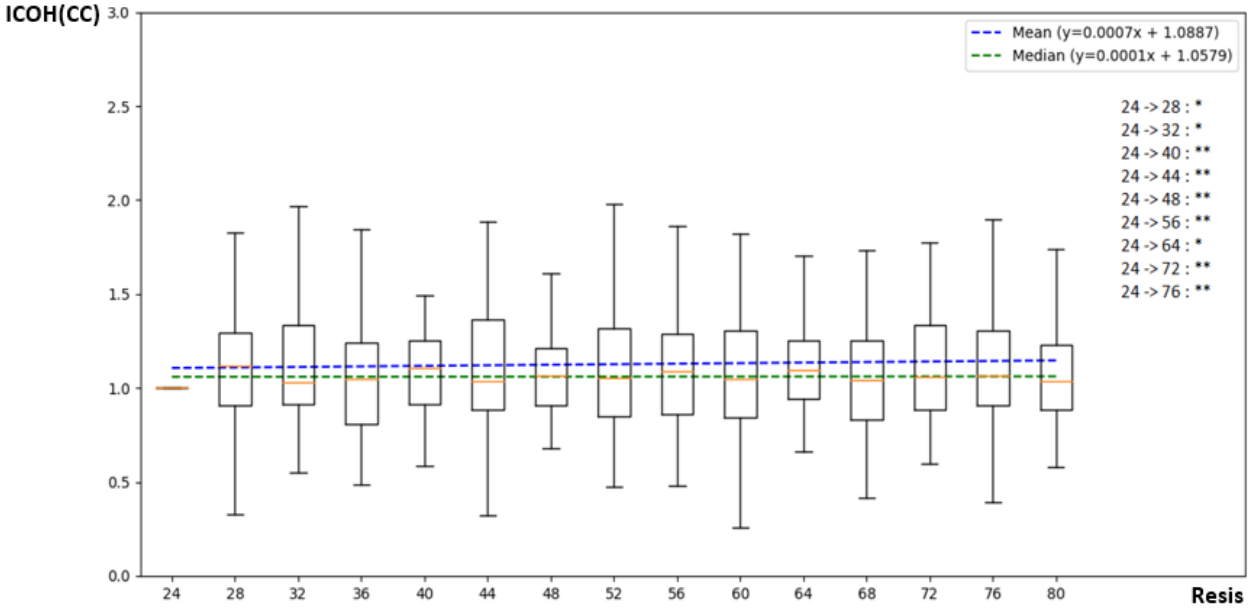

Figure B.144 Evolution of ICOH(CC) function of the tissue Resistance

Annex C: Median and Mean slopes with the ranking

Table C.1 Mean slops for Lambada_sig

Method	H2(Str)	FW_ h2(PR)	R2(Eff)	FW_ h2(BC)	FW_ h2	FW_ h2(Str)	FW_ h2(CC)	FW_ h2(Eff)
Mean	**0.0255**	**0.0089**	**0.0033**	0.0021	0.0017	0.0015	0.0007	0.0005
Rank	1	2	3	4	5	6	7	8
Method	ICOH (Eff)	ICOH (BC)	ICOH (CC)	ICOH	H2(CC)	H2(Eff)	ICOH (Str)	H2
Mean	**0.0002**	-0.0001	-0.0001	-0.0003	-0.0019	-0.0024	-0.0029	-0.0034
Rank	9	10	11	12	13	14	15	16
Method	ICOH (PR)	H2(BC)	H2(PR)	R2(Str)	R2(BC)	R2(CC)	R2(PR)	R2
Mean	-0.0036	-0.0038	-0.0049	-0.0063	-0.007	-0.0078	-0.0092	-0.0102
Rank	17	18	19	20	21	22	23	24

Table C.2 Mean slops for SACCH_nbmax

Method	H2(Str)	ICOH (Str)	FW_ h2(PR)	ICOH (PR)	H2	ICOH	FW_ h2	H2(PR)
Mean	**0.0189**	**0.0168**	**0.0121**	0.0063	0.0051	0.0032	0.0018	0.0016
Rank	1	2	3	4	5	6	7	8
Method	ICOH (CC)	R2(PR)	FW_ h2(CC)	H2(Eff)	R2(Eff)	FW_ h2(BC)	H2(BC)	H2(CC)
Mean	0.0007	**0.0006**	0.0006	0.0003	0.0001	-0.0005	-0.001	-0.0015
Rank	9	10	11	12	13	14	15	16
Method	ICOH (BC)	FW_ h2(Str)	ICOH (Eff)	R2(BC)	FW_ h2(Eff)	R2(CC)	R2(Str)	R2
Mean	-0.0019	-0.002	-0.0021	-0.0062	-0.007	-0.0082	-0.0086	-0.0123
Rank	17	18	19	20	21	22	23	24

Table C.3 Mean slops for beta_sig

Method	R2	FW_ h2(PR)	R2(CC)	R2(BC)	R2(PR)	R2(Str)	ICOH (PR)	H2(Str)
Mean	**0.0353**	**0.0221**	0.0202	0.0143	0.0073	0.0064	**0.0063**	**0.0038**
Rank	1	2	3	4	5	6	7	8
Method	FW_ h2(CC)	H2(BC)	FW_ h2	FW_ h2(BC)	ICOH (CC)	FW_ h2(Eff)	FW_ h2(Str)	H2(CC)
Mean	0.0018	-0.0003	-0.0003	-0.0006	-0.0008	-0.0031	-0.0032	-0.0036
Rank	9	10	11	12	13	14	15	16
Method	H2(PR)	ICOH	ICOH (Str)	H2	ICOH (Eff)	ICOH (BC)	R2(Eff)	H2(Eff)
Mean	-0.0041	-0.0053	-0.0053	-0.0062	-0.0063	-0.0075	-0.0078	-0.0104
Rank	17	18	19	20	21	22	23	24

Table C.4 Mean slops for current_Na_etirement

Method	ICOH (Str)	H2(Str)	H2	ICOH (PR)	H2(PR)	R2(PR)	H2(BC)	FW_ h2(PR)
Mean	**0.0147**	**0.0074**	0.0044	0.0044	0.0032	**0.003**	0.0014	0.0014
Rank	1	2	3	4	5	6	7	8
Method	R2(BC)	FW_ h2	ICOH (CC)	FW_ h2(CC)	H2(Eff)	FW_ h2(BC)	FW_ h2(Eff)	R2
Mean	0.0009	**0.0008**	0.0007	0.0006	0.0004	0.0002	0.0001	-0.0002
Rank	9	10	11	12	13	14	15	16
Method	ICOH	R2(CC)	H2(CC)	ICOH (BC)	R2(Str)	R2(Eff)	FW_ h2(Str)	ICOH (Eff)
Mean	-0.0008	-0.001	-0.0014	-0.0016	-0.0019	-0.0021	-0.0024	-0.0031
Rank	17	18	19	20	21	22	23	24

Table C.5 Mean slops for SACCH_current

Method	ICOH	H2(Str)	R2(PR)	ICOH (Str)	ICOH (PR)	FW_ h2	R2(Eff)	FW_ h2(CC)
Mean	0.031	**0.0188**	**0.0043**	**0.0029**	0.0017	**0.0009**	0.0004	0.0004
Rank	1	2	3	4	5	6	7	8
Method	ICOH (CC)	H2(CC)	H2	FW_ h2(PR)	FW_ h2(Eff)	FW_ h2(BC)	H2(PR)	ICOH (Eff)
Mean	0	-0.0011	-0.0016	-0.0016	-0.0017	-0.0017	-0.0019	-0.0023
Rank	9	10	11	12	13	14	15	16
Method	ICOH (BC)	FW_ h2(Str)	R2(CC)	H2(BC)	R2(BC)	H2(Eff)	R2(Str)	R2
Mean	-0.0025	-0.0027	-0.0035	-0.0044	-0.0047	-0.0049	-0.0071	-0.0073
Rank	17	18	19	20	21	22	23	24

Table C.6 Mean slops for Resistance

Method	H2	H2(Eff)	H2(PR)	FW_ h2(CC)	H2(BC)	FW_ h2(BC)	R2(Str)	R2(PR)
Mean	**-0.0064**	-0.0046	-0.0043	**-0.0037**	-0.0028	-0.0017	**-0.0014**	**-0.0014**
Rank	1	2	3	4	5	6	7	8
Method	R2(CC)	R2	R2(BC)	ICOH (Eff)	FW_ h2(Eff)	H2(CC)	ICOH (BC)	R2(Eff)
Mean	-0.0013	-0.0009	-0.0008	**-0.0007**	-0.0005	-0.0004	-0.0004	-0.0003
Rank	9	10	11	12	13	14	15	16
Method	FW_ h2(PR)	FW_ h2(Str)	ICOH	ICOH (CC)	FW_ h2	ICOH (PR)	H2(Str)	ICOH (Str)
Mean	-0.0003	-0.0001	0.0001	0.0003	0.0006	0.0007	0.0018	0.002
Rank	17	18	19	20	21	22	23	24

Table C.7 Mean methods ranking

Method	FW_h2(BC)	H2(Str)	ICOH(Str)	FW_h2(CC)	FW_h2	FW_h2(Eff)	H2(Eff)	FW_h2(PR)
Sum	46	58	59	61	68	68	71	71
Rank	1	2	3	4	5	6	7	8
Method	H2	ICOH	R2	H2(PR)	R2(CC)	FW_h2(Str)	R2(PR)	ICOH(PR)
Sum	72	72	73	73	75	76	79	79
Rank	9	10	11	12	13	14	15	16
Method	R2(BC)	ICOH(CC)	R2(Eff)	H2(CC)	R2(Str)	H2(BC)	ICOH(BC)	ICOH(Eff)
Sum	81	82	84	84	85	86	86	90
Rank	17	18	19	20	21	22	23	24

Table C.8 Median slops for Lambada_sig

Method	H2(Str)	FW_h2(PR)	FW_h2(BC)	FW_h2	ICOH	FW_h2(Str)	R2(Eff)	FW_h2(CC)
Median	**0.0477**	**0.0276**	0.0027	0.0022	**0.0019**	0.0016	**0.0011**	0.0007
Rank	1	2	3	4	5	6	7	8
Method	FW_h2(Eff)	ICOH(Eff)	ICOH(BC)	ICOH(CC)	R2	R2(PR)	H2(Eff)	H2(BC)
Median	0.0006	-0.0004	-0.0005	-0.0005	-0.0016	-0.0020	-0.0021	-0.0023
Rank	9	10	11	12	13	14	15	16
Method	H2(CC)	H2	R2(Str)	H2(PR)	ICOH(PR)	R2(BC)	R2(CC)	ICOH(Str)
Median	-0.0024	-0.0034	-0.0036	-0.0039	-0.0039	-0.0041	-0.0047	-0.0129
Rank	17	18	19	20	21	22	23	24

Table C.9 Median slops for SACCH_nbmax

Method	H2(Str)	ICOH(Str)	ICOH	H2	H2(Eff)	FW_h2(PR)	FW_h2	H2(PR)
Median	**0.0266**	**0.0067**	0.0054	0.0049	0.0038	**0.0029**	0.0019	0.0013
Rank	1	2	3	4	5	6	7	8
Method	ICOH(BC)	ICOH(CC)	R2(Eff)	FW_h2(BC)	FW_h2(Str)	FW_h2(CC)	ICOH(Eff)	ICOH(PR)
Median	0.0013	0.0013	**0.001**	0.001	0.001	0.0006	0.0006	0.0003
Rank	9	10	11	12	13	14	15	16
Method	H2(BC)	H2(CC)	R2(BC)	R2(Str)	R2(PR)	R2(CC)	FW_h2(Eff)	R2
Median	0.0001	-0.0001	-0.001	-0.0012	-0.0035	-0.0043	-0.0049	-0.0071
Rank	17	18	19	20	21	22	23	24

Table C.10 Median slops for Beta_sig

Method	R2	R2(CC)	R2(BC)	R2(Str)	R2(PR)	FW_h2(Str)	FW_h2(BC)	FW_h2(CC)
Median	**0.0353**	0.0124	0.0075	0.0063	0.0063	**0.0057**	0.0035	0.0023
Rank	1	2	3	4	5	6	7	8
Method	FW_h2(Eff)	FW_h2(PR)	H2(CC)	H2(Str)	ICOH(PR)	ICOH	FW_h2	H2(BC)
Median	0.0021	0.0015	**0.0013**	0.001	**0.0008**	0.0005	0.0002	-0.0005
Rank	9	10	11	12	13	14	15	16
Method	ICOH(Str)	ICOH(CC)	ICOH(Eff)	H2(PR)	R2(Eff)	H2(Eff)	ICOH(BC)	H2
Median	-0.0005	-0.0008	-0.0013	-0.0035	-0.0039	-0.0064	-0.0081	-0.0084
Rank	17	18	19	20	21	22	23	24

Table C.11 Median slops for current_Na_etirement

Method	ICOH(Str)	H2	H2(PR)	H2(Eff)	FW_h2(Eff)	FW_h2(BC)	R2(BC)	H2(BC)
Median	**0.032**	**0.0039**	0.0036	0.0026	0.002	**0.0014**	**0.0013**	0.0011
Rank	1	2	3	4	5	6	7	8
Method	ICOH(PR)	R2(Str)	FW_h2	ICOH(CC)	ICOH(BC)	H2(CC)	FW_h2(CC)	R2(CC)
Median	0.0011	0.001	0.0008	0.0005	0.0004	0.0003	0.0003	0.0002
Rank	9	10	11	12	13	14	15	16
Method	FW_h2(PR)	R2(PR)	R2(Eff)	FW_h2(Str)	R2	ICOH(Eff)	ICOH	H2(Str)
Median	0.0001	-0.0002	-0.0003	-0.0005	-0.0009	-0.0012	-0.0014	-0.0145
Rank	17	18	19	20	21	22	23	24

Table C.12 Median slops for SACCH_current

Method	H2(Str)	ICOH(Str)	ICOH(PR)	ICOH	R2	R2(CC)	H2(CC)	FW_h2
Median	**0.0228**	**0.0064**	0.0024	0.0017	**0.0013**	**0.0013**	0.0012	**0.0011**
Rank	1	2	3	4	5	6	7	8
Method	FW_h2(Eff)	FW_h2(BC)	ICOH(CC)	R2(Eff)	FW_h2(CC)	ICOH(BC)	ICOH(Eff)	R2(PR)
Median	**0.0011**	0.0009	0.0005	0.0004	0.0003	0.0003	0.0001	-0.0001
Rank	9	10	11	12	13	14	15	16
Method	FW_h2(PR)	FW_h2(Str)	R2(BC)	R2(Str)	H2(PR)	H2(Eff)	H2	H2(BC)
Median	-0.0004	-0.0012	-0.0014	-0.0019	-0.0019	-0.0028	-0.0038	-0.0048
Rank	17	18	19	20	21	22	23	24

Table C.13 Median slops for Resistance

Method	H2	H2(PR)	H2(Eff)	FW_h2(CC)	H2(BC)	R2(PR)	R2(CC)	FW_h2(BC)
Median	**-0.0074**	-0.0044	-0.0042	**-0.0031**	-0.0028	**-0.0019**	-0.0015	-0.0014
Rank	1	2	3	4	5	6	7	8
Method	R2	ICOH(Eff)	R2(BC)	R2(Str)	FW_h2(Str)	R2(Eff)	FW_h2(Eff)	ICOH(Str)
Median	-0.0009	**-0.0009**	-0.0008	-0.0007	-0.0006	-0.0004	-0.0004	-0.0004
Rank	9	10	11	12	13	14	15	16
Method	H2(CC)	ICOH(BC)	H2(Str)	FW_h2(PR)	ICOH(PR)	ICOH(CC)	FW_h2	ICOH
Median	-0.0003	-0.0002	0.0001	0.0001	0.0001	0.0002	0.0008	0.0008
Rank	17	18	19	20	21	22	23	24

Table C.14 Median methods ranking

Method	H2(Str)	FW_h2(PR)	FW_h2(CC)	R2(PR)	H2	ICOH(PR)	FW_h2	FW_h2(BC)
Sum	37	41	49	54	56	58	59	63
Rank	1	2	3	4	5	6	7	8
Method	ICOH(Str)	H2(PR)	ICOH(CC)	ICOH	H2(BC)	R2(Eff)	FW_h2(Eff)	R2(BC)
Sum	64	67	72	73	75	84	84	86
Rank	9	10	11	12	13	14	15	16
Method	H2(Eff)	H2(CC)	R2(CC)	FW_h2(Str)	R2	R2(Str)	ICOH(BC)	ICOH(Eff)
Sum	87	88	93	98	99	100	100	101
Rank	17	18	19	20	21	22	23	24